

PHYSICAL MODELING OF LOCAL SCOUR AROUND COMPLEX BRIDGE PIERS

A Dissertation
Presented to
The Academic Faculty

by

Seung Oh Lee

In Partial Fulfillment
of the Requirements for the Degree
Doctor of Philosophy in the
School of Civil and Environmental Engineering

Georgia Institute of Technology

May, 2006

Copyright © Seung Oh Lee 2006

PHYSICAL MODELING OF LOCAL SCOUR AROUND COMPLEX BRIDGE PIERS

Approved by:

Dr. Terry W. Sturm, Advisor
School of Civil and Environmental
Engineering
Georgia Institute of Technology

Dr. Fotis Sotiropoulos
The St. Anthony Falls Laboratory
Department of Civil Engineering
University of Minnesota

Dr. Philip J. Roberts
School of Civil and Environmental
Engineering
Georgia Institute of Technology

Dr. Donald R. Webster
School of Civil and Environmental
Engineering
Georgia Institute of Technology

Dr. Anthony Hayter
School of Industrial and Systems
Engineering
Georgia Institute of Technology

Date Approved: April 4 2006

ACKNOWLEDGEMENTS

This study was accomplished under the invaluable guidance of Professor Terry W. Sturm, thesis advisor and chairman of the committee, to whom I express my deepest appreciation for his constructive inspiration and precious advice. He has tolerated innumerable questions from me and helped me to enrich my understanding of this study. Sincere thanks are due to my committee: Dr. Fotis Sotiropoulos, University of Minnesota, for his perceptive comments and his ongoing efforts to help me to finish this study; Dr. Philip J. Robert, Donald R. Webster, and, Anthony Hayter, Georgia Institute of Technology, for their helpful feedback and for valuable advice to enhance this study.

Thankfulness is expressed to Mark N. Landers and Anthony J. Gotvald in the U.S. Geological Survey for their assistance and provision of field measurements. Laboratory experiments were carried out with the prodigious help of Andrew I. Udell to whom I express my gratitude.

Special thanks to my parents and family who have supplied inestimable and patient support and encouragement. Finally and most importantly, I am extremely indebted to MoonSuk Kim, my wife, for all of her support and faith which have become a robust bridge supporting what I have been and what I will be.

A grant provided by the Georgia Department of Transportation enabled the study to be conducted.

TABLE OF CONTENTS

ACKNOWLEDGEMENTS	iii
LIST OF TABLES	viii
LIST OF FIGURES	x
LIST OF SYMBOLS	xix
SUMMARY	xxiii
CHAPTER 1 INTRODUCTION AND MOTIVATION	1
1.1 Introduction.....	1
1.2 Objectives and Scope.....	2
CHAPTER 2 LITERATURE REVIEW.....	6
2.1 Characteristics of Flow around a Bridge Pier.....	6
2.1.1 Vortex Strength and Size	9
2.1.2 Vortex Shedding Frequency	13
2.2 Analytical Methods.....	17
2.3 Experimental Studies	31
2.3.1 Dimensional Analysis	32
2.3.2 Laboratory Measurements	34
2.3.3 Scale Effects of Laboratory Experiments	49
2.4 Numerical Modeling Approach	53
2.5 Field Observations	58
CHAPTER 3 FIELD STUDIES.....	61

3.1	Site Selection	62
3.2	Chattahoochee River near Cornelia, GA	64
3.3	Flint River at Bainbridge, GA.....	70
3.4	Ocmulgee River at Macon, GA	75
CHAPTER 4 METHODOLOGY OF EXPERIMENTS		81
4.1	Experimental Facilities	81
4.1.1	Horizontal Flume	81
4.1.2	Tilting Flume	83
4.1.3	Flowmeter	85
4.2	Velocity Measurements	85
4.2.1	Stream Probe - Propeller type	85
4.2.2	Electromagnetic Velocimeter.....	86
4.2.3	Acoustic Doppler Velocimeter - ADV	86
4.2.4	Comparison of Mean Velocity Profiles	93
4.3	Flow Visualization.....	94
4.4	Physical River Modeling Strategy	96
4.5	Bed Materials	98
4.6	Bridge Pier Models	100
4.7	Experimental Procedure.....	103
4.8	Velocity and Turbulence Measurements	106
4.9	Scour Depth Measurement.....	114
CHAPTER 5 EXPERIMENTAL RESULTS		117
5.1	The Chattahoochee River Model	118

5.1.1	Temporal Variation of Local Scour Depth	120
5.1.2	Measurement of Maximum Scour Depth and Scour Contour	124
5.1.3	Measurement of Water Surface Profiles	126
5.1.4	Measurement of Velocity Field	127
5.1.5	Comparison with Field Data	134
5.2	The Flint River Model	137
5.2.1	Temporal Variation of Local Scour Depth	139
5.2.2	Measurement of Maximum Scour Depth and Scour Contour	143
5.2.3	Measurement of Water Surface Profile.....	145
5.2.4	Measurement of Velocity Field	146
5.2.5	Comparison with Field Data	155
5.3	The Ocmulgee River Model.....	157
5.3.1	Temporal Variation of Local Scour Depth	158
5.3.2	Measurement of Maximum Scour Depth and Contour.....	160
5.3.3	Comparison with Field Data	162
CHAPTER 6 ANALYSIS OF EXPERIMENTAL RESULTS		165
6.1	Dimensional Analysis	165
6.2	Analysis of Temporal Variation of Local Scour Depth.....	168
6.3	Analysis of Maximum Scour Depth and Location	176
6.4	Performance of Existing Pier Scour Formulas.....	177
6.5	Analysis of Velocity Field and Turbulence Intensity around Piers	182
6.5.1	Temporal Variation of Flow and Turbulence Characteristics upstream of the Bridge Pier	183

6.5.2	Flow Characteristics upstream of the Bridge Pier	188
6.6	Flow Visualization For Motion of Sediment	197
6.7	Effect of the Ratio of Pier Width to Sediment Size	202
6.7.1	Effect of b/d_{50} for $Fr_1 < 0.4$	204
6.7.2	Effect of b/d_{50} for $Fr_1 \geq 0.4$	209
6.8	Effect of Large-Scale Unsteadiness on Scour Depth.....	213
6.8.1	Phase-averaging Technique	214
6.8.2	Effect of Large-Scale Unsteadiness on Scour Depth.....	220
6.9	Evaluation of Scour Depth with Several Predictive Equations	223
6.10	Hydraulic Model Design for Scour Depths around Complex Piers.....	230
CHAPTER 7 SUMMARY AND CONCLUSIONS.....		235
7.1	Summary	235
7.2	Conclusions.....	241
7.3	Suggestions for Future Research	242
APPENDIX A		245
APPENDIX B		257
REFERENCES.....		259

LIST OF TABLES

Table 2.1 Shape Factors for Bridge Piers and Abutments (Melville and Sutherland 1988)	35
Table 2.2 Flow Alignment Factors K_θ for a Bridge Pier (Richardson and Davis 2001)	38
Table 2.3 Definition of coefficients K_1 and K_2 in Equation 2.48 (Ettema 1980).....	45
Table 3.1 Flood discharge-frequency data for Chattahoochee River near Cornelia, GA .	65
Table 3.2 Flood discharge-frequency data for Flint River at Bainbridge, GA	71
Table 3.3 Flood-frequency discharge data for Ocmulgee River, Macon.....	77
Table 4.1 Properties of sediments for this study.....	99
Table 4.2 Bridge model scales, pier shape and pier width.....	100
Table 5.1 Summary of measured experimental data for the Chattahoochee River models	119
Table 5.2 Summary of dimensionless experimental data for the Chattahoochee River models	120
Table 5.3 Summary of experimental data for the Flint River models	138
Table 5.4 Summary of dimensionless experimental data for the Flint River models....	138
Table 5.5 Summary of experimental data for the Ocmulgee River model	157
Table 5.6 Summary of dimensionless experimental data for The Ocmulgee River models	158
Table 6.1 Comparison of integral time scales for before and after scour cases.....	197
Table 6.2 Summary of dimensionless experimental data for Chattahoochee River model pier bent	214
Table 6.3 Summary of the discrepancy ratio and root mean square error for each formula	225
Table A.1 Correction factor for pier nose shape, K_s (Richardson et al. 1991)	248

Table A.2 Correction factor for alignment, K_θ for square nosed pier (Richardson et al. 1991)	248
Table A.3 Correction factor for bed condition, K_b (Richardson and Davis 2001).....	250
Table A.4 Correction factor for armoring effect, K_a by d_{90}	250
Table A.5 Exponent m -values of $d_{\max} = \sigma_g^m d_{50}$ for a logarithmic distribution	253

LIST OF FIGURES

Figure 2.1 Schematic of flow structures and local scour hole around a cylindrical pier (Graf and Istiarto 2002)	7
Figure 2.2 Schematic of a generic vortex	9
Figure 2.3 Schematics of mechanism of vortex shedding at rear of a bridge pier.....	14
Figure 2.4 Variation of Strouhal number with Reynolds number for a square cylinder (Okajima 1982)	15
Figure 2.5 Experimental results of Chabert and Engeldinger (1956) and mathematical equation (Carstens 1966) for bridge pier scour.....	20
Figure 2.6 Definition sketch for the analysis of Nakagawa and Suzuki (1975)	22
Figure 2.7 Effect of flow intensity on the relative scour depth at a cylindrical pier in a uniform sediment (Breusers and Raudkivi 1991)	37
Figure 2.8 Separation distance upstream of the centerline of the pier from the literature	39
Figure 2.9 Equilibrium scour depth and pier Froude number (Shen et al. 1969)	40
Figure 2.10 Illustration of the temporal variation in scour depth (Richardson 1995)	42
Figure 2.11 Scour depth with time; $u_*/u_{*c} = 0.90$, $30 \leq b/d_{50} \leq 130$ (Ettema 1980)	46
Figure 3.1 Central bridge pier bent on Chattahoochee River near Cornelia, GA.....	65
Figure 3.2 Schematic of central pier bent with prototype elevations and dimensions for Chattahoochee River bridge near Cornelia	66
Figure 3.3 Temporal variation of bed elevation and discharge around central pier bent in Chattahoochee River from July 1, 2003 to July 3, 2003.....	67
Figure 3.4 Comparison of cross-sections at the upstream side of the bridge over Chattahoochee River near Cornelia	67
Figure 3.5 Layout of surveyed cross section at Chattahoochee River near Cornelia, Georgia (USGS).....	68
Figure 3.6 Aerial photo at Chattahoochee River near Cornelia, Georgia (USGS)	69

Figure 3.7 Particle size distribution of bed material samples in Chattahoochee River near Cornelia.....	69
Figure 3.8 Bridge pier bents in Flint River at Bainbridge, GA.....	70
Figure 3.9 Sketch of the main pier bent in Flint River at Bainbridge, GA.....	72
Figure 3.10 Temporal variation of bed elevation around bridge pier bent in the Flint River from March 25, 2005 to April 14, 2005 by the USGS.....	73
Figure 3.11 Historical comparison of cross-sections at the upstream side of the bridge over the Flint River at Bainbridge, GA.....	73
Figure 3.12 Layout of surveyed cross sections in Flint River at Bainbridge.....	74
Figure 3.13 Aerial photo of the bridge site in Bainbridge, Georgia (USGS)	74
Figure 3.14 Particle size distribution of bed material sample at the upstream side of the bridge over Flint River at Bainbridge, GA	75
Figure 3.15 Bridge piers in Ocmulgee River at Macon, Georgia	76
Figure 3.16 Sketch of the central bridge pier bent in the Ocmulgee River at Macon, Georgia.....	76
Figure 3.17 Temporal variation of bed elevation at upstream side of Ocmulgee River, Macon from May 5, 2003 to May 11, 2003 by the USGS.....	77
Figure 3.18 Layout of surveyed cross-sections in Macon, Georgia	78
Figure 3.19 Aerial photo around 5th street in Macon, Georgia (USGS)	79
Figure 3.20 Cross-section comparison at upstream side of the bridge over Ocmulgee River, Macon.....	79
Figure 3.21 Particle size distribution of bed material in Ocmulgee River, Macon	80
Figure 4.1 Horizontal flume: (a) Entrance section of the horizontal flume and (b) Tailgate of the flume to adjust the flow depth downstream.....	82
Figure 4.2 Calibration of the relation between bed slope and counter number	84
Figure 4.3 Tilting flume (a) head box (b) test section with glass wall	84
Figure 4.4 Comparison of the distances from boundary measured by the down-looking MicroADV and the point gage.....	87
Figure 4.5 Comparison of bed shear velocity obtained from the Clauser method and the Reynolds stress profiles for different bed conditions	90

Figure 4.6 Comparison of time series of SNR between without kaolin and with kaolin in a horizontal flume ($Q = 0.038 \text{ m}^3/\text{s}$, $y_1 = 0.107 \text{ m}$, $C_o = 1000 \text{ mg/L}$).....	91
Figure 4.7 Comparison of time series of velocity data between with kaolin and without kaolin in a horizontal flume ($Q = 0.038 \text{ m}^3/\text{s}$, $y_1 = 0.107 \text{ m}$, $C_o = 1000 \text{ mg/L}$).....	92
Figure 4.8 Time-averaged velocity with turbulence intensity shown for each data sample (average value of $U = 0.567 \text{ m/s} \pm 0.004 \text{ m/s}$ ($\pm 0.7\%$)).....	93
Figure 4.9 Comparison of mean velocity profiles ($Q = 0.032 \text{ m}^3/\text{s}$, $y_1 = 0.3 \text{ m}$)	94
Figure 4.10 Tracer delivery system: (a) the brass effluent nozzle and (b) pump stand with 30 liter conical bottom tank and rotameter	95
Figure 4.11 Sediment size distribution of the bed materials for this study.....	100
Figure 4.12 Bridge models for this study: (a) Bridge model in Chattahoochee River model with 1:23 scale, (b) Bridge model in Chattahoochee River model with 1:40 scale, (c) Bridge model in Flint River model with 1:33, (d) Bridge model in Flint River model with 1:50 scale, (e) Bridge model in Flint River with 1:90 scale, and (f) Bridge model in Ocmulgee River with 1:45 scale.	101
Figure 4.13 River model for Chattahoochee River near Cornelia, GA	102
Figure 4.14 River model for Flint River at Bainbridge, GA.....	103
Figure 4.15 River model for Ocmulgee River at Macon, GA	103
Figure 4.16 Schematic description of turbulent flow over rough bed	108
Figure 4.17 Mean velocity profile ($Q=0.085 \text{ m}^3/\text{s}$, $y_1 = 0.19 \text{ m}$, $u_* = 0.025 \text{ m/s}$).....	110
Figure 4.18 Reynolds stress profile ($Q=0.085 \text{ m}^3/\text{s}$, $y_1 = 0.19 \text{ m}$, $u_* = 0.022 \text{ m/s}$).....	110
Figure 4.19 Turbulent intensity ($Q=0.085 \text{ m}^3/\text{s}$, $y_1 = 0.19 \text{ m}$, $u_* = 0.025 \text{ m/s}$).....	114
Figure 4.20 Replicated scour development with time for flat bed experiments in Chattahoochee River modeling ($V_1/V_c = 0.83$, $y_1/b = 4.2$, $b/d_{50} = 13.9$)....	115
Figure 5.1 Temporal variation of scour depth at nose of the first pier in flat bed experimental run FB11 on Chattahoochee River model (Scale= 1:23, $T_{eq} = 25 \text{ hours}$, $V_1/V_c = 0.85$, $y_1/b = 4.16$, $b/d_{50} = 86.84$)	122
Figure 5.2 Temporal development of scour depth for flat bed experiments in the Chattahoochee River models	123

Figure 5.3 Temporal development of scour depth for river model experiments in the Chattahoochee River models	123
Figure 5.4 Scour depth contours for experimental run FB5 in Chattahoochee model (a) plan view and (b) scour depth profile at $y/b = 0$	125
Figure 5.5 Scour depth contours and scour depth profile for experimental run RM2 in the Chattahoochee River model (a) plan view and (b) scour depth profile along the centerline of bridge bent	126
Figure 5.6 Water surface profile along the centerline of bridge pier bent in flat bed model experiment FB1 in the Chattahoochee River model.	127
Figure 5.7 Mean velocity vectors for before scour at 20 percent of the approach depth for experimental run FB7 in Chattahoochee River model.....	129
Figure 5.8 Mean velocity vectors and scour contour for after scour at 20 percent of the approach depth for experimental run FB7 in Chattahoochee River model ..	129
Figure 5.9 Mean velocity vectors after scour at 40 percent of the approach depth for experimental run RM6 in the Chattahoochee River model	130
Figure 5.10 Plan view of central bridge pier bent and locations of detailed turbulence measurements for the Chattahoochee River model	131
Figure 5.11 Longitudinal turbulence intensity around bridge pier for experimental run FB7 in the Chattahoochee River model	131
Figure 5.12 Vertical turbulence intensity around bridge piers for experimental run FB7 in the Chattahoochee River model	132
Figure 5.13 Turbulent kinetic energy profiles along the bridge piers for experimental run FB7 in the Chattahoochee River models	133
Figure 5.14 Comparison of cross sections at the upstream side of the bridge in Chattahoochee River near Cornelia	136
Figure 5.15 Comparison of velocity on left side of the bridge pier bent in main channel of Chattahoochee River from experimental run RM6 for bank-full flow at $385 \text{ m}^3/\text{s}$ (July 2, 2003 measured by USGS).....	136
Figure 5.16 Temporal variation of the bed elevations around the pier bent according to the discharge in Flint River from March 25, 2005 to April 2, 2005 by USGS	139
Figure 5.17 Temporal variation of scour hole in the initial process in experimental run FB10 on Flint River model (Scale= $1/33$, $T_{eq}=11$ hours, $V_1/V_c = 0.93$,	

$y_1/b = 3.09, b/d_{50} = 105$).....	141
Figure 5.18 Temporal development of scour depth for flat-bed experiments in the Flint River model.....	142
Figure 5.19 Temporal development of scour depth for river model experiments in the Flint River model.	142
Figure 5.20 Scour contour and scour depth profile for experimental run FB7 in the Flint River model (a) plan view and (b) scour depth profile at $y/b = 0$	144
Figure 5.21 Scour contour and scour depth profile for experimental run RM1 in the Flint River model (a) plan view and (b) scour depth profile along the centerline of bridge bent	145
Figure 5.22 Water surface profile for experimental run FB1 in flat-bed model of the Flint River bridge pier bent	146
Figure 5.23 Velocity vectors for before scour measured at 40 percent of the approach flow depth of the experimental run FB1 in the Flint River model.....	148
Figure 5.24 Velocity vectors at cross section A-A in Figure 5.23 ($x/b = -1.6$).....	149
Figure 5.25 Velocity vectors at cross section B-B in Figure 5.23 ($x/b = 3.8$)	149
Figure 5.26 Scour contour lines and velocity vectors for after scour measured at 40 percent of the approach flow depth of experimental run FB1 in the Flint River model.....	150
Figure 5.27 Velocity vectors at cross section A-A in Figure 5.26 ($x/b = -1.6$).....	150
Figure 5.28 Velocity vectors at cross section B-B in Figure 5.26 ($x/b = 3.8$)	151
Figure 5.29 Scour contour lines and velocity vectors for after scour measured at 40 percent of the approach flow depth of experimental run RM1 in the Flint River model.....	152
Figure 5.30 Plan view and measured points for near-field turbulence intensity for experimental run FB1 in the Flint River model.....	153
Figure 5.31 Turbulence intensity for the streamwise direction relative to mean approach velocity of experimental run FB1 in the Flint River model.....	154
Figure 5.32 Turbulence intensity for the vertical direction relative to mean approach velocity of experimental run FB1 in the Flint River model.....	154
Figure 5.33 Turbulent kinetic energy relative to approach velocity for experimental run	

FB1 in the Flint River model	155
Figure 5.34 Comparison of cross sections at Flint River upstream of the bridge.....	156
Figure 5.35 Comparison of velocity upstream of the bridge pier from experimental run RM1 in Flint River model for Tropical Storm Alberto.....	156
Figure 5.36 Temporal development of local scour depth of FB1 in Ocmulgee River experiments	159
Figure 5.37 Temporal development of local scour depth of river model experiments in Ocmulgee River experiments.....	160
Figure 5.38 Scour contour and scour depth profile for experimental run FB1 in the Ocmulgee River model (a) plan view and (b) scour depth profile at $y/b = 0$	161
Figure 5.39 Scour contour and scour depth profile for experimental run RM1 in the Ocmulgee River model (a) plan view and (b) scour depth profile along the centerline of bridge bent	162
Figure 5.40 Comparison of cross sections at upstream of the bridge in Ocmulgee River at Macon, GA.....	163
Figure 5.41 Comparison of velocity upstream of the bridge pier from experimental run RM1 in Ocmulgee River models for the 1998 flood	164
Figure 6.1 Influence of the flow intensity, V_1/V_c , on the equilibrium time, T_{eq}	169
Figure 6.2 Comparison of temporal development of scour depth of FB4 and FB7 in the Chattahoochee River modeling (Scale=1/23, $y_1/b = 4.2$, $b/d_{50} = 13.95$) .	171
Figure 6.3 Comparison of temporal development of scour depth of RM5 and RM7 in the Chattahoochee River modeling (Scale=1/40, $y_1/b = 7.0$, $b/d_{50} = 24.5$)	171
Figure 6.4 Comparison of temporal development of scour depth of RM6, RM8 and RM9 in the Chattahoochee River modeling (Scale=1/40, $y_1/b = 4.0$, $b/d_{50} = 24.5$)	172
Figure 6.5 Comparison of temporal variation of scour depth between FB1 and FB3 in the Flint River modeling (Scale=1/50, $y_1/b = 4.3$, $b/d_{50} = 11.08$)	173
Figure 6.6 Effect of b/d_{50} on temporal development of scour depth of FB9 and FB12 in the Chattahoochee River modeling (Scale=1/23, $y_1/b \approx 3.1$, $V_1/V_c \approx 1.0$).	175
Figure 6.7 Effect of b/d_{50} on temporal development of scour depth of FB4 and FB7 in	

the Flint River models (Scale=1/50, $y_1/b \approx 4.3$, $V_1/V_c \approx 0.9$).....	175
Figure 6.8 Comparison of measured scour depths in Chattahoochee River flat-bed model with scour prediction formulas (Scale=1/23, $y_1/b \approx 4.0$, $b/d_{50} = 13.9$).....	178
Figure 6.9 Comparison of measured scour depths in Chattahoochee River model with scour prediction formulas (Scale=1/40, $y_1/b \approx 4.0$, $b/d_{50} = 24.5$).....	179
Figure 6.10 Comparison of field and laboratory measurements of scour depths and scour prediction formulas for Chattahoochee River model (Scale=1/40, $y_1/b \approx 4.0$, $b/d_{50} = 24.5$)	181
Figure 6.11 Comparison of field and laboratory measurements of scour depths and scour prediction formulas for Flint River model (Scale=1/90, $y_1/b \approx 7.0$, $b/d_{50} = 18.8$).....	181
Figure 6.12 Comparison of field and laboratory measurements of scour depths and scour prediction formulas for Ocmulgee River model (Scale=1/45, $y_1/b \approx 5.0$, $b/d_{50} = 36.9$)	182
Figure 6.13 Schematic of the locations for measuring the temporal variation of flow characteristics with the flat bed model in Chattahoochee River modeling (Scale=, 1/23, $V_1/V_c = 0.85$, $y_1/b = 4.17$, $b/d_{50} = 86.8$).....	184
Figure 6.14 Mean velocity profile with time at LOC1 (Scale=1/23, $V_1/V_c = 0.85$, $y_1/b = 4.17$, $b/d_{50} = 86.8$)	186
Figure 6.15 Mean velocity profile with time at LOC2 (Scale=1/23, $V_1/V_c = 0.85$, $y_1/b = 4.17$, $b/d_{50} = 86.8$)	187
Figure 6.16 Temporal variation of turbulence intensity profile with time at LOC1 (Scale=1/23, $V_1/V_c = 0.85$, $y_1/b = 4.17$, $b/d_{50} = 86.8$).....	187
Figure 6.17 Temporal variation of turbulence intensity profile with time at LOC2 (Scale=1/23, $V_1/V_c = 0.85$, $y_1/b = 4.17$, $b/d_{50} = 86.8$).....	188
Figure 6.18 Flow visualization of horseshoe vortex with tracer injection in experimental run FB10 in Flit River model: (a) $t=t_1$ and (b) $t= t_1+2.26\text{sec}$	189
Figure 6.19 Schematic of temporal variation of horseshoe vortex upstream of a pier: (a) $t=t_1$ and (b) $t= t_1+\Delta t$, where dotted lines show bimodal regions for velocity components in streamwise and vertical direction	190

Figure 6.20 Velocity probability distribution from experimental run FB7 in the Chattahoochee River model at $x/b = -0.33$, $z/b = 0.17$	191
Figure 6.21 Schematic of the plate for quadrant analysis (Marchioli and Soldati 2002b)	192
Figure 6.22 Joint frequency distribution of u' and w' for before-scour case at $x/b = -0.33$, $z/b = 0.17$ for experimental run FB7 in the Chattahoochee River model.....	195
Figure 6.23 Joint frequency distribution of u' and w' for after-scour case at $x/b = -0.40$, $z/b = 0.18$ for experimental run FB7 in the Chattahoochee River model ...	195
Figure 6.24 Profile of the 1:40 scale model of the Chattahoochee River bridge with $d_{50} = 0.5\text{mm}$ ($V_1/V_c = 0.70$, $y_1/b = 5.0$, $b/d_{50} = 50.9$).....	198
Figure 6.25 Sequence of the captured motions of sediments with dimensionless time scale, $t V_c / y_1$ ($V_1/V_c = 0.70$, $y_1/b = 5.0$, $b/d_{50} = 50.9$)	199
Figure 6.26 Profile of the 1:40 scale model of the Chattahoochee River bridge with $d_{50} = 3.3\text{mm}$ $V_1/V_c = 0.72$, $y_1/b = 5.0$, $b/d_{50} = 8.2$).....	200
Figure 6.27 Sequence of the captured motions of sediments with dimensionless time scale, $t V_c / y_1$ ($V_1/V_c = 0.72$, $y_1/b = 5.0$, $b/d_{50} = 8.2$)	201
Figure 6.28 Variation of relative local scour depth with the values of pier and sediment sizes.....	203
Figure 6.29 Effect of b/d_{50} on the corrected d_s/b for $Fr_1 < 0.4$	205
Figure 6.30 Plot of the ratio, b/d_{50} versus the corrected relative scour depth, d_s/b for selected field data with $Fr_1 < 0.4$ (Mueller and Wagner 2005)	209
Figure 6.31 Effect of the pier and sediment size, b/d_{50} , on the corrected relative scour depth, d_s/b for $Fr_1 \geq 0.4$	212
Figure 6.32 Effect of the pier Froude number on the pier scour depth, d_s/b , for $Fr_1 \geq 0.4$ and $b/d_{50} < 20$	212
Figure 6.33 Plot of the ratio, b/d_{50} versus the corrected relative scour depth, d_s/b with the selected field data for $Fr_1 \geq 0.4$ (Mueller and Wagner 2005).....	213
Figure 6.34 Schematic of velocity decomposition for phase averaging technique.....	216

Figure 6.35 Comparison of the ratio of phase averaged mean velocity, U_p , to global mean velocity, U , with the relative window size.....	218
Figure 6.36 Comparison of the ratio of root mean square value of u_p in vertical direction to streamwise direction after phase averaging with the relative window size	218
Figure 6.37 Ratio of the turbulence intensity to root mean square value of u_p in streamwise direction after phase averaged	220
Figure 6.38 Comparison of measured relative scour depth from laboratory experiments including Ettema, R.(1980) and Sheppard, et al (2003; 2004) data with selected pier scour equations for $Fr < 0.4$ (∇ =HEC-18 (2001); Δ =Melville and Sutherland formula (1988); O=Sheppard et al. formula (2004); \square =This study).....	226
Figure 6.39 Comparison of measured relative scour depth in field (Mueller and Wagner 2005) with selected pier scour equations for $Fr < 0.4$ (∇ =HEC-18 (2001); Δ =Melville and Sutherland formula (1988); O=Sheppard et al. formula (2004); \square =This study)	227
Figure 6.40 Probability distribution of the discrepancy ratio for the laboratory data (∇ =HEC-18 (2001); Δ =Melville and Sutherland formula (1988); O=Sheppard et al. formula (2004); \square =This study).....	228
Figure 6.41 Probability distribution of the discrepancy ratio for the field data (∇ =HEC-18 (2001); Δ =Melville and Sutherland formula (1988); O=Sheppard et al. formula (2004); \square =This study).....	229
Figure 6.42 Correction factor for the effect of b/d_{50}	233
Figure 6.43 Schematic flowchart showing how to determine the experimental conditions for physical model.....	234

LIST OF SYMBOLS

b	Width of a bridge pier
C_D, C_L	Coefficients of drag and lift, respectively
C_0	Dimensionless Chezy's coefficient, $= C/\sqrt{g}$, C is the Chezy's coefficient
D_v	Diameter of the primary horseshoe vortex
d_{50}	Median sediment diameter for which 50 percent of the sediment particles are smaller by weight
d_s	Scour depth
d_{se}	Maximum equilibrium scour depth
$d_{s \max}$	Maximum scour depth
d_*	Dimensionless sediment diameter, $= [((\gamma_s/\gamma - 1)g d^3)/\nu^2]^{1/3}$
\dot{d}_i	Initial scour rate
F	Semi-empirical pickup function, $= [C_D N_s^2 (8.2 \cos \alpha) - \tan \alpha - \tan \phi]^{2.5}$
Fr_1	Froude number of approach flow
Fr_b	Pier Froude number, $= V_1/\sqrt{g b}$
Fr_d	Densimetric particle Froude number, $= V_1/\sqrt{g' d_{50}}$
F_s	Frequency measured in Streamflo probe
f	Oscillation frequency
f_p	Coefficient of proportionality as function of geometry, sediment, and flow properties
f_v	Frequency of rotation at the vortex core
g	Acceleration due to gravity
g'	Reduced gravitational acceleration, $= [(\rho_s - \rho)/\rho]g$

k_s	Equivalent roughness height
L_r	Length scale of the model equal to the length ratio of model to prototype
l	Length of a bridge pier
n	Manning's roughness coefficient
N	Shape factor equal to 1 for circular and 1.25 for rectangular pier
N_r	Number of shaft rotations
N_s	Sediment number, $= V_1 / \sqrt{(SG-1) g d_{50}}$
N_{sc}	Sediment number at the limit of zero transport
p_s	Probability that a particle moves in one second
p_d	Probability that a particle falling to the bed comes to rest after traveling a step length λ
q_x, q_y	Sediment discharge in x and y directions, respectively
Q	Flowrate
Q_s	Rate of scour transport
Q_{so}, Q_{si}	Input and output sediment transport functions, respectively
r_o	Radius of horseshoe vortex on a flat bed
R	Radius of a vortex
Re_b	Pier Reynolds number, $= U b / \nu$
S_o	Bed slope of flume
SG	Specific gravity of a sediment
T_{eq}	Time to reach the equilibrium scour depth
t	Time scale
U	Global mean velocity over long time
U_c	Mean approach velocities corresponding to initiation of scour at the pier
u, v, w	Instantaneous velocity components in x, y, z directions
u_0	Surface velocity of the approach flow
u_b	Mean velocity at particle level

u_o	Reference velocity of the vortex
u_p	Phase averaged velocity with coherent structure
u_*	Shear velocity
u', v', w'	Fluctuation of velocity components in x, y, z directions
$u''(t)$	Instantaneous value of turbulent fluctuations
$\hat{u}(t)$	Statistical contribution of the organized periodic component
V_1	Depth averaged velocity of approach flow
V_c	Critical velocity of sediment corresponding to initiation of sediment motion
V_θ	Tangential vortex velocity, $= \omega_o R$
$V_{\theta e}$	Maximum tangential velocity of vortex
w_f	Fall velocity of a particle
x, y, z	Longitudinal, lateral and vertical direction
y_1	Flow depth of approach flow
α	Angle of bed slope
Γ_o	Initial horseshoe vortex strength
γ_s	Specific weight of a particle
ε	Angle of repose of the scour hole sides
κ	von Karman constant
λ_v	Porosity of the bed
μ	Dynamic viscosity of fluid
ν	Kinematic viscosity of fluid
ρ	Density of fluid
ρ_s	Density of sediment
σ_g	Geometric standard deviation of sediment size distribution
τ_0	Shear stress at bed
τ_c	Critical shear stress

ϕ	Angle of repose
ϕ_x	Dynamic angle of repose
ω_o	Angular velocity of initial horseshoe vortex
∇	Volume of scour hole

SUMMARY

Local scour around bridge foundations has been recognized as one of the most significant causes of bridge failures. Even though numerous studies of local scour around bridge foundations have been conducted since the 1950s, there remain problems in scour prediction because of difficulties in understanding the complex flow structures and scour mechanisms around bridge foundations. The objective of this study is to investigate the relationships among field, laboratory and numerical data for the purpose of improving scour prediction methods that currently tend to overpredict bridge scour depths because they are based on laboratory studies of simple bridge pier geometries conducted in rectangular flumes with a flat bed. In this study, three field sites in Georgia were selected for continuous monitoring and corresponding laboratory models were fabricated with physical scale ratios that modeled the full river and bridge cross sections to consider the effect of river bathymetry and bridge geometry. Three different sizes of sediment and several geometric scales of bridge pier models were used in this study to investigate the scaling effect of relative sediment size, which is defined as the ratio of the pier width to the median sediment size. The velocity and turbulence fields for each bridge model were measured using an acoustic Doppler Velocimeters (ADV) to explain the complicated hydrodynamics of the flow field around bridge piers. Flow visualization and analysis of temporal variations of the flow characteristics upstream of the bridge pier were conducted in order to investigate the relationship between the large-scale unsteadiness of the

horseshoe vortex and scour prediction equations. From a combination of the experimental results for scour and the detailed measurements of the dynamics of the horseshoe vortex, a modified scour prediction formula was developed that includes the effect of relative sediment size. Using this knowledge to select the sediment size in each physical model that included modeling of river bathymetry, the comparison between the results of laboratory experiments and prototype field measurements showed good agreement for the maximum pier scour depth in front of each bridge pier bent. Comparison of the improved scour prediction formula with a wide range of laboratory and field data showed that it performs better than existing scour prediction formulas. As an additional benefit, the improved scour prediction formula provided the basis of a proposed comprehensive procedure for modeling scour around complex pier bents with realistic river bathymetry and bridge geometry.

CHAPTER I

INTRODUCTION AND MOTIVATION

1.1 Introduction

Scour around bridge foundations can be generally divided into three categories. First, long term aggradation or degradation represent changes in bottom elevation and accompanying changes in width of the river over a long period of time due to geomorphic adjustments. Contraction scour occurs when a flow is restricted by natural causes or existence of any obstruction like a constriction caused by a bridge opening. Local scour around the bridge foundation occurs when the flow is obstructed by the presence of bridge piers and abutments placed in the main channel and floodplain of the river.

One thousand bridges have collapsed over the last 30 years in the United States and 60 percent of those failures are due to hydraulic failure including bridge foundation scour (Shirole 1991). Bridge failure results in the loss of lives and financial losses for reconstruction and rehabilitation. In 1987, the collapse of the New York State Thruway bridge resulted in the loss of ten lives. When a section of the US 51 bridge fell into the Hatchie River near Covington, Tennessee, eight people were killed in 1989. Two people were killed in 1989 due to the collapse of spans of a bridge in the Great Miami River near Miamitown, Ohio. In 1995, seven people were killed due to the collapse of the Interstate 5 bridges over Arroyo Pasajero in California (Miller 2003). The total financial loss to the

Georgia Department of Transportation was approximately \$ 130 million because more than 100 bridges had to be replaced and repaired due to flooding from tropical storm Alberto in Georgia in 1994 (Richardson and Davis 2001).

Although numerous studies have been conducted since the late 1950s on scour around bridge piers, unfortunately challenging problems remain because of the difficulties in understanding the complicated flow and scouring mechanisms combined with the complex geometries of bridges and various erodible bed materials like gravel, sand and clay. The dominant feature of the flow around bridge foundations is the large-scale eddy structure, or system of vortices (Breusers et al. 1977). The vortex system around bridge piers and abutments removes the erodible bed materials, and finally may cause failure due to bridge foundation scour.

1.2 Objectives and Scope

The study of local scour around complex bridge piers needs to begin with continuous field monitoring and then be extended to the design of experiments to investigate and simulate local scour in the laboratory with the inclusion of river bathymetry in the physical model. The objective of this dissertation is to improve previous laboratory-based scour equations and suggest a design method for local scour around complex bridge piers considering field conditions and comparing laboratory data from a physical model including river bathymetry with field measurements.

Accurate prediction of local scour depth around a bridge pier is crucial in designing of bridges. Underestimation can result in loss of life and structural collapse while overestimation can cause large financial losses on construction of a single bridge.

Numerous predictive equations for bridge pier scour have been suggested, but most of them are based on laboratory experiments, which have been conducted with simple channel and bridge geometry, or solely on field measurements which produce a wide range in values of the equilibrium scour depth. Therefore, there may be a weak relationship between laboratory and field data, and overestimation of scour depth may occur when laboratory-derived equations are applied to calculate the local scour depth in the field for bridge foundation design.

Numerous studies have been done on local scour depth around bridge piers, but most of the experiments have been conducted on a single cylindrical pier. For example, scour was observed around a cylindrical pier founded on a cylindrical caisson by Chabert and Engeldinger (1956). Although some research has been conducted with a non-cylindrical single pier, only a very few studies (Sheppard et al. 2000) show results for scour around a scaled model having the same shape as actual field bridge piers including river bathymetry.

In summary, this study focuses on the following tasks to meet the thesis objective:

- Assess the suggested equations for local scour depth around a bridge pier;
- Determine the important hydraulic parameters influencing local scour around a bridge pier;
- Understand in more detail the flow structure and scour mechanisms for local scour around bridge piers such as vortex strength, vortex shedding frequency, and shear velocity;

- Determine the time scale and evaluate temporal changes in scour depth based on experimental data;
- Compare the laboratory scour depth from flat-bed models and river models which include river bathymetry at relatively the same location and time scale;
- Examine the effect of river bathymetry on pier scour in laboratory experiments after comparison with field measurements;
- Suggest a design method to simulate live bed scour occurring in the field using laboratory results in clear-water regime;
- Estimate the field scour depth based on evolution of local scour depth and consideration of scaling from model to prototype data;
- Compare shear stresses and other turbulence quantities from experimental results and from numerical modeling and understand their influence on scour depths.

Chapter 2 reviews several approaches to study the local scour depth around a bridge pier. First, analytical methods are discussed for obtaining both the equilibrium scour depth and the temporal variation of scour depth around a bridge pier. Second, the experimental studies based on dimensional analysis is presented to elucidate the effect of several parameters, and a review of physical model studies is undertaken. Third, numerical modeling approaches of the problem are discussed followed by a consideration of field measurements.

Chapter 3 presents the location, historical discharge and bed elevations for selected field sites, namely, the bridge on Duncan Rd. over the Chattahoochee River near

Cornelia, the bridge on US 27 over the Flint River at Bainbridge, and the bridge on 5th St. over the Ocmulgee River at Macon, Georgia.

Facilities and equipment in the hydraulics laboratory of the School of Civil and Environmental Engineering at the Georgia Institute of Technology are described, and physical modeling and experimental procedures for this study are given in Chapter 4. Experimental results for flat bed models and river models are summarized in Chapter 5 including the velocity field and scour contours around each bridge model.

Temporal variation of scour depth, the effect of the relative sediment size and comparison of laboratory and field results for velocity distribution and scour depth at each field site are discussed in Chapter 6. In addition, the proposed modified scour prediction equation for the effect of sediment size is compared with the commonly accepted scour formulas in the literature in Chapter 6. Finally, a summary and conclusion are provided in Chapter 7 in which future research for scour prediction and design is discussed. Existing scour prediction formulas for local scour depth in the literature are summarized in Appendix A. In Appendix B, a numerical example is given to show how to decide the sediment size for physical modeling of local scour depth.

CHAPTER II

LITERATURE REVIEW

2.1 Characteristics of Flow around a Bridge Pier

Bridge pier scour is one type of local scour which manifests itself as a scour hole around a bridge pier caused by sediment transport that is driven by the local flow structure induced by a bridge pier; therefore, it is necessary to be acquainted with the flow structure and the related scour mechanisms around a bridge pier. In general, the local flow structure around a bridge pier consists of the downflow at the upstream face of the pier in the vertical plane, the horseshoe vortex system that wraps around the base of the pier which is the primary contributor to local scour upstream of the pier, the bow wave near the free surface on the upstream face of the pier, and the wake vortex system at the rear of the bridge pier that extends over the flow depth as shown in Figure 2.1. These features greatly complicate the understanding of the local flow structure (Dey 1996). The comprehensive effect of this complex flow structure is to increase the local sediment transport resulting in local scour around a bridge pier.

Open channel flow, a boundary layer flow, approaches a bridge pier and the velocity becomes zero on the upstream face of the bridge pier. The resulting streamwise adverse pressure gradient causes separation of the boundary layer and the formation of a horseshoe vortex system that wraps around the pier at its base.

The stagnation pressure on the nose of the pier decreases with the distance below the free surface due to the nonuniform velocity distribution in the boundary layer

resulting in a weak pressure gradient along the upstream surface of the bridge pier that drives the downward flow. The downward flow increases from the free surface to a point near the bed where the magnitude of downward flow becomes maximum with a velocity that is approximately 40% of the mean approach flow velocity. This downward flow produces a reverse bottom current near the bed which encounters the approach channel flow at some distance from the nose of the bridge pier, where there occurs a stagnation point. In the region where a very thin layer of reverse flow occurs, bimodal velocity distributions are shown to exist from the histogram of longitudinal velocity fluctuations.

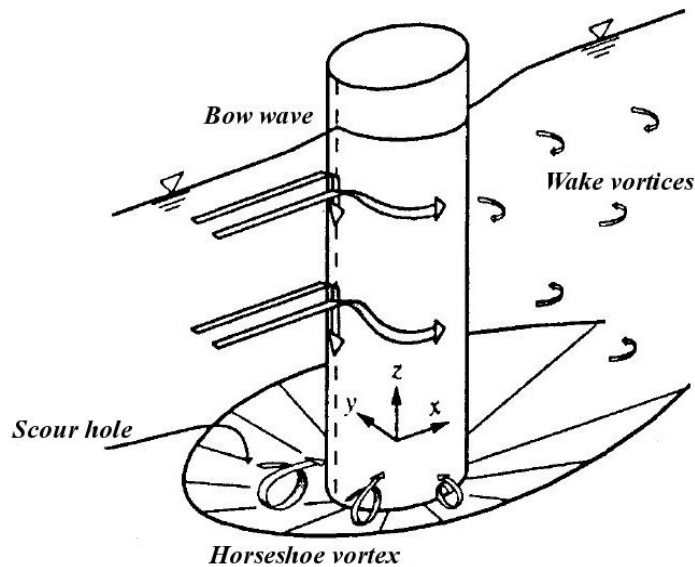


Figure 2.1 Schematic of flow structures and local scour hole around a cylindrical pier (Graf and Istiarto 2002)

Due to the strong adverse pressure gradient imposed by the bridge pier in the streamwise approach flow direction, the boundary layer separates upstream of the bridge pier. In the separated region, several vortices are consecutively developed and subsequently stretched around the base of the bridge pier giving rise to what is called a

horseshoe vortex system. The primary horseshoe vortices rotate in the same sense as the approach boundary layer vorticity, but secondary vortices have the opposite rotation to preserve streamline topology. During the time that the horseshoe vortex nearest the bridge pier is decreasing in size due to stretching, a newer and younger secondary separation vortex is induced upstream of the primary vortex. The size and strength of the secondary horseshoe vortex increases with time while the size of the primary vortex continues to be reduced by stretching. At some time, the secondary and smaller vortices merge with the primary horseshoe vortex or leapfrog it to strengthen the primary horseshoe vortex, which is finally stretched completely around the bridge pier temporarily stabilizing the flow. Subsequently, instability occurs and the primary vortex forms again. The process is then repeated irregularly (Dargahi 1989; Simpson 2001).

A bow wave is generated when the upward flow forms a circulation near the free surface that causes the flow depth to increase in front of a bridge pier (Dargahi 1989; Melville and Raudkivi 1977; Simpson 2001). It is noted that a bow wave does not dominate the local pier scour mechanism unless the flow depth is too shallow and about equal to the sum of the diameters of a horseshoe vortex and a bow wave. As the flow depth decreases and the horseshoe vortex and the bow wave interfere with each other, the horseshoe vortex is still maintained; however, the downflow is interrupted and becomes weaker.

The wake vortex system is formed by the rolling up of the unstable shear layers generated at the surface of the pier which are detached from either side of the pier at the separation line behind the pier. The wake vortex system acts like a vacuum in removing the bed material which is then carried downstream by the eddies shedding from the pier.

Since the turbulence intensity increases, erosion and transport of bed materials is intensified (Breusers et al. 1977).

2.1.1 Vortex Strength and Size

The horseshoe vortex upstream of a bridge pier is most evidently and significantly instrumental in the scour process. As a result, the size and strength of the horseshoe vortex have been referred to as the most significant factors causing local scour around a bridge pier. Thus, numerous researchers have shown that the characteristics of the horseshoe vortex are related to the pier width and the approach flow velocity. Vortex strength is generally defined as circulation around a vortex core, as shown below:

$$\Gamma = \oint \vec{V} \cdot d\vec{s} = \int_0^{2\pi} V_{\theta} r d\theta = 2\pi R V_{\theta} \quad (2.1)$$

where, R is the radius of the vortex and V_{θ} is the tangential vortex velocity defined as $V_{\theta} = \omega_0 R$ wherein ω_0 is the angular velocity of revolution of each particle about the vortex core shown in Figure 2.2.

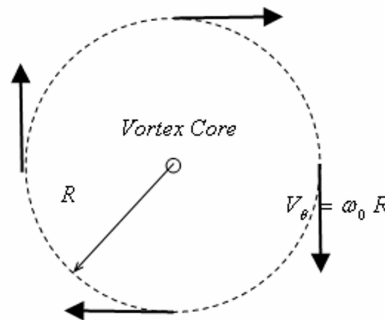


Figure 2.2 Schematic of a generic vortex

Baker(1980) assumed that the vortex strength in the scour hole could be calculated from a circular forced vortex motion of specific radius, which may be represented in terms of the vortex radius and scour depth as follows:

$$\Gamma = 2\pi R V_{\theta} = 2\pi (r_o + k_2 d_s) V_{\theta} \quad (2.2)$$

where r_o is the radius of the horseshoe vortex on a flat bed which is related to the pier width, d_s is the scour depth and k_2 is a constant during the scouring process. The vortex strength in the scour hole can be assumed to be equal to that on a flat bed as scour depth develops because the rate of vorticity diffusion increases and the total vorticity of the vortex will tend to decrease. Hence, if the vortex strength on the flat bed is represented by

$$\Gamma_o = k_1 (2 \pi r_o V_1) \quad (2.3)$$

where, Γ_o is the vortex strength on the flat bed, k_1 is a constant, and V_1 is the upstream free stream velocity, the tangential velocity can be obtained by equating Equation 2.2 and Equation 2.3 to yield

$$V_{\theta} = \frac{k_1 r_o}{r_o + k_2 d_s} V_1 \quad (2.4)$$

Thus, the vortex strength of the horseshoe vortex can be evaluated for given pier width and free stream velocity using Equation 2.2, and it is found from Equation 2.4 that the tangential velocity decreases with increasing scour depth during the scour process.

Qadar(1981) experimentally hypothesized the maximum scour depth to be a function of the initial vortex strength which is composed of terms for vortex size and

velocity as follows (SI units):

$$\Gamma_o = \begin{cases} 9.2 \times 10^{-3} \cdot \left(1 + \frac{0.025}{b}\right) b^{0.5} V_1^{0.83} & \text{for } b \geq 0.025\text{m} \\ 9.2 \times 10^{-3} \cdot b^{0.5} V_1^{0.83} & \text{for } b \gg 0.025\text{m} \end{cases} \quad (2.5)$$

where, b is the width of the bridge pier and V_1 is the approach flow velocity. An enveloping curve is proposed to show the relationship between scour depth and initial vortex strength based on laboratory data. It is quantitatively evaluated by comparing with laboratory and field data.

From a regression analysis of experimental data on flow around a cylindrical pier, Kothyari et al. (1992b) presented the diameter of the primary vortex as

$$D_v = 0.28 b^{0.85} y_1^{0.15} \quad (2.6)$$

where, b is the width of the bridge pier and y_1 is the approach flow depth. He also mentioned that the diameter of the primary vortex is dependent on the bridge opening width in comparison to the pier diameter. Equation 2.6 is valid for a narrow pier in a wide channel.

Ram(1998) expressed the initial diameter of the horseshoe vortex based on investigations by Muzzammil et al. (1989) as

$$\frac{D_v}{b} = 90.5 \frac{V_1}{\sqrt{(SG-1) g d_{50}}} \text{Re}_b^{-0.7} \frac{1}{\sqrt{\sin(\phi_x - 30^\circ)}} \quad (2.7)$$

where, ϕ_x is the dynamic angle of repose that is approximately 20% greater than the angle of repose of sediments with no flow. Equation 2.7 indicates that the initial diameter

of the vortex decreases with increasing pier Reynolds number given by $Re_b = V_1 b / \nu$. However, it is found by Muzzammil and Gangadhariah (2003) that the relative vortex size, D_v / b , is weakly influenced by the pier Reynolds number for higher values on a rigid flat bed. This means that vortex size is only dependent on the pier width for higher values of the pier Reynolds number as given by

$$D_v = 0.2 b \quad \text{for } Re_b \geq 10^4 \quad (2.8)$$

The vortex velocity (V_θ) is defined by (Muzzammil and Gangadhariah 2003)) as

$$V_\theta = \pi f_v D_v \quad (2.9)$$

where, f_v is the frequency of rotation at the vortex core. Therefore, the vortex strength of a horseshoe vortex can be represented by the diameter of the horseshoe vortex, D_v and the tangential horseshoe vortex velocity, V_θ for higher pier Reynolds numbers as follows:

$$\Gamma = \pi D_v V_\theta = (0.2 \pi b)^2 f_v \quad (2.10)$$

As the scour depth develops, the strength of the horseshoe vortex is reduced; thus, the transport rate of sediment around the bridge pier decreases. In the clear water scour regime, as the scour depth increases, the shear stress beneath the horseshoe vortex is reduced until the shear stress becomes less than the critical shear stress and sediment movement ceases in the scour hole. Most methods presented in the literature for describing the horseshoe vortex properties have not considered turbulent characteristics or unsteadiness of the horseshoe vortex, but in fact the bed materials around a bridge pier

move irregularly in time even if the approach flow is steady. It is found in the literature that the strength and size of the horseshoe vortex are closely related to the pier geometry and the approach flow velocity upstream of the bridge site while the scour depth cannot be accurately predicted unless a clear relationship between the large-scale unsteadiness of the horseshoe vortex and sediment size is presented quantitatively.

2.1.2 Vortex Shedding Frequency

Scouring in the wake region is related to the wake vortices which mainly contribute to sediment particle movement through the processes of suspending, sliding, rolling and jumping. Understanding of the flow structure in the wake region of a bridge pier, therefore, must be important to predict the scour depth around the downstream side of the bridge pier but not necessarily in front of the pier. In the wake region of a rectangular bridge pier, a non-streamlined object, the flow separates from the two edges of the pier as shown in Figure 2.3. The boundary layer detaches and curls back on itself forming vortices. It is also noted that the distance between these vortices is about constant and depends only on the size of the bridge pier for higher Reynolds numbers (Sumer and Fredsoe 1997). When the vortex is formed on one side of the bridge pier, the flow velocity becomes higher and the pressure is lower. As the vortex moves downstream, it grows in size and strength and finally is detached or shed at a constant frequency. This is followed by formation of a vortex on the other side of the bridge pier. Alternating vortices are spaced at constant distances, which is called vortex-shedding, as shown in Figure 2.3. The relationship among vortex shedding frequency, flow velocity, and characteristic length scale can be established with the Strouhal number since the vortex shedding frequency is directly proportional to the flow velocity and inversely

proportional to the characteristic length scale but independent of fluid properties such as density and viscosity of the fluid over a wide Reynolds number range; for instance, the Strouhal number has a constant value of about 0.13 for $3 \times 10^2 < Re_b < 3 \times 10^4$ as shown in Figure 2.4 for a square cylinder.

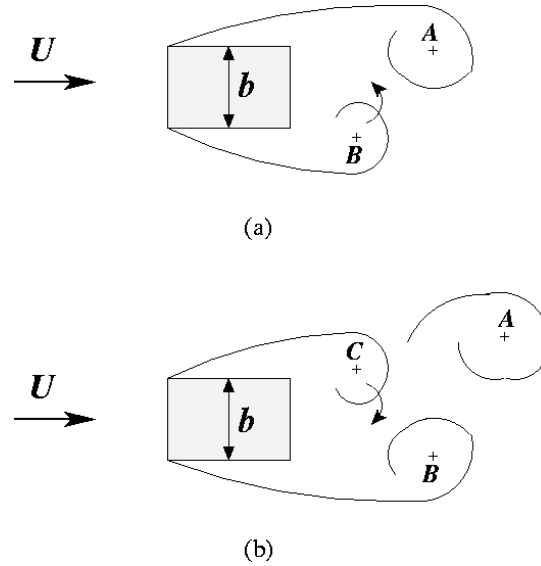


Figure 2.3 Schematics of mechanism of vortex shedding at rear of a bridge pier

The Strouhal Number is a significant dimensionless parameter when analyzing oscillating, unsteady flow dynamics problems. It represents a measure of the ratio of inertial forces due to the unsteadiness of the flow or local acceleration to the inertial forces due to changes in velocity from one point to another in the flow field, and it is expressed as

$$St = \frac{f b}{U} \quad (2.11)$$

where f is the oscillation frequency (like vortex-shedding frequency in wake region); b

is the width of a bridge pier and U is the upstream flow velocity.

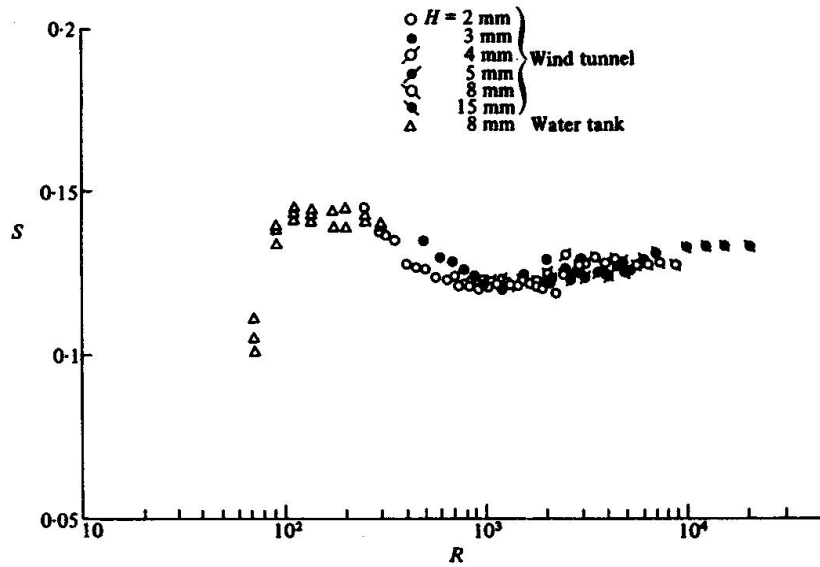


Figure 2.4 Variation of Strouhal number with Reynolds number for a square cylinder (Okajima 1982)

The value of the Strouhal number is determined experimentally, and it is generally found to be constant over a wide range of Reynolds numbers. The Strouhal number is a dimensionless calibration factor used to characterize various bluff bodies. If their Strouhal numbers are the same, then the flow field around two different object bodies behave similarly. Even when the pier Reynolds number, $Re_b = V_1 b / \nu$, increases, the Strouhal number (St) or vortex shedding frequency is approximately constant within a wide range (i.e. $Re_b = 300 \sim 3 \times 10^5$ for cylindrical shape). There is a sudden increase of St at a certain value of Re_b (i.e. $Re_b = 3 \sim 3.5 \times 10^5$ for cylindrical shape). However, the Strouhal number of a bluff body like a rectangular cylinder is less sensitive to the Reynolds number because the separation points are relatively fixed at the leading edges,

which means that the Strouhal number of a bluff body is generally less than for a circular shape as shown in Figure 2.4. The angle of attack on a bridge pier causes slight changes in the Strouhal numbers (Sumer and Fredsoe 1997).

It has been observed that the primary vortices formed on the side of a cylindrical pier are shed periodically with a constant frequency of about 0.33 Hz for $Re_b = 6,000 \sim 65,000$ within the relative flow depth range of $z/y_1 = 0.1 \sim 0.9$ (Dargahi 1989). The relationship between the scaling of wake vortices to the strength and frequency of wake vortices shed from a bridge pier was suggested by Kirkil et al. (2004). They conducted several experiments by changing the width of a pier at constant flow properties for $Re_b = 29,000 \sim 186,000$. The median sediment size was $d_{50} = 1.05\text{mm}$, approach flow depth was 1.0m and the average approach flow velocity was 0.46m/s. The range of the cylindrical pier diameters was from 0.064m to 0.406m. It was found that the frequency of vortex shedding from a pier decreases with the increasing width of a pier based on the power spectrum analysis of the streamwise point velocities measured with an ADV in the wake. Large-scale Particle Image Velocimetry (LSPIV) was used to visualize and measure the strength or intensity of the wake vortices at the flow free surface. As tracers at the flow surface, 2 mm diameter polypropylene beads were used to seed the flow during image recording. Also, they proposed an adjustment factor for measured pier scour depth to account for the mis-scaling of the wake vortices (Ettema et al. 2006).

The strength of the horseshoe vortex is positively related with the width of a cylindrical pier according to (Dargahi 1989). In addition, Dargahi (1989) observed a constant shedding frequency for wake vortices over the range of pier Reynolds number

investigated (6.6×10^3 – 6.5×10^4), while Kirkil et al. (2004) and Ettema et al. (2006) showed from their experimental results that the shedding frequency of wake vortices for cylindrical piers decreases with increasing pier Reynolds number (2.9×10^4 – 1.9×10^5) consistent with a constant Strouhal number in this range (Sumer and Fredsoe, 1997). As scour depth is developing, the strength of the horseshoe vortex become less and its size increases as discussed before. However, the frequency and intensity of wake vortices may not change significantly during the scour process. The horseshoe vortex system is not influenced by the wake vortices as discussed by Dargahi (1989). He found little or no influence of the wake vortices on the horseshoe vortex system, which is primarily responsible for the scour, when he measured the horseshoe vortex frequency for both a cylindrical pier and an elongated pier.

2.2 Analytical Methods

Local scour due to the bridge pier is mainly attributed to the geometry of the bridge pier and the consequent vortex system around it which generally consists of the horseshoe vortex, corner vortex immediately upstream of the pier, and vortex shedding downstream of the bridge pier. The horseshoe vortices are generated by the adverse pressure gradient and separated shear layer, which result in the initiation of sediment motion around the bridge pier. Hence, many researchers have adopted an analytical approach to study the relationship between the vortex system around a bridge pier and bridge pier-scour, even though early studies have had their primary investigation objectives anchored in dimensional analysis of small-scale laboratory experiments since the 1950s. Early

analytical investigations relied on a combination of dimensional analysis, approximations based on potential flow theory, and an analogy to a foreshortened contraction (Shen et al. 1969).

Carstens (1966) proposed that the forces causing scour were the resultant of the drag and lift forces around a typical particle and applied an equation for the sediment transport rate, which was a function of the ratio of the disturbing force on the particle to the effective weight of the particle, and the sediment continuity equation, to different experiments. These experiments included scouring around a cylindrical pier. The result of the analysis was an expression for scour depth as a function of time. In the sediment continuity equation, the net rate of sediment transport out of the scour hole was related to the time rate of change of scour hole volume, \forall , where the scour hole was assumed to have the shape of an inverted frustum of a right circular cone with a base diameter equal to the pier diameter, b , and a side slope equal to the angle of repose, ϕ . The resulting expression is

$$Q_s(out) - Q_s(in) = \frac{d\forall}{dt} \quad (2.12)$$

where $Q_s(out)$ is the rate of sediment transport out of the scour hole and $Q_s(in)$ is the rate of sediment transport into the scour hole. If clear water scour occurs, $Q_s(in)$ is equal to zero and only $Q_s(out)$ is considered for analysis of scour around the cylindrical pier. According to the assumed scour-hole geometry mentioned above, the volume of the scour hole becomes

$$\nabla = \frac{\pi}{3 \tan \phi} \left(\frac{d_s^3}{\tan \phi} + \frac{3 b d_s^2}{2} \right) \quad (2.13)$$

where d_s is the scour depth; b is the diameter of the cylindrical pier; ϕ is the angle of repose; and d_{50} is the median grain diameter of sediment. Equation 2.13 is differentiated with respect to t and then substituted into Equation 2.12 for clear-water scour to give

$$Q_s(out) = \frac{\pi}{\tan \phi} \left(\frac{d_s}{\tan \phi} + b \right) d_s \frac{dd_s}{dt} \quad (2.14)$$

The approximate rate of sediment transport, $Q_s(out)$, based on Chabert and Engeldinger's (1956) experiments for scour around the cylindrical bridge pier was suggested as

$$\frac{Q_s(out)}{V_1 \left(\frac{b + 2d_s}{\tan \phi} \right) d_{50}} = 1.3 \times 10^{-5} (N_s - N_{sc})^{5/2} \left(\frac{d_s}{b} \right)^{-3} \quad (2.15)$$

where V_1 is the mean velocity of approaching flow; N_s is the sediment number ($= V_1 / \sqrt{(SG - 1) g d_{50}}$); SG is the specific gravity of the sediment; and N_{sc} is the value of sediment number at the limit of zero transport. After combining Equation 2.14 and Equation 2.15 the resulting equation can be integrated using that $d_s = 0$ at $t = 0$ as the initial condition resulting in

$$4.14 \times 10^{-6} (N_s^2 - N_{sc}^2)^{5/2} \frac{V_1 t d_{50}}{b^2} = \frac{(d_s/b)^5}{\tan \phi} + \frac{(d_s/b)^4}{16} - \frac{\tan \phi (d_s/b)^3}{24} + \frac{\tan \phi (d_s/b)^2}{32} - \frac{(\tan \phi)^3 (d_s/b)}{24} + \frac{(\tan \phi)^4}{64} \ln \left(\frac{2(d_s/b)}{\tan \phi} + 1 \right) \quad (2.16)$$

It may be observed from Figure 2.5 that Equation 2.16 can reproduce the experimental data for scour around a bridge pier for $d_{50} = 50$ mm and 100 mm. Equation 2.16 and Figure 2.5 show that the scour depth seems to increase continuously with the time. This is because the equilibrium scour depth in clear-water scour is reached when the shear stresses at the surface of the scour hole become less than that needed to move a particle. It can theoretically only occur at infinite time (Laursen and Toch 1956).

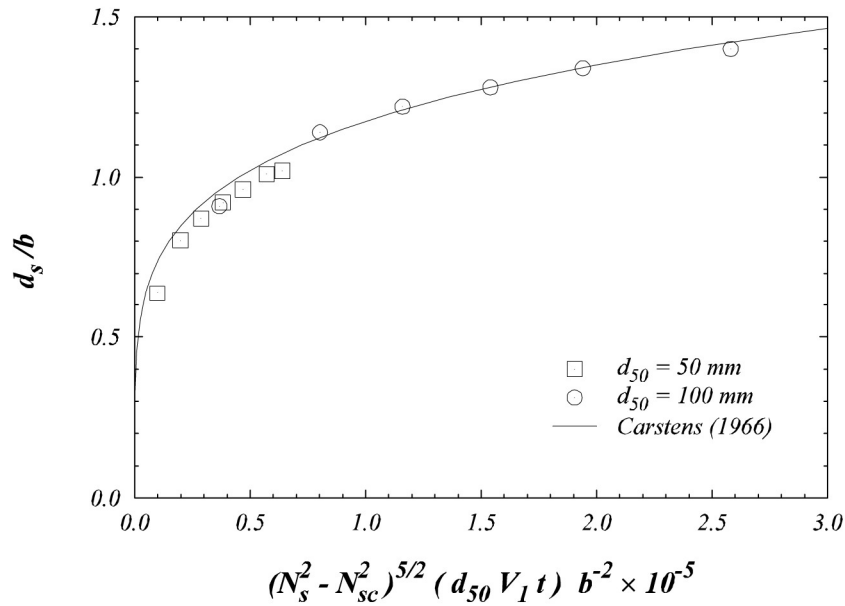


Figure 2.5 Experimental results of Chabert and Engeldinger (1956) and mathematical equation (Carstens 1966) for bridge pier scour

Melville (1975) has observed that the size and circulation of the horseshoe vortex

increase rapidly, and the velocity near the bottom of the hole decreases as the scour hole is enlarged. According to Melville, the magnitude of the downflow seems to be directly associated with the rate of scour. However, this is because he compared the vortex core circulation on a flat bed with the value of the maximum scour hole circulation when an equilibrium depth of scour has been reached. Because the size of the scour hole is much larger than the size of the vortex core, such a calculation would predict wrongly that the circulation increases as scour proceeds (Baker 1980).

The horseshoe vortex core circulation can also be used semi-empirically to derive an equation to predict the scour depth (Baker 1980). As discussed in a previous section, the circulation around the vortex core on a flat bed can be presented as function of the radius of vortex core, r_0 , and the upstream free stream velocity, U . Also, the vortex strength within scour hole can be expressed by the radius of the horseshoe vortex, r , which is assumed to be $r = r_0 + k_2 d_s$; k_2 is a constant and the tangential velocity, V_θ , at the edge of the vortex as given in Equation 2.2 and 2.3, respectively. If Γ is assumed to be constant within the scour hole and equal to Γ_0 , the tangential velocity at the edge of the horseshoe vortex can be evaluated as given by Equation 2.4. The critical velocity of a sediment particle, V_c , can be determined by assuming equilibrium of the forces acting on the particle, which are the drag, lift, and gravity force, resulting in

$$V_c = \left[\frac{8}{3} \frac{\cos(60^\circ - \varepsilon)}{C_D \sqrt{3} + C_L} \left(\frac{\rho_s}{\rho} - 1 \right) g d_{50} \right]^{1/2} \quad (2.17)$$

where ε is the angle of repose of the scour hole sides; C_D and C_L are coefficients of drag and lift, respectively; and ρ_s is the density of sediment. The equilibrium scour

depth in clear-water scour condition occurs when $V_\theta = V_c$ so that $d_s = d_{se}$ which yields

$$\frac{d_{se}}{b} = \frac{k_3}{k_2} \left[k_1 \left(\frac{8}{3} \frac{\cos(60^\circ - \varepsilon)}{C_D \sqrt{3} + C_L} \right)^{-1/2} N_s - 1 \right] \left(k_4 \frac{y_1}{b} \right) \quad (2.18)$$

where k_3 and k_4 are constants; and N_s is the sediment number. Equation 2.18 is compared with experimental results from Baker (1978) and Chabert and Engeldinger (1956), by plotting the equilibrium scour depth, d_{se}/b against N_s , which shows each linear relationship for different sediment sizes, respectively.

Nakagawa and Suzuki (1975) assumed that the scale and strength of the primary horseshoe vortex, which is drawn in triangle H0L of Figure 2.6, were constant during evolution of the local scour hole as shown in Figure 2.6.

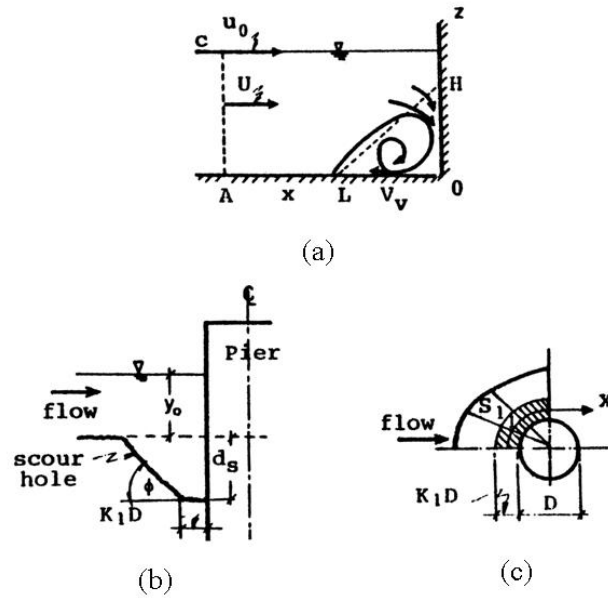


Figure 2.6 Definition sketch for the analysis of Nakagawa and Suzuki (1975)

The initial circulation of the horseshoe vortex was given by

$$\Gamma_o = -\frac{u_0 b}{2} \quad (2.19)$$

where u_0 is the surface velocity of the approach flow; and b is the diameter of a pier.

The circulation inside of the triangle H0L was given by

$$\Gamma_2 = \int_0^{2\pi} R \omega R d\theta = -2 \pi \omega R^2 = -2 \pi R V_\theta \quad (2.20)$$

where R is the radius of rotation of the horseshoe vortex; ω is the angular velocity; and V_θ is the tangential velocity at the circumference of the horseshoe vortex core assuming it to be acting at particle level below the horseshoe vortex. They suggested that the relative distances, $L0/D$ and $H0/D$, were 0.60 and 0.65 respectively, and also gave $R = 0.177 b$ regardless of pier size and pier Reynolds number after observation of the flow pattern by using dye injection. The tangential velocity, V_θ , at the bed can be obtained from Equation 2.19 and Equation 2.20, and it is related to the mean velocity of the approach flow as follows:

$$V_\theta = 0.45 u_0 = 0.45 V_1 \left(1 + \frac{n \sqrt{g}}{\kappa y_1^{0.167}} \right) \quad (2.21)$$

where y_1 and V_1 are flow depth and mean velocity of the approach flow, respectively; κ is the von Karman constant, and n is the Manning's roughness coefficient. They further showed that the dimensionless shear stress could be expressed by using the drag force on a particle and Equation 2.21 to yield

$$\tau_* = \frac{\tau_0}{\gamma_s d} = \frac{u_*^2}{SG g d} 0.2025 \left(1 + \frac{n\sqrt{g}}{\kappa y_1^{0.167}} \right)^2 \frac{C_D}{2} \frac{V_1^2}{SG g d} \quad (2.22)$$

where τ_0 is the shear stress at bed; γ_s is the specific weight of a particle; u_* is the shear velocity; SG is the specific gravity of a particle; d is the mean particle size; and C_D is the drag coefficient.

Nakagawa and Suzuki (1975) then introduced the stochastic nature of particle movement, and thus defined p_s and p_d as the probabilities that a particle on the bed moves in one second, and that a particle falling to the bed comes to rest after traveling a step length λ . Based on these concepts, the sediment transport rate was given by

$$Q_s = \exp\left(-\frac{p_d}{\lambda} x\right) \int_0^x \left(\frac{A_2}{A_1} dp_s\right) \exp\left(\frac{p_d}{\lambda} x\right) dx \quad (2.23)$$

where A_1 and A_2 are constants and x is measured from the pier in upstream direction shown in Figure 2.6 (a). If the motion is restricted to the stagnation plane, where $x = 0$, the sediment transport rate could be rewritten as follows:

$$Q_s = \frac{A_2}{A_1} d p_s \quad (2.24)$$

where p_s is related to τ_* from Equation 2.22 by a sediment transport model.

The hollow formed around a pier in Figure 2.6 was observed to have approximately a constant width $K_i b$ where $K_i = 0.25$. Assuming that all sediment starts to move from the scour hole via the hollow, and that sediment is fed into the hollow by sliding down along the side slope of the scour hole, the area of the sloping region in

Figure 2.6 (c) becomes

$$S_1 = \frac{(1 + 2 K_i) d_s}{(1 + K_i) \sin \phi} + \frac{d_s^2}{(1 + K_i) \tan \phi \sin \phi b} \quad (2.25)$$

where ϕ is the angle of the slope. Thus, the rate of sediment supplied into the scour hole by sliding down becomes $S_1 \cos \phi dd_s/dt$. The sediment continuity equation for scour along the x-direction then becomes

$$\left(K_i + \frac{S_1}{b} \cos \phi \right) \frac{dd_s}{dt} + \left(\frac{K_i}{1 - \lambda_v} \right) \frac{dQ_s}{dx} = 0 \quad (2.26)$$

where λ_v is the porosity of the bed. After substituting Equation 2.24 into Equation 2.26 and multiplying by $\sqrt{d/SGg}$ to nondimensionalize with respect to the time, the scour depth divided by the pier width is given in Equation 2.27 as

$$\left(K_i + \frac{S_1}{b} \cos \phi \right) \frac{d(d_s/b)}{d(t/\sqrt{SGg})} + \left(\frac{\varepsilon K_i}{1 - \lambda_v} \right) \frac{A_2}{A_1} \frac{d}{b} p_s \sqrt{\frac{d}{SGg}} = 0 \quad (2.27)$$

where ε is the rate of transportation at which the particles are transported outside the scour hole. Finally, putting Equation 2.25 into Equation 2.27 and then integrating with the boundary condition $d_s = 0$ at $t = 0$ gives

$$\left(\frac{K_i}{1 - \lambda_v} \right) \frac{A_2}{A_1} \frac{d}{b} p_s t = \left(\frac{d_s}{b} \right) + \frac{1 + 2 K_i}{2 (1 + K_i) \tan \phi} \left(\frac{d_s}{b} \right)^2 + \frac{\varepsilon}{3 (1 + K_i) \tan^2 \phi} \left(\frac{d_s}{b} \right)^3 \quad (2.28)$$

where $A_1 = \pi/4$, $A_2 = \pi/6$, $\lambda_v = 0.4$ and $\tan \phi = 1$ are chosen. They also conducted experiments and concluded that the maximum scour is dependent on the horseshoe vortex

for which the length scale is characterized by the pier width. Equation 2.28, expressing the scouring time in terms of d_s/b , showed good agreement with their experimental data during the initial stage of scour. However, Equation 2.28 is not able to estimate the equilibrium scour depth, because the scour depth calculated by this model continuously increases with time (Nakagawa and Suzuki 1975).

Another scour-prediction equation using the stochastic nature of particle movement was proposed by Hjorth (1977), who used the method originally suggested by Einstein (1950), in which the probability of particle motion was defined as the probability that the erosive strength of the eddy was greater than the resisting force of a particle in direct contact with the turbulent eddy. The lift force, however, was assumed to be negligible and the normalized Gaussian distribution was selected for the probability of particle entrainment in this model.

Based on analytical models relating scour depth to horseshoe vortex properties, Muzzammil and Gangadhariah (2003) proposed that equilibrium scour depth is a function of the horseshoe vortex size, tangential velocity, and vortex strength in the scour hole. They found that the mean size of the horseshoe vortex is about 20% of the cylindrical pier diameter, and the vortex tangential velocity is around 50% of the mean velocity of approach flow for $10^4 \leq Re_b \leq 1.4 \times 10^5$ at fixed flat-bed conditions. The size of the vortex was assumed to be independent of the sediment mobility. Using these variables, they suggested a maximum equilibrium scour-depth equation for clear-water scour given by

$$\frac{d_{se}}{b} = \left[10.93 \left(\frac{U_c}{V_c} \right)^2 d_*^{0.02} \left(\frac{U_c}{V_{\theta e}} \right)^{0.25} \right] \left(\frac{y_1}{b} \right)^{1/3} \quad (2.29)$$

where d_{se} is the maximum equilibrium scour depth ; U_c and V_c are the mean velocities corresponding to initiation of scour at the pier and initiation of sediment motion upstream, respectively; U_c can be computed by Equation 2.30 proposed by Garde et al. (1989) and V_c can be calculated using Shield's initiation criterion for upstream sediment motion; $V_{\theta e}$ is the maximum tangential velocity of vortex; and d_* is the dimensionless sediment diameter (Muzzammil and Gangadhariah 2003).

$$\frac{U_c}{SG d_{50}} = 1.2 \left(\frac{b}{d_{50}} \right)^{-0.11} \left(\frac{y_1}{d_{50}} \right)^{0.16} \quad (2.30)$$

Laboratory data from Chabert and Engeldinger (1956), Shen et al. (1969) and Jain and Fischer (1980) are used for the comparison of prediction scour depth calculated by Equation 2.29 and well accepted prediction formulas (Breusers et al. 1977; Hancu 1971; Jain 1981; Laursen and Toch 1956; Shen et al. 1969). However, Equation 2.29 shows overprediction for the data from Chabert and Engeldinger (1956) and Jain and Fischer (1980) while it underpredicts for data from Shen et al. (1969).

Yanmaz and Altinbilek (1991) suggested a differential equation for the temporal variation of local scour depth, assuming that the shape of the scour hole is an inverted circular cone, which is similar to the approach proposed by Carstens (1966):

$$\begin{aligned}
Q_s &= \frac{dV}{dt} = Q_{so} - Q_{si} \\
&= \frac{d}{dt} \left[\frac{\pi}{3 \tan \phi} \left(\frac{d_s^3}{\tan \phi} + \frac{3b d_s^2}{2} \right) \right] \\
&= \frac{\pi}{\tan \phi} \left(\frac{d_s^2}{\tan \phi} + b d_s \right) \frac{dd_s}{dt}
\end{aligned} \tag{2.31}$$

where Q_{so} and Q_{si} are the input and output sediment transport functions, respectively; b is the width of pier; and ϕ is the angle of repose of sediment. The output sediment transport function, Q_{so} , for the scour hole around a pier can be represented in a dimensionless form using a semi-empirical pickup function, F (LeFeuvre et al. 1970) as follows:

$$\frac{Q_{so}}{u_b d_{50} \left(\frac{2d_s}{\tan \phi} + b \right)} = f_p F \tag{2.32}$$

where the left-hand side of Equation 2.32 is regarded as the volume of sediment transported from a unit area of particle size times the projected width of the scour hole perpendicular to flow direction, $d_{50} (2d_s/\tan \phi + b)$, in unit time; u_b is the mean velocity at particle level; $F = [C_D N_s^2 (8.2 \cos \alpha) - \tan \alpha - \tan \phi]^{2.5}$, where α is the bed slope; and f_p is the coefficient of proportionality, which is able to consider the difference between one scour hole and another one as function of geometry, sediment, and flow properties. By substitution of Equation 2.32 into Equation 2.31 for clear-water scour, $Q_{si} = 0$, f_p becomes

$$f_p = \frac{\int \frac{\pi}{\tan \phi} \left(\frac{d_s^2}{\tan \phi} + b d_s \right) dd_s}{\int u_b \left(\frac{2d_s}{\tan \phi} + b \right) d_{50} F dt} \quad (2.33)$$

Based on experimental data, the relationship between f_p and other dimensionless parameters like d_s/b , N_s , C_D and $\tan \phi$ was acquired as follows:

$$f_p = b_0 \left(\frac{u_b t}{d_{50}} \right)^{b_1} N_s^{b_2} C_D^{b_3} (\tan \phi)^{b_4} \quad (2.34)$$

where $b_1 = 3000$; $b_2 = 5.8$; $b_3 = 2.8$; and $b_4 = 6.4$. Instead of d_s/b , $u_b t/d_{50}$ was chosen to consider the temporal evolution of scour depth and the effect of approach velocity. Combining Equation 2.31 and Equation 2.32, dd_s/dt can be obtained as follows:

$$\frac{dd_s}{dt} = \frac{F f_p d_{50} \tan \phi}{\pi} \left(\frac{2d_s + b}{d_s^2 + b d_s \tan \phi} \right) \quad (2.35)$$

Yanmaz and Altinbilek (1991) solved Equation 2.35, a first-order nonlinear differential equation, with the second-order Runge-Kutta method but they admitted the shortcoming of f_p caused by the sensitivity of the drag coefficient to the sediment size. Also, their analysis can be applied only for $4.7 \text{ cm} < b < 6.7 \text{ cm}$. Therefore, impractical results may occur when the parameters are outside of the range for which Equation 2.35 was calibrated. For instance, the temporal rate of scour depth development from Equation 2.35 can be negative for $d_{50} > 0.35 \text{ mm}$, and for finer sediments the scour depth calculated by Equation 2.35 becomes much smaller than expected.

Johnson and McCuen (1991) investigated the time dependence of scour including hydrologic input to analyze the scour depth around bridge piers. They proposed Equation 2.36 with the assumption that the erosion rate is proportional to the difference between the downward velocity at the bed and the terminal fall velocity:

$$\frac{\Delta d_s}{\Delta t} = C_8 \left[K C_1 V_1 (1 - e^{-C_2 b y_1}) - C_6 \sqrt{\frac{2 \rho_s g d_{50} \sin \phi}{3 \rho \sqrt{2} (1 - \sin \phi)^{0.5}}} + C_7 \left(\frac{d_{84}}{d_{50}} \right) e^{-C_5 V_1} \right] \quad (2.36)$$

where constants C_1 through C_8 were determined using the nonlinear least squares method to fit the model to laboratory data from Melville (1975) and Chiew (1984).

Sumer et al. (1992) described the rate of local scour under steady and periodic flow conditions with time scales from waves to tidal flows.

Kothyari et al. (1992b) investigated the temporal variation of local scour depth around circular piers in uniform, nonuniform, and stratified sediments under steady and unsteady flow conditions. However, they assumed the time scale can be based on the removal of one sediment particle and that the diameter of the horseshoe vortex is independent of flow velocity.

Many sediment transport formulas have been developed based on the bed shear stress. The bed shear stresses due to the horseshoe vortex system at the equilibrium scour depth can be used to estimate the scour depth because the bed shear stress is one of the most significant factors causing scour. Melville and Raudkivi (1977) investigated the mean bed shear stress for the initial flat bed, at an intermediate time 30 minutes after the beginning of scour, and for the equilibrium scour hole. Mean bed shear stress was calculated from mean velocity measurements in the scour region for clear-water scour

conditions as

$$\tau = K \frac{\Delta \bar{u}}{\Delta y} \quad (2.37)$$

where K is the calibration constant ($= 2.0$) acquired by comparison with the slope of the logarithmic velocity profiles of the approach flow and $\Delta \bar{u}$ is the local mean velocity at distance $\Delta y (= 2 \text{ mm})$ from the bed. Alternatively, Dey and Bose (1994) showed that the bed shear stress can be computed from turbulent boundary layer analysis by integrating the Navier-Stokes equations with Pohlhausen's method assuming an arbitrary $1/7$ th power velocity distribution shape. Velocity profiles in the scour hole, however, do not tend to follow a single typical shape of velocity distribution due to the unsteadiness of the horseshoe vortex.

Some investigators have introduced the three-dimensional turbulent boundary layer concept to investigate bridge pier flow and compared their experimental results with several proposed analytical models to analyze the cross-flow, such as Perry and Joubert's model (Ahmed and Rajaratnam 1997; Ahmed and Rajaratnam 1998). They showed, however, that a larger scour hole pulls the flow much more towards the channel center to diminish the cross-flow.

2.3 Experimental Studies

The experimental approach for local scour around a bridge pier is the most common and significant method of analysis since the interaction between the flow and bed materials is hard to understand and quantify clearly due to the complexity of the flow field and

properties of bed materials around a bridge pier. Experimental studies can be mainly divided into two categories: (1) those that focused on explication of the three-dimensional flow field around a bridge pier and (2) those that developed empirical correlations to predict the maximum scour depth around a bridge pier. As representative prediction formulas for the maximum pier scour depth, CSU, Melville and Sutherland, and Sheppard's formulas are well known, which are discussed in detail in Appendix A (Melville and Sutherland 1988; Richardson and Davis 2001; Sheppard et al. 2004a). Other prediction formulas from the literature are also presented in Appendix A.

In order to elucidate and identify the effect of each parameter, dimensional analysis should be carried out before experimental study. Also, the experimental data can be unified and presented in terms of dimensionless parameters through dimensional analysis and dynamic similitude.

2.3.1 Dimensional Analysis

Numerous experimental studies have been conducted to investigate the relationships among the related variables and to present the equations adequate for design of a bridge pier foundation depth. The analysis of scouring parameters implemented by Chabert and Engeldinger (1956) accentuated the magnitude of the maximum scour depth, which is of primary interest for designers to decide the pier foundation depth below the river bed. This confined early studies related to local scour to the evaluation of the equilibrium scour depth, d_{se} , which occurred in the laboratory after a sufficient duration of the experiment.

Breusers et al. (1977) introduced many parameters which influence the local scour around a bridge pier:

- Parameters related to fluid properties
 - g : acceleration due to gravity
 - ρ : density of the fluid
 - ν : kinematic viscosity of fluid
- Parameters related to flow properties
 - y_1 : approach flow depth
 - V_1 : approach mean flow velocity
- Parameters related to sediment properties
 - ρ_s : density of the sediment
 - d_{50} : median sediment size
 - σ_g : geometric standard deviation of sediment size distribution
 - cohesion of sediment
- Parameters related to the bridge pier
 - shape of the bridge pier
 - width of the bridge pier
 - alignment of the bridge pier

The result of dimensional analysis of the problem of local scour around a bridge pier can be given as (Sturm 2001)

$$\frac{d_s}{b} = f \left(K_s, K_\theta, \frac{y_1}{b}, \frac{V_1}{\sqrt{g y_1}}, \frac{\rho V_1 b}{\mu}, \frac{V_1}{V_c}, \frac{b}{d_{50}}, \sigma_g \right) \quad (2.38)$$

where d_s is the equilibrium scour depth; b is the width of bridge pier; K_s is the shape factor; K_θ is the pier alignment factor; g is the acceleration due to gravity; d_{50} is the median sediment size; σ_g is the geometric standard deviation of sediment size distribution; μ is the fluid dynamic viscosity; ρ is fluid density; V_c is the critical velocity for initiation of sediment motion in the approach flow; and y_1 and V_1 are approach depth and velocity, respectively. Most pier scour relationships proposed from laboratory experiments can be placed in the form of Equation 2.38, but only some of the dimensionless ratios on the right hand side, not necessarily the same ones, are utilized in all of the relationships (Ettema et al. 1998).

2.3.2 Laboratory Measurements

As an initial approach to study of local scour around bridge piers, laboratory experiments in combination with dimensional analysis have been utilized to understand the complex three-dimensional flow structure around a bridge pier, and to predict maximum possible scour depths for safe and economic design of bridge foundations since the 1950s (Breusers et al. 1977).

Effect of Pier Shape

Starting with Laursen and Toch (1956), several studies on the effect of the shape factor on pier scour depth have been completed. Melville and Sutherland (1988) presented values of the shape factor, K_s , which are reasonably constant for the shapes given in

Table 2.1. Shape factors for bridge abutments, however, vary over a wider range as shown in Table 2.1 (Melville 1997; Melville and Sutherland 1988).

Table 2.1 Shape Factors for Bridge Piers and Abutments (Melville and Sutherland 1988)

Foundation Type	Shape	K_s
Pier	Circular cylinder	1.0
	Round nosed	1.0
	Squared nosed	1.1
	Sharp nosed	0.9
Abutment	Vertical wall	1.0
	Wing wall	0.75
	Spill through 0.5:1 (H:V)	0.6
	Spill through 1.0:1 (H:V)	0.5
	Spill through 1.5:1 (H:V)	0.45

Effect of Flow Depth

When the flow depth increases, the interference of the surface roller formed ahead of the bridge pier with the downflow and horseshoe vortex is reduced and the effect of flow depth becomes insignificant (Ettema 1980). Kandasamy (1989) concluded that for shallow-depth flows compared to the pier size, the scour depth is proportional to the flow depth, while the scour depth is affected by both flow depth and the pier size for intermediate-depth flows.

Effect of Flow Intensity

It is shown in the pier-scour literature that the initiation value for clear water scour

condition can be placed between $V_1/V_c = 0.4$ and 0.5 . In general, for $V_1/V_c \leq 0.5$, no scour occurs (Breusers et al. 1977; Hancu 1971) and a clear-water scour regime can be defined for $0.5 \leq V_1/V_c \leq 1.0$, where the scour depth increases almost linearly with increasing V_1/V_c . Scour depth may fluctuate with time due to incoming sediment and the passage of bedforms through the scour hole for $V_1/V_c \geq 1.0$, which is the live-bed scour regime as shown in Figure 2.7. As a result, the scour depth is considered to be independent of flow intensity under live-bed scour conditions (Melville 1997).

Effect of Relative Sediment Size and Size Distribution

In the field, the effect of sediment size would not seem to be important because the ratio of pier width to sediment size, b/d_{50} , would seem to be large enough not to affect the scour depth (Breusers and Raudkivi 1991; Raudkivi 1986). In the laboratory, the scour depth tends to decrease with smaller b/d_{50} and be independent of the ratio when b/d_{50} is greater than 50 based on laboratory results; thus, the effect of sediment size can be one of the most significant parameters in laboratory experiments (Raudkivi 1986). Sheppard et al. (2004) have suggested that relative scour depth may also decrease at very large values of b/d_{50} based on experiments in a very large flume. Scour depth decreases with an increasing value of the ratio of geometric standard deviation of grain size distribution (σ_g) to median sediment size (d_{50}) for $\sigma_g/d_{50} \geq 0.3$, which is caused by the armoring effect inside the scour hole (Ettema 1976).

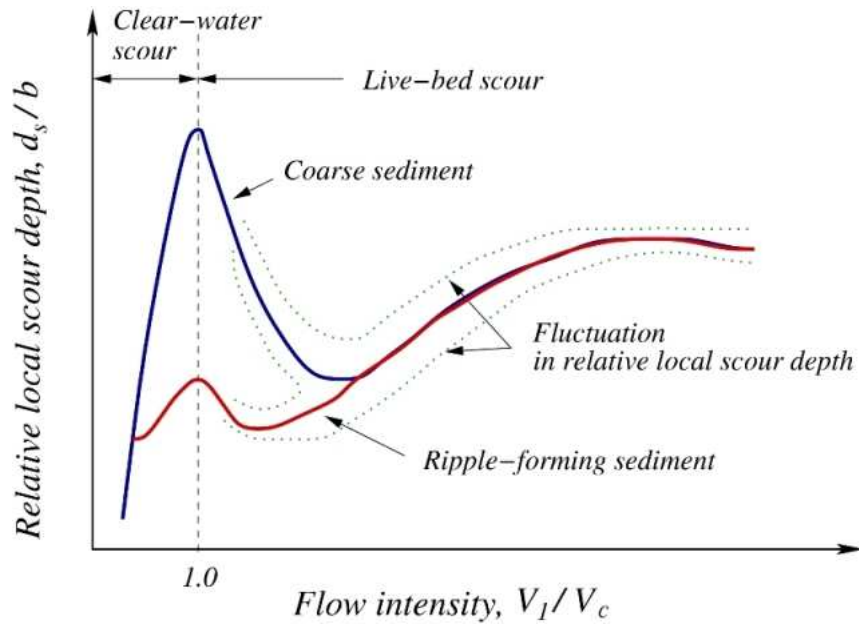


Figure 2.7 Effect of flow intensity on the relative scour depth at a cylindrical pier in a uniform sediment (Breusers and Raudkivi 1991)

When sandy soil containing from 10% to 40% clay was used in pier-scour experiments by Hosny (1995), the scour depths were found to decrease with increases in percent clay. Ting et al. (2001) found that the equilibrium scour depth in clay is very similar to that in sand. Briaud et al. (2002) observed that the maximum scour depth in both sand and clay was approximately the same but the scour rate was remarkably different. Under similar experimental conditions, the initial rate of scour, dd_s/dt , for the sand was much higher than that for the clay even though the maximum scour depth might be similar.

Effect of attack angle of flow

Laursen and Toch (1956) proposed the coefficient K_θ , which reflects the effect of attack angle of the approach flow relative to the alignment of the bridge pier. The data for verification of its value was based on the scour experiments of Chabert and Engeldinger

(1956) and Varzeliotis (1960). The effect of attack angle of the flow, or flow alignment, is clearly shown to be one of most significant factors affecting local scour around bridge piers in Table 2.2, in which l/b is the ratio of pier length to width and θ is the angle of attack of the approach flow velocity.

Table 2.2 Flow Alignment Factors K_θ for a Bridge Pier (Richardson and Davis 2001)

l/b	$\theta (^\circ)$				
	0	15	30	45	90
4	1.0	1.5	2.0	2.3	2.5
8	1.0	2.0	2.75	3.3	3.9
12	1.0	2.5	3.5	4.3	5.0

Effect of pier Reynolds number

In the study of local scour around a pier, the pier Reynolds number based on approach flow velocity and width of a pier has not usually been considered to have a strong influence on scour depth for fully turbulent flow around a bridge pier (Ettema et al. 1998).

Shen et al. (1969) attempted to relate local scour around a bridge pier with the horseshoe vortex strength which is a function of the pier Reynolds number, $Re_b = V_1 b/\nu$, as shown by

$$d_{se} = 0.00073 Re_b^{0.619} \quad (2.39)$$

in which d_{se} is the equilibrium depth of scour in ft. However, Shen et al. (1969) found that Equation 2.39 provides only an upper envelope of the data. The pier Reynolds number alone is insufficient to collapse the data for different sediment sizes or different

pier diameters. In fact, Shen et al. (1969) show that by dividing Equation 2.39 by the pier diameter, the result is a dependence of d_{se}/b on the pier Froude number as shown in the next section.

Since the distance to the separation point measured upstream of the centerline of the pier nondimensionalized by the width of the pier, x_s/b , becomes a measure of the size of the horseshoe vortex, the size of horseshoe vortex influencing the scour depth upstream of a pier may be independent of the pier Reynolds number for higher pier Reynolds numbers as shown in Figure 2.8.

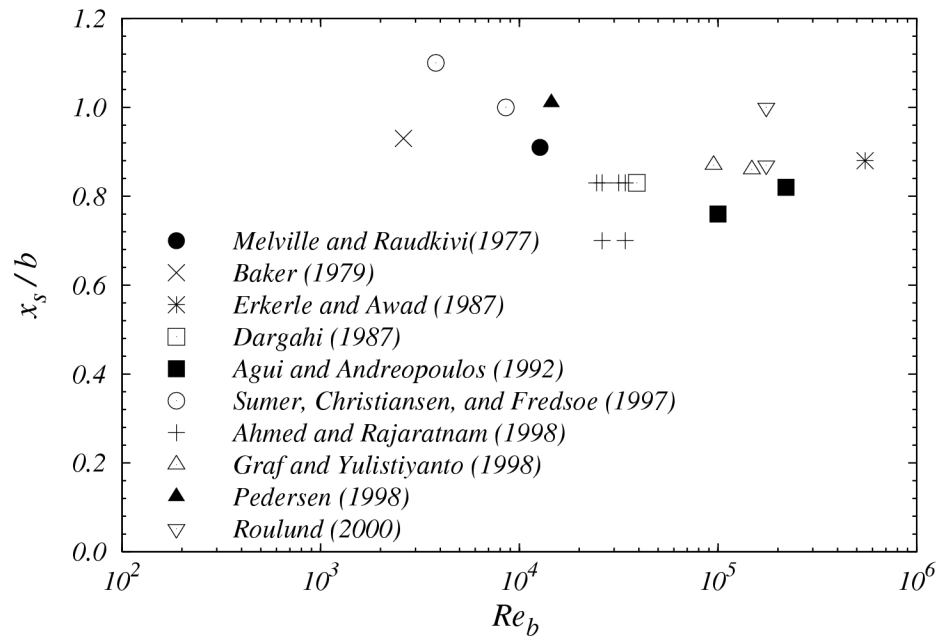


Figure 2.8 Separation distance upstream of the centerline of the pier from the literature

For smaller pier Reynolds numbers (less than $Re_b \cong 1 \times 10^4$), the separation distance may be influenced by the pier Reynolds number, however, the data do not show

significant change in separation distance with respect to higher values of pier Reynolds number.

Effect of pier Froude number

The pier Froude number based on approach flow velocity and width of a pier is found to be a significant variable of local scour around a pier. After conducting a least-squares fit of the data from Chabert and Engeldinger (1956), Shen et al. (1969) suggested that

$$\frac{d_{se}}{b} \propto Fr_b = \frac{V_1}{\sqrt{g b}} \quad (2.40)$$

where Fr_b is the pier Froude number. The relationship of Equation 2.40 is given in two different forms as shown by Equation 2.41 and Equation 2.42 and in Figure 2.9.

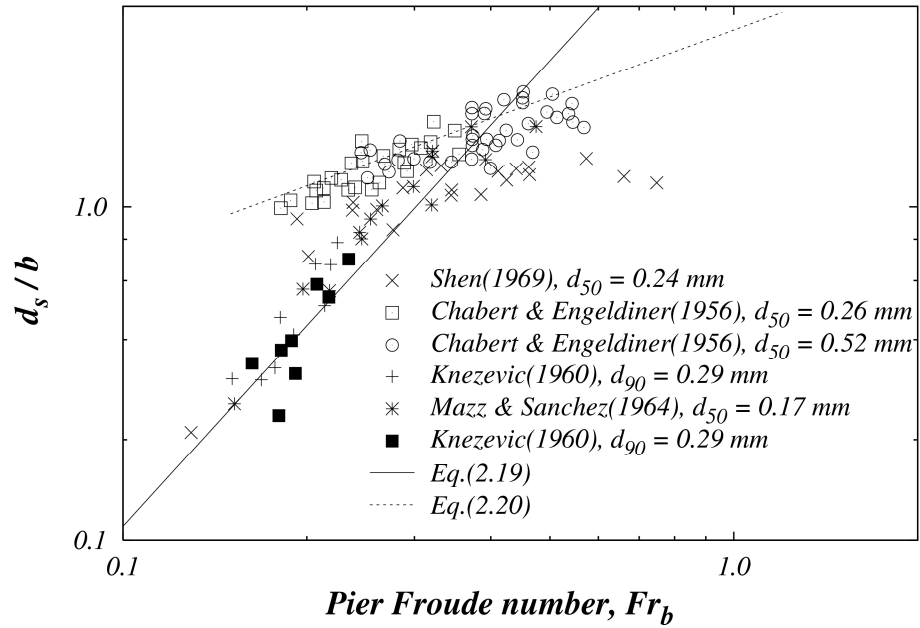


Figure 2.9 Equilibrium scour depth and pier Froude number (Shen et al. 1969)

$$\frac{d_{se}}{b} = 11.0 Fr_b^2 \quad (2.41)$$

$$\frac{d_{se}}{b} = 3.4 Fr_b^{0.67} \quad (2.42)$$

Ettema et al. (1998) suggest that dependence of scour depth on pier Froude number is not adequately accounted for in leading scour formulas. They suggest that pier Froude number reflects the variation of flow gradients around the pier in a free surface flow which are caused by a stagnation head at the face of the pier and flow acceleration around the pier.

Time rate of scour depth development from experiments

Evolution of scour depth under clear-water conditions takes longer to reach equilibrium than for live-bed conditions. Live-bed scour develops more rapidly at initial stages and then begins to oscillate with time due to the influx of sediment upstream of a pier and the passage of bedforms through the scour hole as shown in Figure 2.10. The equilibrium scour depth in clear water conditions is approximately 10 percent more than the equilibrium scour depth in live bed conditions (Shen et al. 1969).

Most of the present local scour equations for predicting depth of bridge pier scour have focused on the equilibrium scour depth without regard to the temporal effect, which means the equilibrium scour depth may be conservative as an estimate of prototype clear-water scour unless the time effect is considered (Melville and Chiew 1999). The equilibrium time to scour, taken when the local scour approaches the equilibrium scour depth in the asymptotic clear-water scour process, is affected by the size of piers because the area and volume of the scour hole around the piers are in proportion to the size of the

piers (Raudkivi 1986).

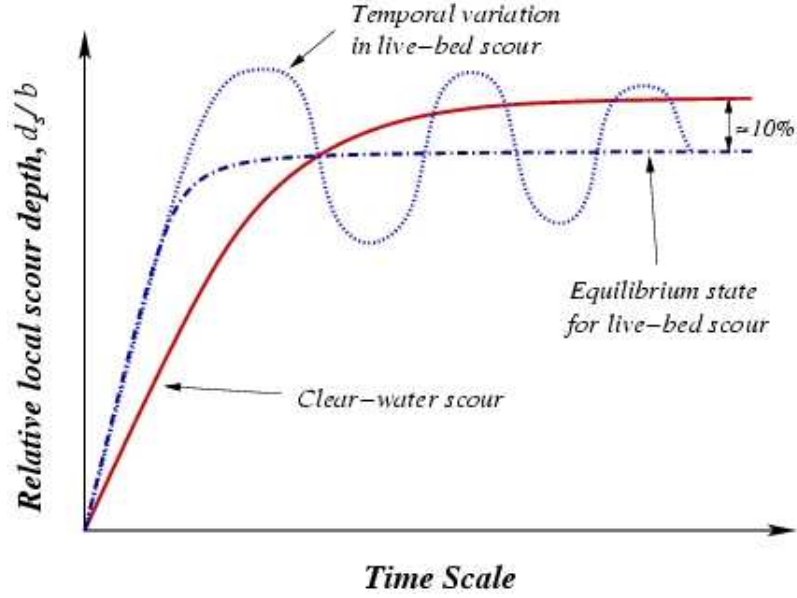


Figure 2.10 Illustration of the temporal variation in scour depth (Richardson 1995)

Melville and Chiew (1999) introduced the time factor and suggested a formula for an equilibrium time to scour in uniform sediments. The equilibrium time to scour, defined as the time when the increment of scour depth is less than 5% of the bridge pier diameter during 24 hours, was given by

$$T_{eq} \text{ (day)} = \begin{cases} 48.26 \frac{b}{V_1} \left(\frac{V_1}{V_c} - 0.4 \right) & \text{for } \frac{y_1}{b} > 6 \\ 30.89 \frac{b}{V_1} \left(\frac{V_1}{V_c} - 0.4 \right) \left(\frac{y_1}{b} \right)^{1/4} & \text{for } \frac{y_1}{b} \leq 6 \end{cases} \quad (2.43)$$

As an example, a prototype pier width of 4 ft and approach velocity of 8 ft/s, with $y_1/b > 6$, would require some 14 days to reach equilibrium at maximum clear-water

scour, while the corresponding equilibrium time in a 1:50 scale model with Froude number similitude would be only 2 days.

As a result of all the complicating factors involved in the scour process, most scaled laboratory experiments have been carried out under idealized environments such as a flat bed, steady uniform flow, uniform sediment size, and a simple shaped single pier. Hence there are difficulties in elucidating the complicated scour process and velocity structure and applying these experimental results directly to field conditions. Additional understanding of the physics of the scour process is required for designing bridge foundations in the field to prevent scour failures.

The time rate of local pier scour is significant when flow fields are investigated to understand development of scour around bridge piers. Even though numerous studies have been conducted to investigate the equilibrium scour depth or maximum scour depth around piers, research on the time rate of local scour development is relatively scarce (Gosselin and Sheppard 1995). Carstens (1966) proposed a dimensionless form of the sediment-transport formula and applied it to scour around a vertical cylinder using similarity criteria for the temporal evolution of clear water scour in Equation 2.16 which was based on a small range of laboratory-scale parameters. Shen et al. (1966) tried to fit data into several combinations of parameters including time rate of scour, but their equation, given below as Equation 2.44, is not suited for practical application since it was constructed based on a narrow range of flow data (Cunha 1975) and is given by

$$\frac{d_s}{b} = 2.5 Fr_1^{0.4} \left(\frac{b}{y_1} \right)^{0.6} (1 - e^{mE^2}) \quad (2.44)$$

where b is the diameter of pier; Fr_1 is the approach Froude number ($= V_1 / \sqrt{g y_1}$); y_1 is the approach flow depth; V_1 is the approach mean velocity; $m = 0.026 e^{-2.932 y_1}$ and

$$E = \left(\frac{b}{y_1} \right)^{0.33} Fr_1^{0.33} \ln \left(\frac{V_1 t}{y_1} \right) \quad (2.45)$$

where t is the time scale.

Torsethaugen (1975) conducted local scour experiments for wide diameter piers and suggested that the time history of clear-water scour on a polystyrene particle bed proceeds as follows:

$$\frac{d_s}{d_{se}} = \exp \left[- \left(\frac{T_{eq}}{t} \right)^{0.5} \right] \quad (2.46)$$

where T_{eq} is the time required to develop equilibrium scour depth, d_{se} , which is defined by

$$\frac{d_{se}}{b} = 1.8 \left(\frac{V_1}{V_c} - 0.54 \right) \left(\frac{y_1}{b} \right) \quad \text{for } \frac{y_1}{b} < 1.0 \quad (2.47)$$

Three dimensionless parameters, d_s/b , $u_* t/b$ and $v/u_* b$, were selected from dimensional analysis to describe the similarity in the evolution of local scour depth with time by Ettema (1980). He compared the temporal developments of scour depths by plotting d_s/b versus $(d_{s0}/b)(u_* t/b)(v/u_* b)$ at similar values of the relative size

parameter, b/d_{50} . Three segments were contained in all figures plotted on the semi-logarithmic plot such as Figure 2.11. The first segment represented the rapid development of scour by downflow at the initial stage; the middle segment showed that scour depth developed as the horseshoe vortex moved away from the bridge pier and grew in strength; and the last segment represented the equilibrium scour depth (Raudkivi and Ettema 1983). Each segment was of the form

$$\frac{d_s}{b} = K_1 \ln \left[\left(\frac{d_{50}}{b} \right) \left(\frac{u_* t}{b} \right) \left(\frac{\nu}{u_* b} \right) \right] + \ln K_2 \quad (2.48)$$

where u_{*c} is the critical shear velocity; and K_1 and K_2 are the coefficients representing the slope and vertical location of the line, respectively, and are given in Table 2.3.

Table 2.3 Definition of coefficients K_1 and K_2 in Equation 2.48 (Ettema 1980)

u_*/u_{*c}	b/d_{50}	Segment 1		Segment 2		Segment 3	
		K_1	K_2	K_1	K_2	K_1	K_2
0.9	$30 \leq b/d_{50} \leq 130$	0.67	1.43	1.13	1.26	0.12	7.92
	$130 < b/d_{50}$	0.81	1.04	1.68	1.43	0.09	7.61
0.95	$30 \leq b/d_{50} \leq 130$	0.92	1.73	0.24	1.43	0.10	8.02
	$130 < b/d_{50}$	0.87	1.73	1.22	1.43	0.18	8.25

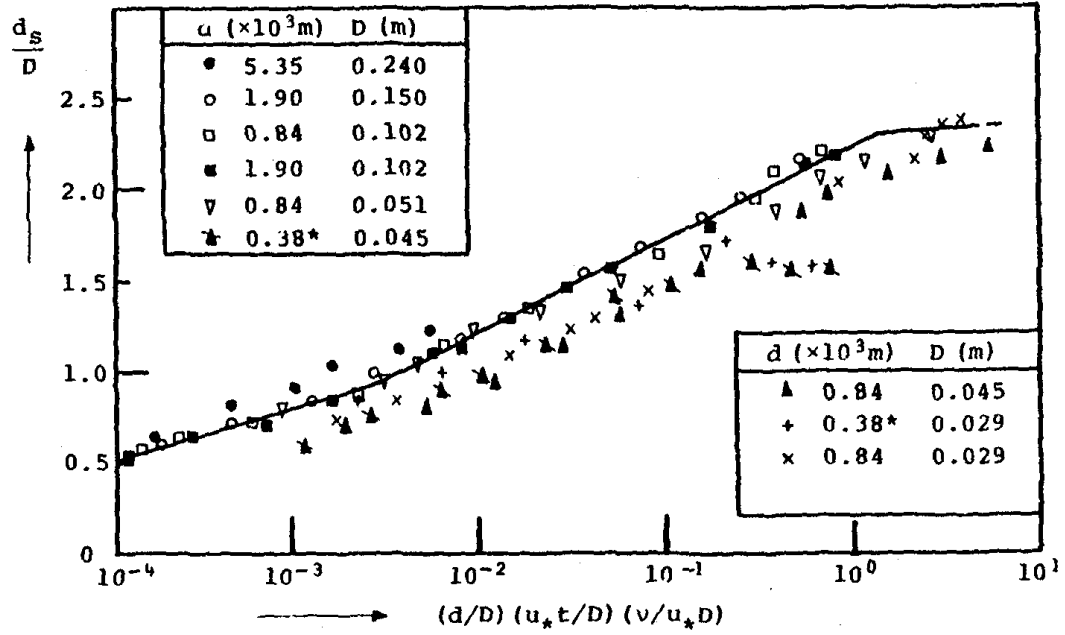


Figure 2.11 Scour depth with time; $u_*/u_{*c} = 0.90$, $30 \leq b/d_{50} \leq 130$ (Ettema 1980)

Melville and Chiew (1999) proposed a method for determination of the time scale to develop the equilibrium scour depth, which is called an equilibrium time scale, and an equation for prediction of temporal development of local scour at cylindrical bridge piers in a uniform sand bed was given by

$$\frac{d_s}{d_{se}} = \exp \left[-0.03 \left| \frac{V_c}{V_1} \ln \left(\frac{t}{T_{eq}} \right) \right|^{1.6} \right] \quad (2.49)$$

where V_1 is the mean approach velocity; V_c is the mean approach velocity at threshold conditions for sediment movement; T_{eq} is the time to reach the equilibrium scour depth as

given in Equation 2.43, and d_{se} is the equilibrium scour depth. Their analysis was based on the extended laboratory data set obtained at the University of Auckland and the Nanyang Technological University, including Ettema's (1980) and Graf's (1995) experimental observations.

Oliveto and Hagger (2002) summarized the laboratory data conducted at ETH Zurich, Switzerland. They suggested incorporating the effect of densimetric particle Froude number as defined by Equation 2.50 on the temporal development of scour depth:

$$Fr_d = \frac{V_1}{\sqrt{g' d_{50}}} \quad (2.50)$$

where g' is the reduced gravitational acceleration ($= [(\rho_s - \rho)/\rho]g$, in which ρ_s is the density of sediment). They concluded that the scour is mainly influenced by the densimetric particle Froude number, the width of a pier and the shape of a pier as follows:

$$\frac{d_s}{b^{2/3} y_1^{1/3}} = 0.068 N \sigma^{-0.5} Fr_d^{1.5} \log \left(\frac{\sqrt{g' d_{50}}}{b^{2/3} y_1^{1/3}} \times t \right) \quad (2.51)$$

where N is the shape factor equal to 1 for circular and 1.25 for rectangular pier. Their equation was verified using the existing literature data from Chabert and Engeldinger (1956), Ettema (1980), Yanmaz and Altinbilek (1991) and Melville and Chiew (1999). However, Equation 2.51 can only be applied in a straight channel with rectangular cross sectional geometry and uniform sediment. There is no consideration of the approach flow velocity skewness or the unsteadiness of the flood events.

Based on the sediment transport theory of Yalin (1977), Mia and Nago (2003)

proposed a method for computation of temporal variation of scour depth around a cylindrical pier. The mixing layer, which refers to the layer from which the materials can be entrained by the flow, was used to calculate the equilibrium scour depth in nonuniform sediment. The scour depth evolution for nonuniform sediment was formulated based on regression analysis of the time-dependent scour rate obtained from experimental data as follows (Chang et al. 2004):

$$d_s = \begin{cases} 0.08 K_\sigma \left(\frac{V_1}{V_c} - 0.4 \right) T_c^{-1.3} \left(\frac{t}{T_{eq}} \right) & \text{for } 0 \leq \frac{t}{T_{eq}} \leq T_c \\ d_{se} - 0.27 K_\sigma \left(\frac{V_1}{V_c} - 0.4 \right) \left[\left(\frac{t}{T_{eq}} \right)^{-0.3} + 0.41 \right] & \text{for } T_c \leq \frac{t}{T_{eq}} \leq 0.04 \\ d_{se} - 1.10 K_\sigma \left(\frac{V_1}{V_c} - 0.4 \right) \left[\left(\frac{t}{T_{eq}} \right) - 2.22 \left(\frac{t}{T_{eq}} \right)^{0.45} + 1.22 \right] & \text{for } 0.04 \leq \frac{t}{T_{eq}} \leq 1 \end{cases} \quad (2.52)$$

where K_σ is the coefficient related to σ_g , t and T_{eq} are the time and equilibrium time of scour, respectively; d_s is the scour depth corresponding to t ; and d_{se} is the equilibrium scour depth. Scour depth was found to increase linearly with time in the initial, very short period of time, T_c , which was given by

$$T_c = \left[\frac{d_{se}}{0.35 K_\sigma (V_1/V_c - 0.4)} - 0.31 \right]^{-3.33} \quad (2.53)$$

The rate of scour development is strongly related to the approach flow velocity and sediment size, which can be comprehensively represented by the flow intensity. Thus,

most proposed formulas involve the effect of flow intensity, and Oliveto and Hagger (2002) utilized an extensive data set to verify their formula. However, no one has comprehensively considered the effect of sediment size on the development of scour depth upstream of a pier. Even though the time scale for scour development has been recognized as a significant parameter in scour prediction and design, most research on the evolution of the scour depth has a weak link with hydrology. In general, the flood event in the field does not last as long as the expected equilibrium time for clear-water scour depth since most scour conditions are live-bed scour regime in field. More practical and economic scour evaluation should be based on field situations.

2.3.3 Scale Effects of Laboratory Experiments

Due to the difficulty in reproducing prototype local scour depths utilizing laboratory model experiments, the scaling procedure has to be carefully considered when comparing laboratory data with prototype data. In addition, the need for using the appropriate non-dimensional parameters is essential when laboratory experiments are designed and conducted so that the nondimensionalized results can be compared with field data. One of the dominant characteristics of local pier scour is the horseshoe vortex around a bridge pier which should be related to the maximum local scour depth. In that case, the maximum scour depth should be correlated with the strength of the horseshoe vortex presented by (Qadar and Ansari 1991) as

$$d_s = k_s (\Gamma_0)^m \quad (2.54)$$

where d_s is the maximum scour depth below the initial bed elevation; k_s is the

coefficient empirically dependent on the sediment size, for instance, $k_s = 538$ for finer sediment up to 0.5mm; m is experimentally determined equal to 1.28; and Γ_0 is the initial vortex strength defined by $\Gamma_0 = u_o r_o$ in which r_o is the radius of the vortex and u_o is the reference velocity of the vortex, which are given by Qadar (1981):

$$r_o = 0.1 b \quad (2.55)$$

$$u_o = 0.092 b^{-0.5} V_1^{0.83} \quad (2.56)$$

Using the above equations, Qadar and Ansari (1991) suggested that the ratio of the maximum prototype local scour depth to maximum scour depth in a geometrically similar laboratory model should be given as follows:

$$\frac{d_{sp}}{d_{sm}} = \left[\frac{(u_o r_o)_p}{(u_o r_o)_m} \right]^{1.28} = \left[\left(\frac{b_p}{b_m} \right)^{0.5} \left(\frac{V_{1p}}{V_{1m}} \right)^{0.83} \right]^{1.28} \quad (2.57)$$

where the subscript p and m stand for the prototype and model, respectively. In the prototype, the approach velocity and flow depth are affected at the same time if the flow discharge in the river changes, which induces Froude number of the approach flow to become a key factor; thus, Froude number similitude is applicable for Equation 2.57 to yield

$$\frac{d_{sp}}{d_{sm}} = \left[\left(\frac{1}{L_r} \right)^{0.5} \left(\frac{1}{L_r} \right)^{0.83} \right]^{1.28} = \left(\frac{1}{L_r} \right)^{1.173} \quad (2.58)$$

where L_r is the length scale of the model equal to the length ratio of model to prototype.

When physical model studies of local pier scour have been conducted at most laboratories for high Reynolds number, all dimensionless parameters mentioned previously in the dimensional analysis of Equation 2.38 could be maintained with the same values as the prototype except for b/d_{50} . For example, if the length ratio of model to prototype is 1:40 and it is applied to the corresponding prototype sediment size, d_{50} , in the sand size range, the model sediment would be too cohesive or too small to be managed in laboratory experiments. Therefore, it would be hard to accomplish the same ratio b/d_{50} between the prototype and the physical model. The effect of b/d_{50} , however, has been considered to be negligible with respect to local pier scour depths when the value of b/d_{50} is greater than 25 (Breusers and Raudkivi 1991; Melville and Chiew 1999). However, Sheppard et al. (2004b) showed that the normalized scour depth, d_s/b , decreases with increasing values of b/d_{50} beyond $b/d_{50} \sim 45$. They also suggested that underprediction of prototype scour depths can occur when the sediment size, d_{50} , of the physical model is significantly larger than that of the prototype and the geometric scale, L_r , is relatively small. If the relationship for decreases in local scour depth with increasing values of b/d_{50} , which can be very large in prototype situations, is well known, then it can be used to evaluate the prototype local scour depth from the measured model value of local scour depth. The difficulty is that most prototype values of b/d_{50} greatly exceed values that can be obtained in even the largest laboratory models.

Briaud et al. (1999) proposed a laboratory-based methodology for predictions of maximum scour depth in cohesive sediments. The incipient shear stress of undisturbed samples from the bridge pier site in the field can be obtained by a surface erodibility test,

from which a curve is developed showing the relationship between the scour rate and shear stress. The maximum shear stress induced around a bridge pier is calculated by numerical modeling using the CHIMERA-RANS method (Wei 1997), and the initial scour rate can be determined corresponding with the maximum shear stress on the curve for the relationship between the scour rate and shear stress. The maximum scour depths were obtained through laboratory experiments and were evaluated as follows:

$$d_{s \max} = 0.18 \text{Re}_b^{0.635} \quad (2.59)$$

where $d_{s \max}$ is the maximum scour depth. Then laboratory experiments were conducted in order to measure the time evolution of local scour and the hyperbolic model for temporal scour depth was given as

$$d_s = \frac{t}{1/\dot{d}_i + t/d_{s \max}} \quad (2.60)$$

where \dot{d}_i is the initial scour rate found on the curve at the maximum shear stress. Thus, the corresponding maximum scour depth in the field can be predicted using their proposed method when the width of a pier and the approach velocity are given from the field. However, this methodology cannot correctly predict maximum scour depth in the field since the curve for the scour rate versus the shear stress is obtained under pipe flow conditions in which the influence of turbulence characteristics induced from the vortex system around a bridge pier and the scale effect is not considered in terms of length scale, e.g., the effect of b/d_{50} .

2.4 Numerical Modeling Approach

Initial numerical approaches to modeling bridge pier scour have been conducted using the two dimensional depth-averaged Navier-Stokes equations extended to turbulent flow using first-order closure techniques with comparisons of the numerical results with experimental data (Vincent et al. 1993). This approach obviously does not consider the full 3D characteristics of flow causing the bridge pier scour. Olsen and Melaaen (1993) proposed and investigated a full 3D numerical model of bridge pier scour. However, their model was not able to consider all cases of scour, and it was not well-suited to calculate the maximum scour depth at a bridge pier because the transient terms in the Navier-Stokes equations were neglected. Instead, the changes in bed elevation were simulated by a sediment transport formula presented for suspended load calculations by van Rijn (1987) instead of a bed load sediment transport equation.

A sediment transport capacity formula is one of the basic approaches in sediment transport engineering to predict sediment discharges. Most sediment discharge formulas are empirical and are valid for steady uniform flow in rivers with equilibrium sediment transport. However, such formulas are hardly likely to be adequate in predicting the unsteady, three-dimensional sediment discharge out of a scour hole around a bridge pier.

In order to carry out numerical calculations to evaluate the rate of sediment transport for local scour around a bridge pier, (Dou et al. 1998; Dou and Jones 2000) . proposed an effective sediment transport capacity (STC) formula which included the effects of downflow, vortices, and local turbulence to simulate local scour depth in a 3-D numerical model. It was given by

$$STC = f_0 \frac{V_1^3}{g y_1 w_f} + f_1 \sum \cdot \left[e^{-\kappa(d_s/b)} + f_2 (1 - e^{-\kappa(d_s/b)}) \right] \quad (2.61)$$

where the first term on the right hand side of Equation 2.61 represents the general scour in which V_1 is the depth-averaged velocity; y_1 is the flow depth; w_f is the fall velocity of a particle; d_s is the scour depth; and b is the characteristic length which is commonly the pier width for local scour around a bridge pier. In the second term, \sum is a distribution parameter calculated as a linear average of three normalized parameters that come directly from the magnitude of downflow, the strength of vortices and the turbulent intensity induced by a bridge pier in which f_1 , f_2 and κ are the coefficients to be determined; and f_0 is the coefficient shown below (Dou 1974):

$$f_0 = \frac{K_s}{C_0^2} \frac{\gamma \gamma_s}{\gamma_s - \gamma} \quad (2.62)$$

where K_s is a constant ($=0.034$); C_0 is the dimensionless Chezy's coefficient ($= C/\sqrt{g}$, C is the Chezy's coefficient); and γ and γ_s are the specific weight of flow and sediment, respectively. The local scour simulation at Woodrow Wilson Bridge over the Potomac River near Washington DC was implemented using Equation 2.61 with CCHE3D, a 3D hydrodynamic and sediment transport model developed by the Center for Computational Hydroscience and Engineering at the University of Mississippi.

Mendoza-Cabrales (1993) suggested that the standard $k-\varepsilon$ model is not adequate to simulate 3-D flow in the vicinity of a vertical circular pier after the numerical calculations for the flow field and the corresponding bed shear stress computed with the

standard $k - \varepsilon$ model are compared with the experimental data from Melville (1975).

Ali et al. (1997) used the renormalized group (RNG) $k - \varepsilon$ model to predict the flow field and bed shear stress around piers and their calculations were compared with experimental results. The calculated flow fields showed quantitatively a good agreement with the experimental results, while there was only one fair agreement in comparison of the bed shear stresses (Ali and Karim 2002).

Sahaheldin et al. (2004) examined the performance of three different types of $k - \varepsilon$ models, which were the standard $k - \varepsilon$, RNG $k - \varepsilon$, and realizable $k - \varepsilon$ model, and the Reynolds stress model (RSM) in applying for the numerical simulation of the velocity field and the computation of bed shear stress around a bridge pier. FLUENT, which is the commercial software presented by Fluent Inc., was used to solve the three-dimensional Reynolds-averaged Navier-Stokes equations for incompressible flow. However, the calculation of sediment transport and local scour depth at a bridge pier was excluded (Salaheldin et al. 2004).

Ali and Karim (2002) proposed a methodology for calculation of local scour depth with increasing time. The numerical results for the three-dimensional flow field using FLUENT were used to estimate the bed shear stress along the center line of a bridge pier and to calculate the sediment discharge using van Rijn's (1984) formula. The one-dimensional continuity equation for sediment was then applied to estimate the local scour depth as given by

$$(1 - p) \frac{\partial z}{\partial t} + \frac{\partial Q_s}{\partial x} = 0 \quad (2.63)$$

where p is the porosity; z is the elevation of the bed above a datum; t is the time from

initial motion of sediment; Q_s is the sediment discharge; and x is the developed length in the flow direction. However, FLUENT is not able to simulate the variation of the water surface, with which most numerical calculations are conducted assuming that the free surface is represented by a smooth closed-lid. Also FLUENT cannot predict the turbulent bursts which can make significant contributions to the sediment motion from the bed (Ali and Karim 2002).

Sand movement by wind around several cylindrical bodies was investigated by Kan and Kawamura (2000) and Kawamura et al (1999). When the three-dimensional flow field around a cylindrical body was calculated, the marker and cell (MAC) method was utilized and the estimation of the shape of the bed profile was considered with the conservation of sand along the surface given by.

$$\rho_s \frac{dh}{dt} = -\frac{\partial q_x}{\partial x} - \frac{\partial q_y}{\partial y} \quad (2.64)$$

where h is the normal distance from the bed elevation; and q_x and q_y are the sediment discharge in x and y directions, respectively. However, the effect of turbulence was considered by the simplest eddy viscosity model, and the estimation of sand movement was based only on surface friction.

Olsen and Kjellesvig (1998) suggested a 3D hydraulic numerical model combined with a sediment transport model for the suspended sediment concentration for scour modeling. They conducted numerical simulations of the flow and scour depth around a single cylindrical pier. The bed concentration formula presented by van Rijn (1987) was used for the equilibrium sediment concentration close to the bed, which has some

empirical coefficients, thus the resultant scour depth may not be estimated quantitatively. Their numerical results were not able to give enough information about unsteadiness in the flow.

Ge et al. (2005) proposed an unsteady, fully 3D numerical model which was able to solve the URANS equations for complex bridge foundation geometries. They also calibrated the model to compare with experimental data from a flat-bed model which consisted of four rectangular piers and showed good agreement between numerical and physical models (Ge et al. 2005; Ge and Sotiropoulos 2005).

Tseng et al.(2000) investigated the flow around square and circular piers by using Large Eddy Simulation (LES), which resolves the unsteadiness of the flow (Tseng et al. 2000).

Constantinescu, et al. (2004) suggested that numerical simulation with RANS and URANS are inadequate to predict the flow and scour depth around a cylindrical pier even though URANS simulation can predict some large scale deterministic unsteadiness but can't capture the evolution of the coherent structures and their effect on bed-sediment transport around a cylindrical pier. They also suggested a parallel LES code using a collocated, finite-volume method on unstructured grids and a dynamic Smagorinsky subgrid scale model. But, they used FLUENT to investigate the flow field around a circular cylinder at a small value of the pier Reynolds number, $Re_b = 5000$.

In order to consider the non-hydrostatic pressure distribution and local anisotropic turbulence around a bridge pier, Nagata et al. (2005) adopted RANS closed with the nonlinear $k-\varepsilon$ turbulence model with moving boundary fitted coordinates. They proposed the effect of non-equilibrium sediment transport to simulate the bed

deformation including a stochastic method for sediment pickup and the momentum equation of sediment particle for deposition. However, the nonlinear $k - \varepsilon$ model relies on empirical functions; thus, all coefficients including eddy viscosity coefficients have to be determined. Their model cannot simulate the unsteadiness of the horseshoe vortex system. The moving grid was applied only for vertical movements, which probably cannot adequately describe the motion of sediment in a scour hole.

2.5 Field Observations

Field measurements of bridge foundation scour are essential to validate the model results from laboratory and numerical experiments, to provide a better understanding of scour processes and to adequately predict scour depths for prevention of possible damage due to failure of bridge foundations. Extensive field measurements, therefore, are required over long periods. However, it is difficult not only to collect field data but also to utilize it for comparison with experimental data or numerical calculations due to the complexity of channel geometry, various pier shapes, variability of sediment type and uncertainty in field measurements.

As an early example of field measurements, total scour depths from 1924 to 1942 at 17 bridges over rivers in India were observed. Scour was mainly due to contraction and local scour around bridge piers (Inglis 1949).

Laursen and Toch (1956) utilized the electric resistivity device to measure scour depth at the nose of a single rounded pier in the Skunk River in Iowa. Scour depth data on bridges at la Corey and Beaver Crossing on the Beaver River in Canada were given by

Neill (1965).

Breusers (1971) compared local scour from the Onitsha Bridge on the Niger River with the results of a scaled laboratory model and the ratio of field to laboratory scour depths ranged from 1 to 53. Melville (1975) presented field data from four bridge sites in New Zealand and compared them with predictions based on the Shen et al. (1969) methodology. The equation for clear-water scour presented by Shen et al. (1969) was preferred for design purposes by Melville (1975), but it was found that predictions with the equations for live-bed scour by Shen et al. (1969) showed a better agreement with Melville's field data (Breusers et al. 1977).

Norman (1975) collected scour depth data around piers at seven bridges in Alaska and four other bridge sites. Including Norman's field data, Froehlich (1988) summarized both published and unpublished field data from 1960 to 1984 which were measured using sonic depth finders, sounding weights, and sounding rods.

An extensive data base of pier scour measurements under clear-water and live bed conditions has been developed by state highway departments, the Federal Highway Administration (FHWA), and the U. S. Geological Survey (USGS) in the National Bridge Scour Project. Ninety piers from 44 bridges in 12 states were the subject of field measurements over the last several years (Landers and Mueller 1996). They evaluated variables of selected equations with their collection of field data and compared the observed and computed scour depths. It was concluded that none of the selected scour equations precisely estimated scour depth for all of the measured conditions. Also, Muller and Wagner (2005) provided additional field data as the second USGS field-data collection funded by the U.S. Federal Highway Administration (FHWA) .

Radar systems have also been utilized to monitor and measure the scour depth around bridge foundations (De Falco and Mele 2002; Forde et al. 1999; Millard et al. 1998). The monitoring systems for local scour at bridge piers using radar produced a stratigraphic profile on the bottom of the river bed which is applicable to obtain the historical scour depth. An alternate method called 'Sedimentri' uses diodes facing each other and mounted on a rod which detect when sediment comes between them. The rod is placed in a hole installed vertically along a bridge pier. It is able to detect whether the sensor is covered or uncovered; thus the depth of erosion can be observed (De Falco and Mele 2002).

CHAPTER III

FIELD STUDIES

Many studies for prediction of local scour depth due to bridge piers have been developed from laboratory experiments with a uniform rectangular channel geometry and a simple pier shape such as a single circular cylinder. Therefore, relations and estimations of the pier scour depth developed from laboratory data tend to overestimate the actual pier scour depths measured at field sites (Landers and Mueller 1996). Furthermore, most of the predictive formulas presented in the literature based only on laboratory data have not been verified by field data because there are few long-term stations that monitor the scour process at a specific bridge site including real-time velocity measurements (Mueller and Wagner 2005).

In this study, laboratory pier scour experiments on particular bridges in Georgia were conducted considering the hydraulic conditions and river bathymetry based on field data acquired by the U.S. Geological Survey (USGS). The USGS has been gaging streamflow at the chosen bridge sites for long periods of record, but detailed monitoring, including continuous measurement (30-minute intervals) of pier scour using fathometers and velocity from an acoustic velocity meter, has been underway since 2002 as part of a larger scour study for the Georgia DOT (Sturm et al, 2004). Full three-dimensional scale models of prototype bridge pier bents, embankments and abutments as well as river bathymetry were fabricated to reproduce the scour depth and hydraulic characteristics in the field, which is one of the main objectives of this study. To accomplish this objective,

field data collected from long-term monitoring have been analyzed including the temporal variation of scour depth around bridge piers and velocity measurement for specific flood events. Selected data measured in the field are presented in this chapter; however, the comparisons of bed elevations and velocity distributions with laboratory experimental data will be presented in Chapter 5.

3.1 Site Selection

The physical modeling of local scour at bridge piers has to start with the selection of bridge sites where conspicuous local scour has occurred during historically large flood events. Essentially, the data for investigation of pier scour depth should include the historical cross-sectional data, discharge records, approach water depths, approach velocities and bed material characteristics (Mueller and Wagner 2005).

Recently, tropical storm Alberto produced peak flood discharges greater than the 100-year event in July 1994 in south Georgia and caused numerous bridge failures. On the Flint River, for instance, at the U.S. Highway 82 crossing of the Flint River near Albany, Georgia, the depth of local scour at the bridge foundation was approximately 5.5m (Stamey 1996). One of the bridge sites on the Flint River was chosen as the prototype bridge site for physical modeling in this study. Specifically, the bridge over the Flint River at Bainbridge, Georgia was chosen partly because cross-sectional data and velocities along the bridge deck were measured adequately by the USGS during Alberto and partly because it was representative of the Georgia coastal plain. The second bridge site chosen was the Georgia Highway 384 (Duncan Bridge Road) bridge on the Chattahoochee River in the Piedmont physiographic province near Cornelia, Georgia. In

2003, the USGS recorded a peak discharge of $385 \text{ m}^3/\text{s}$ at this bridge which corresponded with a bank-full flow. Approximately 1.8m of local scour occurred at the bridge foundation during that flood event. The USGS also measured the cross-section bed elevations upstream of the bridge pier bents and presented mean velocities measured by the in situ acoustic velocity meter at the left side of the central pier. The third bridge site chosen was the Fifth St. bridge over the Ocmulgee River at Macon, Georgia located in the physiographic Fall Line region. The historical peak discharge at this site is $1841 \text{ m}^3/\text{s}$ measured in March 1998 along with approximately 3.3m of total scour depth including contraction scour on the upstream side of the bridge pier bent located in the main channel. The cross-section bed elevations and mean velocities along the upstream side of the bridge deck were also measured for an event with a peak discharge of $1388 \text{ m}^3/\text{s}$ (Hong 2005; Sturm et al. 2004).

A standard USGS stage-discharge station is located at each of the three bridge sites chosen for modeling. At each bridge site, bed sediment samples were collected with manual samplers both upstream and downstream of the bridge. Continuous velocity data were measured using a cross-channel acoustic Doppler velocity sensor which provided two-dimensional velocity components in the bridge approach section at 15-minute intervals. Temporal variations of channel bed elevations near the main bridge pier bent were measured by several fathometers attached to the wall of the bridge piers. The horizontal locations of the bridge pier bents were determined by a kinematic differential Global Positioning System (GPS), which was also used to establish the horizontal positions where elevations and velocity were measured at each cross-section. An acoustic Doppler current profiler (ADCP) and a digital fathometer were deployed in a manned

boat during large flood events to measure three-dimensional velocities and channel bathymetry (Sturm et al. 2004).

3.2 Chattahoochee River near Cornelia, GA

The horizontal location of the bridge site on the Chattahoochee River near Cornelia, Georgia is latitude 34°32'27", longitude 83°37'14" NAD83. The stream gage installed in 1957 by the USGS is located at the Georgia Highway 384 bridge at the Habersham-White county line in northeast Georgia. The datum of the gage is 343.98 m above sea level NGVD29. The drainage area is 816 km² and the width of the main channel is approximately 70 m. The channel at this site is fairly straight for several hundred meters upstream and downstream of the bridge. The control is a rock ledge that runs diagonally from the right bank downstream to the left bank at a river station located about 150 m downstream of the bridge. The channel reach in the vicinity of the bridge is a long quiet pool about 49 m wide at lower flows, which extends from the rock ledge to about 914 m upstream of the bridge (Sturm et al. 2004).

Each bridge pier bent consists of four rectangular concrete columns and rectangular concrete footings as shown in Figure 3.1 and Figure 3.2. One of the bridge pier bents is located in the center of the channel and the others are on each side on the left and right banks. Two of the pier bents, including the one in the center of the channel, have an inner web as a part of the original pier bents. Two outer piers of each pier bent were constructed to widen the Georgia Highway 384 bridge in 1988. The bridge piers were designed to be aligned with the flow. The pier width of the most upstream pier is

1.07 m as shown in Figure 3.2.



Figure 3.1 Central bridge pier bent on Chattahoochee River near Cornelia, GA

A bank-full flow at this site occurred on July 2, 2003. The recorded peak discharge was $385 \text{ m}^3/\text{s}$. The flood recurrence interval for this event is close to 2 years at this site as shown in Table 3.1. The recorded peak velocity was approximately 2 m/s, and about 0.7 m of scour depth was measured by the fathometer at the nose of the bridge pier in the main channel as shown in Figure 3.3.

Table 3.1 Flood discharge-frequency data for Chattahoochee River near Cornelia, GA

Recurrence Interval (years)	Discharge (m^3/s)
2	334
10	609
50	833
100	923
500	1121

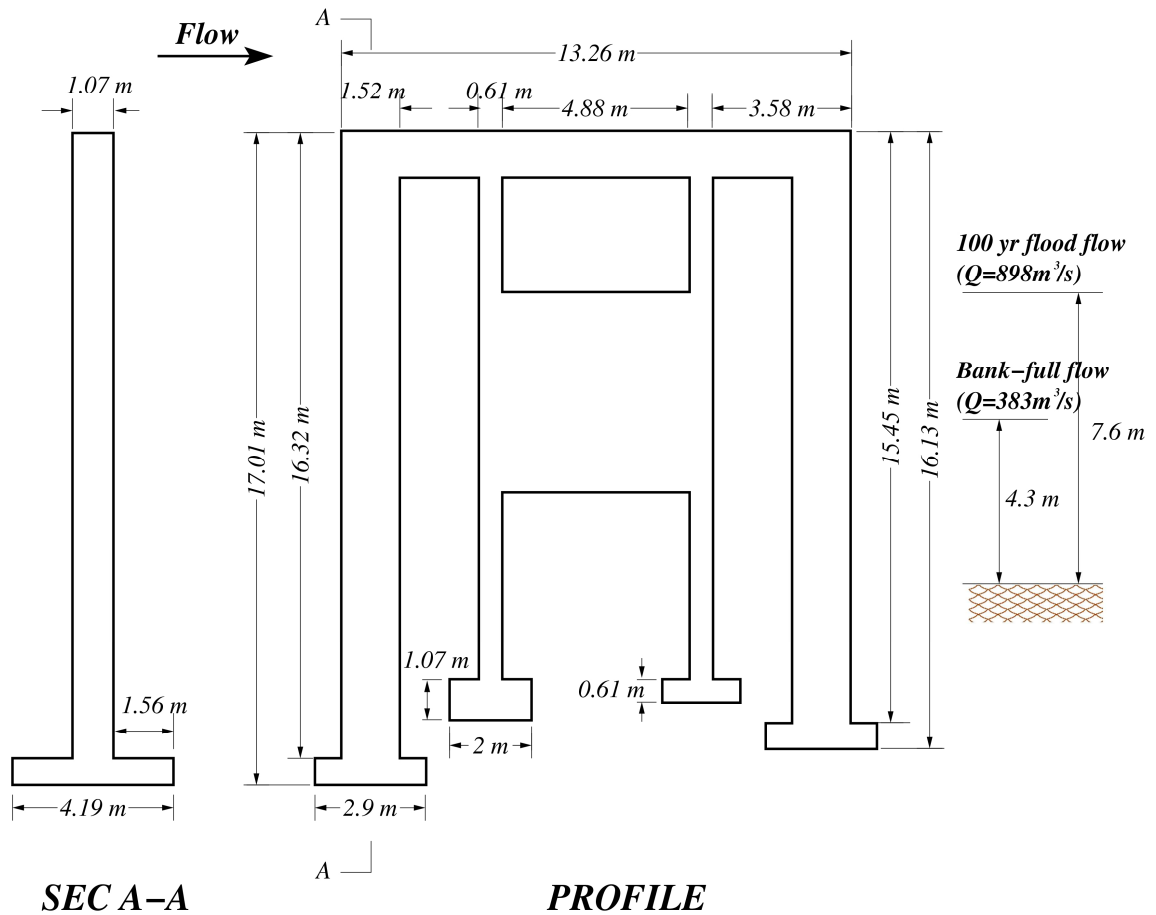


Figure 3.2 Schematic of central pier bent with prototype elevations and dimensions for Chattahoochee River bridge near Cornelia

As shown in Figure 3.3, an event with a peak discharge of $371 \text{ m}^3/\text{s}$ occurred on December 12, 1961, and this event is similar in magnitude to the July, 2, 2003 event. When the cross-sections at the upstream side of the bridge for both flood events are compared in Figure 3.4, the shapes of the scour holes are approximately the same and the maximum scour depths at the nose of the bridge pier are also practically equal with a difference of only 0.06% despite the intervening time interval of 42 years during which many cycles of alternate scouring and filling occurred.

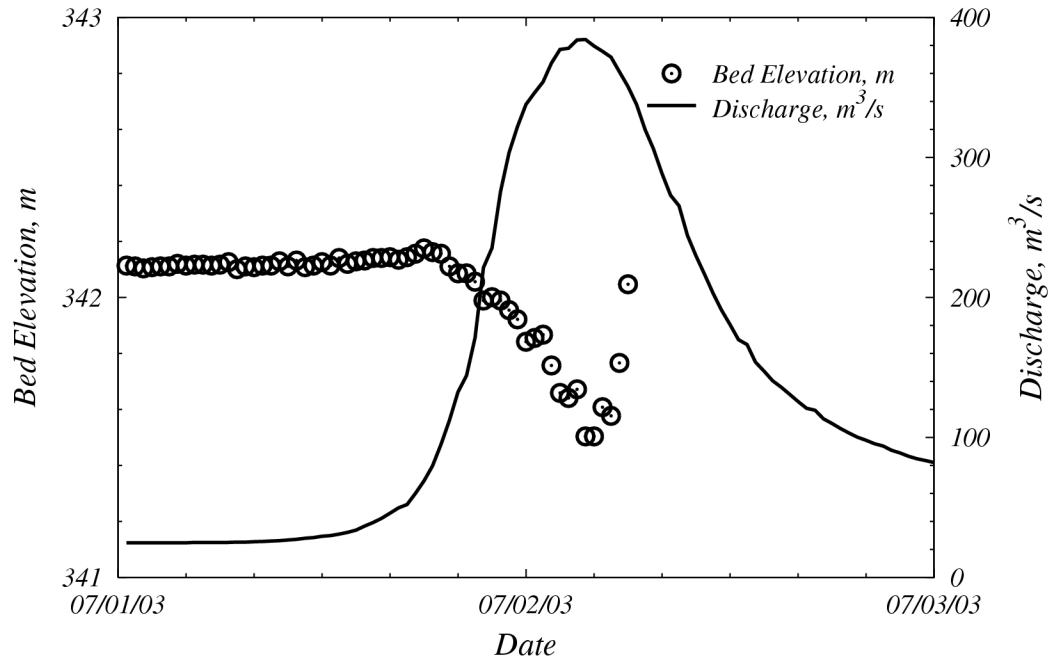


Figure 3.3 Temporal variation of bed elevation and discharge around central pier bent in Chattahoochee River from July 1, 2003 to July 3, 2003

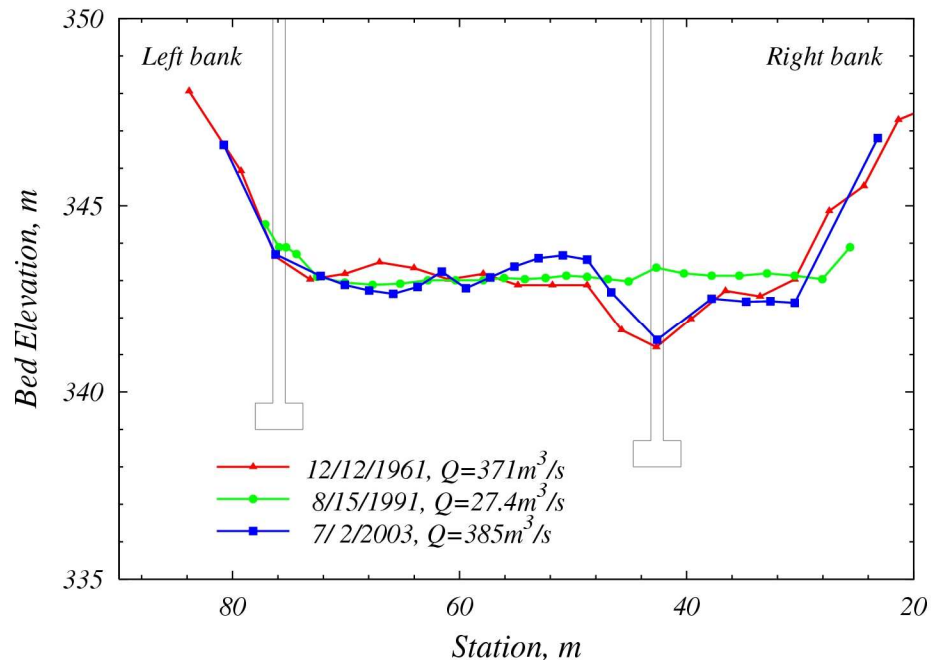


Figure 3.4 Comparison of cross-sections at the upstream side of the bridge over Chattahoochee River near Cornelia

Figure 3.5 shows the layout of surveyed cross sections for this site. The USGS determined the horizontal location of each surveyed point in the cross sections using a global positioning system along with the bed elevation determined by a sonar instrument mounted on a boat. The data for the eleven surveyed cross-sections were used to construct the river bathymetry for physical modeling in the laboratory. An aerial photo near the selected field site is presented in Figure 3.6.

Bed material samples were collected from the approach cross section of the bridge site. Figure 3.7 shows the sediment particle size distribution of the bed materials sampled at the left, right side and center of the approach cross section. The median size of bed material around the center of the channel is about 0.7 mm and the geometric standard deviation is 1.6 as shown in Figure 3.7

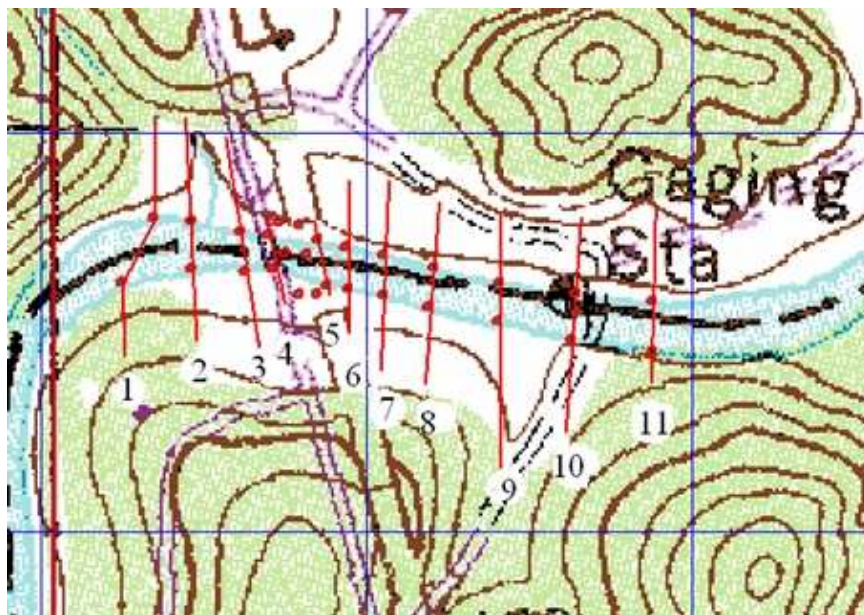


Figure 3.5 Layout of surveyed cross section at Chattahoochee River near Cornelia, Georgia (USGS)



Figure 3.6 Aerial photo at Chattahoochee River near Cornelia, Georgia (USGS)

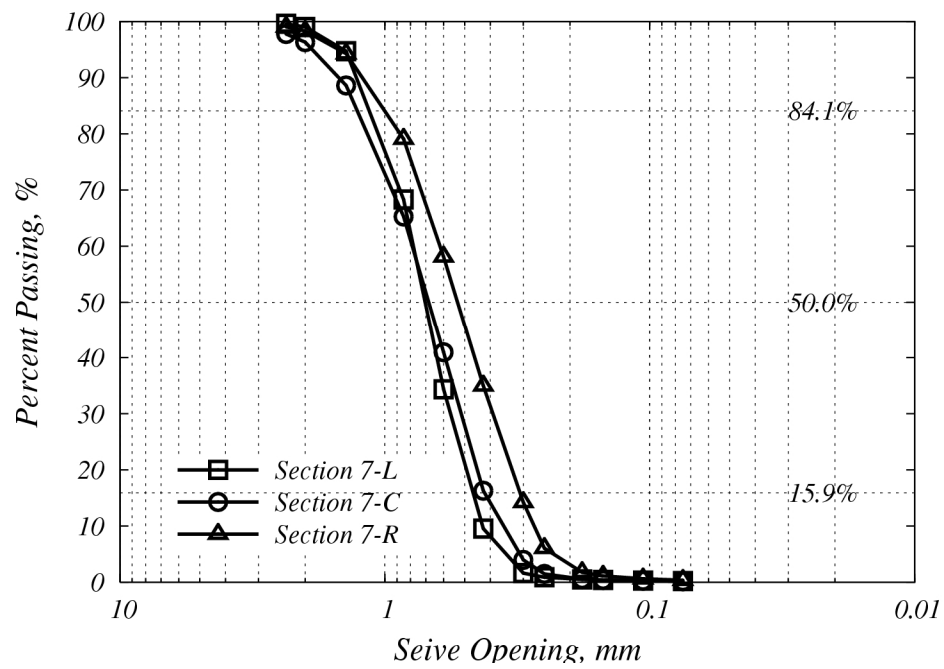


Figure 3.7 Particle size distribution of bed material samples in Chattahoochee River near Cornelia

3.3 Flint River at Bainbridge, GA

The USGS has measured stage and discharge since 1908 at the Business Highway 27 Bridge over the Flint River in Bainbridge, Georgia. The location of this bridge site is latitude 30°54'41" and longitude 84°34'48"(NAD27). The drainage area is 19,606 km² and the datum of the gage is 17.7 m above sea level (NGVD29). The width of the main channel is approximately 150 m and there is a very wide and flat floodplain. The channel is straight for hundreds of meters upstream and has a sharp bend about 150 m downstream of the bridge. The effect of backwater propagated from the Jim Woodruff Reservoir exists at lower stages but the backwater can be neglected at higher stages (Sturm et al. 2004).



Figure 3.8 Bridge pier bents in Flint River at Bainbridge, GA

There are four bridge pier bents two of which are situated in the main channel while the other two are located on each bank as shown in Figure 3.9. For each pier bent, there are two square concrete pier columns placed on large stepped square concrete footings as shown in Figure 3.8. The upstream pier column width is 1.83 m. The footings of one of the bridge bents in the main channel protruded from the streambed while the top elevations of the footings of the other one corresponded with the bed elevation in March 10, 1980 and March 20, 2002 as shown in Figure 3.9.

Table 3.2 Flood discharge-frequency data for Flint River at Bainbridge, GA

Recurrence Interval (years)	Discharge (m ³ /s)
2	875
10	1,645
50	2,370
100	2,687
500	3,455

The peak discharge at the Bainbridge bridge site was recorded as 3,058 m³/s on July 14, 1994 during tropical storm Alberto, which was greater than the 100-year flood event as given in Table 3.2. The discharge measurement and velocity distribution along the upstream side of bridge site were recorded during tropical storm Alberto. The maximum scour depth was recorded as approximately 3 m during the 1994 flood event. Figure 3.10 shows the temporal changes in bed elevations in front of the pier during a flood in May 2005, while Figure 3.11 displays the comparison between previous and recent cross-sections.

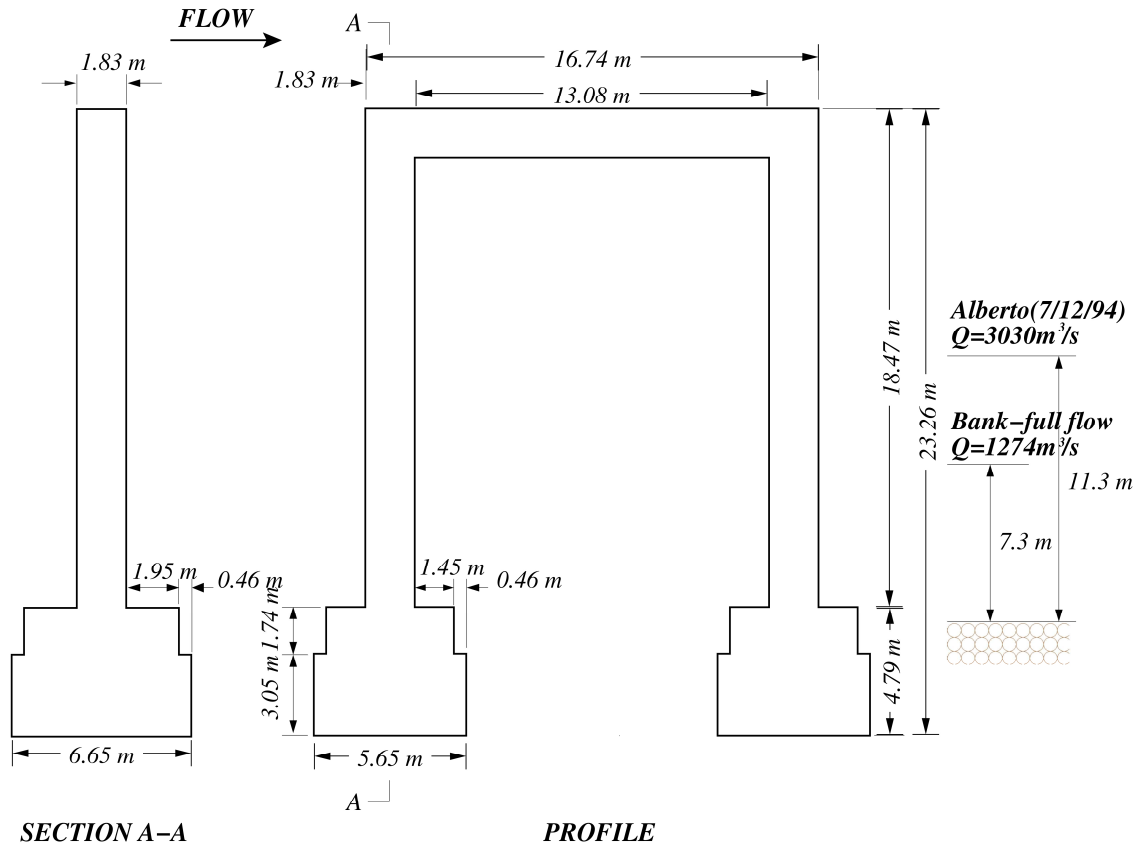


Figure 3.9 Sketch of the main pier bent in Flint River at Bainbridge, GA

Five cross-sections were surveyed throughout the channel reach including the railroad bridge upstream of the bridge site as shown in Figure 3.12. The USGS also measured the bed elevation near old embankments upstream of the bridge site that were left after construction of the new bridge. The location of the old bridge is shown in Figure 3.12, but the new bridge can be seen in the aerial photograph given in Figure 3.13. The red dots in Figure 3.12 at cross sections 3 and 4 measured along the bridge site by the USGS correspond with the actual location of the new bridge in Figure 3.13. The USGS also surveyed the railroad bridge upstream of the bridge pier bent. All information was used to fabricate the physical model for this study.

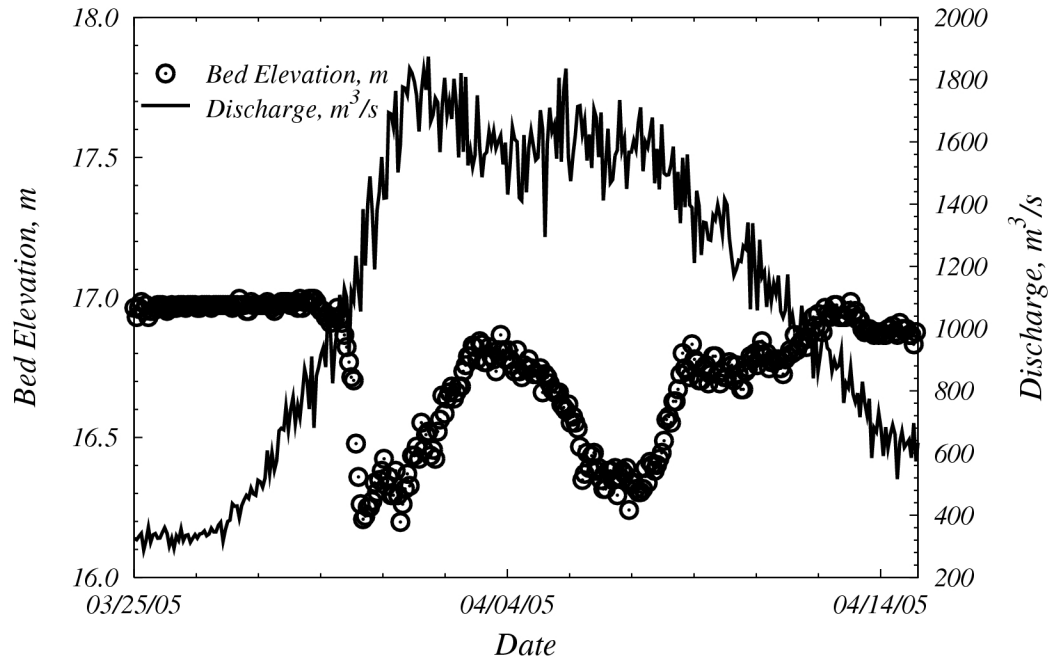


Figure 3.10 Temporal variation of bed elevation around bridge pier bent in the Flint River from March 25, 2005 to April 14, 2005 by the USGS

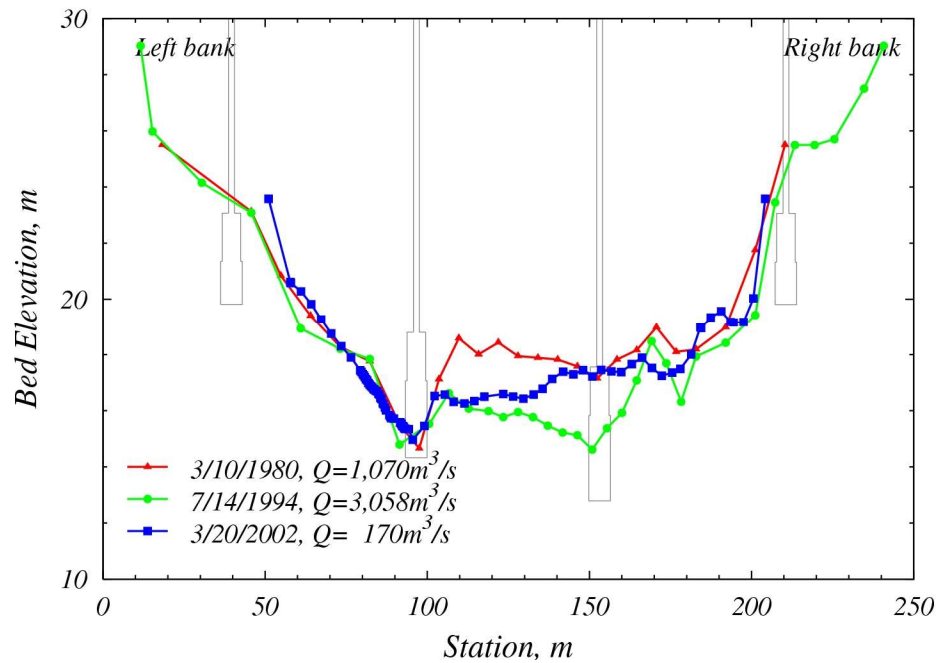


Figure 3.11 Historical comparison of cross-sections at the upstream side of the bridge over the Flint River at Bainbridge, GA



Figure 3.12 Layout of surveyed cross sections in Flint River at Bainbridge.



Figure 3.13 Aerial photo of the bridge site in Bainbridge, Georgia (USGS)

The sediment particle size distribution of a bed material sample collected on the upstream side of the bridge site is shown in Figure 3.14. The median size of the bed material sample is approximately 0.4mm and the geometric standard deviation is 2.17.

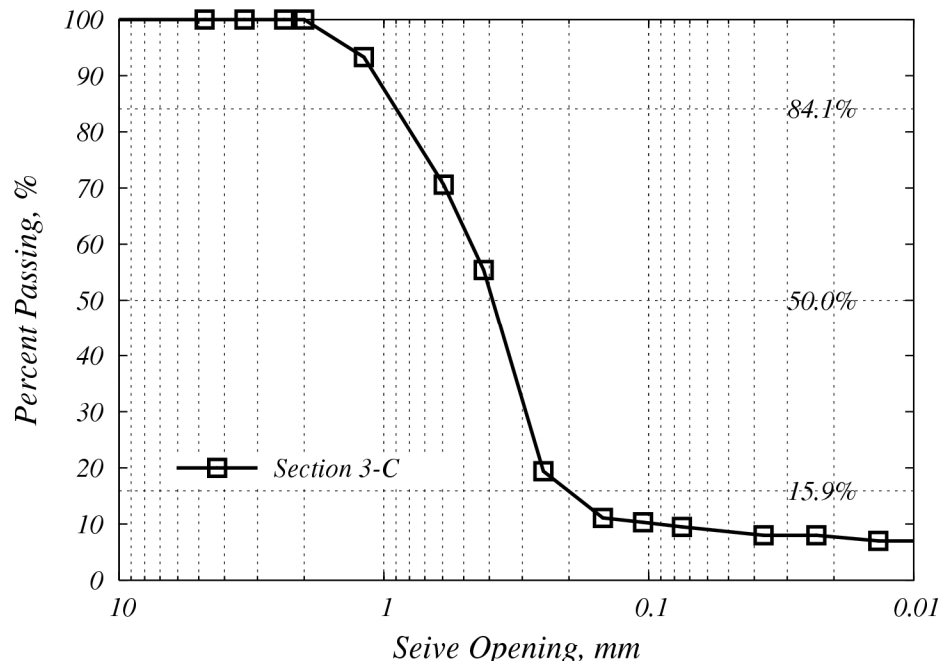


Figure 3.14 Particle size distribution of bed material sample at the upstream side of the bridge over Flint River at Bainbridge, GA

3.4 Ocmulgee River at Macon, GA

The third site chosen in this study is the 5th Street (Martin Luther King Jr. Blvd.) bridge over the Ocmulgee River at Macon, Georgia. The USGS has measured stage and discharge at this site since 1895. The drainage area is approximately 5,802 km² and the river is relatively straight for about 300 m upstream of the bridge and for 460m downstream of the bridge. The control is a shifting sand streambed. The bridge pier bents consist of four circular cylinders each having a diameter of 1.83m placed on rectangular

concrete footings as shown in Figure 3.15 and Figure 3.16. All bridge pier bents in the main channel are aligned with the flow.



Figure 3.15 Bridge piers in Ocmulgee River at Macon, Georgia

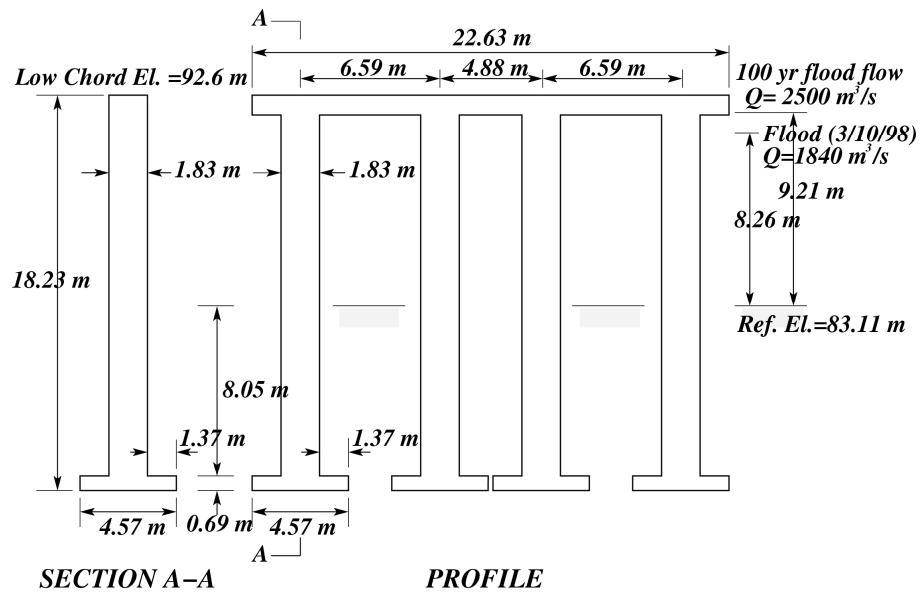


Figure 3.16 Sketch of the central bridge pier bent in the Ocmulgee River at Macon, Georgia

Data on temporal variations of bed elevations near the central bridge pier bent were collected in May, 2003 when the peak discharge was $722 \text{ m}^3/\text{s}$, which is equal to the 2-year recurrence interval flood event as given in Table 3.3. Due to this flood event approximately 1 m of scour depth occurred additionally around the central bridge pier as shown in Figure 3.17.

Table 3.3 Flood-frequency discharge data for Ocmulgee River, Macon

Recurrence Interval (years)	Discharge (m^3/s)
2	807
10	1591
50	2243
100	2500
500	3070

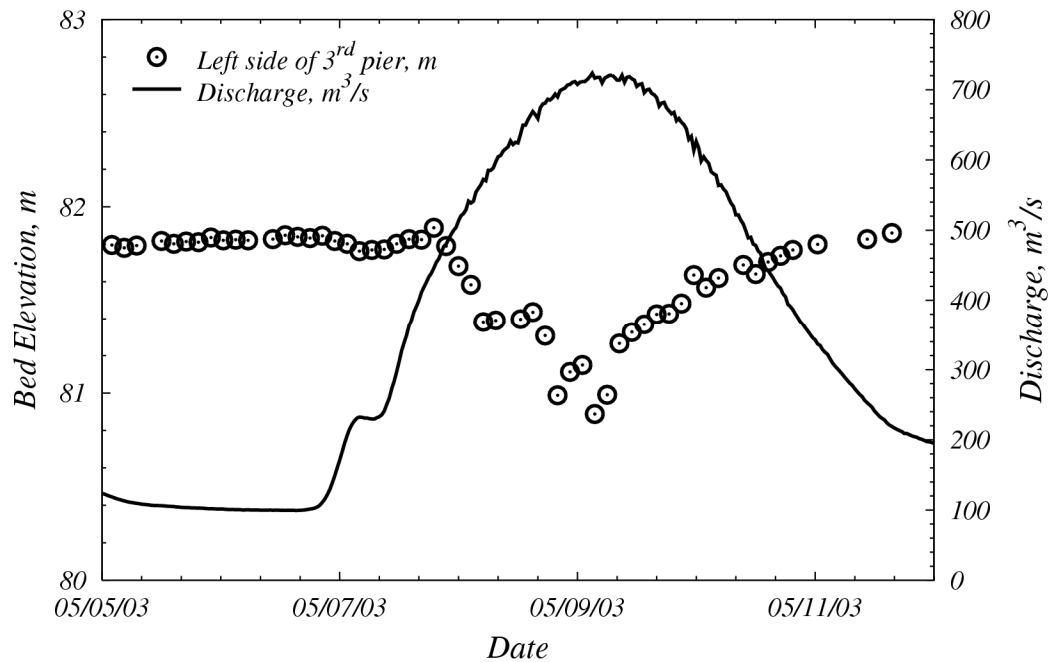


Figure 3.17 Temporal variation of bed elevation at upstream side of Ocmulgee River, Macon from May 5, 2003 to May 11, 2003 by the USGS

The USGS surveyed seven cross-sections throughout the channel reach as shown in Figure 3.18. Figure 3.19 shows the aerial photo near the selected field site. The railroad bridge is shown downstream of the bridge site, but the USGS did not survey the railroad bridge because it is located relatively far from the selected bridge site so that its effect on local scour around the 5th St. bridge can be considered negligible for this study. This information was used to construct the physical model.

Figure 3.20 shows the historical cross-section comparison at the upstream side of the bridge and it is observed that about 3.5 m of scour depth at the main pier bent including contraction scour occurred due to the high flood event in March, 1998. The peak velocity was recorded to be nearly 3 m/s during that flood event.



Figure 3.18 Layout of surveyed cross-sections in Macon, Georgia



Figure 3.19 Aerial photo around 5th street in Macon, Georgia (USGS)

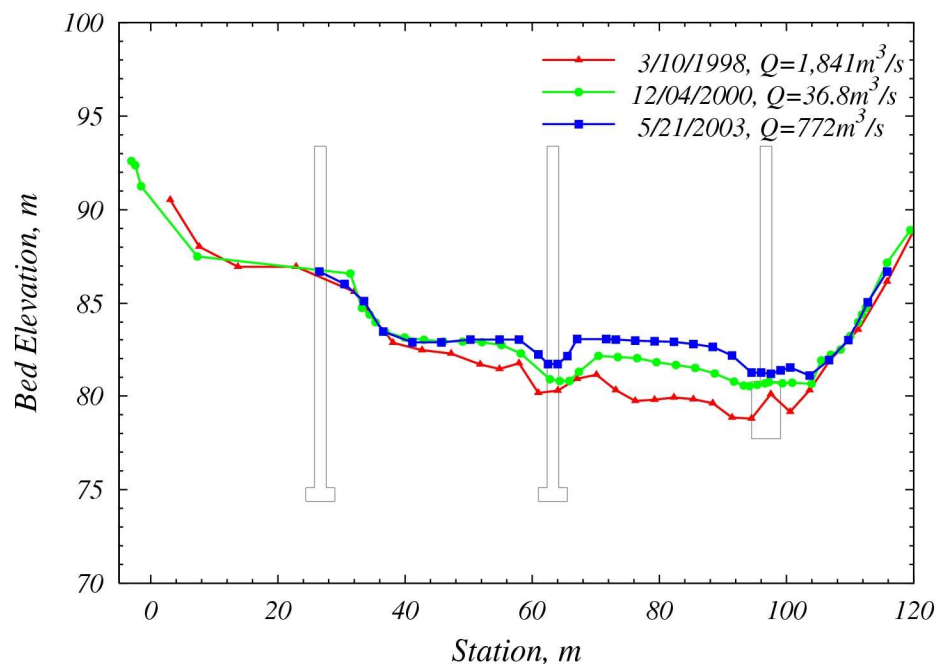


Figure 3.20 Cross-section comparison at upstream side of the bridge over Ocmulgee River, Macon

The stream bed at this site is sandy. The particle size distribution of the collected bed material sample on the upstream side of the bridge pier in the main channel is shown in Figure 3.21. The median size of bed material is about 0.8 mm and the geometric standard deviation is 2.13.

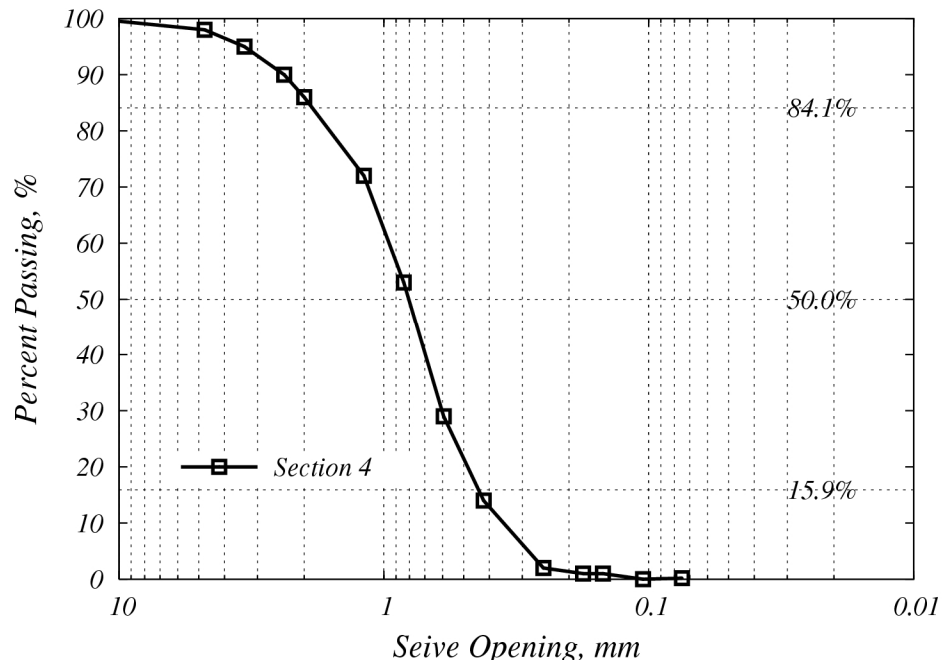


Figure 3.21 Particle size distribution of bed material in Ocmulgee River, Macon

CHAPTER IV

METHODOLOGY OF EXPERIMENTS

4.1 Experimental Facilities

All experiments of local scour around bridge piers were conducted in the hydraulics laboratory of the School of Civil and Environmental Engineering at the Georgia Institute of Technology, Atlanta. Flat-bed models and river models were built inside a 4.3 m wide by 24.4 m long horizontal flume and 1.1m wide by 24.4 m long rectangular tilting flume in the hydraulics laboratory. The maximum water flowrate in the laboratory is 0.3 m³/s supplied by two centrifugal pumps and a large constant-head tank through a 305 mm diameter pipe. Water supply to the flume is recirculated such that water flows into the laboratory sump at the downstream end of the flume from which it is continuously pumped into an overflowing constant-head tank. The flowrate into the flume is controlled by a gate valve installed in a 305 mm supply pipe for high flowrates, and by a separate gate valve in a 152 mm pipe for flowrates less than 0.06 m³/s .

4.1.1 Horizontal Flume

The horizontal flume has a length of 24.4 m, a width of 4.3 m, and a maximum depth of 0.8 m. It consists of reinforced steel walls sealed to the concrete floor of the laboratory. For experiments on pier models installed in a rectangular movable-bed flume (flat bed

model), an interior channel width of 2.4 m was constructed by installing concrete blocks as interior walls of the flume, but river model experiments were operated with the full flume width of 4.3 m in which the complete river bathymetry and bridge were modeled.

In order to reduce the turbulence generated at the entrance of the flume where the water flows into a head box vertically downward from the 305 mm supply pipe, three chain fence rolls wound with horse-hair filter are set up between the head wall of the flume and an overflow weir. Downstream of the overflow weir two baffles are installed one of which is made of offset wood slats and the other of which is a steel plate with 10 mm diameter holes having a spacing of 14 mm. A horse-hair filter is also inserted between the two baffles. A horizontal diffuser pipe in the transverse direction is connected to the end of the vertical 305 mm. supply pipe so that the inflow distribution is uniform across the flume as shown in Figure 4.1.

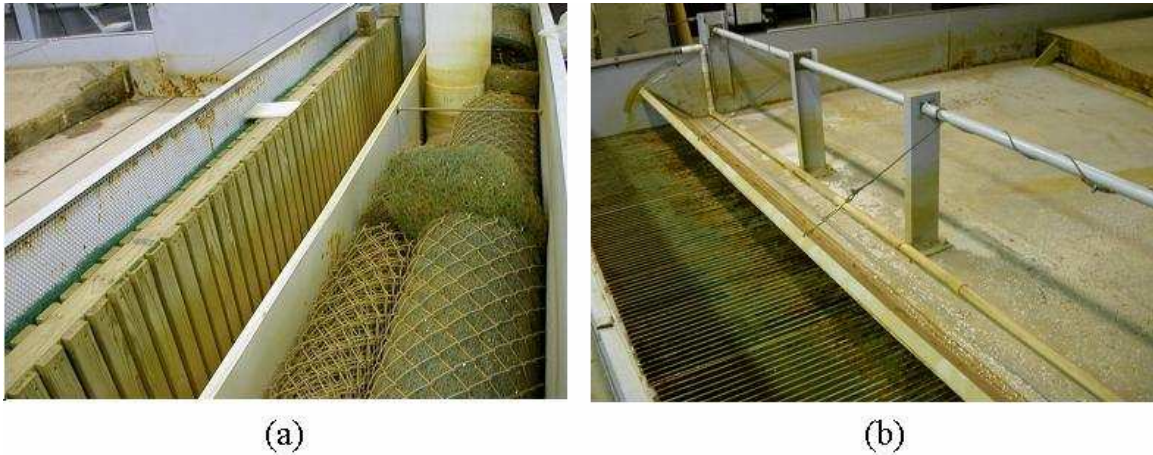


Figure 4.1 Horizontal flume: (a) Entrance section of the horizontal flume and (b) Tailgate of the flume to adjust the flow depth downstream

A tailgate to adjust the tailwater depth is located at the downstream end of the flume to control the flow depth as shown in Figure 4.1. An instrument carriage is set up on longitudinal steel rails attached by leveling bolts to the flume walls. The carriage can be moved upstream or downstream along the flume by an electric motor and a steel cable system. The point gage used for measurement of elevations and the velocity meter are mounted on that carriage and can be positioned accurately in three-dimensions.

4.1.2 Tilting Flume

The tilting flume has a length of 24.4 m, a width of 1.1 m, and a depth of 0.5 m. The tilting flume is supported by two steel beams that pivot about the center of the flume and are tilted up or down by pairs of screw jacks located at the upstream and downstream ends of the flume. The flow depth is controlled by an adjustable tailgate driven by an electric motor. In order to produce a uniform open channel flow for a given flowrate, the bed slope and flow depth are adjusted. The bed slope of the flume is adjusted by the rotation of a longitudinal shaft running under the flume that drives the screw-jack support system. The relationship between bed slope and number of shaft rotations as indicated on a counter was quantified as shown in Figure 4.2 with the best-fit equation given by

$$S_o = 5.34 \times 10^{-6} N_r - 0.005163 \quad (4.1)$$

where, S_o is the bed slope of flume and N_r is the number of rotations.

There are several baffles in the upstream head box in order to reduce the turbulence generated at the flume entrance (Figure 4.3 (a)). The wall of the flume at the test section located from 16.3 m to 17.8 m downstream of the entrance is glass to provide

optical access for flow and temporal scour visualization. An instrument carriage that rolls on the flume rails was used to support the velocity meter and point gage (Figure 4.3 (b)).

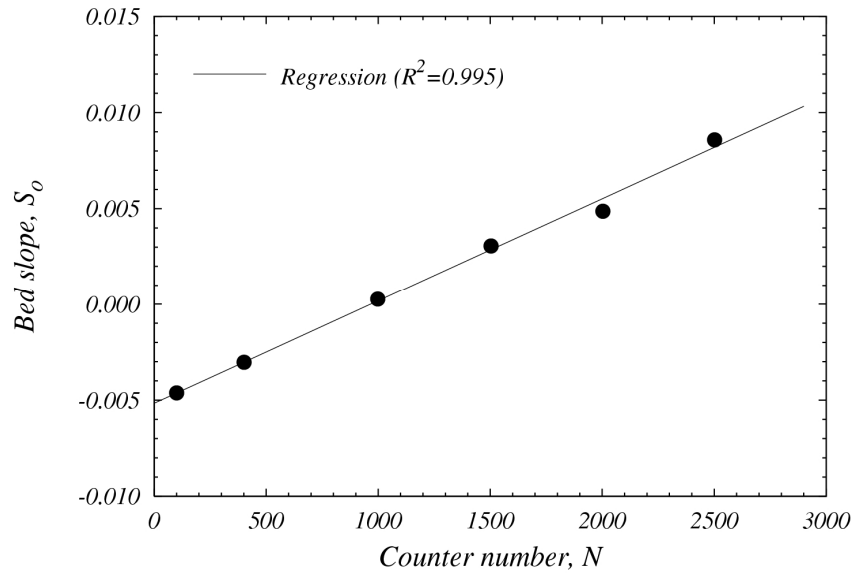


Figure 4.2 Calibration of the relation between bed slope and counter number

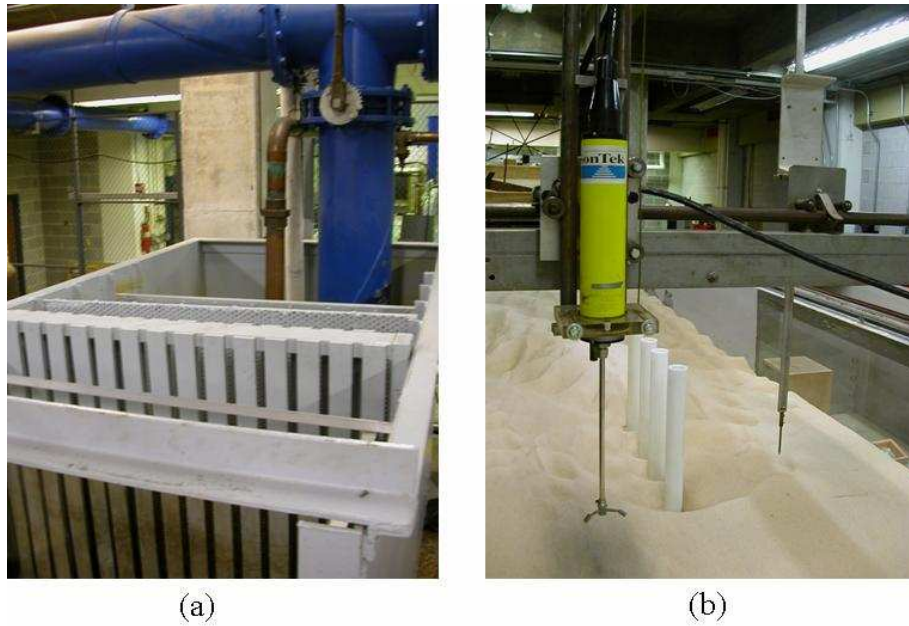


Figure 4.3 Tilting flume (a) head box (b) test section with glass wall

4.1.3 Flowmeter

The flowrate in the 305 mm supply pipe is measured by a magnetic flow meter which has an expected uncertainty of $\pm 2.8 \times 10^{-4} \text{ m}^3/\text{s}$. A separate magnetic flow meter is installed in the 152 mm supply pipe which can feed the 305 mm pipe at smaller flowrates, and it also has an uncertainty of $\pm 2.8 \times 10^{-4} \text{ m}^3/\text{s}$ (Foxboro 2004).

4.2 Velocity Measurements

4.2.1 Stream Probe - Propeller type

A Nixon Streamflo probe is a velocity meter of the propeller type that can be inserted into the water to measure a point velocity from 0.05 to 1.5 m/s. When the rotor of the probe is rotated by the flow, impedance produced by the passage of the rotor blades is measured by an electronic detector circuit to obtain frequency which can be converted to point velocity with an uncertainty of $\pm 1.5\%$ of true velocity. The frequency is measured and averaged over a 60-sec time interval. The related calibration equations between the measured frequency, F_s (Hz), and true velocity, V (m/s), are presented as (Sadiq 1992):

$$V \text{ (m/s)} = \begin{cases} 0.005208 (F_s + 7.2) & \text{for } 10 \leq F_s \leq 50 \\ 0.005250 \left(F_s + \frac{20}{3} \right) & \text{for } 50 \leq F_s \end{cases} \quad (4.2)$$

This propeller meter was used to measured vertical profiles of longitudinal point velocities at the approach flow section. It was also used to measure velocities in the

floodplain where it is difficult to make measurements with a larger probe like an acoustic Doppler velocity meter (ADV) because the flow depth is shallow.

4.2.2 Electromagnetic Velocimeter

The Marsh-McBirney Model 523 Electromagnetic Velocimeter consists of a 13-mm spherical electromagnetic velocity sensor and signal processor with an output voltage that can be converted to two-dimensional mean velocities using NI Multi-function Data Acquisition (DAQ) Devices. The signal amplification introduces some noise at the beginning stage; thus, low-pass filters are applied to the output signals resulting in a peak-to-peak noise content of 0.009 m/s at the output voltage jack with a one-second time constant (Marsh-McBirney 2002). Similar to the propeller meter, this velocimeter was used to measure point velocities at the approach section and in shallow floodplain flows. This velocimeter provides 2-D velocity components that can be compared with results from the ADV.

4.2.3 Acoustic Doppler Velocimeter - ADV

An acoustic Doppler velocimeter (ADV) was utilized to measure instantaneous point velocities and turbulence quantities with different types of probes: 3D down-looking, 3D side-looking and 2D side-looking. When velocity measurements were needed at points close to the free surface and at shallow water depths, the 2D and 3D side-looking ADV probes were used. The ADVs were mounted on a manufactured point gage located on the steel rail of the instrument carriage to measure the elevation of the sampling volume. The distance between the bed and sampling volume, which is 246 mm³ in size for the 10 MHz ADV and 82 mm³ for the 16 MHz MicroADV, was measured by the 3D down-

looking ADV (Marchioli and Soldati 2002a; SonTek 2001).

The operation principle of the ADV is based on the Doppler frequency shift of emitted acoustic signals after reflection by small sound-scattering particles in the flow which are assumed to be moving at the same velocity as the fluid. Scattering particles can be air bubbles or sediments, for example (Lane et al. 1998). The velocity of the scattering particles can be calculated inversely using the shift in the wavelength of sound if the speed of the wave is known exactly.

The water depth and bed elevations before and after scouring were measured by the point gage and the ADV. The ADV can generally detect a boundary within 25 cm for the 16 MHz MicroADV, and the ADV can measure the distance from the center of the sampling volume to a solid boundary with ± 1 mm uncertainty before starting to measure a point velocity as shown in Figure 4.4.

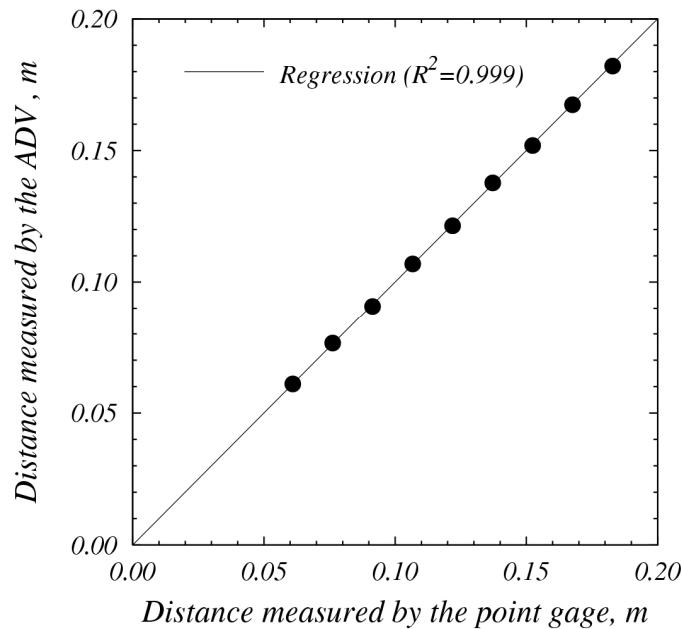


Figure 4.4 Comparison of the distances from boundary measured by the down-looking MicroADV and the point gage

However, sometimes the ADV is not able to detect precisely bed elevations along a steep slope so that measurements with a point gage are needed. The elevation of a reference point can be determined by a point gage and compared to the elevation measured by the ADV before measuring all bed elevations around bridge piers to provide a common elevation datum.

The existence of Doppler noise from the ADV is a common occurrence when measuring the velocity, especially when the flow velocity exceeds the pre-set velocity range or when there is contamination from the previous acoustic pulse reflected from boundaries of complex geometries. Noise also occurs when a high level of turbulence exists at the measuring location. Hence, the examination and filtering of the signal is needed before analyzing the mean point velocity and turbulent kinetic energy. One method for reducing noise is to filter the time series data according to a minimum value of a correlation coefficient and the percentage of data retained after filtering. A correlation coefficient is used as a measure of the quality of data in terms of the coherence of the return signals from two successive acoustic pulses (Lane et al. 1998; SonTek 2001). After filtering the data, it is essential to determine how much data is retained so that the time characteristics of the signal are retained when the bed shear stress is calculated. In some cases, addition of seeding particles helps to measure the turbulence characteristics in highly turbulent flow or highly aerated water because the correlation values and signal strength, which are quality control parameters for acceptance or rejection of the ADV signal, will be higher. In this study, the minimum value of the correlation coefficient was required to be 70 percent for acceptance of each returned data sample consistent with the recommendation of the ADV manufacturer

(SonTek 2001) for measurement of turbulence properties.

In some instances, the noise from a location near the bed or in a highly turbulent region caused an excessive number of data samples in one time record to be rejected in order to satisfy the cutoff value of the correlation of 70 percent. Hence, a second test was made of the time record after filtering such that a minimum of approximately 50% of the data samples was required to be retained in order to preserve the integrity of the time record; otherwise, the entire time record at that location was rejected. The required minimum percent of data retained was chosen as 50% based on the comparison of bed shear stress measured by two methods. One is the Clauser method using the mean velocity profile. The integrity of the mean velocity data requires a recommended correlation of only 40% (SonTek 2001). The other method used to obtain bed shear stress is to extrapolate the directly measured Reynolds stress profiles to the bed. This method is much more sensitive to the percent data retained because it involves turbulent velocity fluctuations. Figure 4.5 shows the relative difference between these two measures of the bed shear velocity for different bed conditions after filtering with the 70 percent correlation filter. It was found that there was approximately only a 3 percent difference between these two methods for calculation of bed shear velocity for at least 50% of the data retained. For values of percent data retained smaller than 50%, the percent difference in bed shear velocity was as high as 12 percent as shown in Figure 4.5. In summary, acceptable turbulence measurements required a correlation of at least 70 percent in terms of signal quality with at least 50% data retention in a time record, while bed shear velocities in the approach section were determined by the Clauser method because the lower correlation of 40 percent could be used for the mean point velocities.

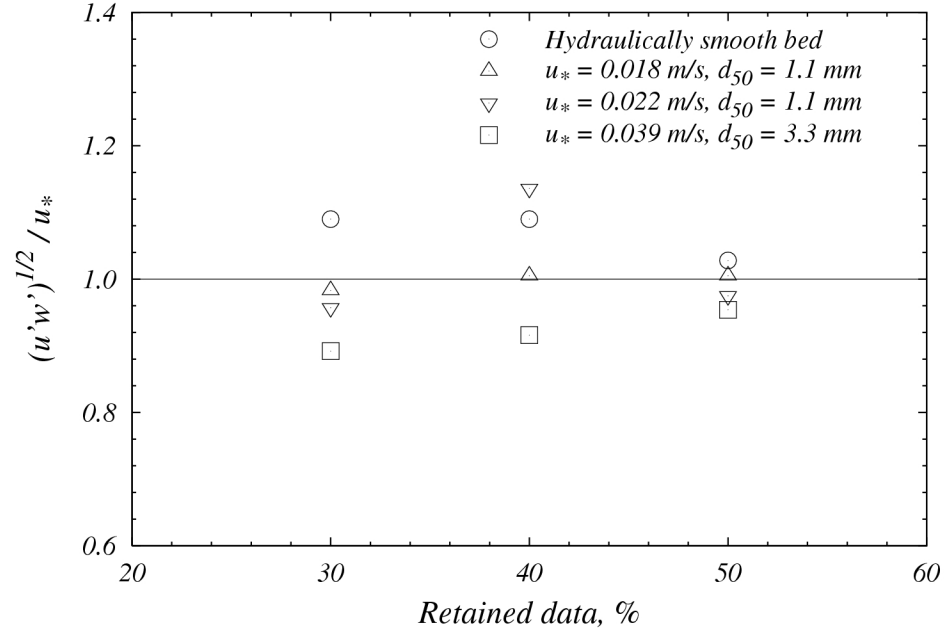


Figure 4.5 Comparison of bed shear velocity obtained from the Clauser method and the Reynolds stress profiles for different bed conditions

In addition, kaolin clay particles were used as seeding materials to improve the signal strength and correlation values. The range of the kaolin clay particle sizes was from $0.2 \mu\text{m}$ to $5 \mu\text{m}$. The signal strength, a measure of the intensity of the reflected signal, is a function of the amount and type of scattering particles in the fluid, hence the reflected signal strength is weaker than the electronics noise if the water in the channel is too clear. It is recommended that the signal to noise ratio, SNR, should be greater than 15 for accurate measurements (SonTek 2001). Before each experiment began, the reliability in terms of the signal strength was investigated since the ADV cannot accurately measure flow characteristics without satisfactory signal strength, and seeding was done if the SNR was too low. Observation of time series showed an extreme difference in SNR of data measured with seeding materials and without seeding materials even though the mean velocities were approximately the same as shown in Figure 4.6 and Figure 4.7.

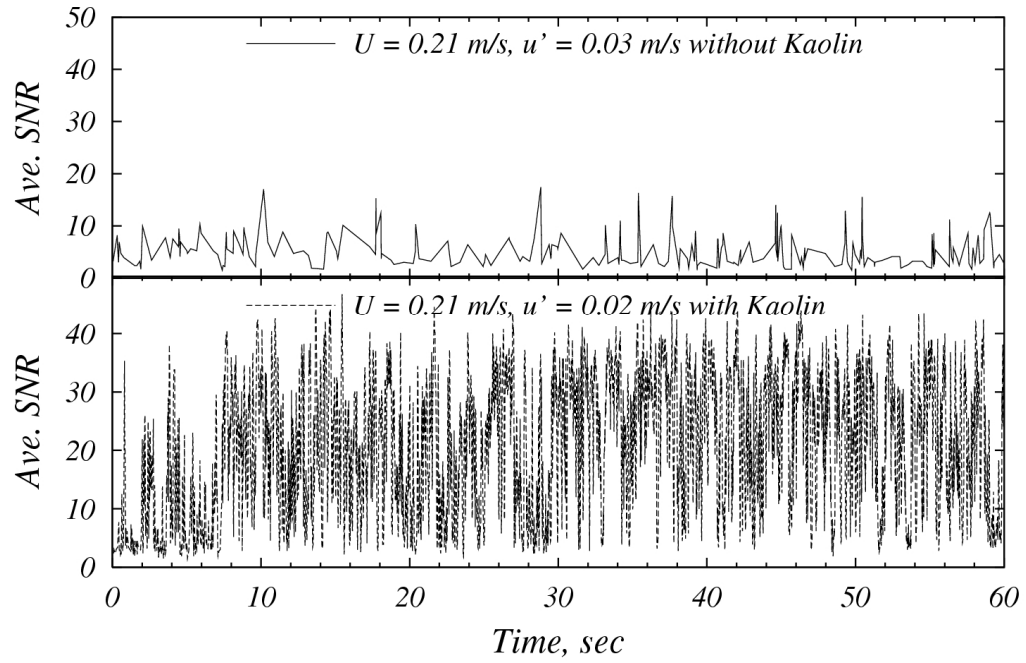


Figure 4.6 Comparison of time series of SNR between without kaolin and with kaolin in a horizontal flume ($Q = 0.038 \text{ m}^3/\text{s}$, $y_1 = 0.107 \text{ m}$, $C_o = 1000 \text{ mg/L}$)

These data presented in Figure 4.6 and Figure 4.7 were measured with the tracer injector placed upstream of the ADV probe near the flume inlet. The injector had a length of 1 m and 8 evenly spaced holes with 1 mm diameter. All data were filtered using the 70 percent correlation criterion for the return signal. Through that filter, data measured without kaolin were retained during only 15 percent of the whole time record while 90 percent of the data measured with kaolin seeding were retained. Turbulent characteristics changed due to the presence or absence of seeding materials when the turbulence intensity was compared. The relative difference in the turbulence intensity was about 30 percent while only 2 percent difference in mean velocity occurred. Data measured without kaolin adequately measured mean velocity but too much data was lost in filtering to provide adequate turbulence characteristics without seeding.

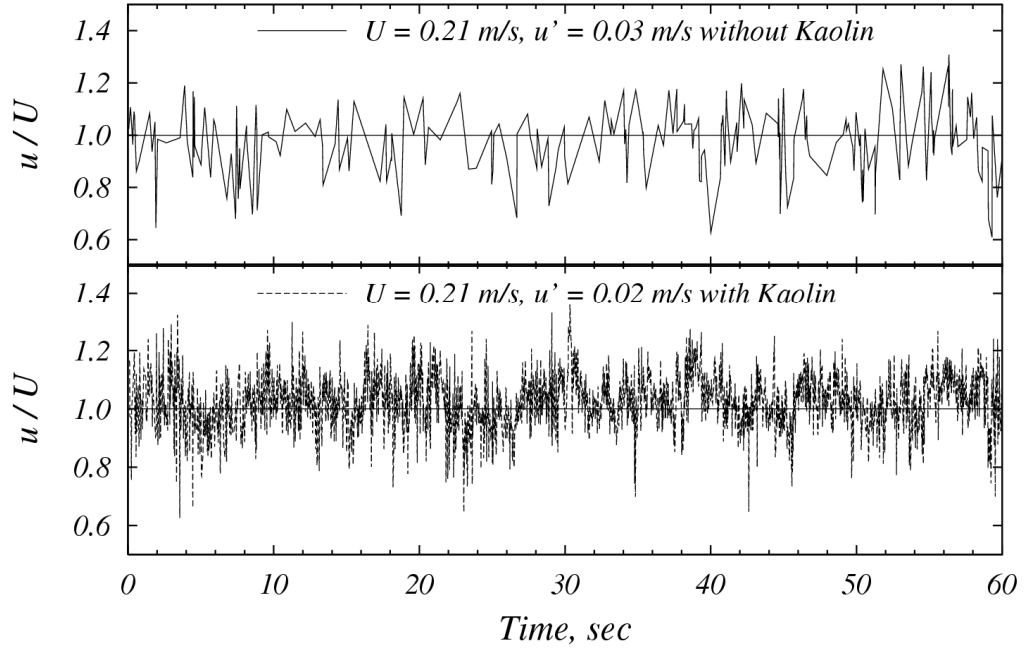


Figure 4.7 Comparison of time series of velocity data between with kaolin and without kaolin in a horizontal flume ($Q = 0.038 \text{ m}^3/\text{s}$, $y_1 = 0.107 \text{ m}$, $C_o = 1000 \text{ mg/L}$)

One approach velocity time series was measured over a 12 minute time interval at a single point and split into 2 minute time periods to produce 6 different samples of velocity measurements. After calculating the time-averaged velocity and the turbulence intensity in three directions for the 6 data sets, the uncertainty in time-averaged velocity for each direction was observed to be approximately 0.7%, 1.9%, and 3.3% in the streamwise, transverse, and vertical directions, respectively. The uncertainty in turbulence intensity was 2.9%, 1.7%, and 2.1% in the streamwise, transverse, and vertical directions, respectively. Figure 4.8 shows the time-averaged velocity and turbulence intensity in the streamwise direction for the six samples.

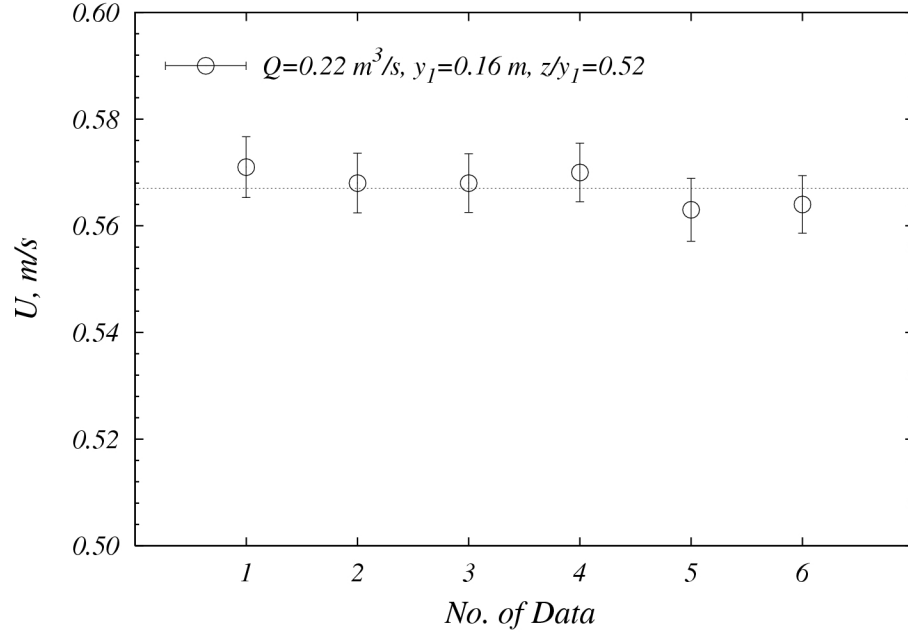


Figure 4.8 Time-averaged velocity with turbulence intensity shown for each data sample (average value of $U = 0.567 \text{ m/s} \pm 0.004 \text{ m/s} (\pm 0.7\%)$)

4.2.4 Comparison of Mean Velocity Profiles

Mean velocity profiles in a horizontal flume were measured by the 2D electromagnetic velocimeter and several types of ADV including the 3D side-looking and down-looking 16 MHz MicroADVs, and the down-looking 10 MHz ADV for comparison. The velocity profiles were measured in a rectangular flume that was 5 m long and 0.4 m wide with smooth boundaries. The flow depth was 0.3 m and the flowrate was $0.032 \text{ m}^3/\text{s}$.

The velocity profiles are shown in Figure 4.9 along with the measured shear velocity for each profile using a logarithmic fit of the velocity data near the bed. The down-looking 10 MHz ADV and the down-looking 16 MHz MicroADV were mainly used to measure the time series of velocity and turbulence characteristics near the piers, while the other instruments were utilized in case of shallow flow depths or near the water

surface where the down-looking probes could not be used. The ADV data points are in close agreement over the full depth of the flow, while the electromagnetic meter data deviates from the side-looking ADV measurements near the free surface because of the surface disturbance caused by the finite size of the electromagnetic sensor.

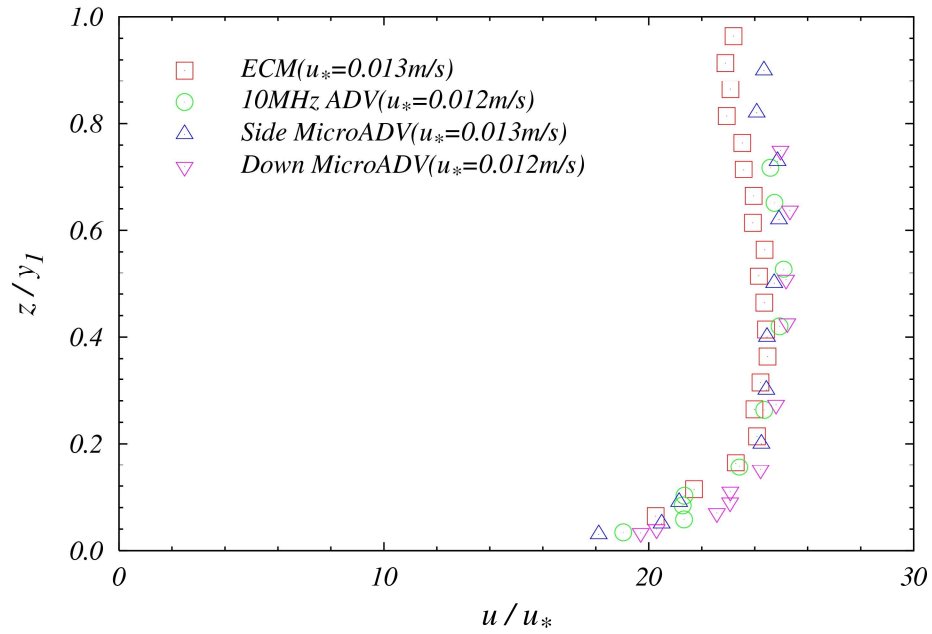


Figure 4.9 Comparison of mean velocity profiles ($Q = 0.032 \text{ m}^3/\text{s}$, $y_1 = 0.3 \text{ m}$)

4.3 Flow Visualization

A kaolinite suspension was used as a tracer upstream of the bridge piers in the tilting flume to show the flow structure around a bridge pier and detect the frequency of the horseshoe vortex system immediately upstream of the pier. The shape of the effluent nozzle as shown in Figure 4.6 was designed to prevent separation and minimize the flow

disturbance with an inner diameter of 4.7 mm. The tracer was transferred from a conical tank by an electric pump operating at a maximum flowrate of $0.003 \text{ m}^3/\text{s}$. The kaolinite suspension was mixed to achieve a concentration of 1000 mg/L in the tank. The flowrate of tracer was adjusted with the aid of a rotameter to produce a release velocity that was the same as the open channel mean velocity.

As the tracer was released at a constant rate, a video camera was used to capture the unsteady dynamics of the swirl of the horseshoe vortex as it amplified and then partially collapsed in size. The video images were analyzed as described in Chapter 6.



Figure 4.10 Tracer delivery system: (a) the brass effluent nozzle and (b) pump stand with 30 liter conical bottom tank and rotameter

4.4 Physical River Modeling Strategy

The local scour around a bridge pier is often governed by multiple parameters as given in the following equation (Ettema 1980; Sturm 2001):

$$\frac{d_s}{b} = f \left(K_s, K_\theta, \frac{y_1}{b}, \frac{b}{d_{50}}, \frac{V_1}{V_c}, Fr_1 \text{ or } Fr_b \right) \quad (4.3)$$

where d_s is the scour depth; b is the width of bridge pier; K_s is the shape factor; K_θ is the pier alignment factor; d_{50} is the median sediment size; y_1 and V_1 are approach depth and velocity, respectively, Fr_1 is the approach Froude number and Fr_b is the approach pier Froude number. However, it is seldom possible to satisfy simultaneously all requisite similarity criteria for physical modeling. The sediment size, for instance, cannot be scaled in the laboratory without becoming so small that interparticle cohesive forces, which do not exist in prototype sand-bed streams, dominate the scour process. Hence, a physically reasonable model strategy is required to predict effectively the prototype behavior.

In this study, Froude number similarity was basically selected since the phenomenon of a local scour around a bridge pier usually occurs in open channel flow. The Froude number governs the water surface profile through the bridge and hence the pressure gradient in the vicinity of the piers. Geometric similarity is maintained in terms of y_1/b in order to preserve the relative size and strength of the horseshoe vortex system. While maintaining Froude number similarity and geometric similarity (y_1/b), the sediment size in the laboratory can be selected to produce a value of $V_1/V_c < 1.0$ to

compensate for the reduction in relative scour depth at large values of b/d_{50} . (Maximum scour depth occurs for $V_1/V_c = 1.0$.)

Using the HEC-RAS (Hydrologic Engineering Center's River Analysis System) software, elementary hydraulic parameters such as flow velocity, depth, and hydraulic radius can be calculated for field conditions. It was observed that the approach Froude numbers did not change drastically for the large prototype flows that were modeled. Keulegan's equation for fully rough turbulent flow was chosen to evaluate the critical velocities for initial motion of sediment in the field and laboratory, which is given by (Sturm 2001):

$$V_c = 5.75 \sqrt{\tau_{*c} (SG - 1) g d_{50}} \log \left(\frac{12.2 R}{k_s} \right) \quad (4.4)$$

in which τ_{*c} , the critical value of Shields' parameter, SG is the specific gravity of the sediment; and d_{50} is the median sediment grain size R is the hydraulic radius, and k_s is the equivalent sand-grain roughness. When V_1/V_c is calculated for field measurements, the scour regime was certainly live-bed scour conditions. However, it is difficult to reproduce live-bed scour conditions in the laboratory, even though a large-scale laboratory model is selected in a large flume. As a result, the relationship between live-bed scour in the field and clear-water scour in the laboratory was used to reproduce the same maximum scour depth between field and laboratory. The laboratory model was constructed using an undistorted scale from Froude number similarity with equality of y_1/b . After determining the scale for laboratory models, discharge was calculated to match Froude numbers as given by:

$$Q_r = V_r \times L_r^2 = L_r^{5/2} \quad (4.5)$$

$$Q_m = L_r^{5/2} \times Q_p$$

where Q_p and Q_m are the discharge of prototype and model respectively, and Q_r , V_r , and L_r represent individually the discharge, velocity, and length ratios of model to prototype quantities. Sediment size for laboratory experiments was decided to give $V_1/V_c = 0.7 \sim 1.0$ at the same Froude number in model and prototype since the maximum scour depth generally occurs at $V_1/V_c \sim 1.0$ in clear-water scour regime. Finally, possible experimental cases in clear-water scour with several flow depths and discharges were determined up to the point where the approach velocity in the laboratory model became close to the calculated critical velocity from Equation 4.4 in the clear-water scour regime.

As it was subsequently determined, live-bed scour depths in the prototype can be reproduced using clear-water scour experiments in the laboratory with Froude number similarity and geometric similarity, y_1/b while choosing appropriate values of both b/d_{50} and V_1/V_c in the laboratory.

4.5 *Bed Materials*

Three different sizes of sediments were utilized for this study. The results of sieve analyses for these three sediments are shown in Figure 4.11. The properties for each sediment are listed in Table 4.1. The size distribution is characterized by the sieve diameter for which 50% is finer by weight, d_{50} , and the geometric standard deviation of

the distribution, $\sigma_g = (d_{84}/d_{16})^{1/2}$. All bed materials for this study can be considered to be uniform in size since the standard deviation of the particle size distribution of each sediment is less than a limit of about 1.5 for uniform size sediments.

The dimensionless particle diameter d_* in Table 4.1 is defined by

$$d_* = \left(\frac{(SG-1) g d_{50}^3}{\nu^2} \right)^{1/3} \quad (4.6)$$

in which SG = specific gravity of sand (=2.65) and ν = kinematic viscosity of water.

The value of the critical shear stress for initiation of motion of each sediment τ_c is given in dimensionless form by the Shields parameter defined by

$$\tau_{*c} = \frac{\tau_c}{(\gamma_s - \gamma) d_{50}} \quad (4.7)$$

in which $(\gamma_s - \gamma)$ = submerged specific weight of the sand. The value of d_* determines the values of the Shields parameter given in Table 4.1 according to the Shields diagram (Sturm 2001). The critical shear velocity, u_{*c} , for the mean particle size, d_{50} , of each sediment in Table 4.1 is simply defined by $(\tau_c / \rho)^{1/2}$.

Table 4.1 Properties of sediments for this study

Sediment	d_{50} , mm	σ_g	d_*	τ_{*c}	u_{*c} .m/s
A	3.30	1.30	89.48	0.045	0.049
B	1.10	1.33	27.83	0.038	0.026
C	0.53	1.17	13.41	0.032	0.017

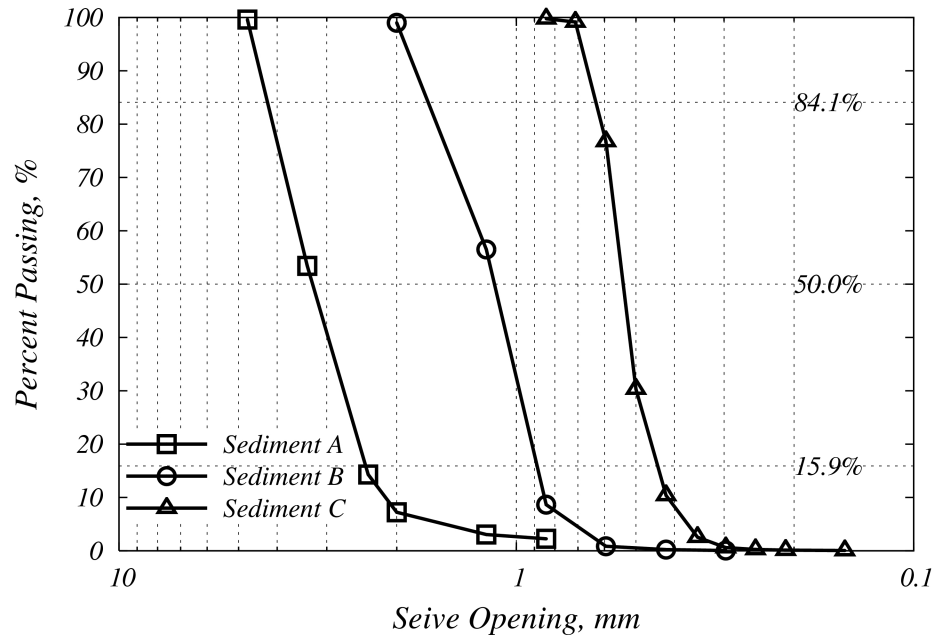


Figure 4.11 Sediment size distribution of the bed materials for this study

4.6 Bridge Pier Models

The schematic of each bridge pier for each river with the prototype dimensions was given in Chapter 3. Five bridge pier models with individual scales were fabricated for this study as shown in Figure 4.12 and Table 4.2.

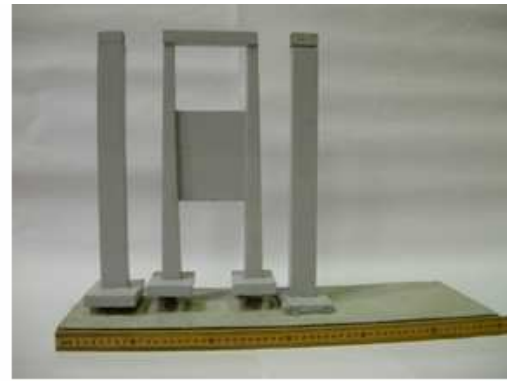
Table 4.2 Bridge model scales, pier shape and pier width

Model	Scale	Pier shape	Pier width, (model),m	Pier width, (field),m	Remark
Chattahoochee River	1:23	Rectangular	0.046	1.067	F ¹
Chattahoochee River	1:40	Rectangular	0.027	1.067	F, R ²
Flint River	1:33	Square	0.055	1.829	F
Flint River	1:50	Square	0.037	1.829	F, R
Flint River	1:90	Square	0.021	1.829	F
Ocmulgee River	1:45	Circular	0.041	1.829	F, R

F¹=Flat bed experiment, R²=River model experiment



(a)



(b)



(c)



(d)



(e)



(f)

Figure 4.12 Bridge models for this study: (a) Bridge model in Chattahoochee River model with 1:23 scale, (b) Bridge model in Chattahoochee River model with 1:40 scale, (c) Bridge model in Flint River model with 1:33, (d) Bridge model in Flint River model with 1:50 scale, (e) Bridge model in Flint River with 1:90 scale, and (f) Bridge model in Ocmulgee River with 1:45 scale.

Information for cross section data presented by the USGS was applied to build the river bathymetry for each river model as shown in Figure 4.13, Figure 4.14 and Figure 4.15, respectively. For Flint River experiments, models were constructed at three different geometric scales and installed in the horizontal and tilting flumes as either a river model, in which the river bathymetry and entire bridge were modeled, or as a flat bed model that included only one pier bent with a sediment bed that was initially flat. All the tilting flume models were flat bed models while both flat bed and river models were installed in the horizontal flume. There were models at two different geometric scales for the Chattahoochee River bridge and a model at one geometric scale for the Ocmulgee River bridge.



(a) Bridge section looking downstream from the right bank



(b) Bridge section with embankment looking downstream from the left floodplain

Figure 4.13 River model for Chattahoochee River near Cornelia, GA



(a) Bridge section looking downstream from the left bank with old embankment



(b) Railroad bridge looking downstream to highway bridge

Figure 4.14 River model for Flint River at Bainbridge, GA



(a) Bridge section looking downstream from the left bank



(b) Bridge section looking downstream from the right bank

Figure 4.15 River model for Ocmulgee River at Macon, GA

4.7 *Experimental Procedure*

First, flat-bed experiments were conducted to investigate the effect of individual parameters and interaction among parameters that affect scour depths. Also, during the flat bed experiments the calibration and uncertainty of the instruments and experimental procedure were investigated by comparison of repeated experiments. Based on river

bathymetry data from the USGS, the river model was fabricated with a proper length scale to fit the horizontal flume. All cross sections were built with plywood templates cut according to the USGS field survey. Bridge pier geometry and location as well as bridge abutments and embankments were modeled according to bridge plans provided by the GDOT and the GPS positions measured in the field by the USGS.

For establishing uniform flow as the inlet flow condition, the most upstream river cross section was duplicated and installed with a horizontal spacing of approximately 1.5 m to provide an approach prismatic channel of length equal to at least 45 flow depths. The flume coordinates, (x_m, y_m) , for the river model experiments were determined from field coordinates, (x_p, y_p) , established by a global positioning system (GPS). This information was used not only to locate the cross sections and the bridge appurtenances but also to establish corresponding positions where the scour results from the experiments were compared with field measurements.

The ADV was used to measure flow velocity, turbulence intensity and bed elevations before and after scour relative to a fixed elevation datum established on the bottom of the flume. The ADV gives the distance from the sampling volume to the bed which can be converted into elevation relative to the datum by reading the point gage vertical scale to which the ADV is attached.

After the bed had been leveled according to the templates installed in the test section, the templates were carefully removed and the bed elevations were measured in detail throughout the test section with a horizontal spacing of approximately 0.06 m. The upstream flow approach point where there is no effect of the existence of bridge piers on the velocity profile was determined by comparing velocity profiles measured upstream of

the main bridge pier at different positions along the pier centerline.

The flume was filled with water for an experiment from a downstream supply hose at a very slow rate so that the sand would be saturated safely and remain undisturbed. After complete saturation, a required discharge was established using the magnetic flowmeter with the flow depth adjusted well above that at which scour began using the tailgate. Then the flow depth was gradually decreased by changing the height of the tailgate until the target approach flow depth was obtained. During this time, the point gage on the instrument carriage was used to monitor the flow depth. Once the target flowrate and flow depth had been reached, vertical profiles of point velocities were measured at the approach point located 10 pier widths upstream of the face of the pier using the ADV and electromagnetic velocimeter. In some experimental runs, the velocity field was measured throughout the test section both in the near field next to the piers and in the far field.

During an experimental run, the temporal change of bed elevation in front of a bridge pier was measured periodically using the ADV temporarily positioned for a moment above the point of scouring. At the completion of an experiment, the final bed elevations were measured in the same way as the initial elevations using the ADV and the point gage. During measurement of bed elevations with the ADV, the flume was not drained because the ADV probe needed to be completely submerged. After finishing with the bed elevation measurements with the ADV, the flume was slowly drained so as not to disturb the scour contours and the final bed elevations near a bridge pier or footing were measured with a point gage. For river model experiments, scour depths and scour contours were calculated by subtracting bed elevation after reaching equilibrium scour

depth from initial bed elevations before starting the experiment. The closing time of the experiment was determined when the local scour depth reached the equilibrium state at which there are negligible changes in bed elevation with time as guided by Melville and Chiew (1999) , but it was never less than 48 hours.

4.8 Velocity and Turbulence Measurements

For the smooth and rough boundary, the mean velocity profile is comprised of two regions, the inner and outer region. The overlapping region between inner and outer regions is generally characterized by a universal logarithmic velocity profile in which the inner law and outer law can be applied. Except in the very near wall region, the mean velocity profile for both smooth and rough boundaries is given as (Bergstrom et al. 2002; Krogstad and Antonia 1999; Rahman and Webster 2005)

$$\frac{U(z)}{u_*} = \frac{1}{\kappa} \ln \left(\frac{z u_*}{\nu} \right) + A - \Delta U^+ + \frac{2 \Pi}{\kappa} \omega \left(\frac{z}{\delta} \right) \quad (4.8)$$

where, $U(z)$ is the time-averaged point velocity at distance z from the bed, u_* is the shear velocity defined as $(\tau_o/\rho)^{1/2}$, κ is the von Karman constant equal to 0.41, A is a constant equal to 5.0, ΔU^+ is the roughness function or shift in the mean velocity due to the bed roughness height, Π is the Coles wake parameter, and ω is the wake function. In the vicinity of the roughness, the viscous length scale of Equation 4.8 can be replaced with the equivalent roughness height, k_s . The resultant mean velocity profile in the overlapping region becomes

$$\frac{U(z)}{u_*} = \frac{1}{\kappa} \ln\left(\frac{z}{k_s}\right) + A_r + \frac{2\Pi}{\kappa} \omega\left(\frac{z}{\delta}\right) \quad (4.9)$$

where, k_s is the equivalent Nikuradse grain roughness and A_r is 8.5 for sand grain roughness based on empirical studies in pipes and open channels (Nezu and Nakagawa 1993). Following the procedure presented by Krogstad et al.(1992), the optimized values for u_* and Π can be found.

At the approach section, which was located at a distance of 10 pier widths upstream of a bridge pier in the streamwise direction, the approach flow for each experiment was a fully developed turbulent open channel flow in both the horizontal and tilting flumes. The acoustic Doppler velocimeter (ADV) was used to measure the velocity time series for all experiments. The time series were analyzed to determine the time-averaged velocity and turbulence intensity profiles at the approach section. The measured velocity profiles were found to agree well with Equation 4.9 in which the time-averaged point velocity is a linear function of the logarithm of the distance from the bed. In this study, the optimal value of Π was zero for the fully developed flow at the approach section. For the data analysis, the velocity data up to 60% of the flow depth were utilized since Nezu and Rodi (1986) measured the longitudinal velocity profiles and turbulence fluctuations in a uniform open channel over a smooth bed and suggested that the log-law was formally able to be used up to 60% of the flow depth if the von Karman constant was taken as 0.40.

The shear velocity is the most essential velocity scale to normalize the turbulent time-averaged velocity and turbulence intensity. The determination of the shear stress over a hydraulically rough bed ($k_s u_* / \nu > 70$) is more difficult because there are more

unknown parameters in the equation for mean velocity profile than over a smooth bed. Several methods to determine the shear velocity are available, including the logarithmic fit to velocity data points near the bed (Clauser method), extension of the measured Reynolds stress profile to the bed, and the uniform flow formula in which the bed shear stress is related to the bed slope and the flow depth. When the shear stress and equivalent Nikuradse sand-grain roughness are examined over a rough bed, the roughness elements penetrate outside the sub-layer shifting the theoretical wall level to a point below the top of the sand or gravel bed as shown in Figure 4.16.

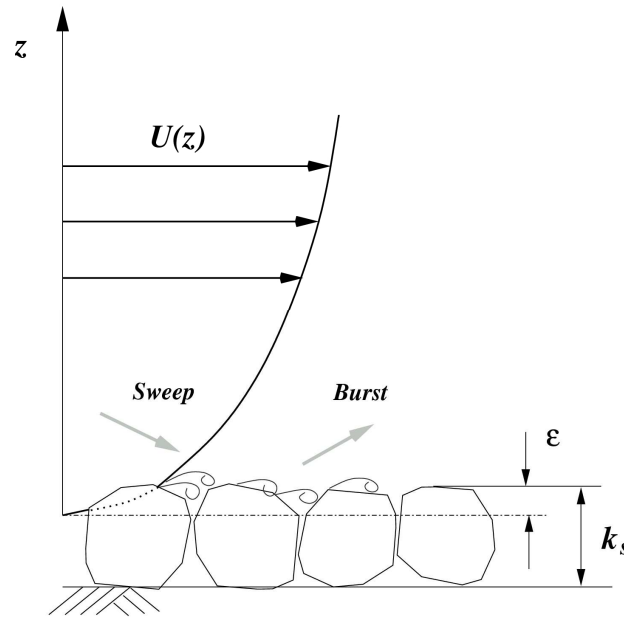


Figure 4.16 Schematic description of turbulent flow over rough bed

The theoretical wall level is set at a position ϵ measured below the top of the roughness elements such that the value of ϵ is between zero and k_s . From several studies, the range of ϵ/k_s is about 0.15~0.3 for sand-grain roughness (Nezu and Nakagawa 1993). However, in this study the theoretical wall level was set at the top of the sediment particle

($\varepsilon = 0$) for convenience based on the examination of the effect of the theoretical wall level on shear stress. The effect of the location of the theoretical wall level was examined in terms of the relative error of the values of shear velocity estimated by regressing $U(z)$ on $\log z$. The relative error in shear velocities calculated by setting the zero offset between $\varepsilon = 0$ and $\varepsilon = 0.3 \times d_{50}$ were only 0.8% for $d_{50} = 0.53\text{mm}$, 1.5% for $d_{50} = 1.1\text{mm}$, and 1.7% for $d_{50} = 3.3\text{mm}$, which is negligible considering the reliability of bed leveling for each experiment and the slight nonuniformity of flow conditions in the river model.

In this study, the mean velocity profile measured by the ADV was utilized to determine the shear velocity and equivalent Nikuradse sand-grain roughness which are estimated from the slope and intercept of the regression equation, regressing $U(z)$ on $\log z$ from the top of sediment to 60% of the approach flow depth as shown in Figure 4.17.

The shear velocity can also be obtained from a linear best fit of the Reynolds stress profile as shown in Figure 4.18 followed by extension of the Reynolds stress profile to the boundary. The relative difference in the shear velocity determined by the two methods in Figure 4.17 and Figure 4.18 is typical and is approximately 10%. The approach flow was not exactly uniform for the river model so that the uniform flow method of shear velocity determination was not possible. Given the scatter in the measured Reynolds stress profiles, it was decided to use the logarithmic velocity fit to obtain the shear velocity as other investigators have done (Kironoto and Graf 1994; Song and Graf 1996; Voulgaris and Trowbridge 1998).

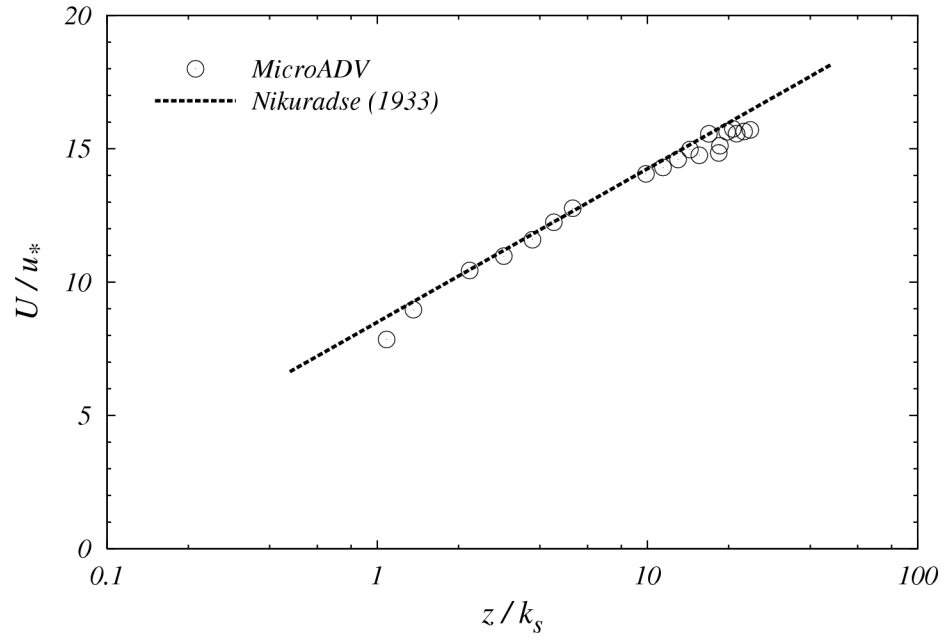


Figure 4.17 Mean velocity profile ($Q=0.085 \text{ m}^3/\text{s}$, $y_1=0.19\text{m}$, $u_*=0.025 \text{ m/s}$)

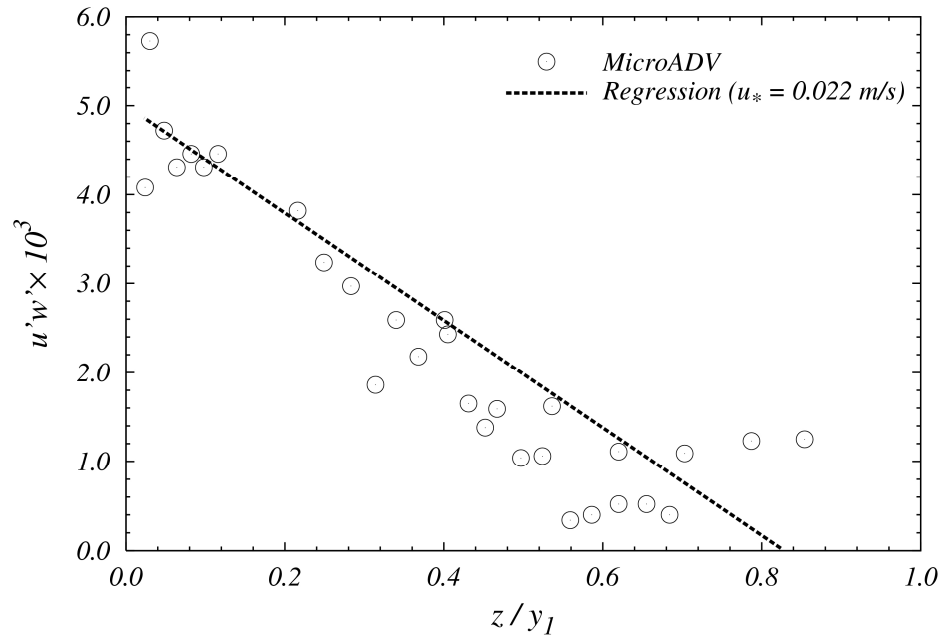


Figure 4.18 Reynolds stress profile ($Q=0.085 \text{ m}^3/\text{s}$, $y_1=0.19 \text{ m}$, $u_*=0.022 \text{ m/s}$)

In order to determine the reliability of ADV measurements of turbulence characteristics, the longitudinal turbulence intensity measured in the approach flow in the model was compared with both theoretical distributions and empirical distributions based on experimental measurements in the laboratory and field.

Nezu and Nakagawa (1993) considered the effect of roughness on turbulence intensity. For a completely rough bed, viscous effects disappear because the roughness elements penetrate the fully turbulent logarithmic layer. This layer is called the quasi-separated layer. The mean flow energy loss consists of the turbulent energy generation and the work done by the slip velocity defined as the velocity at the top of the roughness elements in the quasi-separated layer. The work in the quasi-separated layer generally occurs behind the roughness elements and can be considered as the direct dissipation in the viscous sublayer over the smooth bed. Thus, for the rough beds, the energy equilibrium zone extends over the range $50 < y u_* / \nu < 0.6 u_* h / \nu$. Nezu and Nakagawa, therefore, derived an equation for relative turbulence intensity by integration of the total turbulent energy generation in the extended equilibrium zone for a completely rough bed with the result given by

$$\frac{u'}{u_*} = \left[\frac{(1 - z / y_1)(L_x / y_1)}{K(\kappa z / y_1)} \right]^{(1/3)} \quad (4.10)$$

where, u' is the rms value of the streamwise velocity fluctuations; u_* is the shear velocity; κ is the von Karman constant; y_1 is the depth of water; z is the distance from the bottom of the bed; $K = 0.691 + 3.98 / \sqrt{R_L}$ if $R_L (= u' L_x / \nu)$ is larger than 200, defined as the Kolmogoroff universal constant, and L_x is a macroscale of turbulence that obeys

the ½ power law as given below:

$$\begin{aligned} L_x &= B_1 \sqrt{z y_1} \quad \text{for } \frac{z}{y_1} \leq 0.6 \\ L_x &= 0.77 B_1 y_1 \quad \text{for } \frac{z}{y_1} > 0.6 \end{aligned} \quad (4.11)$$

where, B_1 is almost equal to 1.0 for a Reynolds number $R_* (= u_* z/\nu)$ of 1600.

Kironoto and Graf (1994) empirically modified the equation of Nezu and Nakagawa (1993) with their laboratory experimental data to obtain an empirical distribution for relative turbulence intensity given by

$$\frac{u'}{u_*} = 2.04 \exp\left(-0.97 \frac{z}{y_1}\right) \quad (4.12)$$

The experimental data were collected in a tilting flume with dimensions of 16.8m in length, 0.6m in width and 0.8m in height. They used a rough plate with the height of roughness, $k_s = 4.8 \pm 0.5\text{mm}$, and a gravel bed with $d_{50} = 23 \pm 1.25\text{mm}$ to generate two different types of roughness. A Prandtl tube with a 3 mm outer diameter and a hot film probe were used to measure the velocity and turbulence intensity, respectively. The range of the Reynolds number was from 1.6×10^5 to 5.6×10^5 and the Froude number was changed from 0.23 to 0.48 for their experimental data.

Nikora and Goring (1998) derived a relationship for relative turbulence intensity from the equilibrium layer using parameterization of velocity spectra. They presented the four-range model for the analysis of velocity spectra by adding the spectral range with $S_{ii}(k) \propto k^{-1}$, where S_{ii} is the a wave number auto-spectra, and k is the wave number.

The four-range spectral model predicted that the normalized auto spectra were dependent only on the relative distance from the bed at very low values of the wave number. For the intermediate zone where the turbulence energy production and dissipation exist together, the four- range model was in good agreement with the experimental data. The integration of the spectra for the streamwise velocity component is given by

$$\frac{u'}{u_*} = \left[1.9 - 1.32 \ln \left(\frac{z}{y_1} \right) \right]^{0.5} \quad (4.13)$$

Nikora and Goring also performed field measurements in the Balmoral Irrigation Canal in North Canterbury, New Zealand. The median sediment size was varied from 6.4mm to 13.4mm, the Reynolds number changed from 0.36×10^6 to 1.30×10^6 and the Froude number was measured with the range from 0.17 to 0.38. The comparisons did not show appreciable difference in the intermediate zone (Nikora and Goring 2000).

The measured relative turbulence intensity profile at the flow approach section for an experimental run of the Chattahoochee River model is shown in Figure 4.19 where it is compared with relationships from the literature that were just described. In Figure 4.19, the shear velocity for the above equations was calculated using the logarithmic law fitted to velocity data points near the bed.

The good agreement shown in Figure 4.19 between the ADV measurements of turbulence intensity and relationships suggested by others that are both theoretical and measured in rough-bed channels provide some confidence in additional measurements of turbulence in the flow field. Accordingly, some near-field velocity and turbulence distributions relative to the bridge piers before and after scouring were measured for selected flow conditions to provide a better physical understanding of flow structure and

scour processes.

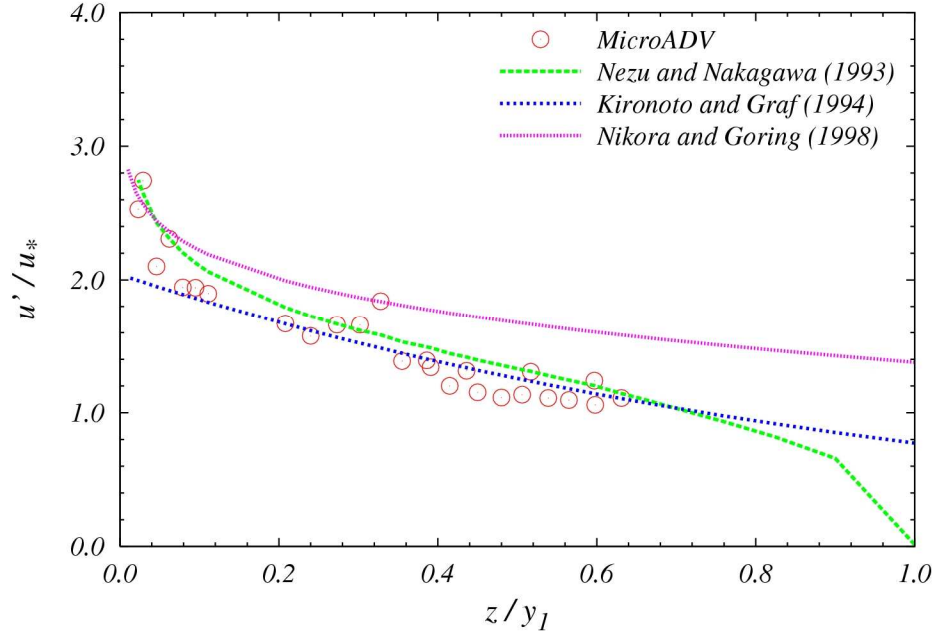


Figure 4.19 Turbulent intensity ($Q=0.085 \text{ m}^3/\text{s}$, $y_1=0.19\text{m}$, $u_*=0.025 \text{ m/s}$)

4.9 Scour Depth Measurement

Local scour depths at the nose of the bridge piers were recorded using the ADV at selected time intervals during a scour experiment as the scour holes developed with time. The distance between the top of the channel bed and the sampling volume of the ADV was measured until a negligible change in scour depth occurred over a duration of 3 hours. The frequency of the measurements decreased as time progressed and the rate of scouring gradually decreased. After equilibrium scour was reached, the bed elevations around the bridge piers were recorded with the aid of a point gage for some points where

the water depth was too shallow and too close to the flank of the bridge piers or an inner web between bridge piers since the ADV could not easily reach the bed in these areas.

Surfer ver8.02, the software provided by Golden Software, Inc. was introduced to interpolate the bed elevations in the vicinity of the bridge piers because the number of points measured before starting experiments could not be exactly identical with the number measured after experiments. It was necessary to measure on a finer grid at locations where significant changes of bed elevation occurred due to the development of scouring, for instance, near the bridge pier bent and the deposition area of sediments downstream of the bridge pier bent. Thus, interpolation is needed to calculate the amount of scouring for experiments with river models.

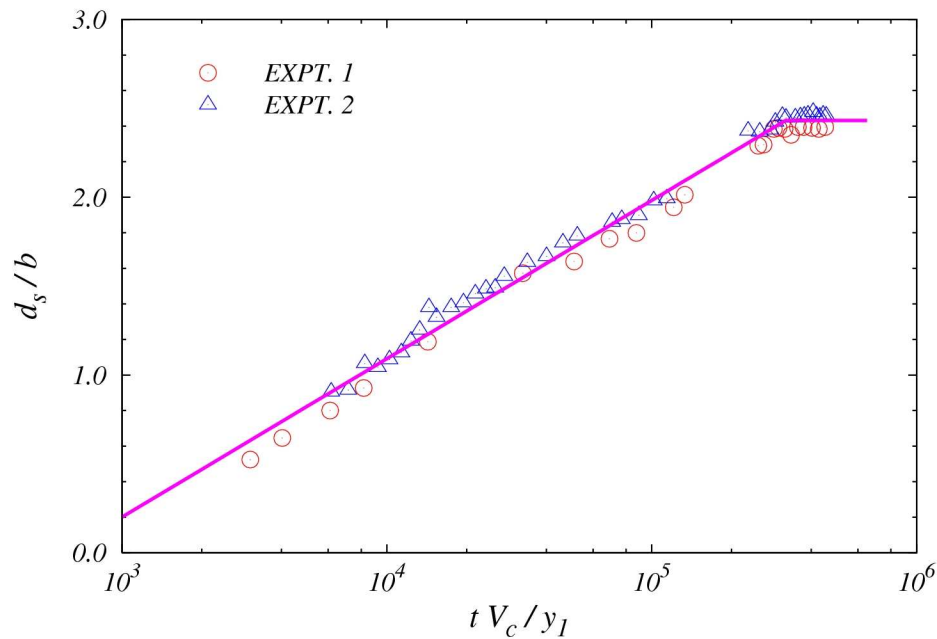


Figure 4.20 Replicated scour development with time for flat bed experiments in Chattahoochee River modeling ($V_1/V_c = 0.83$, $y_1/b = 4.2$, $b/d_{50} = 13.9$)

Scour depth was measured with a point gage having a $\pm 0.3\text{mm}$ scale error and an ADV having a $\pm 1\text{mm}$ scale error. However, the bed elevation in the overlap region measured by both instruments showed a difference of only $\pm 1\text{mm}$, and the bed elevation of the region where maximum scour depth was expected to occur was mainly determined by the elevation data measured with a point gage. Figure 4.20 shows the replicated results for scour development with time. The repeated scour experiments show the identical development of scour depth over the whole time scale including at the equilibrium state with an uncertainty of approximately $\pm 3\text{mm}$, which corresponds with one grain diameter($d_{50} = 3.3\text{mm}$).

CHAPTER V

EXPERIMENTAL RESULTS

In this chapter, experimental results collected from each bridge model experiment are presented. Experiments were of two types: flat-bed (FB), and river model (RM). In the flat-bed experiments, the main pier bent of each bridge was modeled individually in a rectangular channel with a movable sediment bed that was initially leveled to form a horizontal or flat bed prior to the beginning of scour. In the river model experiments, the complete river bathymetry upstream and downstream of the bridge as well as the embankments, abutments, and pier bents of the bridge itself were modeled in detail.

Each section of this chapter presents results of the temporal development of local scour depth, maximum scour depth and scour contours, approach flow depth and mean velocity profile, and comparisons with field data. The maximum scour depth is reported as the deepest scour depth in front of the most upstream pier of the main pier bent located in the main channel. Approach flow depth and mean velocity were measured upstream of the first pier of the main pier bent at a distance of 10 pier widths where there is no measurable effect of the pier on the flow structure. The acoustic Doppler velocimeter (ADV) was mainly used to measure the mean velocity and turbulence intensity distribution with a 25 Hz or 50 Hz frequency probe and a 2 minute sampling time. In order to exclude the friction velocity in all comparisons due to its greater uncertainty and the inability to measure it alongside the piers in the near field, all velocities and turbulence intensities were normalized by the mean approach velocity, V_1 .

5.1 The Chattahoochee River Model

The experimental conditions and results for the Chattahoochee River models are tabulated in terms of flow discharge, Q , sediment size, d_{50} , pier width, b , approach flow depth, y_1 , velocity, V_1 , duration of each experiment, T , and pier scour depth, d_s in Table 5.1 including the field measurements by the USGS. Two different scaled bridge models are fabricated and three different sediments are adopted for the experimental runs in the Chattahoochee River model.

Table 5.2 is a summary of dimensionless parameters for the Chattahoochee River model corresponding to the data given in Table 5.1. These parameters include the approach Froude number ($Fr_1 = V_1 / (g y_1)^{1/2}$), the pier Froude number ($Fr_1 = V_1 / (g b)^{1/2}$), flow intensity (V_1 / V_c), relative flow depth (y_1 / b), relative sediment size (b / d_{50}), and relative local scour depth (d_s / b). The critical velocity of the initiation of sediment motion, V_c , was calculated from Keulegan's equation presented in Chapter 4.

The ranges of dimensionless parameters in Table 5.2 are the result of using models having two different geometric scales with three different sediment sizes. In general, the value of y_1 / b was controlled to agree either with the bankfull value of approximately 4.0 or the 100-yr flood value of approximately 7.0. The sediment size was chosen such that the values of the flow intensity parameter varied from 0.6 to 1.0 with maximum clear-water scour expected at the latter value. Initially, in the flat-bed experiments, the Froude number was not controlled in order to get a wide range of values of b / d_{50} because larger sediment sizes (smaller b / d_{50}) constrained by the value of $V_1 / V_c \leq 1.0$ resulted in Froude numbers that were larger in the model than in the

prototype. Subsequent runs in the river model with a smaller sediment size allowed Froude number similarity in the clear-water scour range in the laboratory.

Table 5.1 Summary of measured experimental data for the Chattahoochee River models

Run	Model	Scale	Q m ³ /s	d_{50} mm	b m	y_1 m	V_1 m/s	T hrs	d_s m
1	FB ¹	1/23	0.196	3.30	0.046	0.166	0.447	24	0.056
2	FB	1/23	0.238	3.30	0.046	0.191	0.504	32	0.081
3	FB	1/23	0.238	3.30	0.046	0.171	0.523	36	0.100
4	FB	1/23	0.273	3.30	0.046	0.191	0.547	36	0.103
5	FB	1/23	0.238	3.30	0.046	0.180	0.554	36	0.121
6	FB	1/23	0.238	3.30	0.046	0.157	0.575	36	0.128
7	FB	1/23	0.289	3.30	0.046	0.191	0.600	36	0.134
8	FB	1/23	0.238	3.30	0.046	0.153	0.626	38	0.134
9	FB	1/23	0.289	3.30	0.046	0.153	0.738	37	0.135
10	FB	1/40	0.030	0.53	0.027	0.107	0.260	28	0.070
11	FB	1/23	0.051	0.53	0.046	0.191	0.257	30	0.093
12	FB	1/23	0.044	0.53	0.046	0.142	0.304	12	0.090
1	RM ²	1/40	0.127	3.30	0.027	0.191	0.546	48	0.062
2	RM	1/40	0.142	3.30	0.027	0.191	0.588	48	0.063
3	RM	1/40	0.069	3.30	0.027	0.109	0.532	48	0.080
4	RM	1/40	0.068	3.30	0.027	0.109	0.546	48	0.088
5	RM	1/40	0.071	1.10	0.027	0.190	0.317	48	0.060
6	RM	1/40	0.038	1.10	0.027	0.107	0.308	47	0.052
7	RM	1/40	0.085	1.10	0.027	0.190	0.348	47	0.059
8	RM	1/40	0.042	1.10	0.027	0.107	0.341	47	0.060
9	RM	1/40	0.047	1.10	0.027	0.107	0.411	47	0.068
1	FD ³	NA	385	0.68	1.067	4.279	2.140	NA	2.003

FB¹=flat-bed model, RM²=river model, FD³=field data from USGS

Table 5.2 Summary of dimensionless experimental data for the Chattahoochee River models

Run	Model	Scale	Fr_1	Fr_b	V_1/V_c	y_1/b	b/d_{50}	d_s/b
1	FB ¹	1/23	0.35	0.67	0.64	3.62	13.95	1.23
2	FB	1/23	0.37	0.75	0.70	4.16	13.95	1.77
3	FB	1/23	0.40	0.78	0.74	3.72	13.95	2.17
4	FB	1/23	0.40	0.81	0.76	4.16	13.95	2.25
5	FB	1/23	0.42	0.82	0.78	3.91	13.95	2.62
6	FB	1/23	0.46	0.86	0.83	3.40	13.95	2.79
7	FB	1/23	0.44	0.89	0.83	4.16	13.95	2.91
8	FB	1/23	0.51	0.93	0.91	3.33	13.95	2.91
9	FB	1/23	0.60	1.10	1.07	3.33	13.95	2.93
10	FB	1/40	0.25	0.51	0.90	3.96	50.92	2.60
11	FB	1/23	0.19	0.38	0.85	4.16	86.84	2.02
12	FB	1/23	0.26	0.45	1.01	3.09	86.84	1.95
1	RM ²	1/40	0.40	1.04	0.76	7.09	8.18	2.32
2	RM	1/40	0.43	1.14	0.82	7.09	8.18	2.33
3	RM	1/40	0.52	1.03	0.82	4.02	8.18	2.96
4	RM	1/40	0.53	1.06	0.84	4.02	8.18	3.28
5	RM	1/40	0.23	0.62	0.71	7.04	24.53	2.23
6	RM	1/40	0.30	0.60	0.75	3.95	24.53	1.92
7	RM	1/40	0.26	0.68	0.78	7.04	24.53	2.19
8	RM	1/40	0.33	0.66	0.83	3.95	24.53	2.23
9	RM	1/40	0.40	0.80	1.00	3.95	24.53	2.51
1	FD ³	NA	0.33	0.66	4.39	4.01	1568	1.88

FB¹=flat-bed model, RM²=river model, FD³=field data from USGS

5.1.1 Temporal Variation of Local Scour Depth

Local scour depth at the nose of the bridge pier in the Chattahoochee River model was recorded with the ADV at selected time intervals throughout the experiments. These measurements were taken at a location determined by maintaining a minimum clearance between the ADV and the pier itself, so they may not correspond to the maximum scour

depth. The maximum scour depth was measured with the ADV and a point gage after scour depth was determined to reach an equilibrium state in which the bed elevation showed no change other than a fluctuation about a mean level over a period of at least 3 hours at the end each experiment.

One example for the temporal development of the scour depth at the nose of the pier is shown in Figure 5.1. The initial scouring began in the vicinity of the pier and then the two conical scour holes merged at the center of the nose of the pier. This process dominated by the flow occurred within only 9 sec. After merging, the horseshoe vortex became the main agent to carry away the sediment from in front of the pier. The scour depth became deeper with the time and after reaching the equilibrium state, the rate of scouring became too small to be measured during at least 3 hours.

Selected temporal variations of local scour depth for each experiment in the Chattahoochee River model are shown in Figure 5.2 and Figure 5.3. Temporal changes of bed elevation for flat-bed experiments are represented in terms of real time on a semi-logarithmic scale in Figure 5.2. All scour depths observed in the flat bed and river model experiments rapidly changed at the initial stage and the rate of scouring became smaller with time. Finally, the scour depth reached the equilibrium state. The slope of the curve is dependent on the combination of the effect of flow depth, y_1/b , flow intensity, V_1/V_c , and relative sediment size, b/d_{50} . The variation of the slopes in Figure 5.3, for example, is much smaller than in Figure 5.2 because of the effects of flow intensity and sediment size. Detailed analysis of temporal development will be explained in Chapter 6.

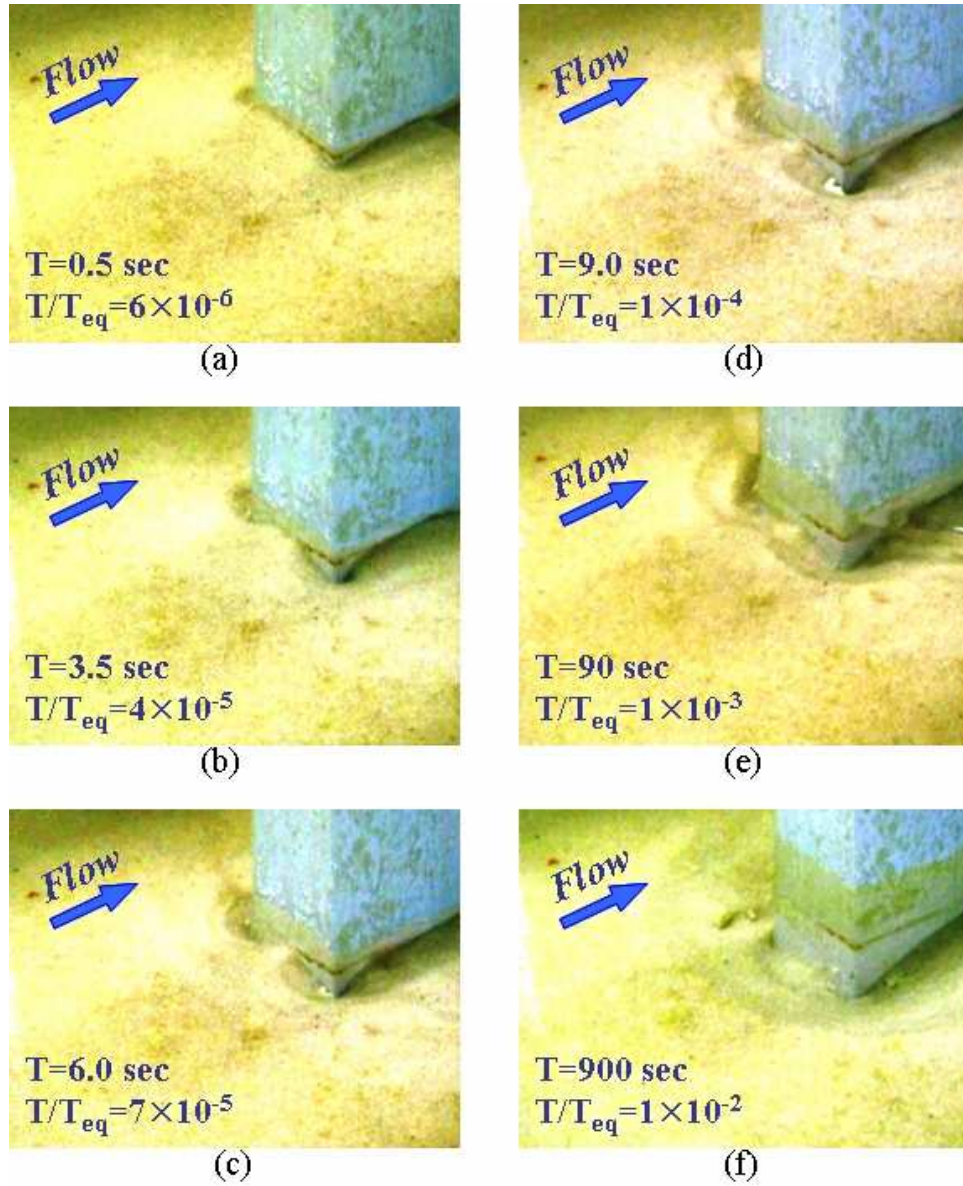


Figure 5.1 Temporal variation of scour depth at nose of the first pier in flat bed experimental run FB11 on Chattahoochee River model (Scale= 1:23, T_{eq} =25hours, $V_1/V_c = 0.85$, $y_1/b = 4.16$, $b/d_{50} = 86.84$)

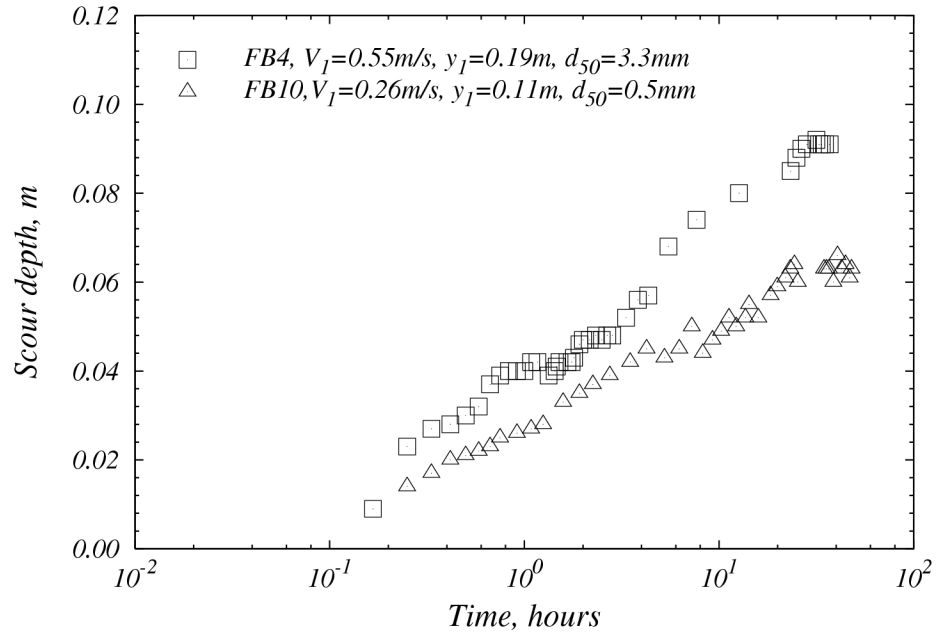


Figure 5.2 Temporal development of scour depth for flat bed experiments in the Chattahoochee River models

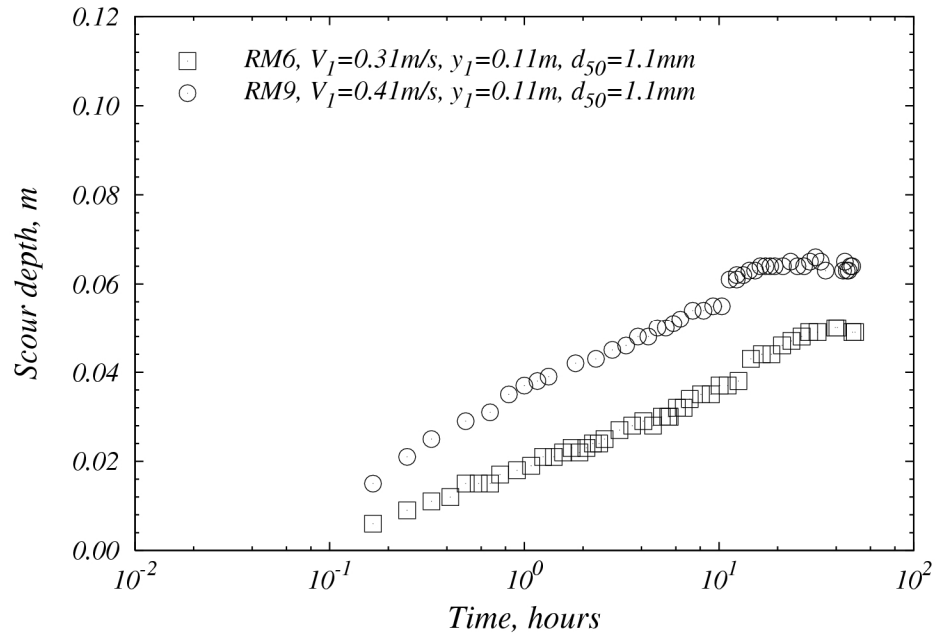


Figure 5.3 Temporal development of scour depth for river model experiments in the Chattahoochee River models

5.1.2 Measurement of Maximum Scour Depth and Scour Contour

In most of the flat-bed experiments for the Chattahoochee River model, the maximum scour depth occurred at the nose of the first pier of the bridge pier bent as shown in Figure 5.4 in which scour depth and X and Y coordinates are presented as dimensionless variables nondimensionalized by the pier width b .

However, it was found that there were also significant scour depths around the second and third pier of the pier bent in the downstream direction. From the scour depth contours for the flat bed experiments, the scour depth profile along the pier bent centerline was extracted as shown in Figure 5.4. In this figure, the location of the deepest scour depth for the flat-bed model experiments can be observed relative to the bottom of the pier footings. Scour depth contours for the river model experiments did not show a symmetrical pattern relative to the pier bent centerline because of river bathymetry, angle of attack and alignment of the bridge pier bent in the main channel. As shown in Figure 5.4, a small deposition region was located between the two inner piers underneath the web connecting them. The region of primary deposition started immediately downstream of the fourth pier.

Scour depth contours and the scour depth profile along the pier bent centerline are shown in Figure 5.5 for the Chattahoochee River model (RM2) for the 100-year flood discharge. The maximum scour depth occurred at the nose of the third pier, not the first pier, and the footing of the third pier was completely exposed. Some scouring occurred under that footing.

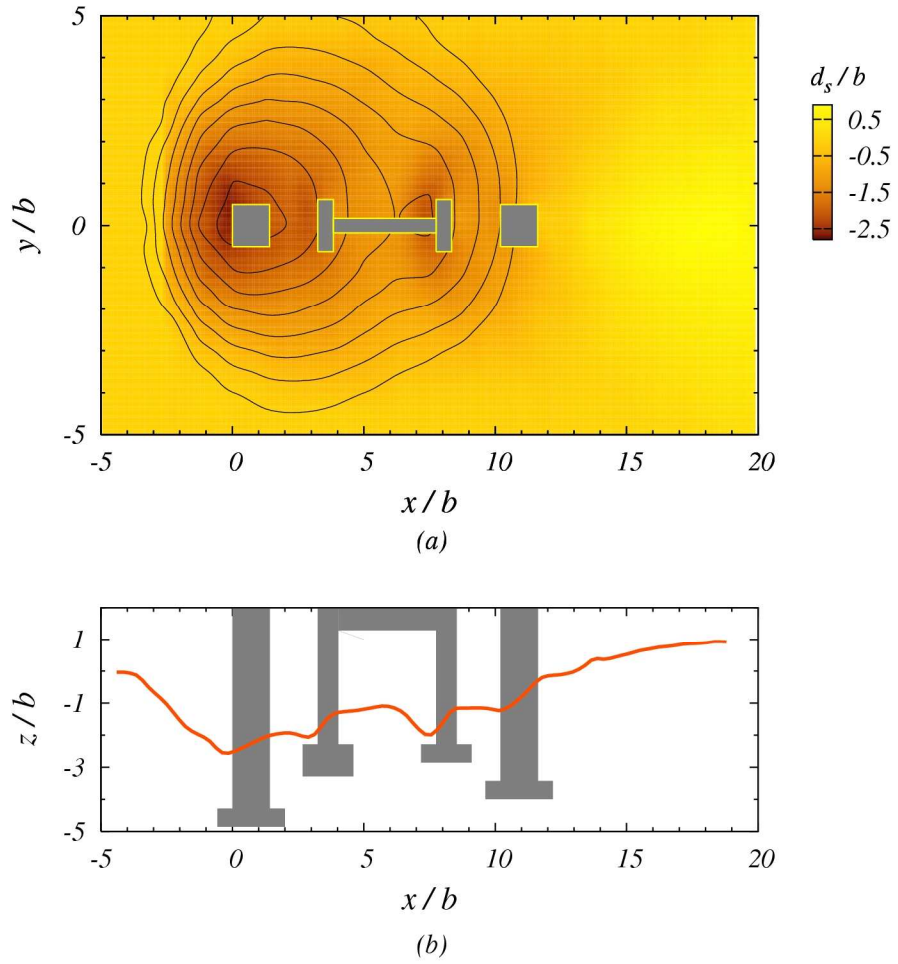


Figure 5.4 Scour depth contours for experimental run FB5 in Chattahoochee model (a) plan view and (b) scour depth profile at $y/b = 0$

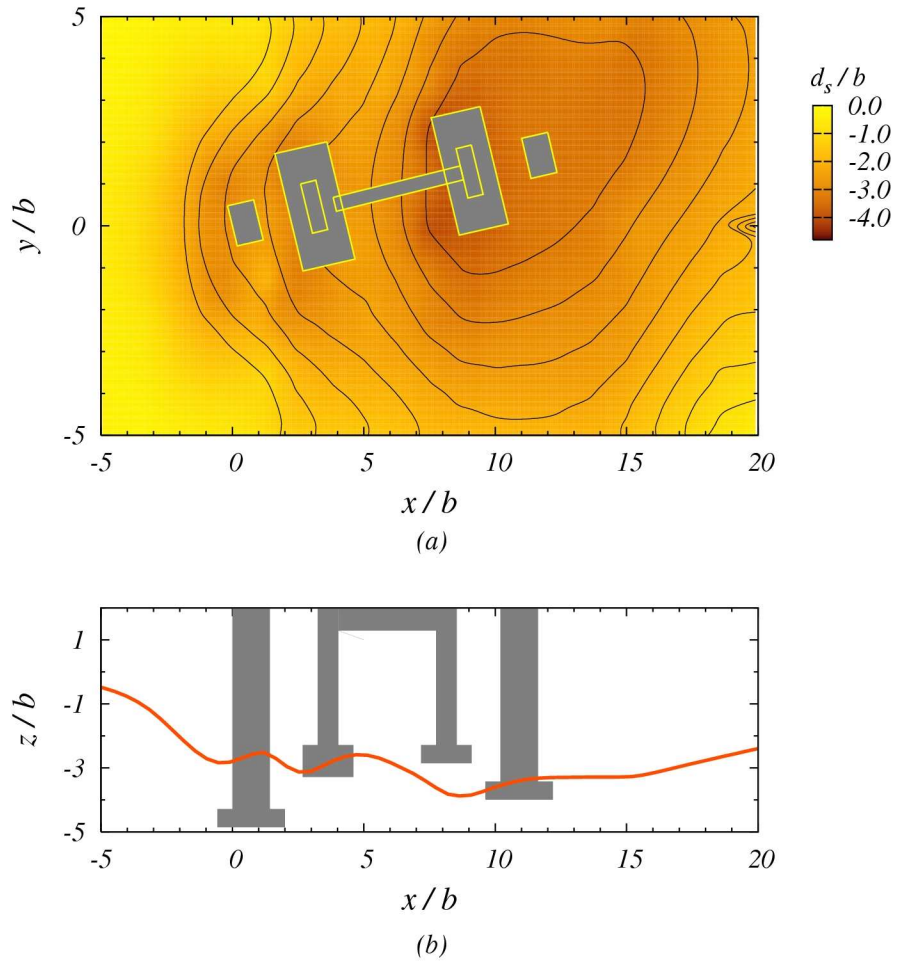


Figure 5.5 Scour depth contours and scour depth profile for experimental run RM2 in the Chattahoochee River model (a) plan view and (b) scour depth profile along the centerline of bridge bent

5.1.3 Measurement of Water Surface Profiles

Water surface profiles were measured in the flat-bed and river model experiments along the centerline of the bridge pier bent which was located in the main channel and was subject to the maximum pier scour. Figure 5.6 shows the water surface profile for experimental run FB1 in the Chattahoochee River model. The inset of Figure 5.6 is

zoomed in on the bridge pier bent where obvious surface rollup was observed at the nose of the most upstream pier. Overall, the water surface profile was an H1 curve excluding the region of the bridge pier bent. The height of rollup and the effect on scour depth will be discussed in detail in Chapter 6.

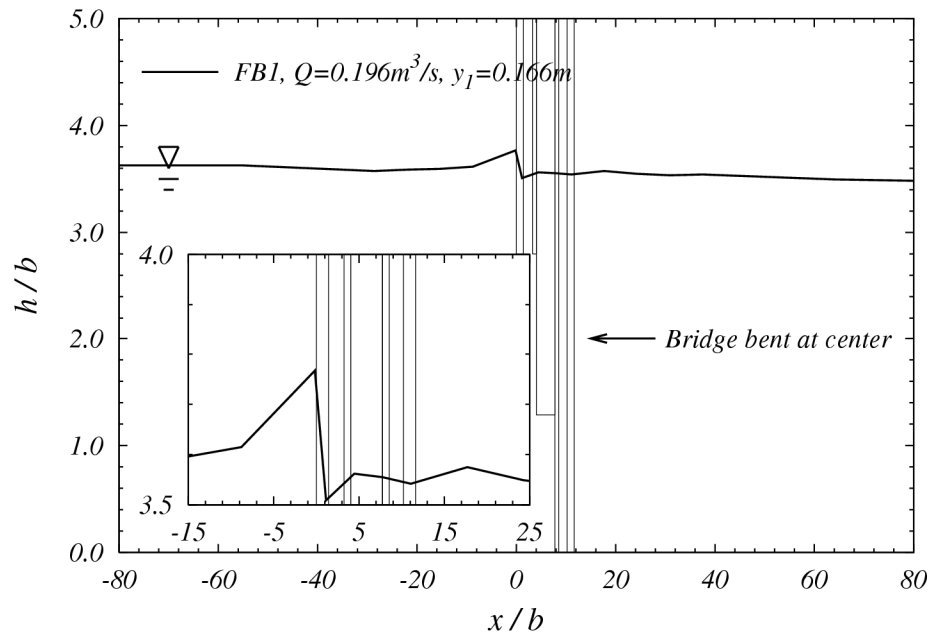


Figure 5.6 Water surface profile along the centerline of bridge pier bent in flat bed model experiment FB1 in the Chattahoochee River model.

5.1.4 Measurement of Velocity Field

The velocity field around the main bridge pier bent for the Chattahoochee River model was measured for the bank-full flow condition in both the flat-bed model and the river model after scour. The near-field velocity vectors were measured at a height above the fixed bed of 20 percent of the approach flow depth under the bank-full flow condition in

Figure 5.7 for a fixed bed. Higher velocities were measured on both sides of the first pier where deeper scour occurred as the flow curved around the pier bent. In the wake zone, the mean velocities became smaller than those in the outer region; however the turbulent intensities of the wake region were higher. The velocity defect in this region gradually recovered in the downstream direction. The magnitude of mean velocities upstream of the first pier along the centerline became smaller approaching the pier stagnation line due to the existence of the pier. Figure 5.8 shows the combination of scour depth contours and the near-field velocities measured at 20 percent of the approach flow depth for the flat-bed model under the same flow condition but at the completion of scour. The near-field velocity distribution for the flat-bed experiments was very close to being symmetric with respect to the centerline of the bridge pier bent as shown in both Figure 5.7 and Figure 5.8. The characteristic decrease in magnitude was observed in near field velocity around the pier bents when comparing results before and after scour. The maximum relative difference in magnitude was approximately 40 percent in the vicinity of the first pier on the right-hand side. However, as shown in Figure 5.9 which also shows superimposed scour contours, it appears that there is asymmetry of the scour contours for the river model experiment under the bank-full condition because of river bathymetry and skewed alignment of the bridge pier bents. Nevertheless, the deepest scour depth occurred at the nose of the most upstream pier in both the flat-bed model and the river model. In addition, the effect of the angle of attack of the approach flow contributes to the asymmetry of the velocity field. The value of the angle of attack was about 4.3° for the river model but only 1.8° in the case of flat-bed experiments on the Chattahoochee River bridge.

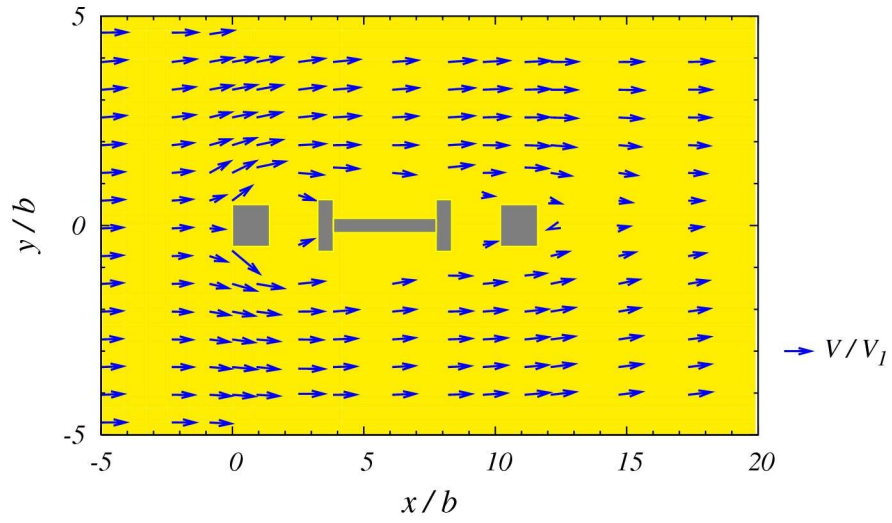


Figure 5.7 Mean velocity vectors for before scour at 20 percent of the approach depth for experimental run FB7 in Chattahoochee River model

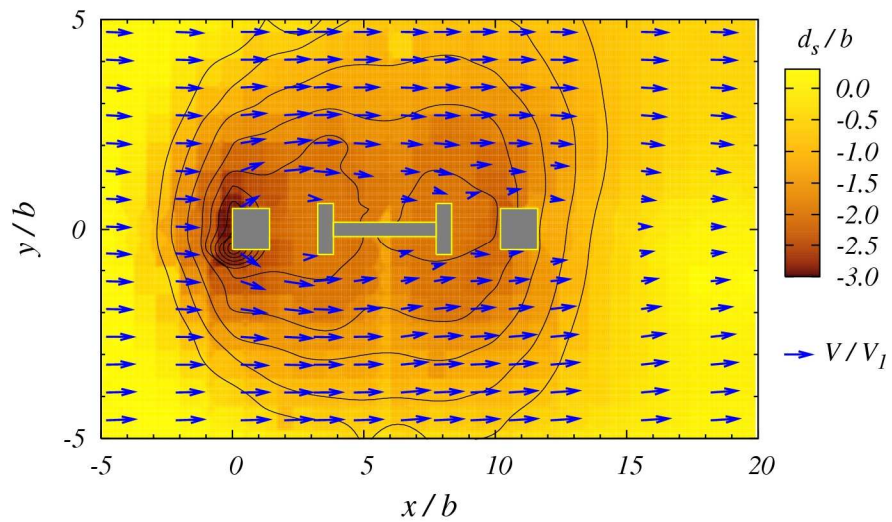


Figure 5.8 Mean velocity vectors and scour contour for after scour at 20 percent of the approach depth for experimental run FB7 in Chattahoochee River model

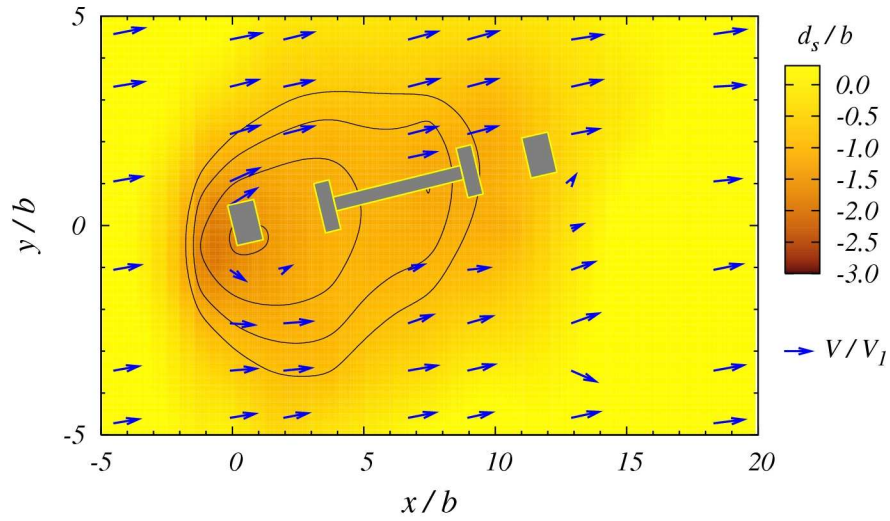


Figure 5.9 Mean velocity vectors after scour at 40 percent of the approach depth for experimental run RM6 in the Chattahoochee River model

In addition to the velocity measurements, the longitudinal and vertical turbulence intensity and turbulent kinetic energy were measured with the ADV with the bed fixed at the initial elevation before scour for experimental run FB7 in the Chattahoochee River model. Locations of fourteen points observed for investigation of turbulence characteristics in the Chattahoochee River flat-bed experiments are shown in Figure 5.10. The distance from the centerline to the measured points is approximately $\pm 2b$ on the left and right sides (looking downstream) of the bridge pier bent.

Turbulence intensity profiles in the longitudinal and vertical direction are shown in Figure 5.11 and Figure 5.12, respectively, nondimensionalized by the mean approach velocity, V_1 . The numbers shown at the top of each subfigure correspond to the location number in Figure 5.10.

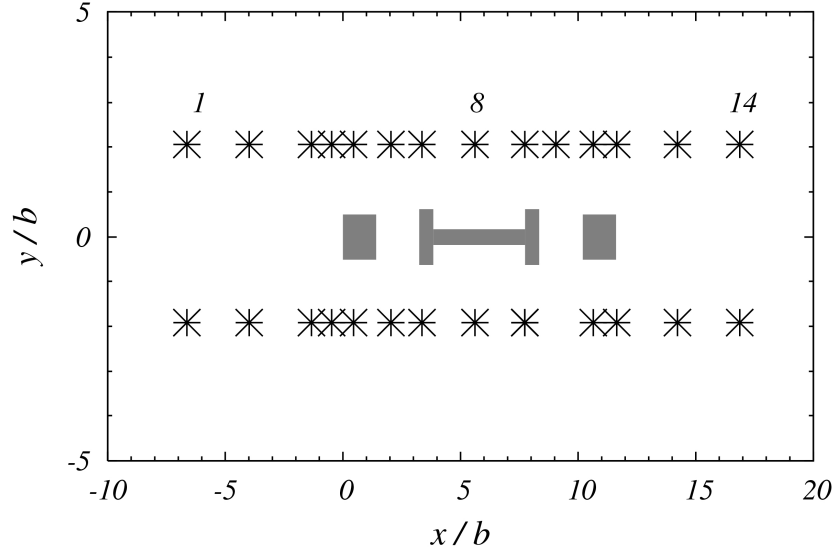


Figure 5.10 Plan view of central bridge pier bent and locations of detailed turbulence measurements for the Chattahoochee River model

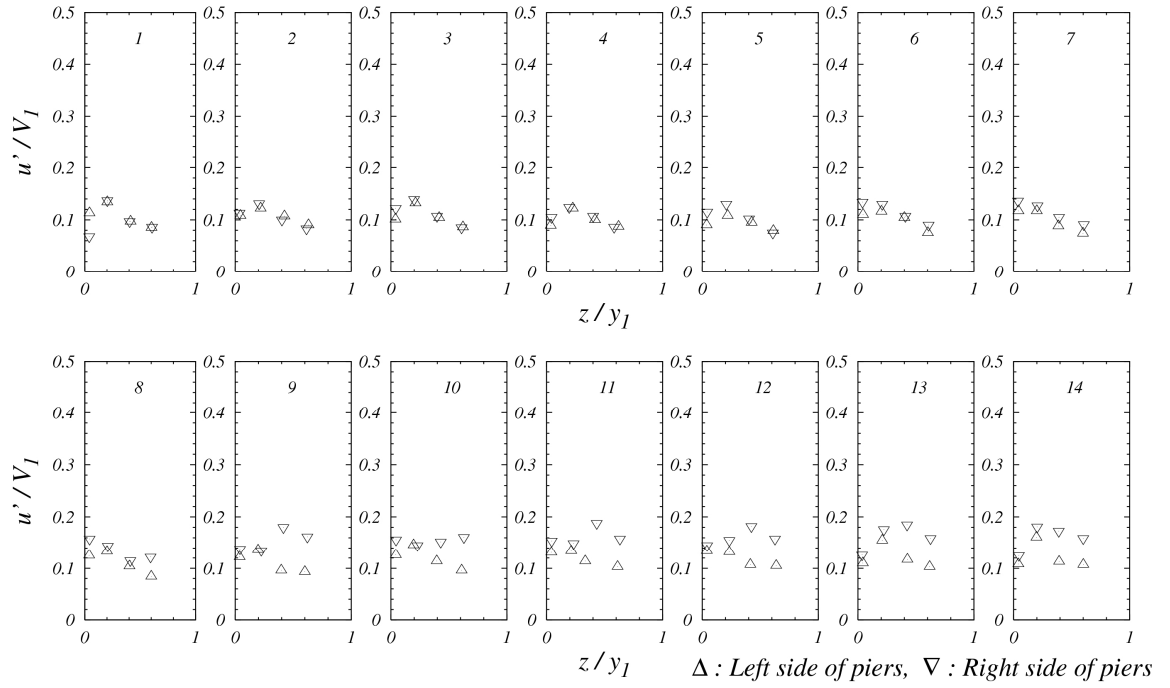


Figure 5.11 Longitudinal turbulence intensity around bridge pier for experimental run FB7 in the Chattahoochee River model

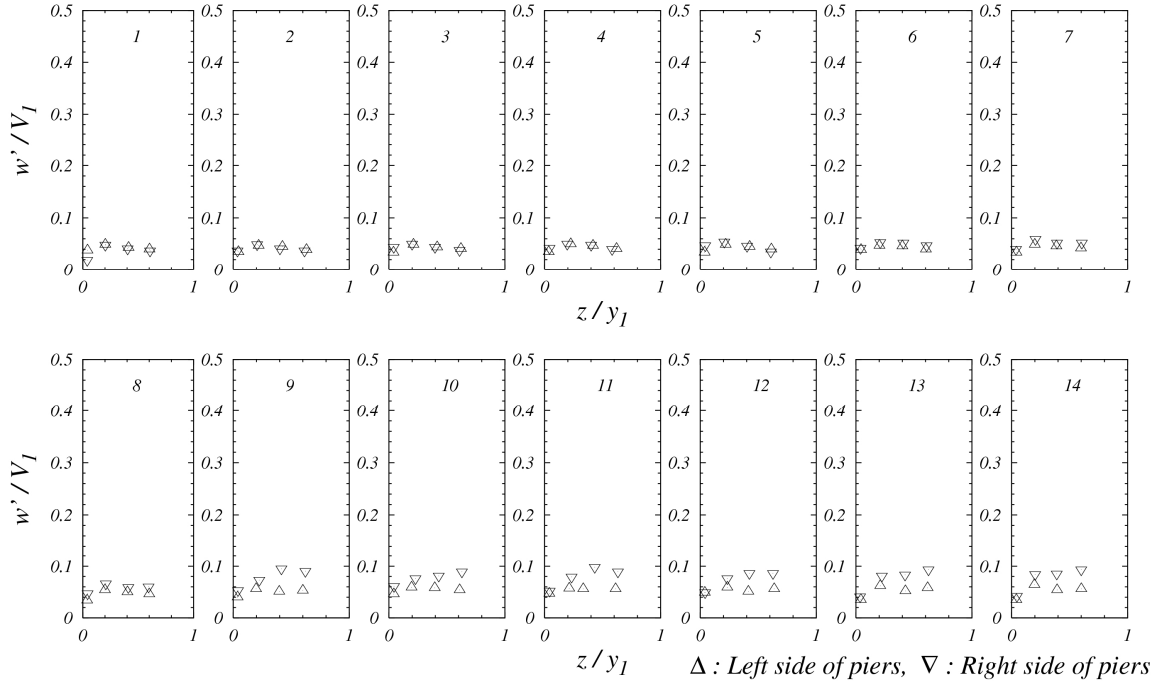


Figure 5.12 Vertical turbulence intensity around bridge piers for experimental run FB7 in the Chattahoochee River model

Turbulence intensity in both the streamwise and the vertical directions exhibits a high degree of symmetry from location 1 to 7. From location 8, profiles show the asymmetry of the turbulence intensity because of the effect of the angle of attack of the approach velocity with respect to the pier bent centerline to be discussed subsequently. Measured horizontal turbulence intensities are about 10 ~ 20 percent of the mean approach velocity while vertical turbulence intensities are 5~10 percent of mean approach velocity. However, the magnitude of the turbulence intensities in both directions increases slightly further downstream.

Total turbulent kinetic energy profiles were nondimensionalized by the approach shear velocity, u_{*1} as shown in Figure 5.13. The profile of the total turbulent kinetic energy at location 1 is nearly identical on the left and right sides of the pier bent except at

points nearest the bed. However, the turbulent kinetic energy on the right side of the bridge pier bent becomes higher than on the left side further downstream due to the misalignment of the approach flow. Higher turbulent kinetic energy was measured in the wake region.

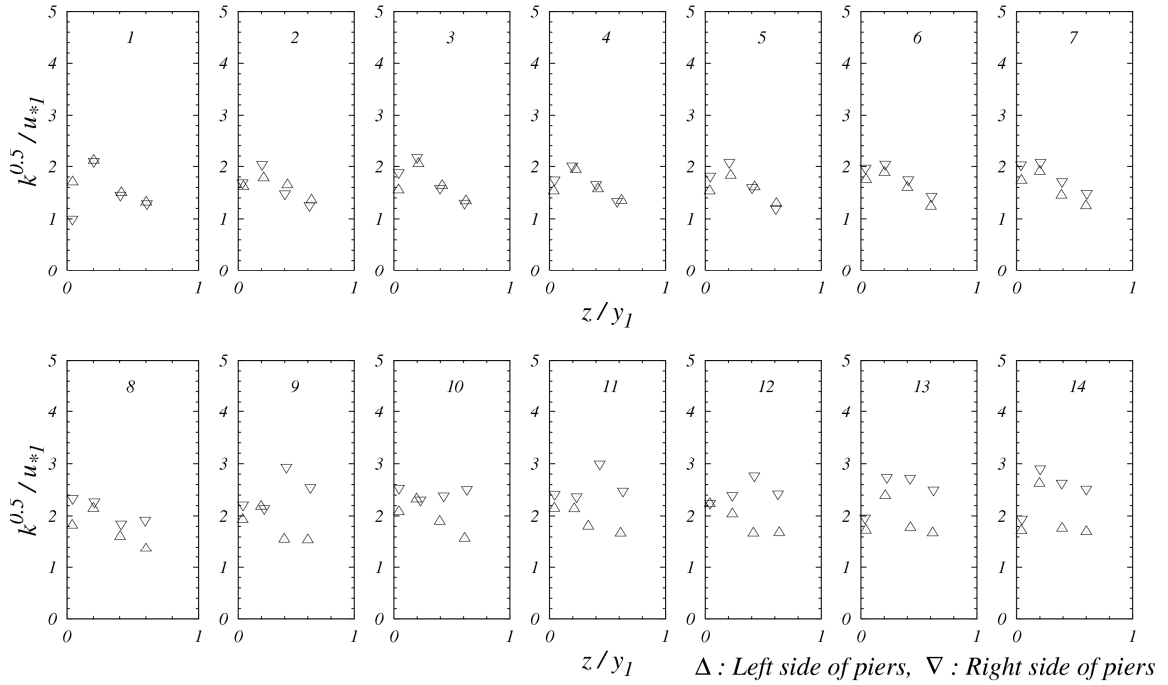


Figure 5.13 Turbulent kinetic energy profiles along the bridge piers for experimental run FB7 in the Chattahoochee River models

The resultant direction of the approach flow was examined to investigate skewness relative to the pier bent as a possible explanation for the observed asymmetry of turbulence characteristics. The skewness of the resultant approach velocity relative to the centerline of the pier bent had a measured value of 1.8° just upstream of the pier. Although the pier bent was set as close to parallel to the oncoming flow as possible in the flat-bed model, this small discrepancy was enough to affect the turbulence characteristics.

The scour, however, was not as sensitive to this degree of skewness as shown previously in Figure 5.6. The angle of attack in the river model experiments, on the other hand, was determined to be 4.3° as a result of the chosen design orientation of the bridge to the river approach flow. This degree of skewness had a much larger effect on the scour contours as shown in Figure 5.9.

5.1.5 Comparison with Field Data

Historical cross sections for the Chattahoochee River bridge near Cornelia were collected by the USGS. The bed cross section for bank-full flow conditions that occurred in July 2003 for a peak discharge of $385 \text{ m}^3/\text{s}$ is compared with laboratory data as shown in Figure 5.14. Laboratory coordinates for the cross section stations were matched to field coordinates measured by GPS with consideration of the width of the bridge deck in the field. The maximum scour depth occurred at the nose of the upstream pier in both field and laboratory with a 2 percent relative error between the two measurements. It is also of interest to note that a flood of similar magnitude ($371 \text{ m}^3/\text{s}$) occurred in December of 1961 and the maximum scour depth is remarkably similar to the 2003 value with a difference of 0.06%. There is some discrepancy between laboratory and field cross sections in the deposition region between the pier bents because the experiment was conducted under clear water scour conditions while live bed scour conditions occurred in the field.

Flow velocities in the field were measured with an acoustic Doppler velocity meter mounted at the side of the upstream pier and pointed in the cross-stream direction. There were three data points or data bins at different distances from the side wall of the

bridge pier located in the main channel. The velocities measured in the field during the 2003 flood are compared with the laboratory data in Figure 5.26, and they show good agreement.

The laboratory and field comparisons given in Figure 5.14 and Figure 5.15 are based on experimental run RM6 in the laboratory. The close agreement between field and laboratory measurements appears to validate the modeling strategy discussed in Chapter 4 in which Froude number similarity and geometric similarity (y_1/b) are maintained while choosing a sediment size in the laboratory that produces a value of $V_1/V_c < 1.0$ and b/d_{50} of the order of 25. As shown in Chapter 6, scour depth decreases with increasing values of b/d_{50} beyond 25. Values of b/d_{50} are quite large in the prototype and so they cannot be reproduced in the laboratory without sediment sizes becoming so small that particle cohesive forces, which do not exist in prototype sand-bed streams, are introduced. In other words, live-bed scour depths in the prototype can be matched using clear-water scour in the laboratory by compensating for an observed decrease in scour depth due to large prototype values of b/d_{50} with a corresponding decrease in V_1/V_c to a value less than 1.0 at which maximum scour depth occurs.

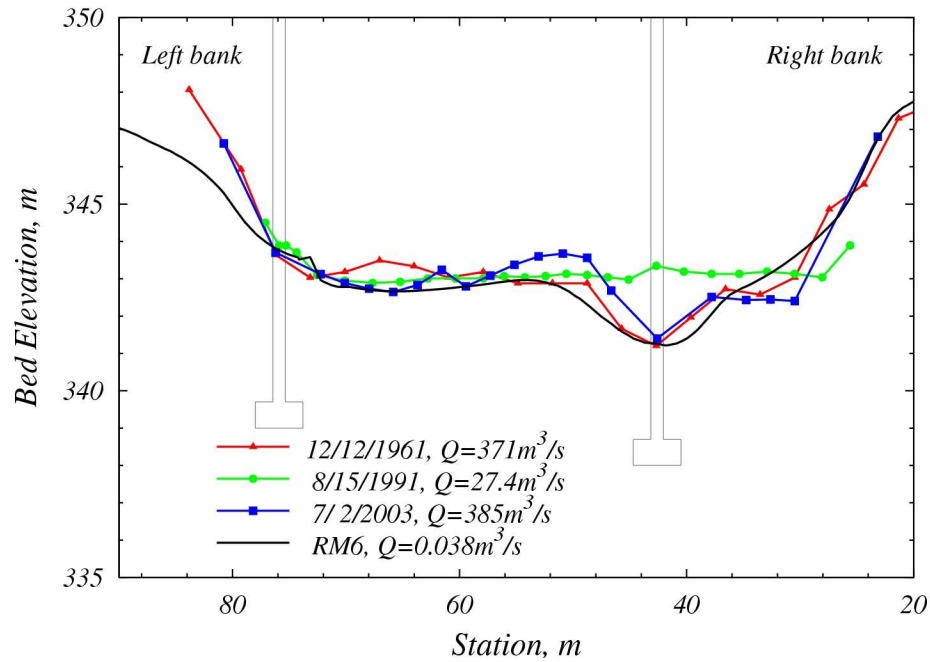


Figure 5.14 Comparison of cross sections at the upstream side of the bridge in Chattahoochee River near Cornelia

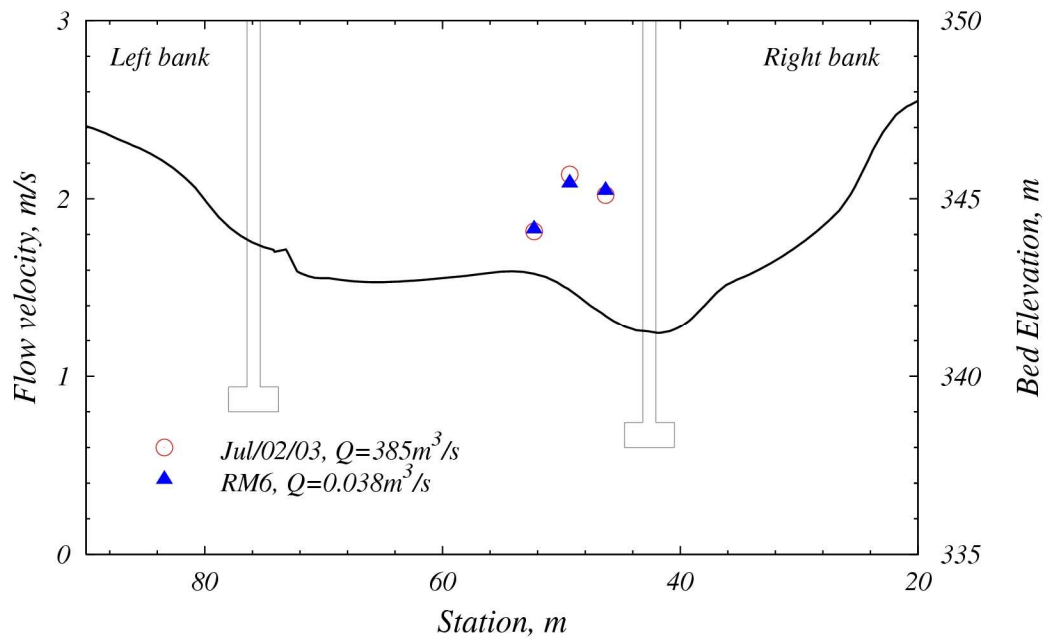


Figure 5.15 Comparison of velocity on left side of the bridge pier bent in main channel of Chattahoochee River from experimental run RM6 for bank-full flow at $385 \text{ m}^3/\text{s}$ (July 2, 2003 measured by USGS).

5.2 The Flint River Model

The tops of the footings of both piers in the Flint River as shown in Chapter 3 are already exposed at the beginning of scour; that is, the elevation of the top of the upper footing is about the same as the bed elevation near the footing. Typically, the effect of an exposed footing is to reduce the rate of local scour due to interception of the downflow feeding the horseshoe vortex upstream of the pier (Coleman 2005; Jones et al. 1992; Melville and Raudkivi 1996); however, the width of the upstream pier column was used as the characteristic length scale for consistency with other river modeling results in this study. Whether the effect of the footing was significant or not will be explored in Chapter 6. A summary of the measured experimental data for the Flint River modeling is presented in Table 5.3, and the data are given in dimensionless form in Table 5.4 with the same parameters mentioned in the previous section.

The maximum scour depths recorded in Table 5.3 were observed in front of the upstream pier in the main channel even though the deepest scour depth occurred further downstream which will be discussed in detail in Chapter 6. Laboratory experiments were conducted with three different geometric scales and three sediment sizes for physical modeling of the Flint River bridge foundation scour.

Initially, in the flat bed experiments the value of y_1/b was matched with the value for the bank-full condition or the 1994 flood (tropical storm Alberto). In order to generate a wide range in values of b/d_{50} , the Froude number was not controlled while the flow intensity varied from 0.7 to 1.0. In river model experiments, however, Froude number similarity was adopted under the clear water scour condition in the laboratory.

Table 5.3 Summary of experimental data for the Flint River models

Run	Model	Scale	Q m ³ /s	d_{50} mm	b m	y_1 m	V_1 m/s	T hrs	d_s m
1	FB ¹	1/50	0.219	3.30	0.037	0.160	0.486	48	0.038
2	FB	1/50	0.218	3.30	0.037	0.152	0.520	48	0.050
3	FB	1/50	0.251	3.30	0.037	0.158	0.537	48	0.053
4	FB	1/50	0.283	3.30	0.037	0.165	0.559	48	0.084
5	FB	1/90	0.026	0.53	0.021	0.128	0.189	143	0.032
6	FB	1/90	0.033	0.53	0.021	0.128	0.237	24	0.041
7	FB	1/50	0.042	0.53	0.037	0.149	0.263	28	0.072
8	FB	1/50	0.079	0.53	0.037	0.226	0.342	12	0.066
9	FB	1/33	0.054	0.53	0.055	0.241	0.215	48	0.046
10	FB	1/33	0.052	0.53	0.055	0.170	0.281	24	0.085
1	RM ²	1/90	0.042	1.10	0.021	0.152	0.247	48	0.022
2	RM	1/90	0.047	1.10	0.021	0.152	0.290	96	0.037
3	RM	1/90	0.051	1.10	0.021	0.152	0.335	96	0.058
1	FD ³	NA	3030	0.38	1.829	11.28	2.306	NA	2.908

FB¹=flat-bed model, RM²=river model, FD³=field data from USGS

Table 5.4 Summary of dimensionless experimental data for the Flint River models

Run	Model	Scale	Fr_1	Fr_b	V_1/V_c	y_1/b	b/d_{50}	d_s/b
1	FB ¹	1/50	0.39	0.81	0.70	4.38	11.1	1.03
2	FB	1/50	0.43	0.87	0.75	4.17	11.1	1.37
3	FB	1/50	0.43	0.90	0.77	4.33	11.1	1.46
4	FB	1/50	0.44	0.93	0.88	4.50	11.1	2.29
5	FB	1/90	0.17	0.42	0.64	6.18	39.1	1.54
6	FB	1/90	0.21	0.53	0.80	6.18	39.1	1.96
7	FB	1/50	0.22	0.44	0.87	4.08	69.0	1.98
8	FB	1/50	0.23	0.57	1.07	6.18	69.0	1.81
9	FB	1/33	0.14	0.29	0.67	4.35	105	0.83
10	FB	1/33	0.22	0.38	0.91	3.07	105	1.53
1	RM ²	1/90	0.20	0.55	0.57	7.35	18.8	1.04
2	RM	1/90	0.24	0.64	0.67	7.35	18.8	1.77
3	RM	1/90	0.27	0.74	0.78	7.35	18.8	2.79
1	FD ³	NA	0.22	0.54	5.27	6.17	4813	1.59

FB¹=flat-bed model, RM²=river model, FD³=field data from USGS

5.2.1 Temporal Variation of Local Scour Depth

Figure 5.16 presents the temporal variation of bed elevation measured by the USGS on the main pier bent of the Flint River bridge at Bainbridge from March 25, 2005 to April 2, 2005 when the discharge increased from approximately 300 to 1800 m³/s . It can be observed in the figure that the bed elevation on the left side of the bridge pier started to decrease first and was rather gradually followed by a more rapid drop in bed elevation at both the nose of the pier and on the left side of the pier.

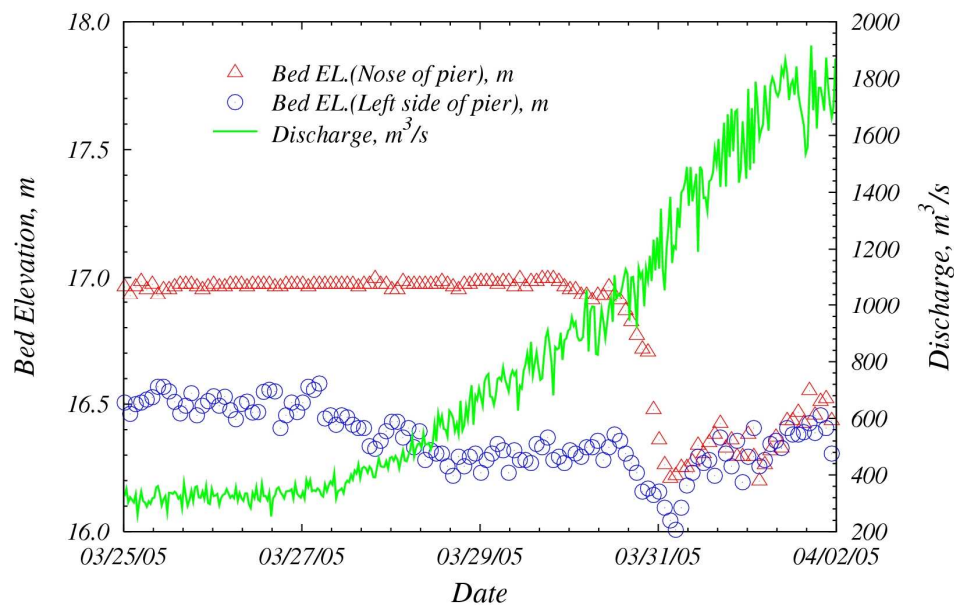


Figure 5.16 Temporal variation of the bed elevations around the pier bent according to the discharge in Flint River from March 25, 2005 to April 2, 2005 by USGS

Similar observations were made in model experiments on the Flint River pier bent as shown in Figure 5.17. The development of local scour depth with time in the laboratory experiment was recorded at the nose of the bridge pier. In the early stages as

shown in Figure 5.17, two conical scour holes developed at both edges of the footing and moved upstream until they converged at the nose of the footing. After convergence, scour depth increased more rapidly as shown in experimental run FB2 in Figure 5.18. In the other two experiments shown in Figure 5.18, the retardation of the developing scour depth was observed to occur in a comparably shorter time period due to the approach flow velocity and sediment size. The subsequent slopes of the scour development with time at the nose of the footing as shown in Figure 5.17 depended on the approach flow velocity and sediment size and will be discussed in more detail in Chapter 6.

It is interesting to note that a secondary peak of scour depth was observed in run FB8 for which $V_1/V_c = 1.07$ and scour conditions were live-bed in Figure 5.18. When the scour depth reached the first maximum value, it decreased for some time period as bed materials from upstream moved into the scour hole and refilled it for a while. Scouring then continued with time without continuous movement of bed forms through the scour hole. A remarkable feature in the temporal variation of the scour depth around the footing of the Flint River bridge is that a mild slope was observed in the middle of the scour process for some experiments due to the existence of the step footing (see Figure 5.17). After the scour hole reached the nose of the footing, the scour depth increased at a constant rate of change until the bed elevation reached the elevation of the second footing. Then development of the scour depth slowed as shown in flat-bed experimental run FB8 in Figure 5.18 and river model experimental run RM3 in Figure 5.19 as the flow structure and strength of the horseshoe vortex changed due to the new geometry. Afterward, scour began increasing at a higher rate followed by the asymptotic approach to the equilibrium state.

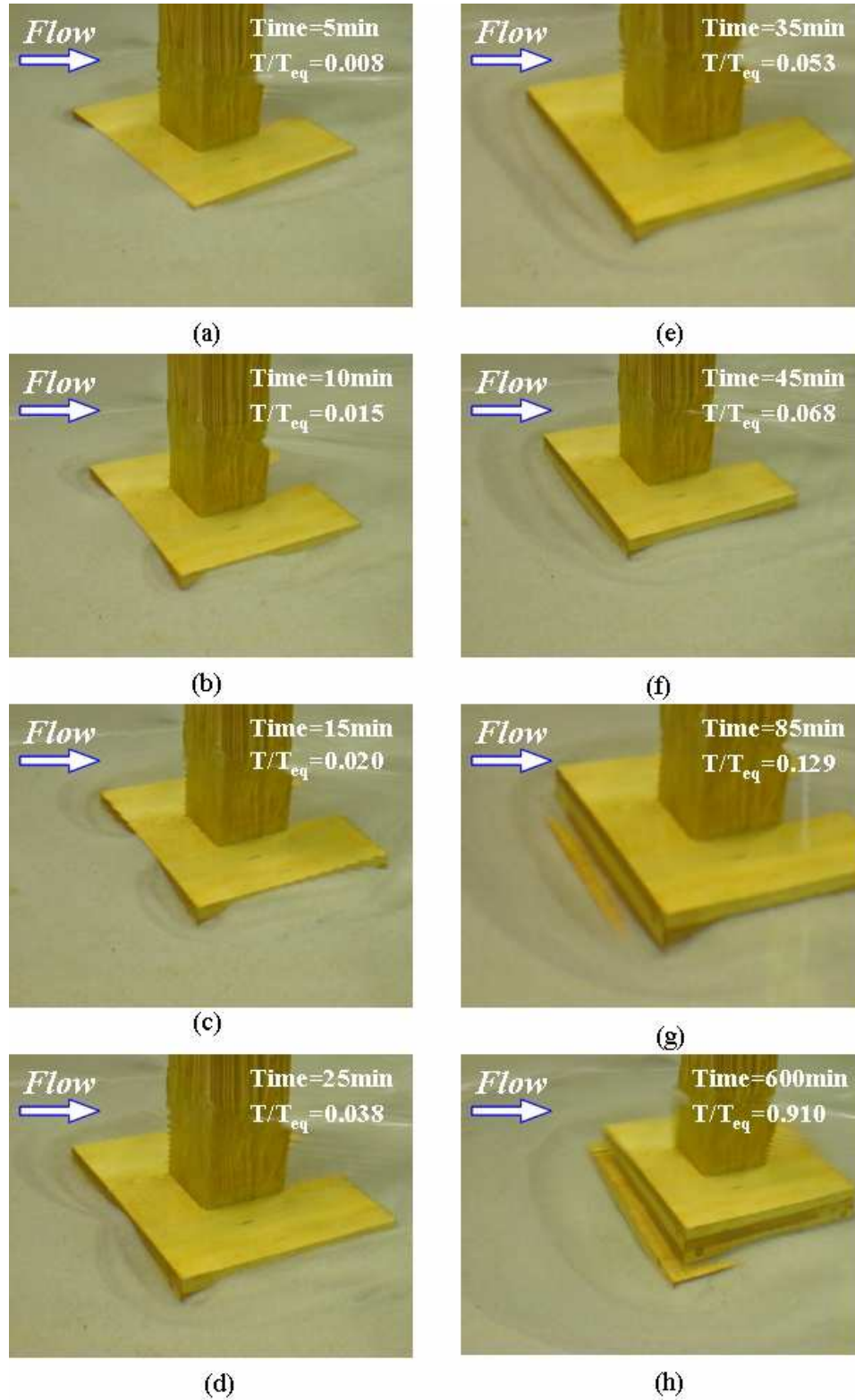


Figure 5.17 Temporal variation of scour hole in the initial process in experimental run FB10 on Flint River model (Scale= 1/33, T_{eq} =11 hours, $V_1/V_c = 0.93$, $y_1/b = 3.09$, $b/d_{50} = 105$)

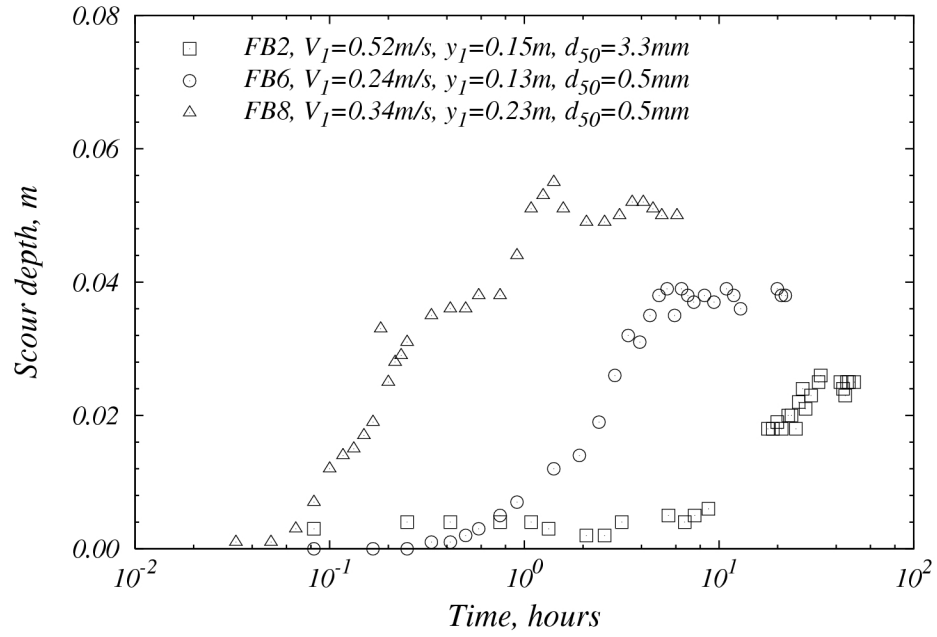


Figure 5.18 Temporal development of scour depth for flat-bed experiments in the Flint River model

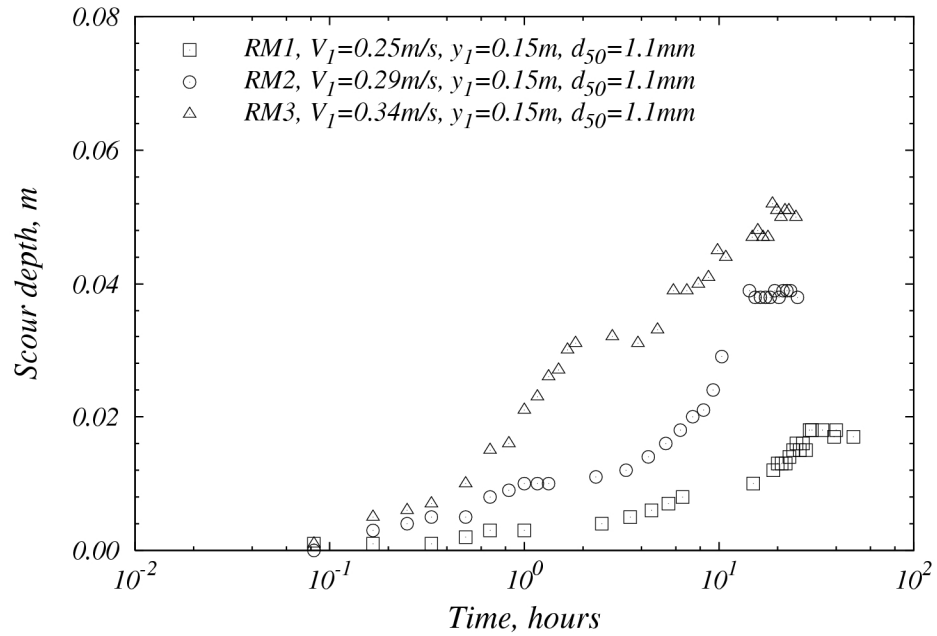


Figure 5.19 Temporal development of scour depth for river model experiments in the Flint River model.

5.2.2 Measurement of Maximum Scour Depth and Scour Contour

The scour contours are very symmetrical for the flat-bed experiment as shown in Figure 5.20 for experimental run FB1 in the Flint River model. The maximum scour depth occurred upstream of the first pier (most upstream pier). The second step of the footing of the first pier was also exposed but the scour depth did not reach under that footing. For the second pier (downstream pier), the top of the upper footing was also exposed at equilibrium scour depth; however, significant scour did not occur around the second pier for the given experimental flow conditions. Deposition of sediments was observed along the centerline of the bridge pier bent downstream of the bridge.

For river model experiments on the Flint River bridge, the region of deposition was changed due to river bathymetry and a different angle of attack according to hydraulic conditions. The location of maximum scour depth varied with the change in approach flow velocity, depth and sediment size. Details will be presented in Chapter 6.

Scour contour and scour depth profile for the river model in the Flint River model are shown in Figure 5.21. Due to the combination of the angle of attack and river bathymetry, this experimental, RM1, run does not show the symmetric scour hole as well as deposition of sediment downstream. The deposition area occurred to the right and rather far downstream of the bridge piers (approximately, $x/b \approx 22$ which is not comparable with run FB7 presented previously) since the angle of attack, which was measured to be 6.4° , and the river bathymetry induced the small wake hole to the right of the downstream side of the bridge pier ($x/b \approx 13$).

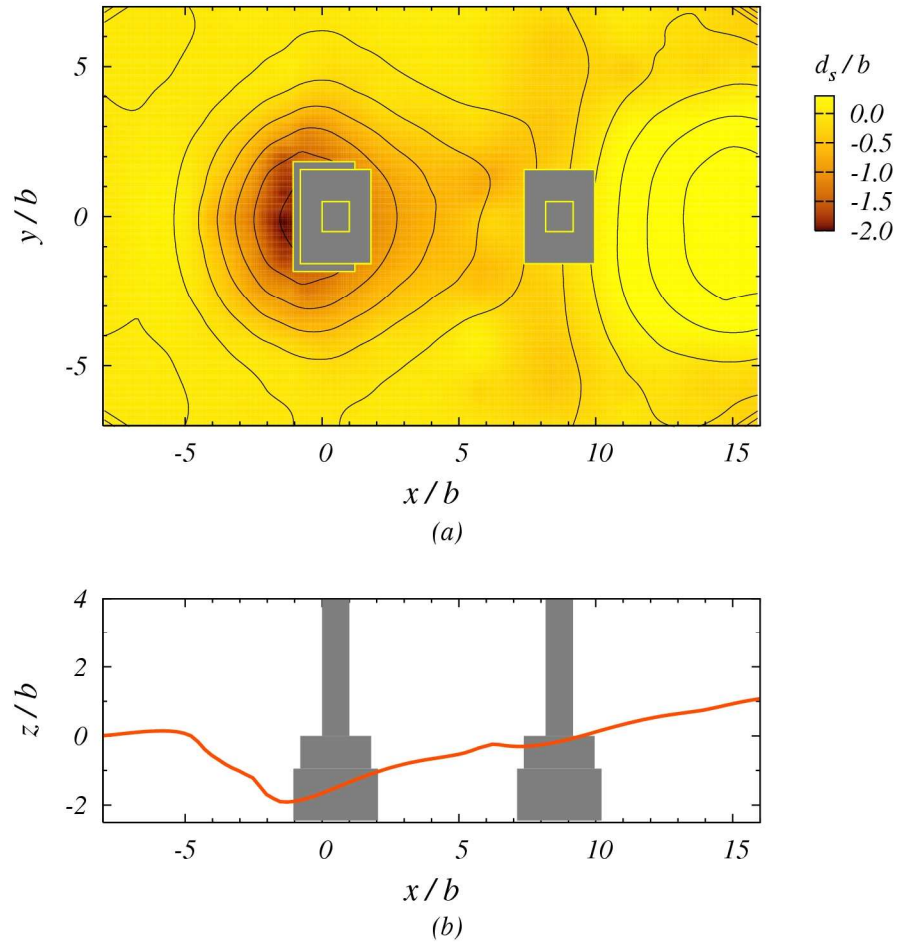


Figure 5.20 Scour contour and scour depth profile for experimental run FB7 in the Flint River model (a) plan view and (b) scour depth profile at $y/b = 0$

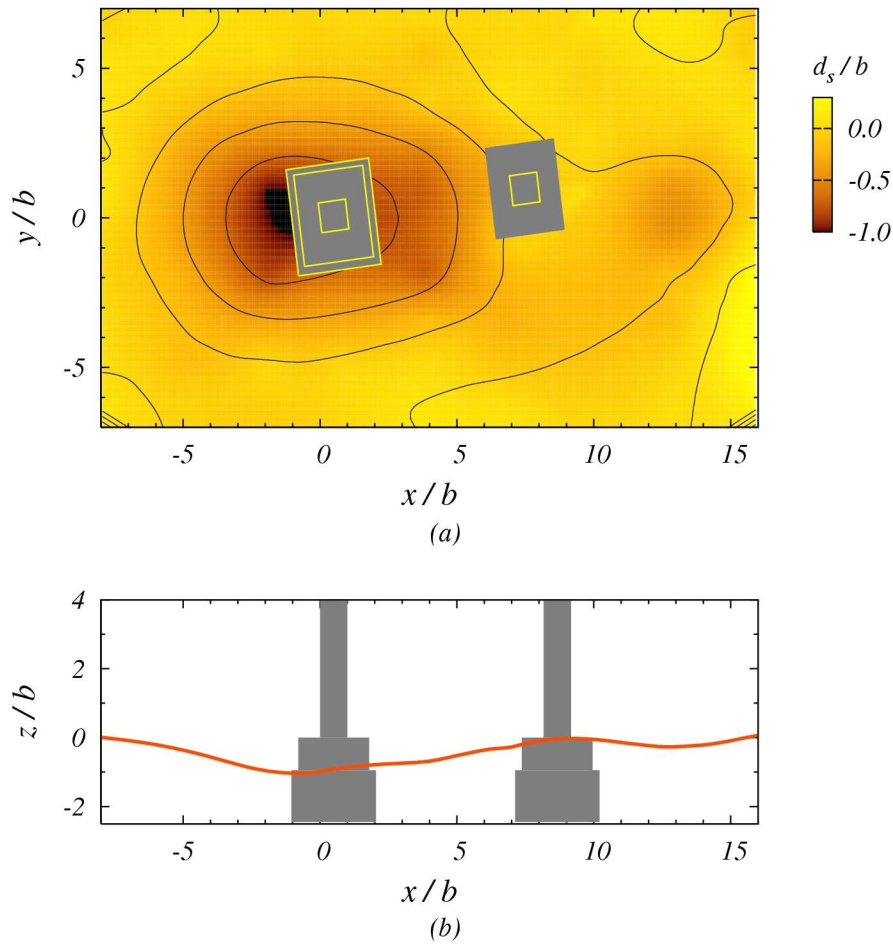


Figure 5.21 Scour contour and scour depth profile for experimental run RM1 in the Flint River model (a) plan view and (b) scour depth profile along the centerline of bridge bent

5.2.3 Measurement of Water Surface Profile

Figure 5.22 shows one measurement of the water surface profile in the Flint River model. The zoomed figure around the bridge pier bent inside of Figure 5.22 shows that a significant surface roll-up was measured at the nose of the first pier, which is similar to the result from the Chattahoochee River model. An H1 water surface profile was assumed as the overall profile except in the bridge section. The effect of the existence of surface

roll-up on local scour depth will be discussed in Chapter 6.

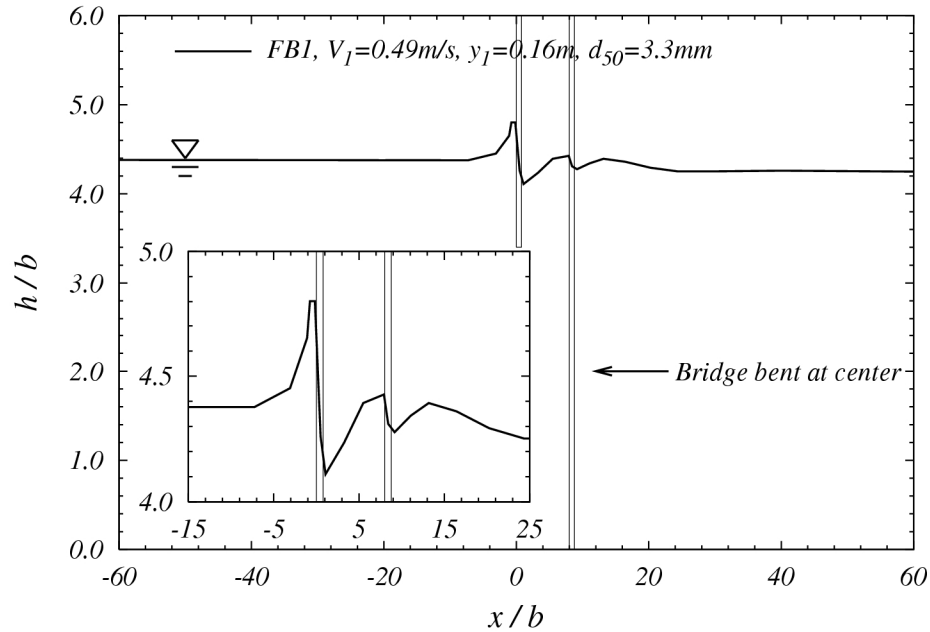


Figure 5.22 Water surface profile for experimental run FB1 in flat-bed model of the Flint River bridge pier bent

5.2.4 Measurement of Velocity Field

Near-field velocity vectors for before-scour condition are shown in Figure 5.23 for the flat-bed experimental run FB1 in the Flint River model. All mean velocities were measured at a height above the fixed bed of 40 percent of the approach flow depth under the bank-full flow condition. The streamwise locations of *SEC A–A* and *SEC B–B* in Figure 5.23 are $x/b = -1.6$, just upstream of the first pier, and $x/b = 3.8$, between the two piers. In the cross sectional velocity vector plots at *SEC A–A*, many downward velocity vectors are easily found and velocity vectors that spread out near the bed are observed in Figure 5.24 due to the characteristic of the downward and outward flow of

the horseshoe vortex. Strong transverse motion toward the bridge pier bent and motion upward near the bridge pier are shown due to the wake vortices at *SEC B – B* as given in Figure 5.25.

At the same flow condition, the velocity field was also measured for after-scour conditions at 40 percent of the approach flow depth and superimposed on the scour contours in Figure 5.26. The maximum scour depth occurred between the two piers with a high degree of symmetry on the left and right sides. The magnitude of the velocity decreased behind the upstream pier and in the wake region. The angle of attack for this experiment was close to zero and the bridge pier bent was aligned well with the approach flow. Therefore, it resulted in symmetry of the scour depth contours and velocity field along both sides of the bridge piers. The locations of *SEC A – A* and *SEC B – B* in Figure 5.26 are the same as in Figure 5.23. The detailed velocity vector fields in x-z coordinates for the two cross sections, *SEC A – A* and *SEC B – B*, are given in Figure 5.27 and Figure 5.28, respectively, for the after-scour condition. The converging velocity vectors and the deceleration of flow in the wake region between the two piers as shown in Figure 5.26 at a fixed elevation of 40 percent of the flow depth cannot clearly explain the scour pattern between the pier bent columns. However, the $v - w$ velocity vector plots at $x/b = -1.6$ and $x/b = 3.8$ in Figure 5.27 and Figure 5.28 help to give a better understanding of the connection between the scour pattern and the mean velocity field. The small upwelling flow is observed at the nose of the first pier near the bottom of the scour hole where the horseshoe vortex system induced by the pier exists in Figure 5.27. The downflow, moving with an angle toward the outside along the scoured bed near the bottom of the scour hole, is induced as the horseshoe vortex system wraps and stretches

around the pier in Figure 5.27. In Figure 5.28, the upwelling appears at the centerline of the pier bent between the piers and two counter-rotating vortices on either side are observed coinciding with the symmetric scour hole, which may contribute to the maximum scour depth at $x/b = 3.8$ instead of at the nose of the first pier. The location of the maximum scour depth is influenced by the combined effect of the horseshoe vortex system, complex geometry of bridge foundations and river bathymetry as will be discussed in detail in Chapter 6.

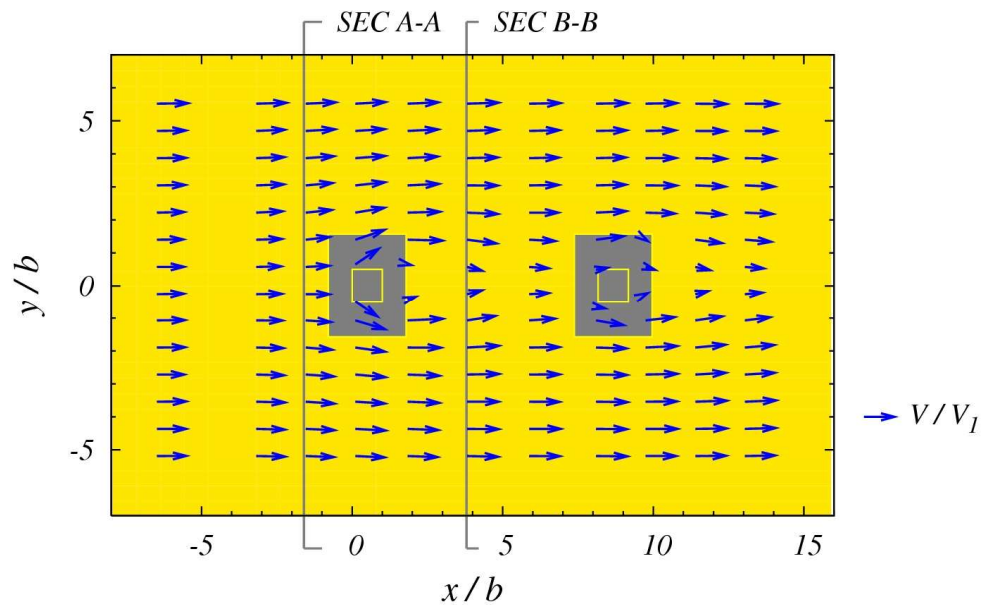


Figure 5.23 Velocity vectors for before scour measured at 40 percent of the approach flow depth of the experimental run FB1 in the Flint River model

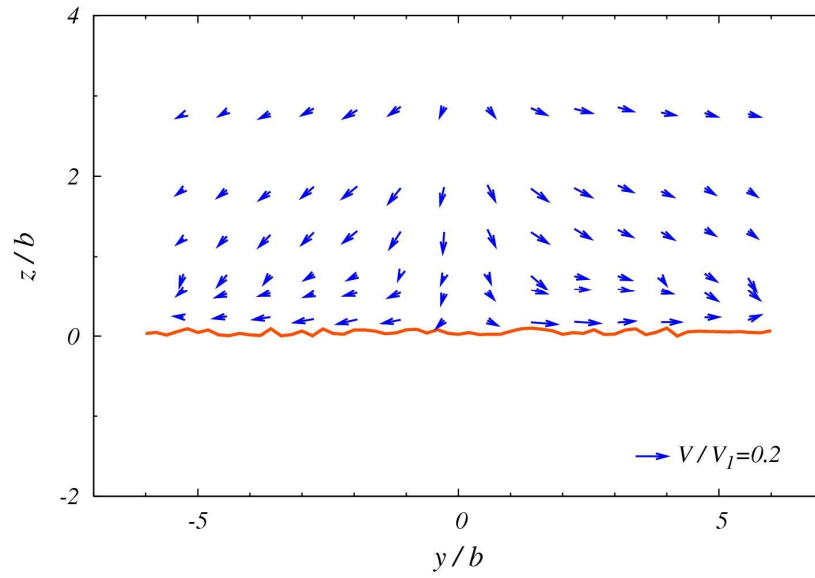


Figure 5.24 Velocity vectors at cross section A-A in Figure 5.23 ($x/b = -1.6$)

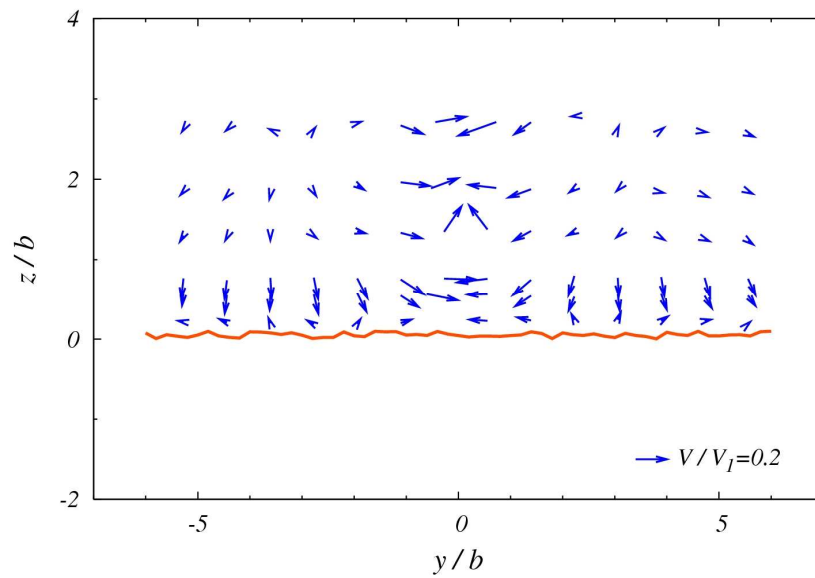


Figure 5.25 Velocity vectors at cross section B-B in Figure 5.23 ($x/b = 3.8$)

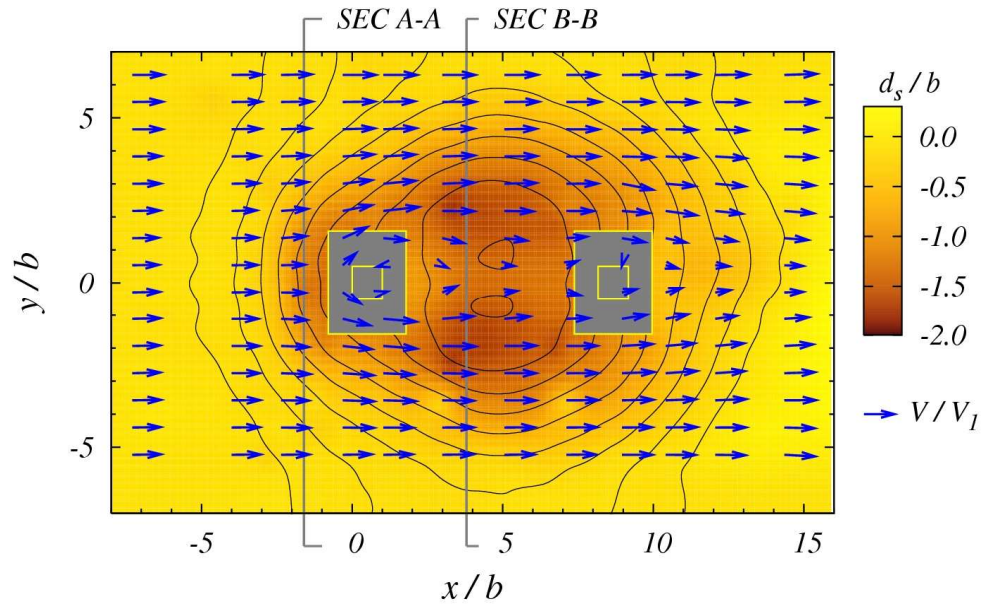


Figure 5.26 Scour contour lines and velocity vectors for after scour measured at 40 percent of the approach flow depth of experimental run FB1 in the Flint River model

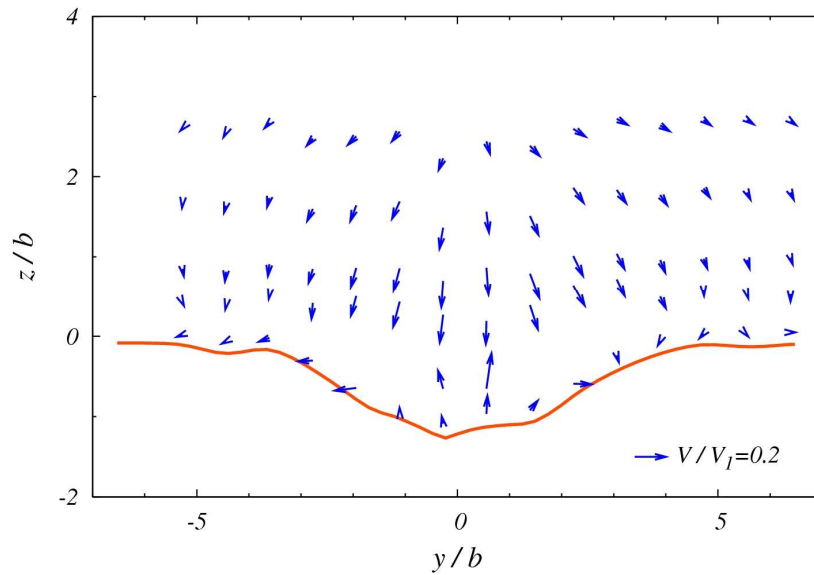


Figure 5.27 Velocity vectors at cross section A-A in Figure 5.26 ($x/b = -1.6$)

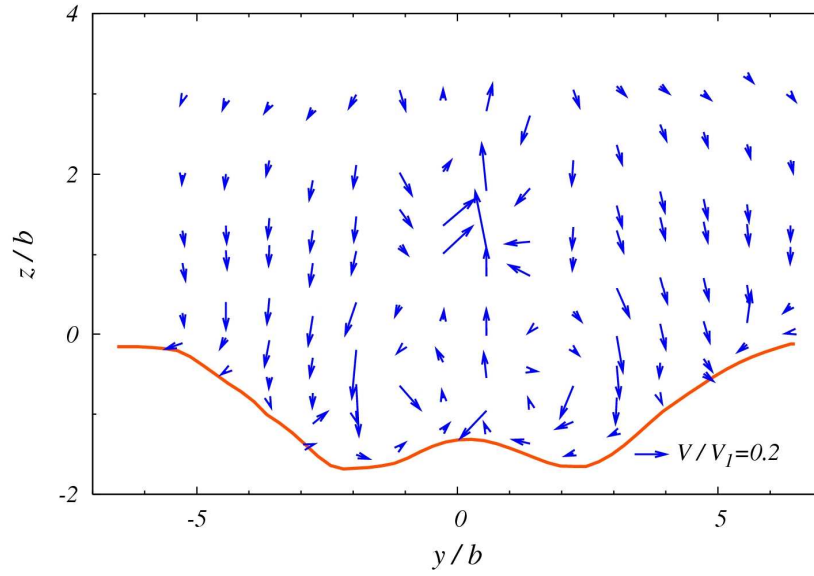


Figure 5.28 Velocity vectors at cross section B-B in Figure 5.26 ($x/b = 3.8$)

Near-velocity field was measured under the flood flow condition ($y_1/b = 7.4$) in the river model, experimental run RM1, in the Flint River model as shown in Figure 5.29. All velocity vectors in Figure 5.29 clearly show the skewness with a measured angle of attack at the approach flow section of 6.4° , which mainly caused the asymmetric scour contour along with the river bathymetry.

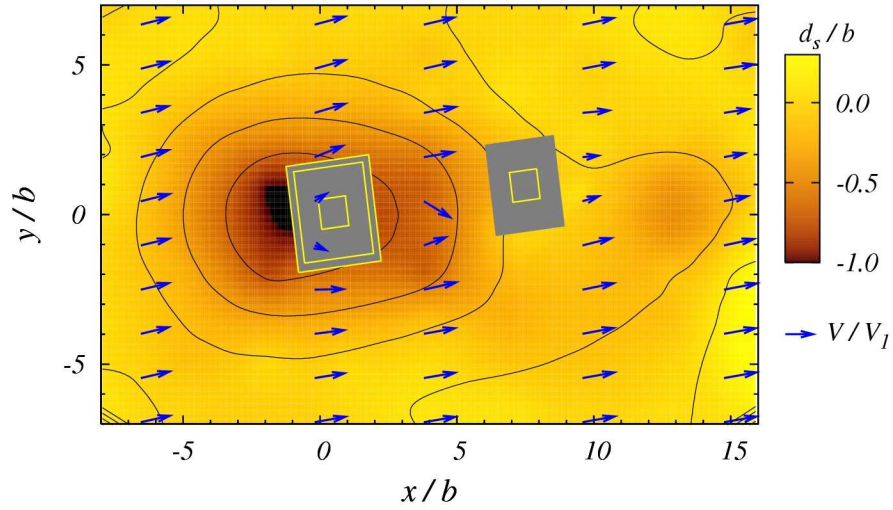


Figure 5.29 Scour contour lines and velocity vectors for after scour measured at 40 percent of the approach flow depth of experimental run RM1 in the Flint River model

Overall, there is an evident effect of the secondary flow near the bed and significant three-dimensional flow effects on the scour process in both the flat-bed model and river model, which cause clearly different scour patterns.

Figure 5.30 shows the points for comparison of turbulence intensity and kinetic energy profiles for before scour on the left and right sides of the bridge pier bent in the flat bed model. The distance between the centerline of the pier bent and measured points on the each side was approximately $1.6b$. Nondimensionalized turbulent intensities in streamwise and vertical directions were highly symmetric along the bridge pier bent as shown in Figure 5.31 and Figure 5.32. It is observed that measured turbulence intensities starting from location 4 for both streamwise and vertical directions increased significantly along the flow direction. Specifically, the turbulence intensity in the vertical

direction became relatively high starting from location 5 which corresponds with the deeper points of the scour hole. The maximum value of streamwise turbulence intensity was detected at location 4 since this was the beginning of the highly unsteady region due to the existence of the pier. Turbulent kinetic energy also became relatively large downstream of location 4 in Figure 5.33. Overall, the streamwise turbulence intensity was of the order of 20 percent of the mean approach velocity, while the vertical turbulence intensity was the order of 10 percent of the mean approach velocity downstream of location 5. Total turbulent kinetic energy profiles were nondimensionalized by the approach shear velocity, u_{*1} as shown in Figure 5.33.

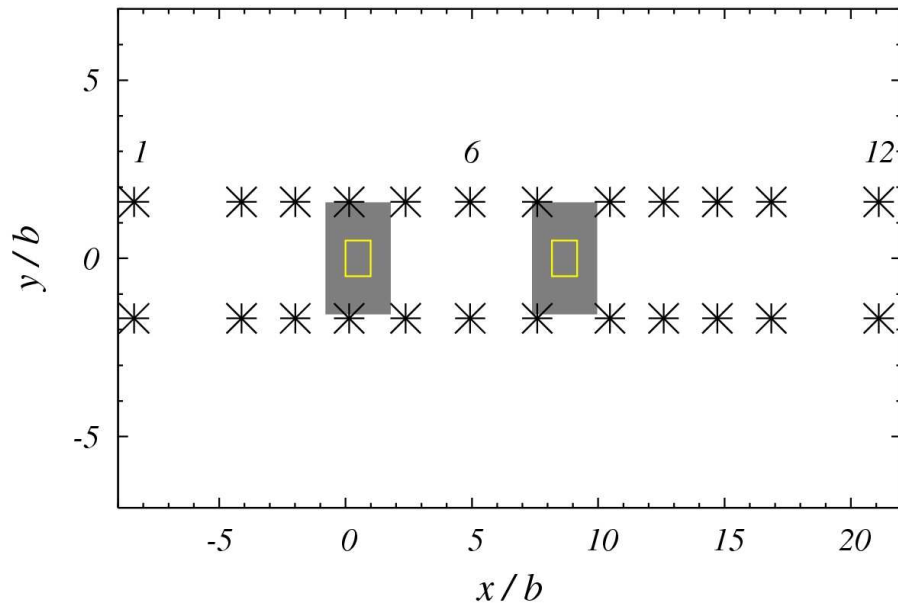


Figure 5.30 Plan view and measured points for near-field turbulence intensity for experimental run FB1 in the Flint River model

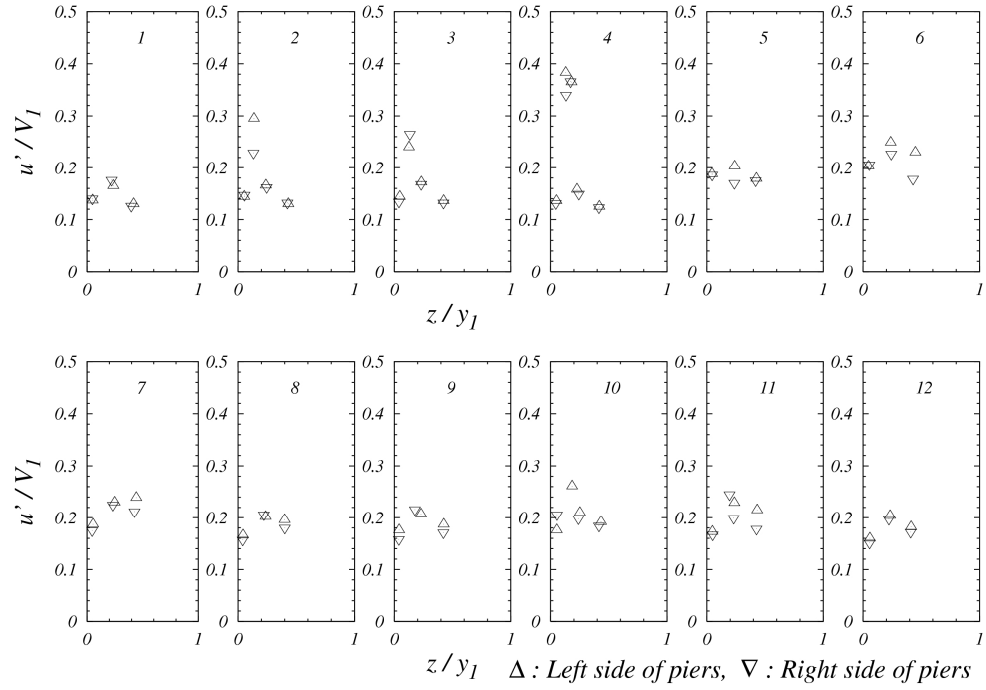


Figure 5.31 Turbulence intensity for the streamwise direction relative to mean approach velocity of experimental run FB1 in the Flint River model

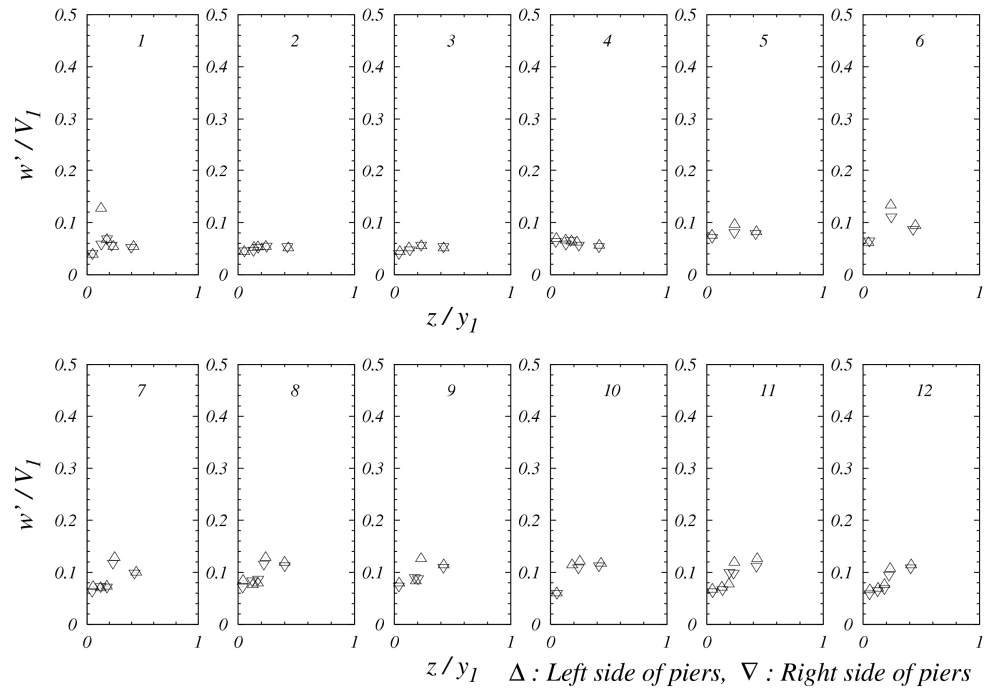


Figure 5.32 Turbulence intensity for the vertical direction relative to mean approach velocity of experimental run FB1 in the Flint River model.

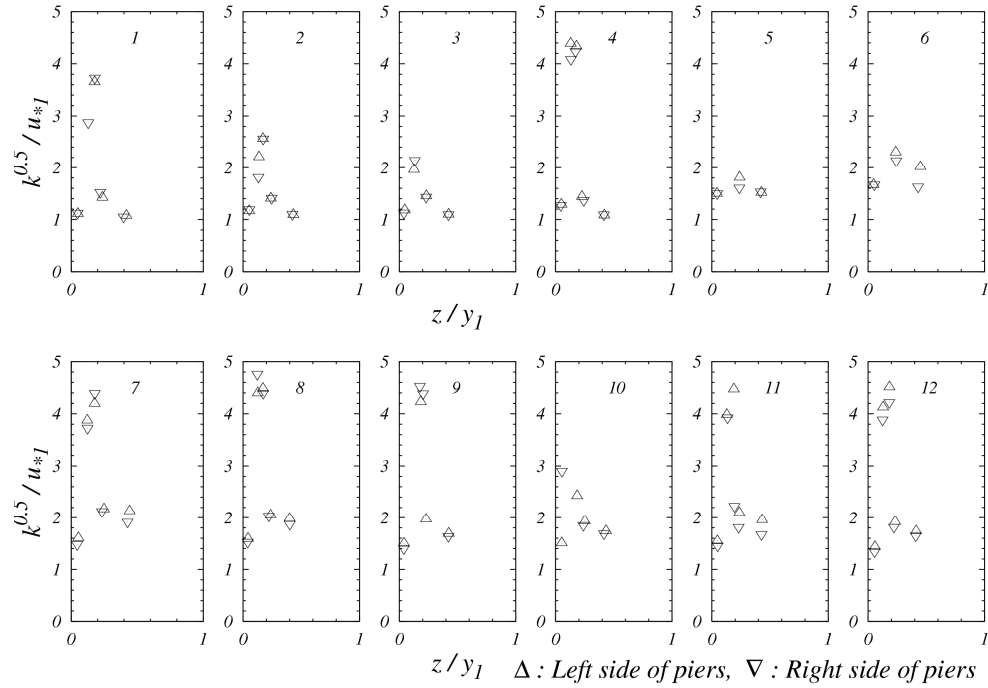


Figure 5.33 Turbulent kinetic energy relative to approach velocity for experimental run FB1 in the Flint River model

5.2.5 Comparison with Field Data

Physical modeling of the Flint River bridge was undertaken for tropical storm Alberto which occurred in 1994. The maximum discharge was $3030 \text{ m}^3/\text{s}$ with a recurrence interval of 200 years. The laboratory results were compared with scour depth data and two-dimensional velocity data measured by the USGS. Local pier scour depths upstream of the first pier in the main channel and the deposition region on the right side of the pier bent were reproduced well in the laboratory model experiment as shown in Figure 5.34. However the contraction scour in the constricted region between two bridge pier bents does not agree well with the field cross section possibly because of the lack of sufficient time for full development of the contraction scour in the laboratory which develops more slowly than the local pier scour (Hong 2005).

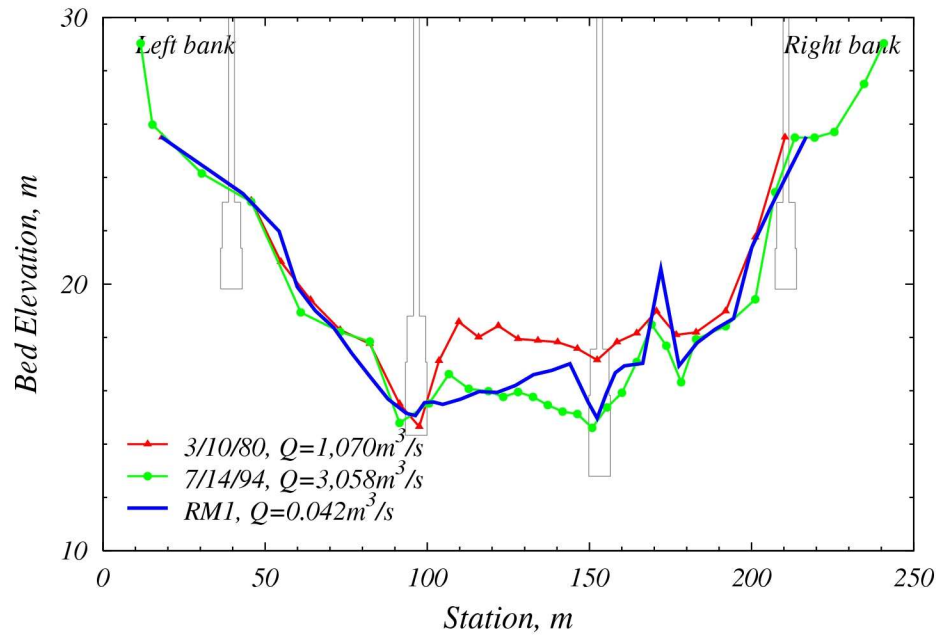


Figure 5.34 Comparison of cross sections at Flint River upstream of the bridge

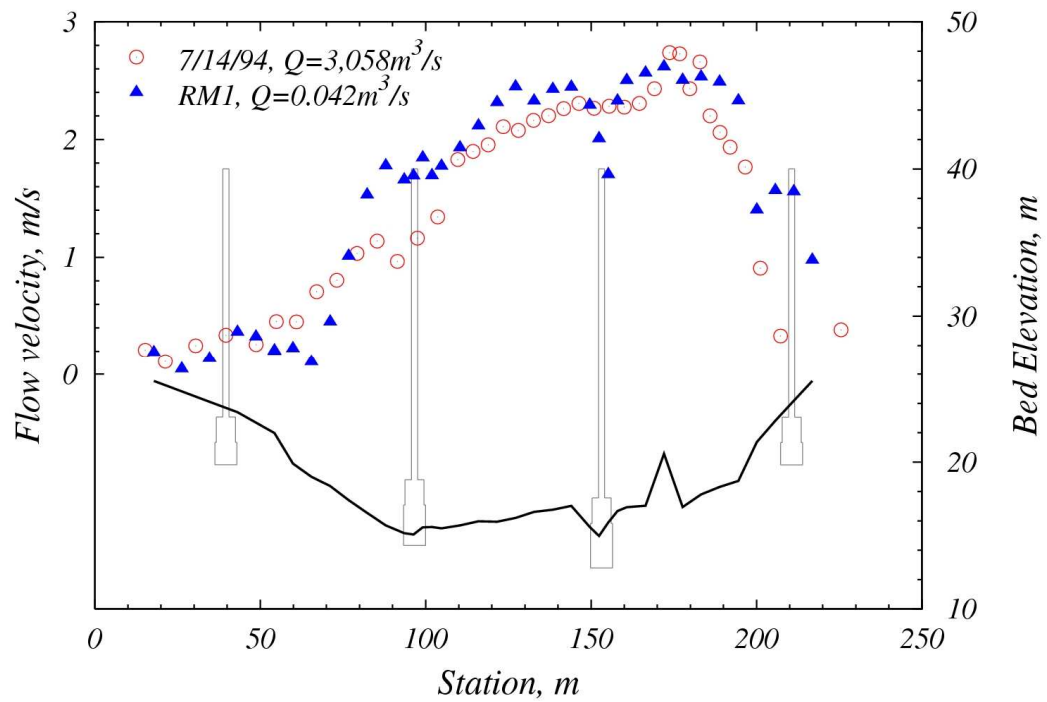


Figure 5.35 Comparison of velocity upstream of the bridge pier from experimental run RM1 in Flint River model for Tropical Storm Alberto

Figure 5.35 shows the streamwise, depth-averaged velocity distribution along the bridge deck including the velocity in the floodplain on the left side of the bridge pier bent where the 2D side-looking ADV was utilized to measure velocity in the laboratory because of the shallow depths. Even though there is some discrepancy in the velocities near the right bank and at the nose of the bridge pier in the main channel, the velocity distribution measured in the laboratory just upstream of the bridge is in good agreement overall with field measurements.

5.3 The Ocmulgee River Model

The raw data for the Ocmulgee River model are given in Table 5.5. Experimental data were collected from the literature where contraction scour was investigated to analyze the effect of pier existence by (Hong 2005). However, the scour depth measured by Hong at the nose of the first pier upstream is used for consistency, and the width of the first pier is defined as the characteristic length scale in Table 5.6.

Table 5.5 Summary of experimental data for the Ocmulgee River model

Run	Model	Scale	Q m ³ /s	d_{50} mm	b m	y_1 m	V_1 m/s	T hrs	T_M hrs	d_s m
1	FB ¹	1/45	0.061	0.53	0.041	0.183	0.333	10	88	0.038
1	RM ²	1/45	0.136	1.10	0.041	0.181	0.312	98	43	0.050
2	RM	1/45	0.165	1.10	0.041	0.191	0.336	92	47	0.053
3	RM	1/45	0.184	1.10	0.041	0.203	0.350	92	48	0.084
1	FD ³	NA	1840.605	0.80	1.829	8.230	2.094	NA	NA	0.032

FB¹=flat-bed model, RM²=river model (Hong 2005), FD³=field data from USGS

The relative scour depth of experimental run FB1 in Table 5.6 was slightly smaller than the value in run RM3 where the Froude number was about 0.25 in both cases even though the ratios of mean approach velocity and critical velocity in FB1 were much higher. If the effect of flow depth can be neglected, since the values of y_1/b were over 3.5 and the relative difference between two cases was about 1%, the sediment size can be the only factor to explain this phenomenon, which will be discussed in detail in Chapter 6.

Table 5.6 Summary of dimensionless experimental data for The Ocmulgee River models

Run	Model	Scale	Fr_1	Fr_b	V_1/V_c	y_1/b	b/d_{50}	d_s/b
1	FB ¹	1/45	0.25	0.53	1.07	4.50	76.7	2.01
1	RM ²	1/45	0.23	0.49	0.70	4.45	36.9	2.05
2	RM	1/45	0.25	0.53	0.75	4.69	36.9	2.20
3	RM	1/45	0.25	0.55	0.78	4.99	36.9	2.19
1	FD ³	NA	0.23	0.49	3.73	4.50	2286	1.78

FB¹=flat-bed model, RM²=river model, FD³=field data from USGS

In the Ocmulgee River model experiments, the detailed velocity field was not measured, but velocity distribution upstream of bridge site was measured and compared with the field data measured by the USGS.

5.3.1 Temporal Variation of Local Scour Depth

Temporal development of scour depth at the nose of the first pier in the Ocmulgee River model was recorded at selected time intervals in the flat-bed and river model experiments as shown in Figure 5.36 and Figure 5.37, respectively. The rate of change of scour depth was high initially and then the slope of the scour depth change with time became milder until the scour depth reached the equilibrium state after only 3 hours in the flat bed

experiment. It took over 20 hours to reach equilibrium scour depth in the river model experiments since the ratio of mean approach velocity to critical velocity in the river model experiments was relatively smaller than in the flat-bed experiment in which the value of V_1/V_c was slightly over 1.0 and thus in the live-bed regime. The sediment size selected in the river model experiments was coarser than in the flat-bed experiment, which is related to the rate of scour depth development as shown in Chapter 6.

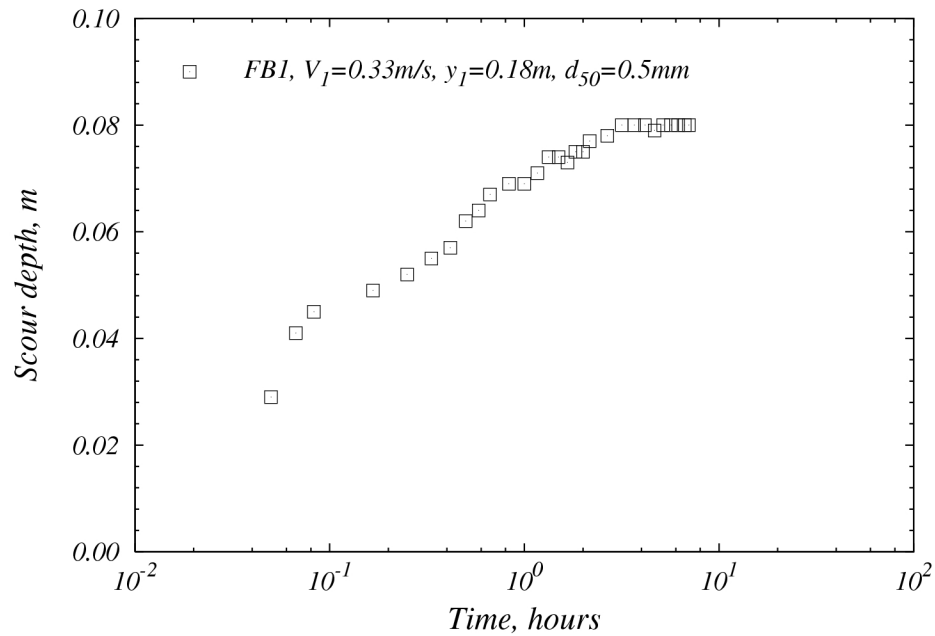


Figure 5.36 Temporal development of local scour depth of FB1 in Ocmulgee River experiments

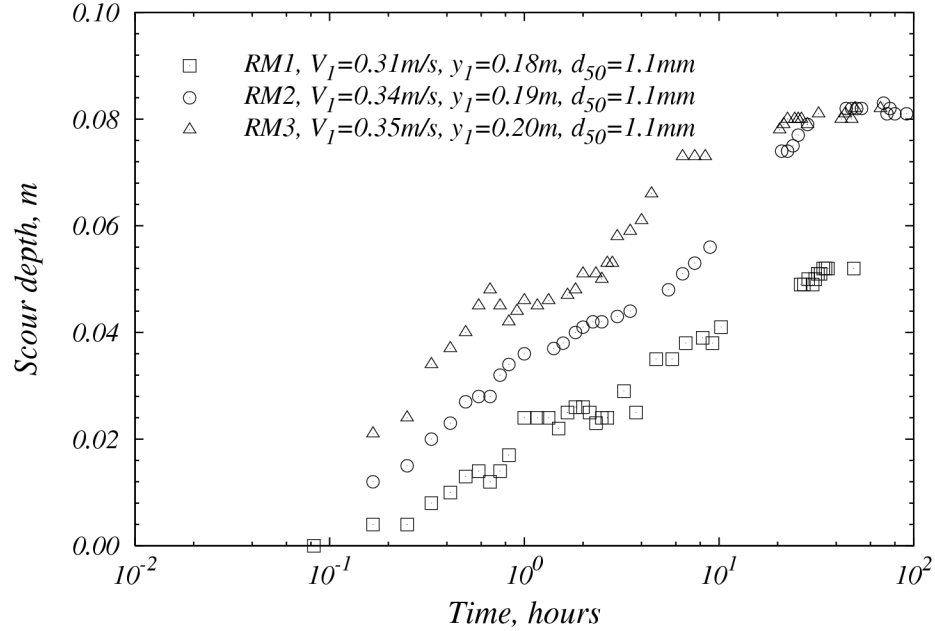


Figure 5.37 Temporal development of local scour depth of river model experiments in Ocmulgee River experiments

5.3.2 Measurement of Maximum Scour Depth and Contour

In Figure 5.38, scour depth contours and the centerline scour depth profile show the location of maximum scour depth and symmetry of the scour hole in the flat-bed experiment. Scour depth in the flat-bed experiments can be a benchmark when considering the contraction scour depth that occurs simultaneously with the local pier scour in the river model experiments (Hong 2005). To investigate the effect of the existence of other piers, additional experiments need to be conducted with a single pier under the same flow conditions. Scour depth measured around the pier bent in the river model experiment (RM1) is shown in Figure 5.39. To measure the scour depth in river model experiments, the reference elevation, the elevation of an undisturbed bed profile without any residual scour, was introduced due to the effect of the residual contraction

and pier scour. Detailed steps to calculate the scour depths with consideration of the reference elevation was presented by Hong (2005). Scour contours in RM1 are slightly asymmetric when compared with that of FB1 because of the river bathymetry and contraction. Location of the major deposition area was also located further downstream in the river model than for the flat bed experimental result.

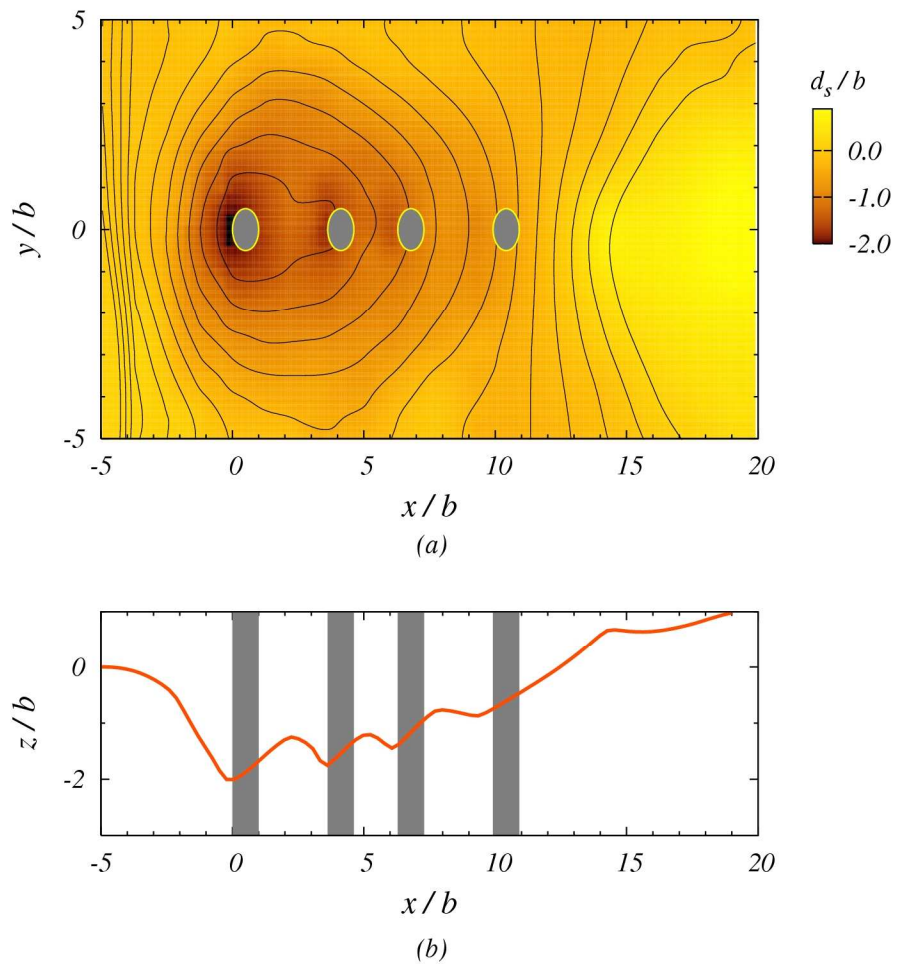


Figure 5.38 Scour contour and scour depth profile for experimental run FB1 in the Ocmulgee River model (a) plan view and (b) scour depth profile at $y/b = 0$

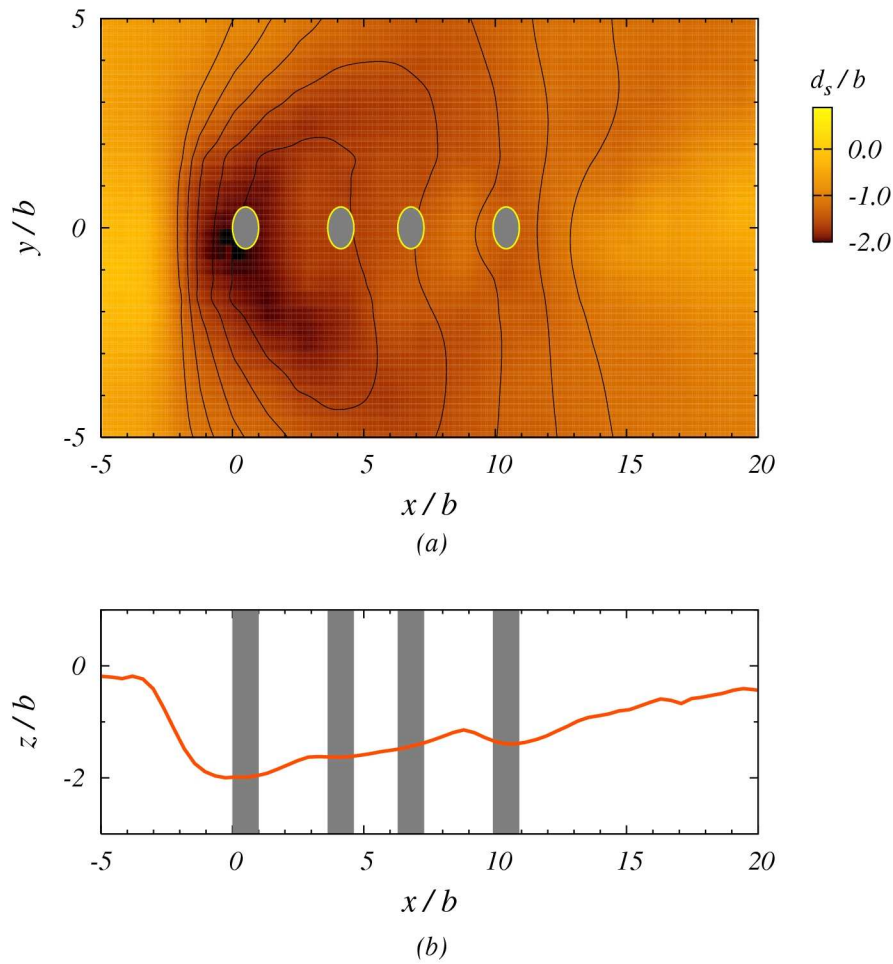


Figure 5.39 Scour contour and scour depth profile for experimental run RM1 in the Ocmulgee River model (a) plan view and (b) scour depth profile along the centerline of bridge bent

5.3.3 Comparison with Field Data

The historical cross sections upstream of the bridge were compared with the experimental run RM1 including the 1998 flood in Figure 5.40. The measured pier scour depth showed a good agreement of the bed elevation with field data while the contraction scour between the central pier and pier on right side did not seem to agree with the field data as well as the pier scour depth.

Figure 5.41 shows the velocity distribution upstream of the bridge between the field data and laboratory measurement. In field data, the velocities were measured at a short time after the occurrence of the peak discharge, $1,841 \text{ m}^3/\text{s}$, when the measured discharge was $1,388 \text{ m}^3/\text{s}$. Therefore, the magnitude of each velocity measured by the USGS was slightly smaller than that of laboratory measurement. However, the shape of the velocity distribution for each case is similar enough to verify the validity of the Froude number similitude (Hong 2005).

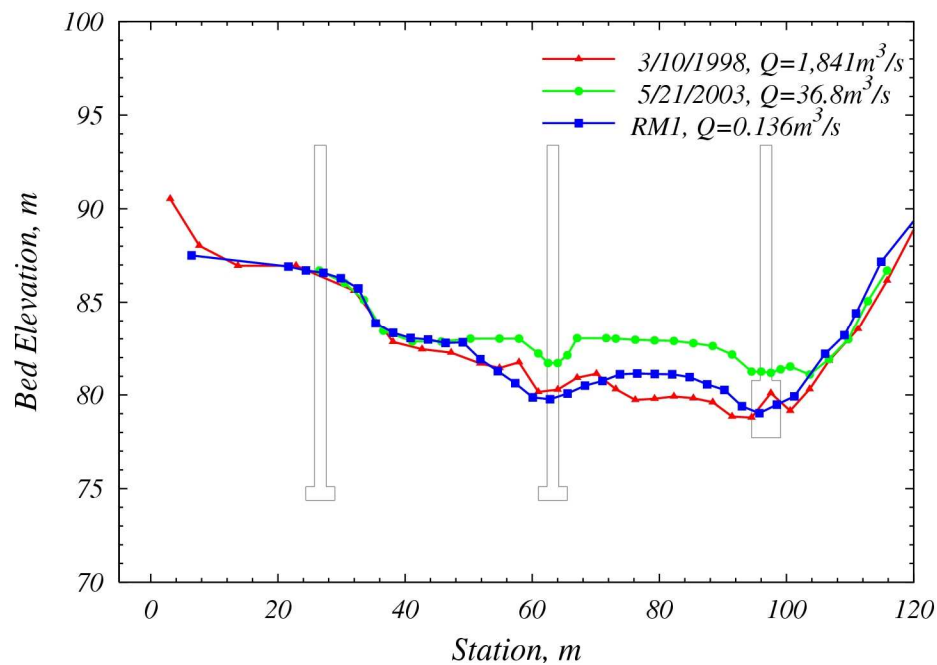


Figure 5.40 Comparison of cross sections at upstream of the bridge in Ocmulgee River at Macon, GA

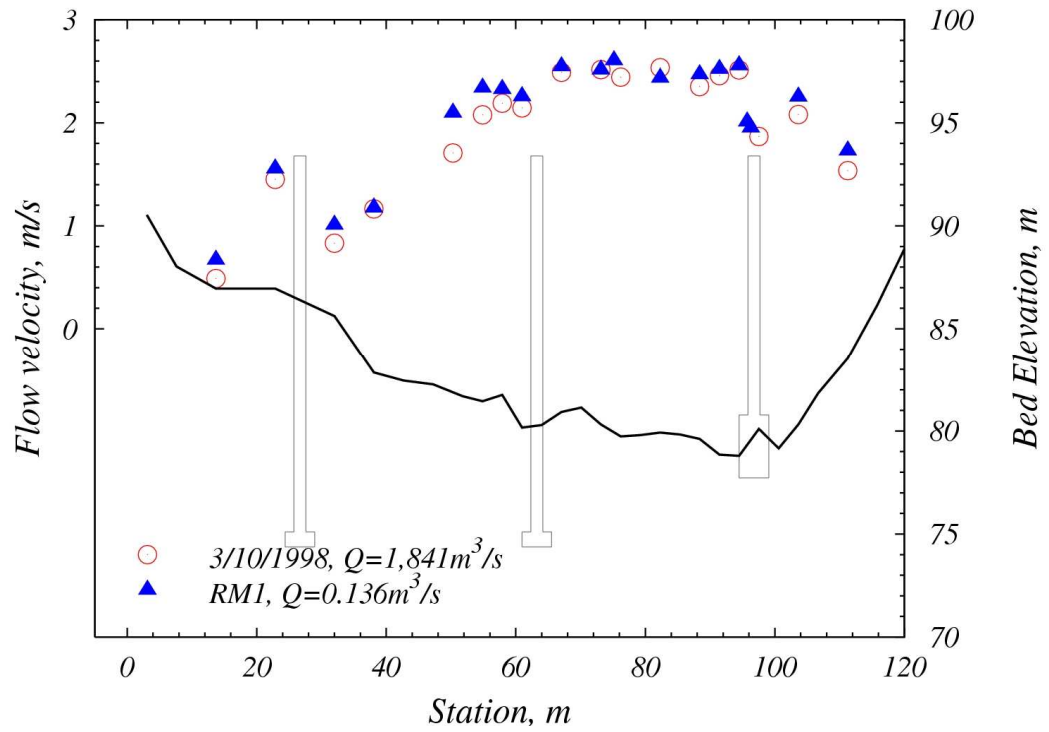


Figure 5.41 Comparison of velocity upstream of the bridge pier from experimental run RM1 in Ocmulgee River models for the 1998 flood

CHAPTER VI

ANALYSIS OF EXPERIMENTAL RESULTS

In this chapter, the laboratory results for temporal development of local pier scour and for maximum pier scour depths are analyzed in terms of a dimensional analysis to test existing pier scour formulas and suggest improvements to the formulas to resolve the inconsistency between predicted scour depths and actual scour depths observed in the field. In so doing, the connection between the flow field and scour is made in a manner not previously developed; namely, the unsteady, large-scale coherent motions associated with the horseshoe vortex are investigated as one of the primary contributors to the overprediction of field values of pier scour depth when using formulas based on laboratory-scale experiments. Based on the laboratory data collected in this study, a modified pier scour formula is then suggested, and the results are compared with field data from several investigators. In addition, a laboratory modeling strategy is developed and verified by comparisons between laboratory and field results collected in this study.

6.1 Dimensional Analysis

Local scouring around a pier is a consequence of the intricate interactions of many parameters, therefore it is recommended that the effect of each parameter needs to be investigated individually through dimensional analysis. The resulting dimensional analysis for local pier scour depth with uniform sediment given in Chapter 4 may be

simplified if the shape and alignment of pier are assumed to be identical for all cases as following:

$$\frac{d_s}{b} = f \left(\frac{y_1}{b}, \frac{V_1}{V_c}, \frac{b}{d_{50}}, Fr_1 \text{ or } Fr_b \right) \quad (6.1)$$

The relative scour depth, d_s/b , can be physically implicated as the scouring that is due to the horseshoe vortex system which is a function of pier width, b . The effect of approach flow depth is expressed by y_1/b . It represents the relative influence of the depth of flow and the size of the horseshoe vortex as reflected by b . The scour depth is affected by y_1/b for smaller values of y_1/b . However, the effect of y_1/b decreases with increasing flow depth and finally, scour depth becomes independent of the flow depth when y_1/b becomes larger than a certain threshold. Usually, the acceptable threshold value of y_1/b is 3~4 in the literature (Breusers et al. 1977; Ettema 1980; Melville 1997). The mobility of bed materials for scouring is expressed by V_1/V_c which is called the flow intensity. For rough bed flow, the exchange of momentum in the boundary layer is generally controlled by the bed roughness rather than the fluid viscosity (Roulund 2000; Roulund et al. 2005). The horseshoe vortex system and the distance to the separation point upstream of the pier are influenced by the bed roughness related to the sediment size. For larger sediment size, the momentum of the downflow at the upstream edge of the pier is more dissipated than for smaller sediment sizes due to bed porosity. With increasing values of b/d_{50} up to a certain threshold, a larger and stronger horseshoe vortex system is expected since the momentum exchange is decreasing, thus the scour depth is also increasing. However, most previous studies have shown that the scour depth

becomes independent of the effect of sediment size when b/d_{50} is greater than a certain threshold. In these studies, an envelope curve is recommended for the effect of b/d_{50} which can cause an overprediction of scour depth. The Froude number, Fr_1 is the functional parameter relating the strength of the horseshoe vortex and gravitational effects as reflected by the depth of the approach flow and the water surface gradient through the bridge opening. For higher Froude numbers, the horseshoe vortex system and flow field in the vicinity of the pier are influenced by the Froude number (Roulund et al. 2005), and the effect of Froude number on the scour depth becomes significant. Therefore, the experimental analysis or formula neglecting the effect of Froude number may lead to discrepancies between field data and measured or calculated values. From an elementary Bernoulli equation analysis along the free surface streamline, the pier Froude number, Fr_b , can be expressed approximately as

$$Fr_b^2 \approx 2 \times \frac{\Delta h}{b} \quad (6.2)$$

where Δh is the height of surface roller on the upstream edge of the pier which induces the pressure gradient along the vertical direction at the upstream edge of the pier, and in which the depth-averaged velocity has been substituted for the free stream velocity in the definition of the pier Froude number. Thus, the pier Froude number can be interpreted as the relative scale difference between the surface roller and the horseshoe vortex. Finally, the time scale, which is not included in Equation 6.1, can be defined as $t V_c / y_1$ to show the development of scour depth in front of the pier.

6.2 Analysis of Temporal Variation of Local Scour

Depth

The dimensionless time scale for scour development at the nose of the pier was formed using the critical velocity, V_c , and approach flow depth, y_1 as indicated previously by the dimensional analysis. Such a grouping has been used by Sturm (2006) for temporal development of abutment scour with the flow intensity as the third dimensionless parameter. Applying regression analysis to the variability of dimensionless scour depth with the logarithm of dimensionless time for a fixed value of flow intensity, the slope of each curve was examined considering hydraulic parameters. For instance, the effect of the flow intensity, V_1/V_c , on the slope of the temporal variation of local scour depth was examined. In addition, the temporal data were used to determine the time at which equilibrium scour was reached, T_{eq} . The effect of the flow intensity and relative sediment size were examined with respect to the slope of the dimensionless time development curves and T_{eq} in this study.

A formula for the equilibrium time by Melville and Chiew (1999) was presented previously in Chapter 2. It can be rewritten in terms of $T_{eq} V_c / y_1$, y_1/b and V_1/V_c as follows:

$$T_{eq} \frac{V_c}{y_1} = 2.67 \times 10^6 \times \left(\frac{y_1}{b} \right)^{-0.75} \times \left[1 - 0.4 \left(\frac{V_1}{V_c} \right)^{-1} \right] \quad (6.3)$$

where, $y_1/b = 6$ for $y_1/b > 6$. After correcting for the effect of the relative flow depth, y_1/b , the variation of the equilibrium time scale with flow intensity is shown in Figure

6.1 using the data of Melville and Chiew (1999), and including Equation 6.3. A considerable discrepancy between the experimental data of Melville and Chiew and Equation 6.3 represented by the solid line is observed over the full range of flow intensity. A modification of that formula is suggested by the dashed curve in Figure 6.1.

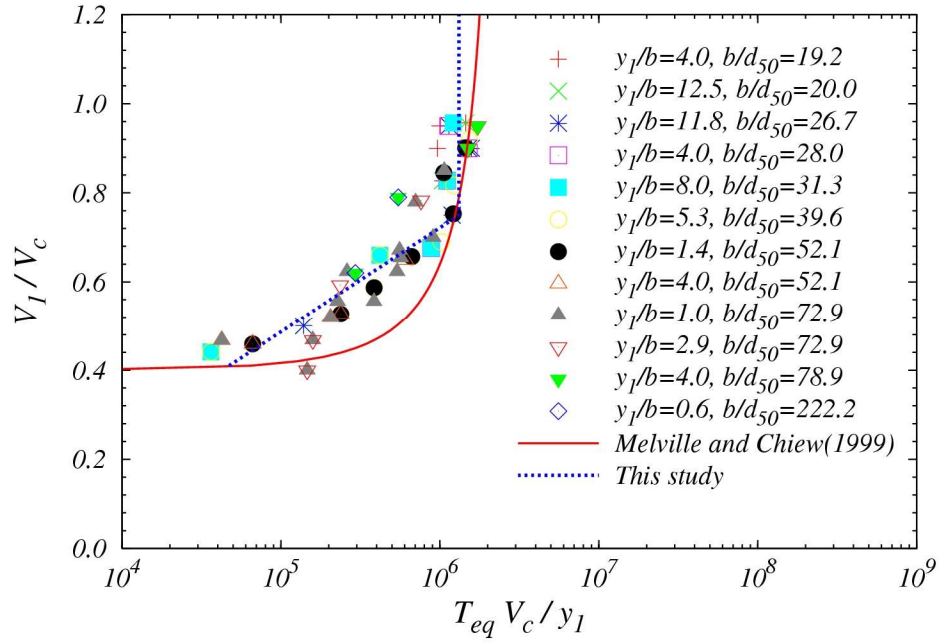


Figure 6.1 Influence of the flow intensity, V_1/V_c , on the equilibrium time, T_{eq}

The modified formula in is given as

$$T_{eq} \frac{V_c}{y_1} = \begin{cases} \left(\frac{y_1}{b} \right)^{-0.75} \times 10^4 \left[\frac{(V_1/V_c + 0.688)}{0.235} \right] & \text{for } \frac{V_1}{V_c} \leq 0.75 \\ 1.316 \times 10^6 \times \left(\frac{y_1}{b} \right)^{-0.75} & \text{for } 0.75 < \frac{V_1}{V_c} \leq 1.0 \end{cases} \quad (6.4)$$

Based on this fitting of the Melville and Chiew data, the equilibrium time scale becomes independent of flow intensity when $0.75 < V_1/V_c \leq 1.0$.

Figure 6.2 and Figure 6.3 show the development of scour depth with time for flat bed experiments and river model experiments, respectively, in the Chattahoochee River modeling. The slope of each curve is clearly dependent on the flow intensity with the slope increasing with increasing flow intensity. The equilibrium time, T_{eq} , is weakly related to flow intensity in both the flat bed experiments and the river model experiments. Observations from Figure 6.2 and Figure 6.3 suggest that the equilibrium time is independent of flow intensity when the development of scouring is monitored at the nose of a pier in agreement with Melville and Chiew's data in Figure 6.1.

To elucidate the difference in time scales for the river model experiments, results for experimental runs RM6, RM8, and RM9 are shown in Figure 6.4, where the slopes of the time-development curves are shown to be dependent on flow intensity. The resultant slopes obtained are 0.72, 0.79 and 0.85 for experimental runs RM6, RM8 and RM9, respectively through regression analysis. Also, the equilibrium time, T_{eq} , for each run is observed to be independent of flow intensity. In experimental run RM9, the slight deviation of points after reaching the equilibrium time can be explained by the fact that the scour regime in RM9 is on the threshold between clear-water and live bed scour since the flow intensity in RM9 has a value of unity. Generally, if the flow intensity has a value of unity, the maximum clear-water scour depth occurs, and the most rapid development of local scour depth can be expected for the clear-water scour condition. Scour depth fluctuates with time in response to bed features passing through the scour hole for the live bed scour condition as illustrated in Chapter 2.

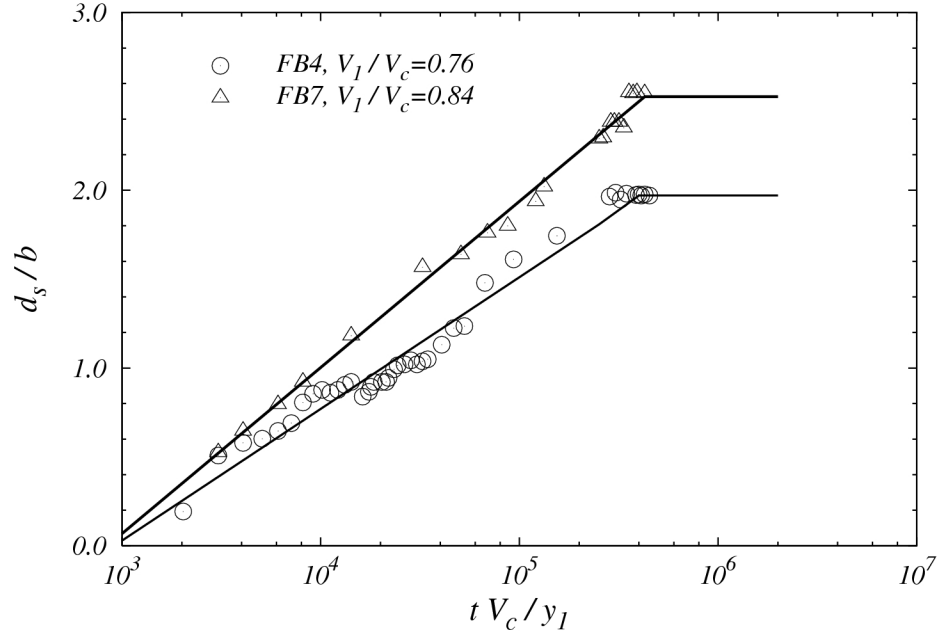


Figure 6.2 Comparison of temporal development of scour depth of FB4 and FB7 in the Chattahoochee River modeling (Scale=1/23, $y_1/b = 4.2$, $b/d_{50} = 13.95$)

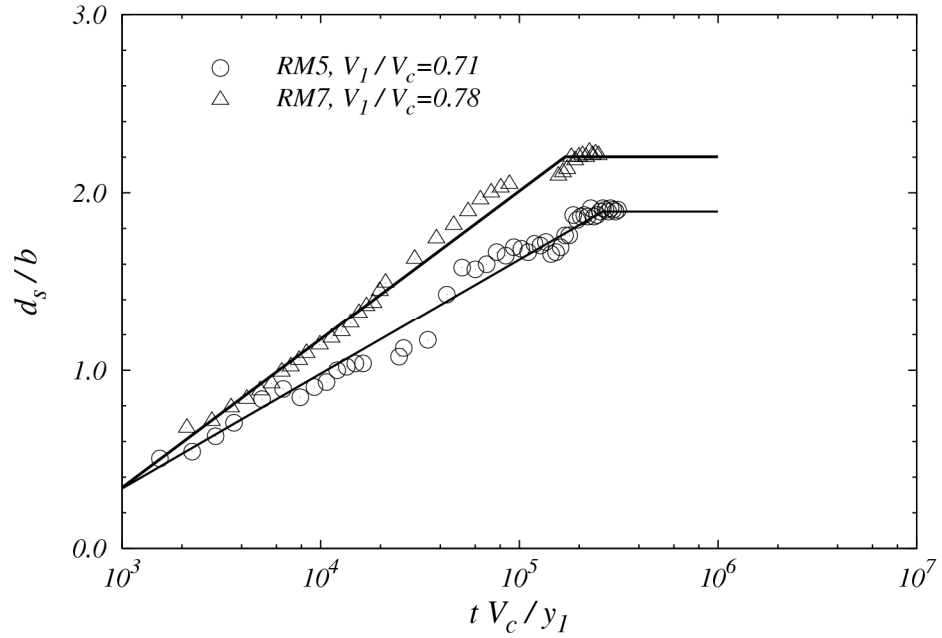


Figure 6.3 Comparison of temporal development of scour depth of RM5 and RM7 in the Chattahoochee River modeling (Scale=1/40, $y_1/b = 7.0$, $b/d_{50} = 24.5$)

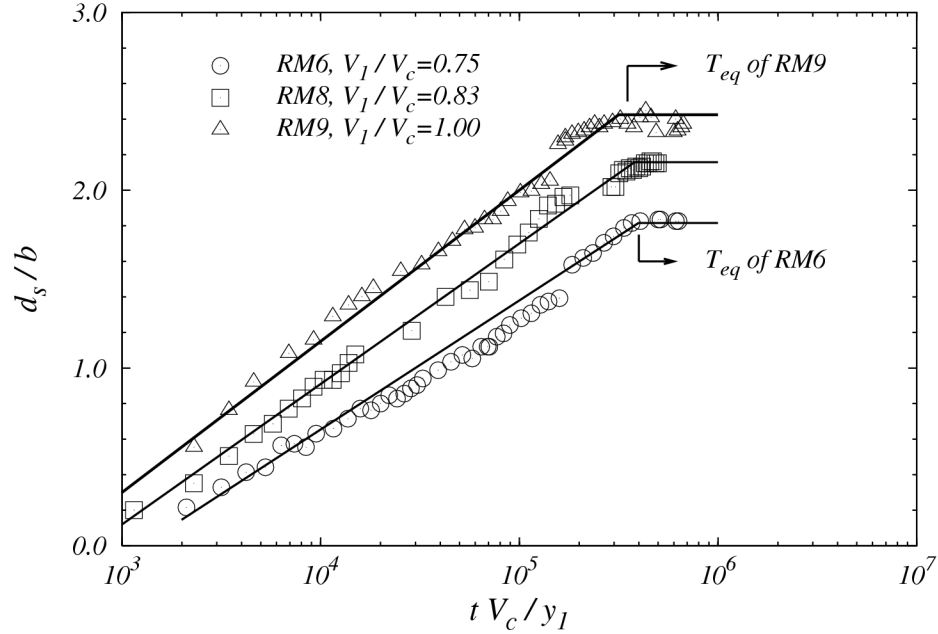


Figure 6.4 Comparison of temporal development of scour depth of RM6, RM8 and RM9 in the Chattahoochee River modeling (Scale=1/40, $y_l/b = 4.0$, $b/d_{50} = 24.5$)

For the Flint River model, the exposed pier footing caused some delay in scour hole development. Since the surface elevation of the footing was about the same as the initial bed elevation at the central bridge pier bent for the Flint River bridge, the development of the scour depth started first at both sides of the footing due to the flow of the horseshoe vortex wrapping around the pier. Two conical-shaped scour holes were detected in the vicinity of the footing on either side as shown previously in Figure 5.17 in Chapter 5. When the two conical scour holes at both sides became larger and then met eventually at the nose of the first pier footing, the local scour depth at the nose of the pier footing started developing. That starting stage was used as the beginning time of the scour depth at the nose of the pier in the Flint River modeling. When the regression analysis on temporal variation of scour depth from experimental results in the Flint River

modeling was conducted, time less the beginning time defined above was eliminated for the regression analysis. The beginning time was dependent on the flow intensity in the Flint River model. It took longer for the scour hole to begin development at the nose of the pier footing for smaller flow intensity as shown in Figure 6.5. However, the slopes from the regression analysis were approximately the same for different flow intensities in the flat-bed experiments as shown in Figure 6.5. A similar result was obtained in the river model experiments. The strength of the horseshoe vortex system in front of the footing may be less than that in front of the pier since the role of the downflow along the upstream face of the pier becomes significantly smaller in the former case. Therefore, the rate of scouring may be less dependent on the flow intensity so that the slopes in Figure 6.5 are comparable.

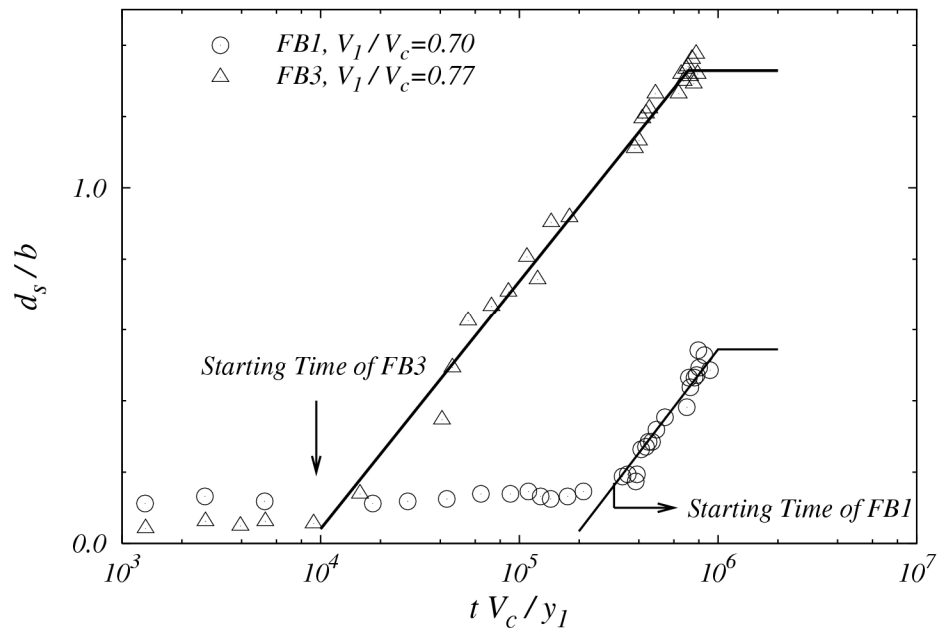


Figure 6.5 Comparison of temporal variation of scour depth between FB1 and FB3 in the Flint River modeling (Scale=1/50, $y_l/b = 4.3$, $b/d_{50} = 11.08$)

The effect of the relative sediment size was examined by comparing experiments with approximately the same values of the flow intensity and the relative flow depth. It was difficult to obtain exact comparisons, but for example, the relative differences in flow intensity and relative flow depth were within 10% between experimental runs FB9 and FB11 in the Chattahoochee River model. Hence, those cases were selected to study the effect of the relative sediment size alone as shown in Figure 6.6. The comparison of experimental runs FB9 and FB11 elucidated the effect of relative sediment size. The rate of scouring was weakly influenced since the slope of the time development curve in each case is almost the same as shown in Figure 6.6 as well as Figure 6.7. However, the equilibrium time, T_{eq} , was highly affected by the relative sediment size, b/d_{50} , in the clear-water condition. When the value of b/d_{50} increased, the dimensionless time to reach equilibrium was reduced since the reduction of the sediment size decreases the critical velocity. Decreasing the critical velocity requires the approach velocity to become smaller to match the same flow intensity, V_1/V_c . If the strength of the horseshoe vortex system is mainly dependent on the pier size and flow condition, then so is the equilibrium time (Dargahi 1989; Kothiyari et al. 1992b; Muzzammil and Gangadhariah 2003; Qadar 1981). Thus, the equilibrium time with small sediment is less than that with large sediment when other conditions are the same. Further investigation of the effect of sediment size or b/d_{50} is needed in order to improve the formula for the equilibrium time. It is also found that the equilibrium scour depth is remarkably affected by b/d_{50} in both Figure 6.6 and Figure 6.7. Therefore, in order to compare the equilibrium scour depth for each case in detail, more consideration of the effect of b/d_{50} on scour depth is required.

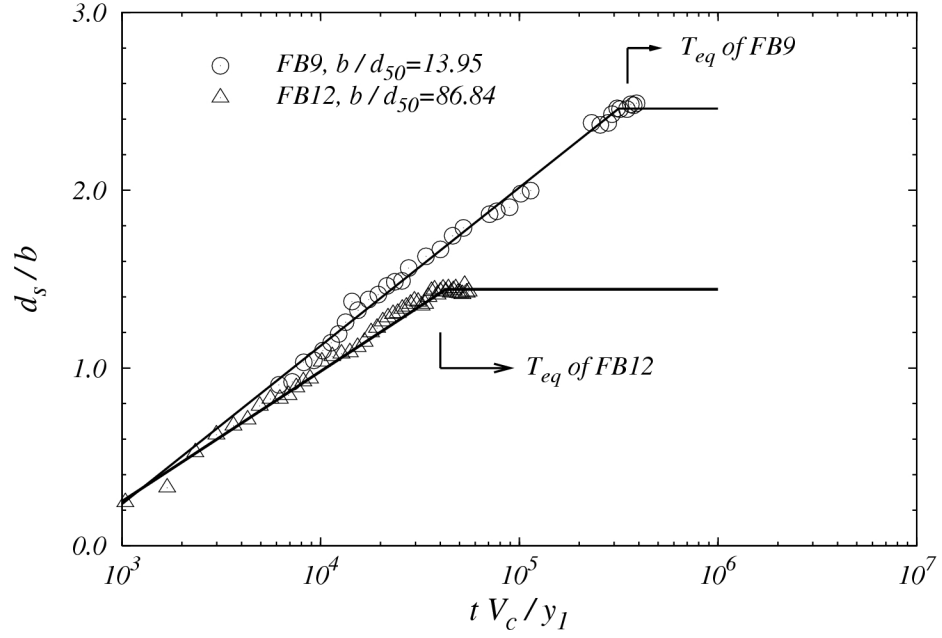


Figure 6.6 Effect of b/d_{50} on temporal development of scour depth of FB9 and FB12 in the Chattahoochee River modeling (Scale=1/23, $y_1/b \approx 3.1$, $V_1/V_c \approx 1.0$)

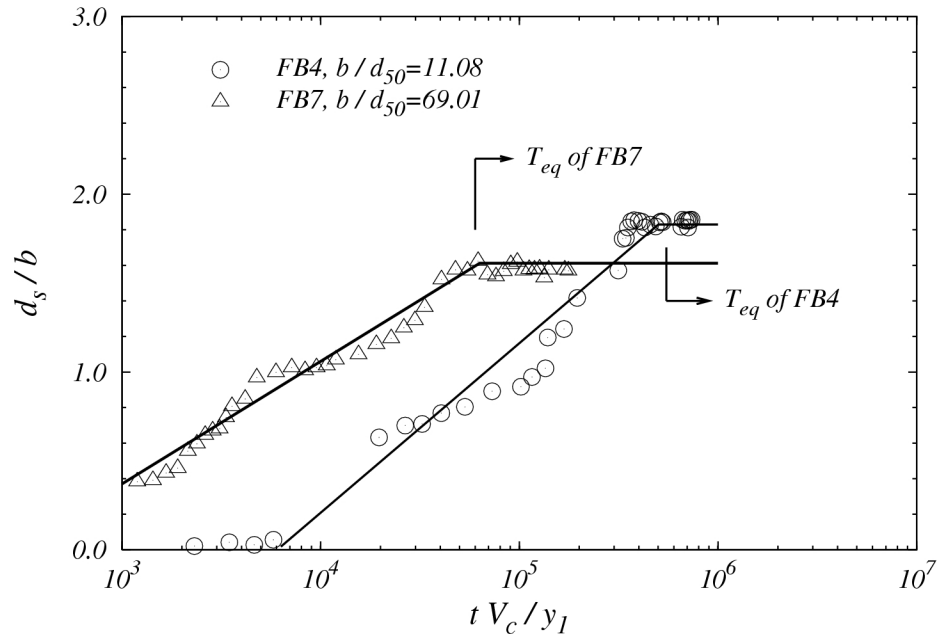


Figure 6.7 Effect of b/d_{50} on temporal development of scour depth of FB4 and FB7 in the Flint River models (Scale=1/50, $y_1/b \approx 4.3$, $V_1/V_c \approx 0.9$)

6.3 Analysis of Maximum Scour Depth and Location

In general, the maximum scour depth around a single pier occurs at the nose of the pier; however, the location of the maximum scour depth for complex bridge piers (multiple piers with variable spacing) does not necessarily occur at the nose of the pier. The location of maximum local scour is dependent on hydraulic parameters, sediment properties and the complexities of the geometry of the pier bents as well as the orientation of the piers and bridge opening to the approach flow. Based on scour contours of each experiment for the Flint River modeling as shown in Figure 5.20, most occurrences of maximum scour depth were indeed at the nose of the first pier except for experimental runs FB1, FB2, FB3, and FB4 for the flat-bed experiments..

For the Flint River models, the Froude numbers were higher and the footings of the bridge pier bent were completely exposed for those exceptional cases in which the maximum scour depth occurred somewhere other than the nose of the pier. The contribution of the downflow to scour development in front of the first pier is reduced when the footing is exposed. The horseshoe vortex wraps around the first pier and footing and is stretched downstream. The degree of the stretching becomes higher as the flow velocity increases and the Froude number becomes larger. The limbs of the horseshoe vortex system along both sides of the pier become longer and stronger causing the location of the maximum scour depth to move downstream.

For the Chattahoochee River modeling, the third pier in the downstream direction sometimes became the critical one in terms of the maximum scour depth among the river model experiments. As the flow separates around the first pier, the whole region around the bridge pier bent becomes separated and tornado vortices are generated just behind

each pier. As mentioned in Chapter 3, the pier bent in the Chattahoochee River models has an inner web between two inner piers. Due to the inner web, the tornado vortices under this web are confined and intensified and contribute to the development of scouring in the region under the inner web. The maximum scour depth occurred around the third pier for the smaller sediment size and lower flow depth even though the Froude number was approximately the same. If the effect of flow depth is neglected and the flow condition is assumed to be equal, the smaller sediment is more susceptible to be suspended and eroded by the tornado vortices under the inner web. Due to the complex bridge pier structure in the Chattahoochee River model, the maximum scour depth was hard to predict with standard equations from the literature.

In the following analyses, pier scour depths will be considered only at the nose of the pier in order to make comparisons with existing formulas and field measurements. However, a procedure will be developed for scaling up of laboratory model results based on reproducing pier scour depths at the nose of the pier so that complex piers, for which the maximum scour depth may occur elsewhere, can be reliably modeled in the laboratory.

6.4 Performance of Existing Pier Scour Formulas

The scour depths measured at the nose of the upstream pier in the Chattahoochee River flat-bed modeling are compared with the commonly accepted scour formulas in Figure 6.8. The effect of the flow intensity, V_1/V_c , on the dimensionless scour depth, d_s/b , is observed by comparison with scour prediction formulas having constant values of

$y_1/b \approx 4.0$ and $b/d_{50} = 13.9$. The approach Froude number is given as a label on each data point. The data points at low values of Fr_1 are close to the Melville and Sheppard formulas while the data points approach the HEC-18 formula as Fr_1 continuously increases. The HEC-18 formula includes the effect of the approach Froude number but does not include the parameter bearing the effect of V_1/V_c . Conversely, the other two formulas, the Melville and the Sheppard formulas, include the effect of V_1/V_c but do not consider the approach Froude number. Also, the Melville and Sheppard formulas include a reduction in d_s/b because the relative sediment size, b/d_{50} is less than 25. The effect of the relative flow depth, y_1/b , has an effect only in the HEC-18 formula because the value of y_1/b is large enough that it has almost no influence in the Melville and Sheppard formulas.

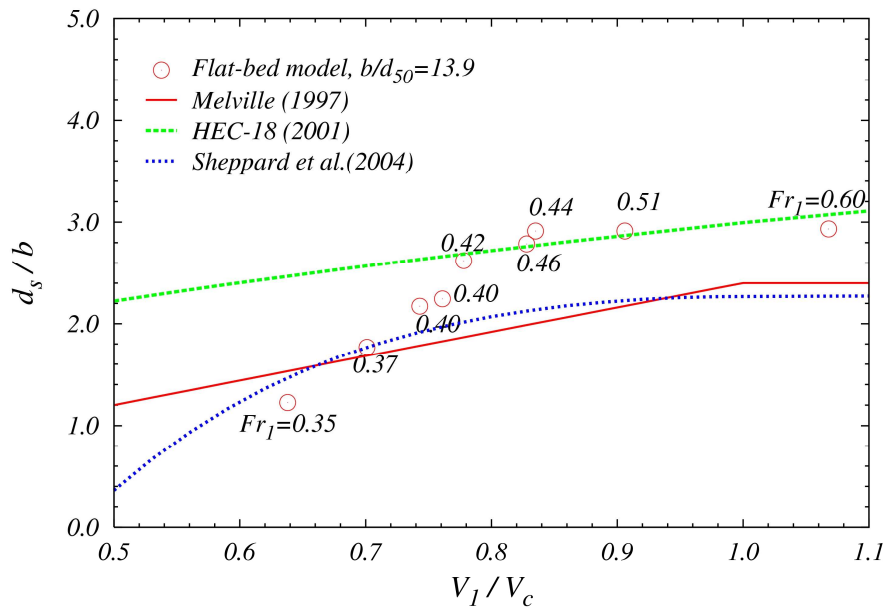


Figure 6.8 Comparison of measured scour depths in Chattahoochee River flat-bed model with scour prediction formulas (Scale=1/23, $y_1/b \approx 4.0$, $b/d_{50} = 13.9$)

In Chattahoochee River model experiments, a smaller sediment size was used and thus the value of b/d_{50} became 24.5 at which the effect of b/d_{50} only slightly influences the predicted scour depth in the Melville and Sheppard formulas. However, changing the sediment size influences the HEC-18 formula since the critical velocity becomes smaller and consequently the approach velocity in the Froude number in the HEC-18 formula becomes smaller for matching the same V_1/V_c in Figure 6.9. In addition, the predicted values of d_s/b by the HEC-18 formula also become smaller for higher values of b/d_{50} as shown in Figure 6.9 where the value of b/d_{50} was changed while the influence of y_1/b is the same as in Figure 6.8. Thus, the three prediction curves are observed to be close to one another. For lower values of Fr_1 , all formulas (the Melville, HEC-18 and Sheppard formula) show relatively good agreement with the laboratory data in Figure 6.9.

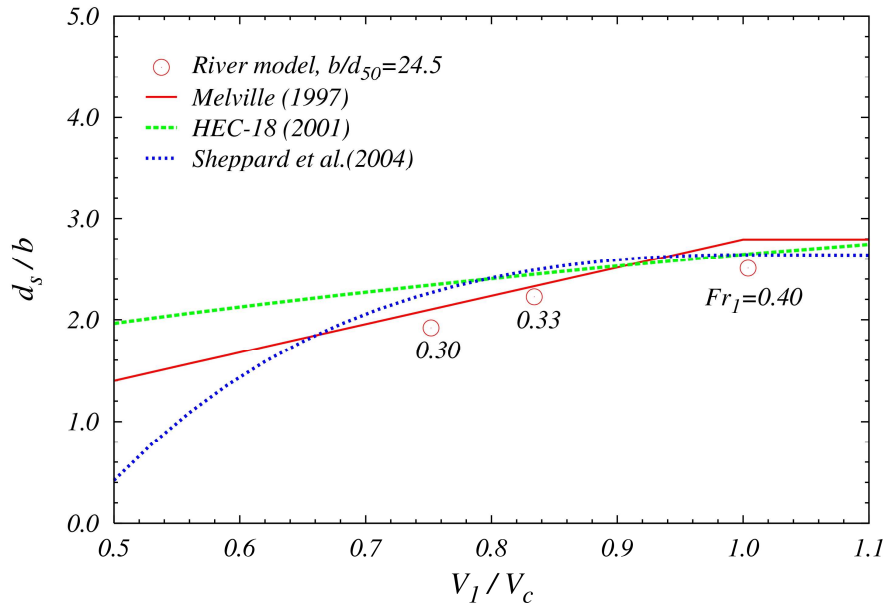


Figure 6.9 Comparison of measured scour depths in Chattahoochee River model with scour prediction formulas (Scale=1/40, $y_1/b \approx 4.0$, $b/d_{50} = 24.5$)

Field measurements by the USGS are compared with the laboratory data from the Chattahoochee River model as shown in Figure 6.10. The approach Froude numbers are shown next to the data points which have a constant value of $y_1/b \approx 4.0$. The laboratory data with $b/d_{50} = 24.5$ agree relatively well with all three formulas even though HEC-18 overpredicts the scour depth for the lowest Froude number. However, the field data is in the live bed scour regime with the values of $y_1/b \approx 4.0$ and $b/d_{50} = 1569$. The Melville and HEC-18 formulas overpredict the dimensionless scour depths while the Sheppard formula shows reasonably good agreement with the field data considering that the Sheppard formula has been extrapolated beyond the maximum value of $b/d_{50} = 564$ in the formula data base. On the other hand, the Sheppard formula underpredicts the dimensionless scour depth for the Flint River field data in Figure 6.11 and the Ocmulgee River field data in Figure 6.12 even though it agrees relatively well with the laboratory data. These comparisons highlight the impression of field engineers that scour formulas based on laboratory data are somewhat unreliable.

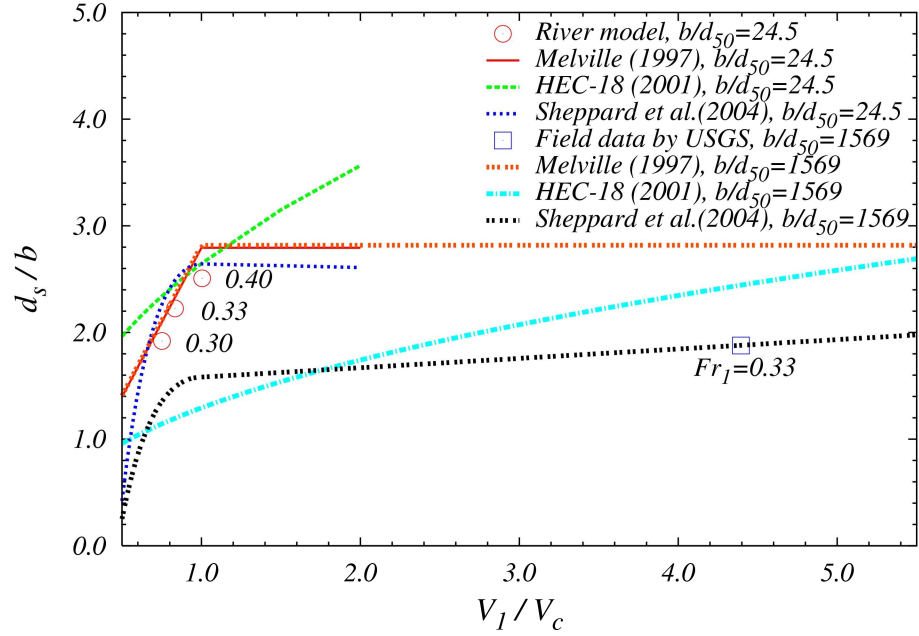


Figure 6.10 Comparison of field and laboratory measurements of scour depths and scour prediction formulas for Chattahoochee River model (Scale=1/40, $y_1/b \approx 4.0$, $b/d_{50} = 24.5$)

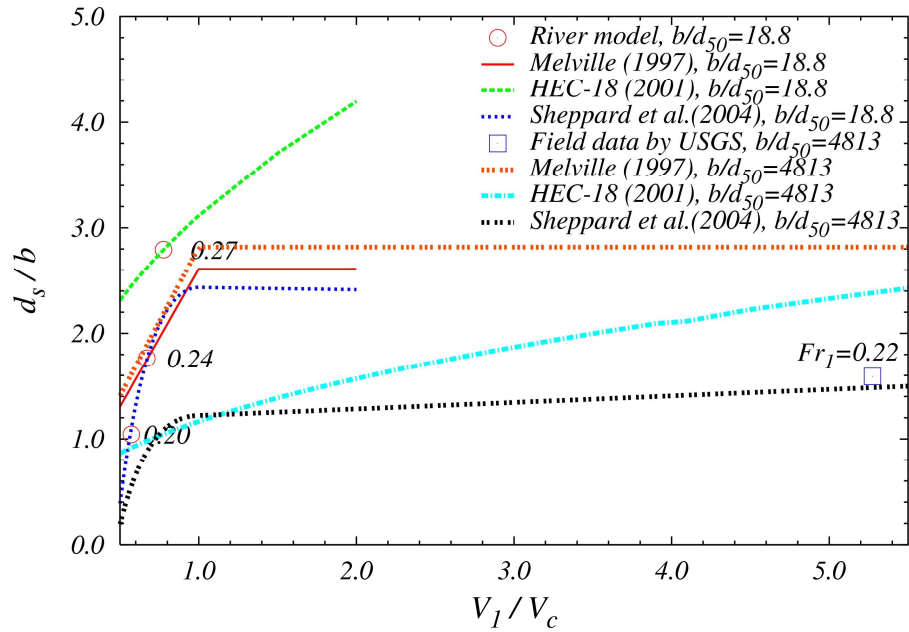


Figure 6.11 Comparison of field and laboratory measurements of scour depths and scour prediction formulas for Flint River model (Scale=1/90, $y_1/b \approx 7.0$, $b/d_{50} = 18.8$)

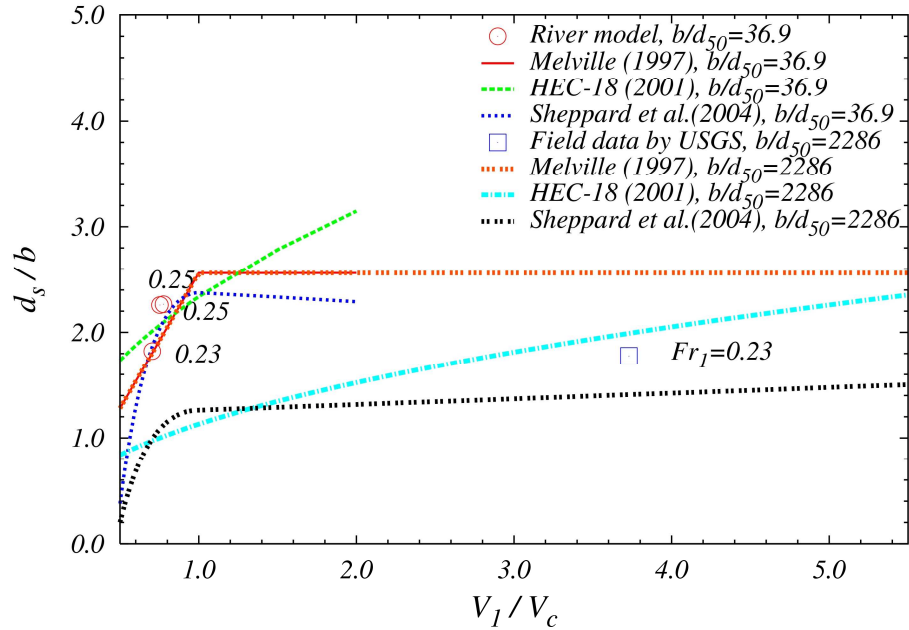


Figure 6.12 Comparison of field and laboratory measurements of scour depths and scour prediction formulas for Ocmulgee River model (Scale=1/45, $y_1/b \approx 5.0$, $b/d_{50} = 36.9$)

6.5 Analysis of Velocity Field and Turbulence Intensity around Piers

Scour patterns and velocity field measurements for the fixed-bed experiments in both the Chattahoochee River model and the Flint River model were shown previously in Figures 5.8, 5.9, 5.22 and 5.23. The horizontal velocity vector plots shown there at a distance of 40 percent of the depth above the bed did not indicate large changes in the velocity field with scour development when comparing the before-scour and after-scour conditions. The velocity vector plots of two cross sections inside the scour hole were also presented in Figure 5.23. A small downflow was observed at the upstream cross section of the pier

located at a distance of $1.6 b$ upstream of the pier, while a symmetric secondary flow pattern was detected and strong upward velocity vectors were shown to occur at the cross section where the maximum scour depth occurred at a distance of $3.8 b$ downstream of the pier.

The measured mean velocity and turbulence kinetic energy (TKE) fields were used to validate the three dimensional numerical model. Most of the simulated velocity profiles at several locations were in good agreement when the measured and simulated cross-stream velocity profiles at various flow depths were compared for the fixed-bed case (Ge et al. 2005). As shown previously in Chapter 5, these results indicate an elevated level of TKE alongside the pier bent when compared with a uniform shear flow, but quantitative connections with the scour depth are difficult to make. In addition, results from a three-dimensional numerical model show that the maximum in mean shear stress on a fixed bed does not correspond with the maximum depth of scour hole in front of the piers (Ge et al. 2005). It is concluded that the details of the horseshoe vortex itself must be investigated further to understand the development of the scour hole in front of the pier rather than the general turbulence characteristics of the near field.

6.5.1 Temporal Variation of Flow and Turbulence Characteristics upstream of the Bridge Pier

In an effort to better understand the relationship between the flow field and the resulting pier scour over time, a separate experiment was run in the tilting flume on the 1:23 scale model of the central pier bent of the Chattahoochee River bridge. Bed elevations and three dimensional velocity components upstream of the bridge pier were measured

intermittently at two fixed points during the scour process to capture the temporal variation of flow characteristics as the scour hole developed. The flow was not stopped for the measurements so they necessarily were made at only two points so that the measurements could be completed in a time duration that was short (approximately 5 minutes) in comparison to the rate of scour hole development. The two measured points were located horizontally at a distance of one pier width upstream of the bridge pier in the streamwise direction. As shown in Figure 6.13, the vertical location of one point (LOC1) was in the scour hole itself where it was varied to maintain a constant vertical displacement above the bed as the scour hole deepened with time. The other point (LOC2) was fixed above LOC1 but at a constant elevation that was close to the initial bed elevation before scour began as also shown in Figure 6.13.

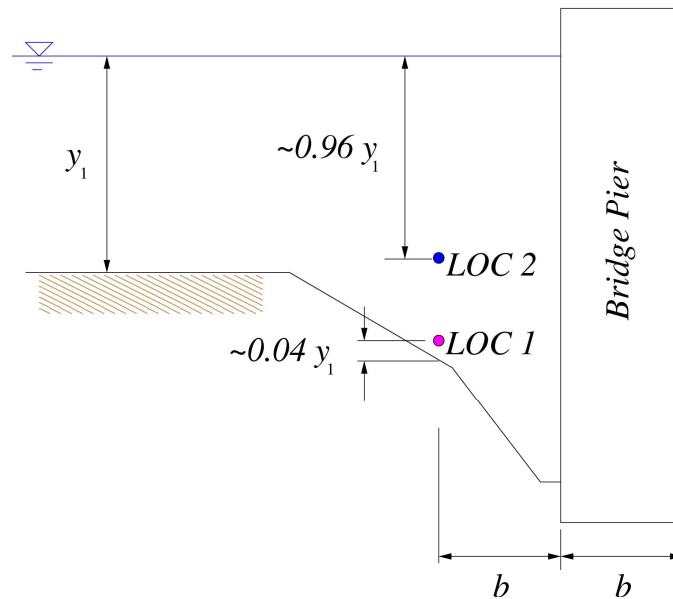


Figure 6.13 Schematic of the locations for measuring the temporal variation of flow characteristics with the flat bed model in Chattahoochee River modeling (Scale=, 1/23, $V_1/V_c = 0.85$, $y_1/b = 4.17$, $b/d_{50} = 86.8$)

The 1:23 scale Chattahoochee River bridge model was chosen for this experiment as the largest model among all of the bridge models excluding the Flint River models because of the complication of exposed footings occurring during scour development in those models. Sufficient clearance between the bridge pier and the ADV probe was needed in order to place the ADV probe without bumping the pier or disturbing the horseshoe vortex system upstream of the bridge pier.

The mean velocity profiles at LOC1 and LOC2 are shown in Figure 6.14 and Figure 6.15. The mean velocities in both vertical and streamwise directions at LOC1 fluctuated slightly with time, but the mean values remained close to zero as the scour depth increased with time which is shown on the secondary y-axis in Figure 6.14. The averaged values became close to zero at LOC1 since it is located near the bed in the separation zone. However, the mean velocities at LOC2 fluctuated significantly with time as shown in Figure 6.15 because the vertical position of LOC2 moved into the highly turbulent region associated with the horseshoe vortex during development of the scour hole. The fluctuations in the streamwise velocity seem to be associated with the intermittent fluctuations in the scour hole depth that may result from the collapse of the sides of the hole followed by further scouring as the hole enlarges.

The turbulence intensity in both the streamwise and vertical directions at LOC1 increased during the initial stage of scour development and then became smaller with time as shown in Figure 6.16. The large fluctuations of streamwise turbulence intensity during the initial stages of scour development may be due to the unsteadiness of the location of the separation point upstream of the pier. As the scour depth changed rapidly during the initial stage, the vertical turbulence intensity became approximately four times

larger than at later stages of scour hole development indicating that the contribution of vertical turbulence intensity to the rate of scour development was very significant during the initial stage.

Figure 6.17 shows that the turbulence intensity in both vertical and streamwise directions at LOC2 approached the same constant value as the scour hole developed. The vertical turbulence intensity at LOC2 was relatively small at the beginning of the scour process but then increased significantly to a value greater than that at LOC1. This is likely due to the movement of the vertical location of LOC2 into the highly turbulent region associated with the horseshoe vortex but it occurred after the scour hole was nearly fully developed.

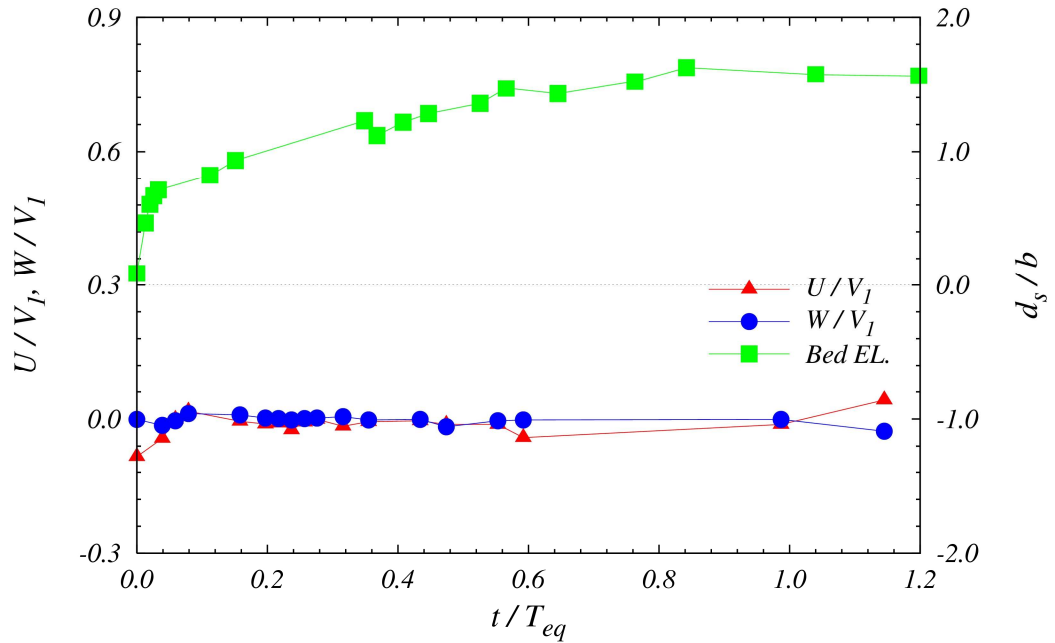


Figure 6.14 Mean velocity profile with time at LOC1 (Scale1/23, $V_l/V_c = 0.85$, $y_1/b = 4.17$, $b/d_{50} = 86.8$)

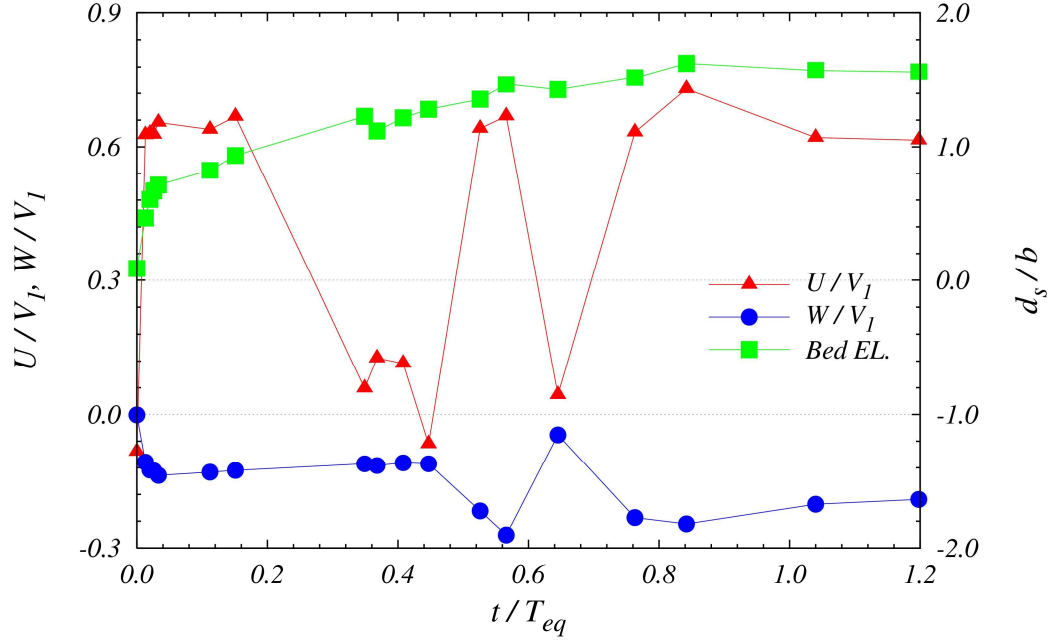


Figure 6.15 Mean velocity profile with time at LOC2 (Scale=1/23, $V_I/V_c = 0.85$, $y_1/b = 4.17$, $b/d_{50} = 86.8$)

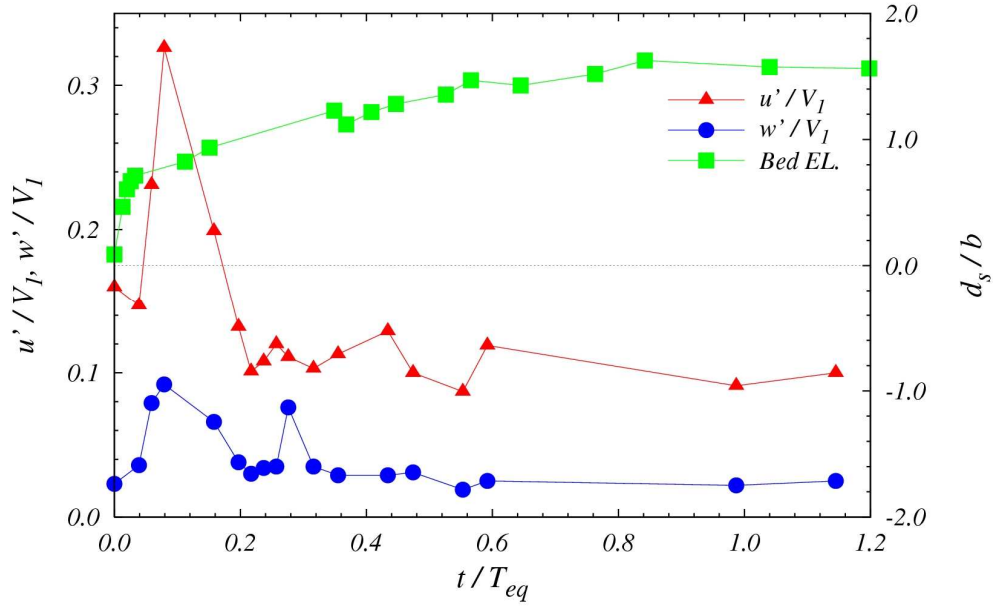


Figure 6.16 Temporal variation of turbulence intensity profile with time at LOC1 (Scale=1/23, $V_I/V_c = 0.85$, $y_1/b = 4.17$, $b/d_{50} = 86.8$)

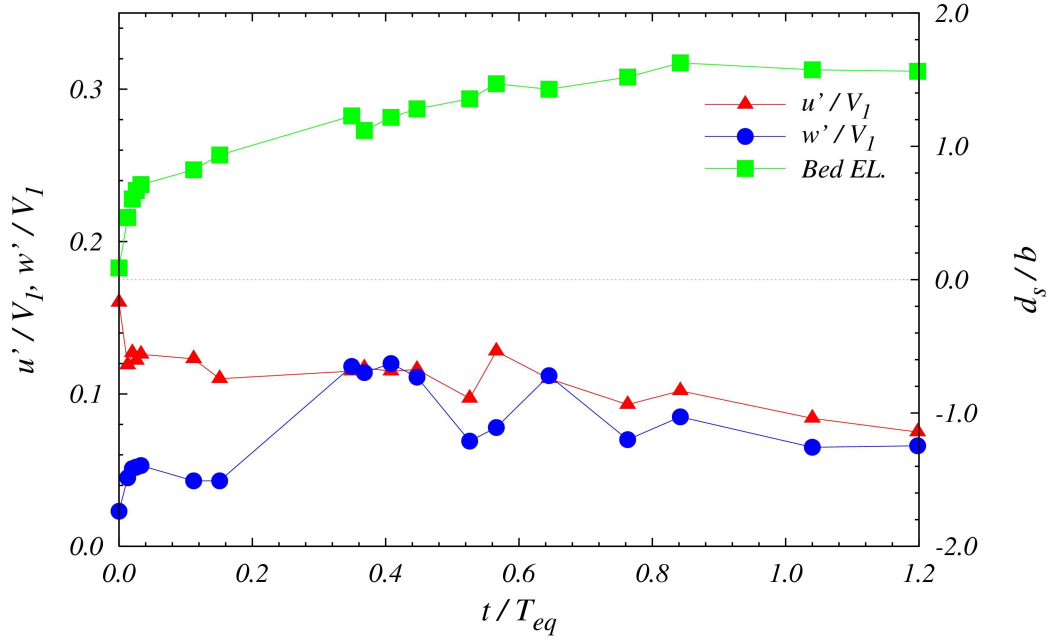


Figure 6.17 Temporal variation of turbulence intensity profile with time at LOC2 (Scale=1/23, $V_l/V_c = 0.85$, $y_1/b = 4.17$, $b/d_{50} = 86.8$)

6.5.2 Flow Characteristics upstream of the Bridge Pier

While in the previous section, the long-term temporal development of the scour hole was considered in relationship to the changing velocity and turbulence characteristics in the scour hole, this section investigates the short-term transient behavior of the flow immediately upstream of the bridge pier on a fixed flat bed in the region of flow separation and the horseshoe vortex. As discussed in Chapter 2, the primary horseshoe vortex is itself unsteady with the formation of a system of secondary vortices that quasi-periodically combine with the primary vortex increasing its size and strength and the degree of stretching around the pier (Dargahi 1989; Simpson 2001). The measurements of flow characteristics near the bed in the region of the fluctuating horseshoe vortex are discussed in this section.

Based on the literature (Devenport and Simpson 1990) and a flow visualization of the horseshoe vortex as shown in Figure 6.18, the temporal variation of the horseshoe vortex upstream of a bridge pier can be sketched conceptually as shown in Figure 6.19. The primary horseshoe vortex oscillates in position and size in an irregular shift between two modes of behavior. The instantaneous velocity time series when measured near the bed at $x/b = -0.33$, for example, alternately exhibits periods of positive streamwise velocity towards the pier followed by negative streamwise velocity away from the pier. The result is a bimodal velocity distribution first described by Devenport and Simpson (1990) for a wing-flat bed junction studied in a wind tunnel. They suggested that these two alternate states of the horseshoe vortex are bistable with the contracted mode occurring about 20-30% of the time. They further hypothesized that the origin of this large-scale unsteadiness is due to regions of turbulent vs. non-turbulent fluid being drawn into the corner formed by the wing and lower solid boundary from the outer portion of the boundary layer.

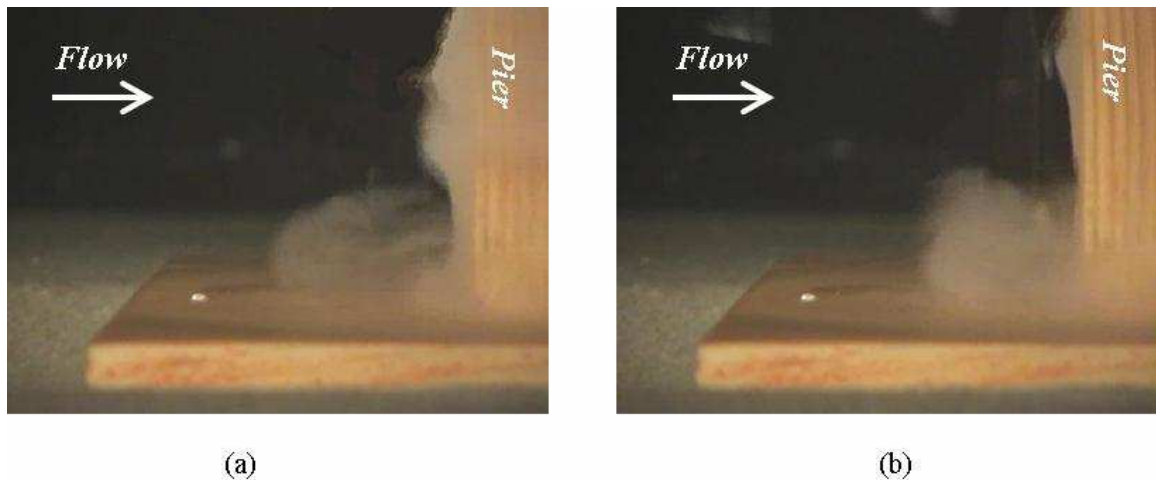


Figure 6.18 Flow visualization of horseshoe vortex with tracer injection in experimental run FB10 in Flit River model: (a) $t=t_1$ and (b) $t= t_1+2.26\text{sec}$

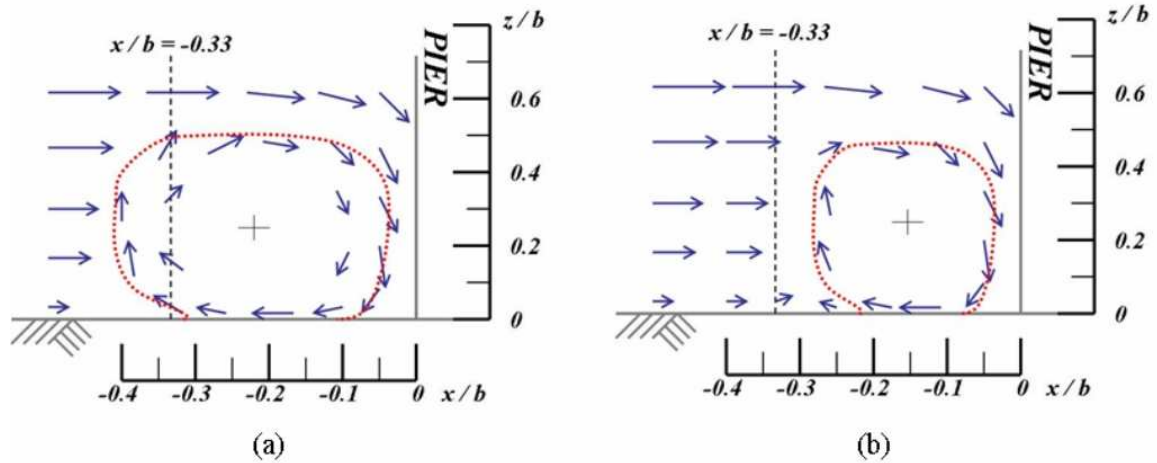


Figure 6.19 Schematic of temporal variation of horseshoe vortex upstream of a pier: (a) $t=t_1$ and (b) $t=t_1+\Delta t$, where dotted lines show bimodal regions for velocity components in streamwise and vertical direction

In order to determine if the large-scale unsteadiness of the horseshoe vortex could be observed quantitatively in the case of a rough flat bed and a rectangular bridge pier, the streamwise and vertical velocity components were measured upstream of the 1:23 scale model of the Chattahoochee River bridge pier at a location of $x/b \approx 0.3$ upstream of the face of the rectangular pier and at a distance above the bed of $z/b = 0.17$ ($z/y_1 = 0.04$). This horizontal location corresponds approximately to the primary separation point of the horseshoe vortex system reported by Dargahi (1989) for a single cylinder.

Because of the existence of two bistable modes of the horseshoe vortex as described by Devenport and Simpson (1990), a bimodal probability distribution with dual peaks having different mean values was also observed in this study for both the streamwise and vertical velocity components at the selected measuring location on a fixed flat bed as shown in Figure 6.20.

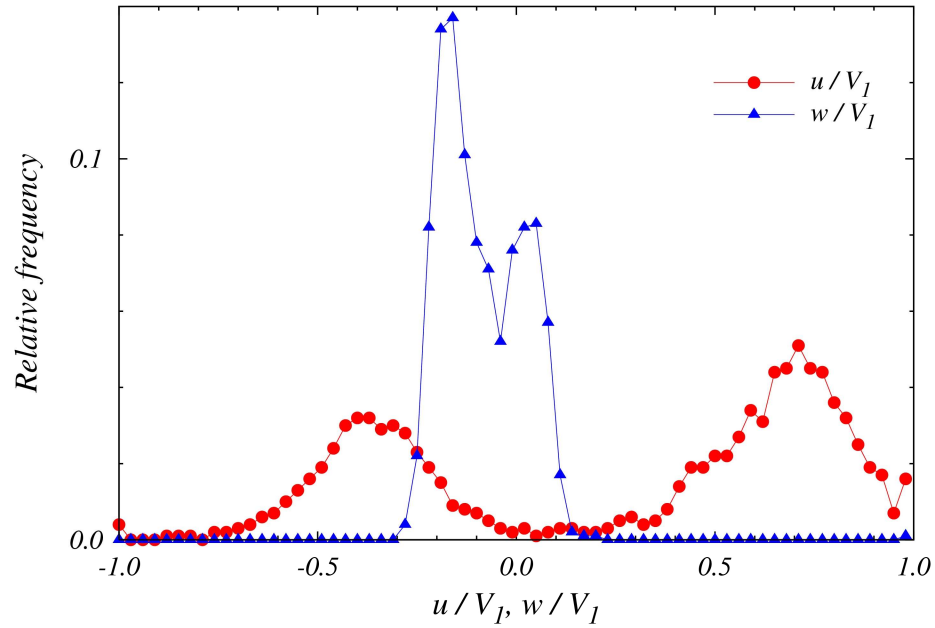


Figure 6.20 Velocity probability distribution from experimental run FB7 in the Chattahoochee River model at $x/b = -0.33$, $z/b = 0.17$

A thin layer of reverse flow exists near the bed due to the horseshoe vortex which accounts for the negative streamwise velocity, but as the separation point switches to a position closer to the pier, the streamwise velocity becomes positive at the measuring location. Practically, the thickness of the reverse flow layer could not be measured with the ADV, but the measurements shown in Figure 6.20 clearly confirm the oscillating nature of the horseshoe vortex system. The negative values of the vertical velocity components were measured about 73.4% of the time while the positive values existed only 26.6% of the time. Hence, the height of the second peak on the positive side is smaller than that on the negative side, which is dependent on the location of the measurement. Since the location of separation in front of the pier also oscillates according to the oscillation of the horseshoe vortex system, the negative vertical velocity components due to the effect of the downflow can be detected much more of the time if

the location of the measurement is closer to the pier. For higher values of z/b or z/y_1 , the bimodal feature of the velocity distribution was not observed to occur. Davenport and Simpson (1990) found that the shape, relative size and distance between the two peaks of the bimodal probability density function of instantaneous velocities are not permanent and stable, but instead vary with the position of the velocity measurement.

With respect to the turbulence characteristics just upstream of the pier in the horseshoe vortex region, quadrant analysis was used to further characterize the turbulent events associated with the large-scale unsteadiness of the horseshoe vortex. Quadrant analysis was employed in this study by examining the joint frequency distribution of the streamwise and vertical components of fluctuating velocity, u' and w' .

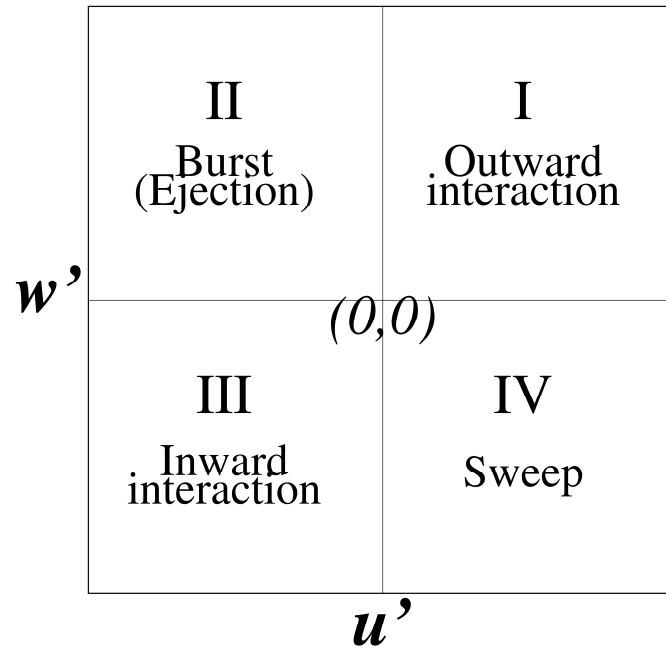


Figure 6.21 Schematic of the plate for quadrant analysis (Marchioli and Soldati 2002b)

The four quadrants shown in Figure 6.21 correspond to four types of turbulent events which are defined as: I. outward interactions; II. ejections or bursts; III. inward interactions; and IV. sweeps that characterize the individual turbulent velocity measurements. The Reynolds stress is generally produced by all four types of events. The first quadrant event, I, is characterized by outward motion of high-speed fluid, with $u' > 0$ and $w' > 0$; the second quadrant event, II, is identified by outward motion of low-speed fluid, with $u' < 0$ and $w' > 0$, which is usually called ejection or bursts; the third quadrant event, III, is associated with inward motion of low-speed fluid, with $u' < 0$ and $w' < 0$; and finally, the fourth quadrant event, IV, represents the motion of high-speed fluid toward the bed, with $u' > 0$ and $w' < 0$, and it is called sweeps.

The relationships between the fluid motions and particle transfer near the wall may be elucidated through quadrant analysis. The ejections and sweeps contribute positively to the bed shear stress since $\overline{u' w'}$ is the flux of forward momentum to the bed, while the outward and inward interactions contribute negatively to the bed shear stress. The presence of a sweep corresponds to a local increase of the shear stress at the bed whereas the occurrence of an ejection corresponds to a local decrease of the shear stress at the bed. Therefore, the coherent sweep and ejection events appear to be responsible for transferring particles toward and away from the bed (Marchioli and Soldati 2002b). However, in nonuniform flows such as the wake region downstream of a backward-facing step, Nelson et al.(1995) have shown that turbulent events with the same shear stress contribute to different sediment transport rates due to the frequency structure of the turbulent events. While the horseshoe vortex is not expected to have the same turbulence structure as a turbulent wake, nevertheless, it does have the property of intermittency that

may be an important contributor to the scour process.

Among the velocity measurements made in experimental run FB7 for the Chattahoochee River models, two time series of velocity data at the nose of the pier were selected to conduct the quadrant analysis and to investigate the change of flow characteristics for the before-scour and after-scour conditions as shown in Figure 6.22 and Figure 6.23.

The first time series analyzed in Figure 6.22 was measured for the fixed bed condition while the time series analyzed in Figure 6.23 was measured inside the scour hole under the same flow conditions (run FB7) at approximately the same distance above the bed. Joint frequency distributions in both figures are normalized to the peak values of 1.0 and it is necessary to multiply the contoured values by the scaling factors in the middle of the top of each figure to produce probability densities instead of frequency. The selected locations were not exactly the same with a 17% difference in streamwise direction but only a 5% difference in vertical direction due to the uncertainty associated with reading the location of the instrument carriage where the ADV was mounted, but the points were both in the region of the horseshoe vortex and separated region upstream of the pier.

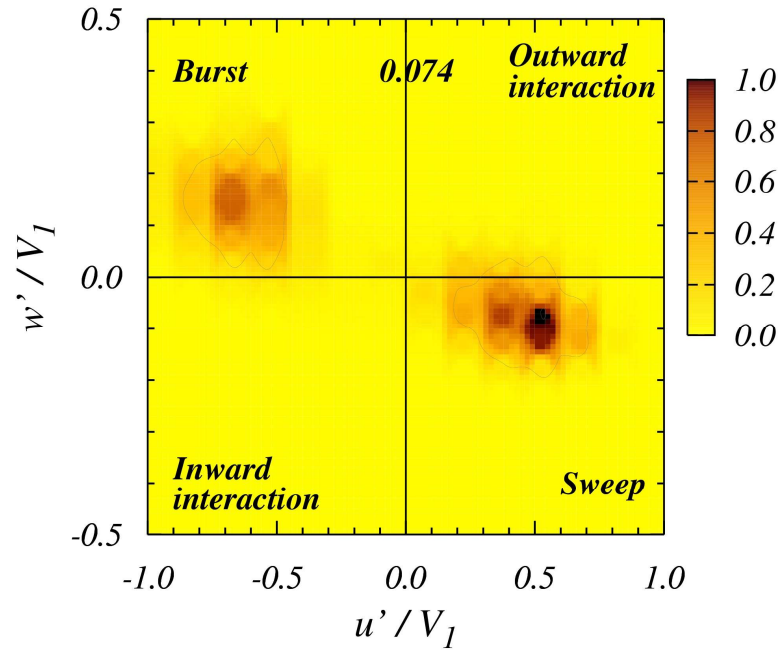


Figure 6.22 Joint frequency distribution of u' and w' for before-scour case at $x/b = -0.33$, $z/b = 0.17$ for experimental run FB7 in the Chattahoochee River model

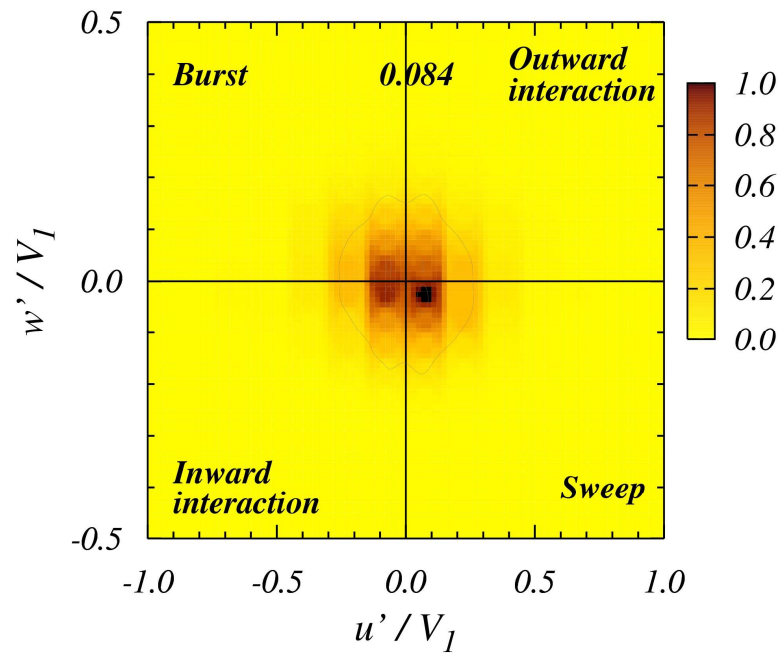


Figure 6.23 Joint frequency distribution of u' and w' for after-scour case at $x/b = -0.40$, $z/b = 0.18$ for experimental run FB7 in the Chattahoochee River model

The results of quadrant analysis show a significant difference between the before-scour and after-scour cases in Figure 6.22 and Figure 6.23. The turbulent events for the before-scour condition were dominated by bursts and sweeps with a bimodal joint frequency distribution at the elevation of $z/b = 0.17$. (A separate measurement at a higher elevation of $z/b = 0.42$ did not show the bimodal distribution in agreement with the measurements of Devenport and Simpson (1990)). In Figure 6.22 before scour, sweeps events had a higher probability of occurrence, and for both types of events, the values of u' were greater than those of w' at the maximum probability of occurrence. The bursts and sweeps are likely the primary forcing function for creating the scour hole because they both represent positive shear stress; however, the more important characteristic is the irregular oscillation between the two types of events as the horseshoe vortex alternately expands and contracts as the separation point moves back and forth. The sediment particles are lifted and entrained in an intermittent fashion as shown by the flow visualization in the following section. In the equilibrium scour hole in Figure 6.23 at approximately the same distance above the bed as for the before-scour condition, the turbulent events no longer display the bimodal distribution with all four types of events becoming approximately equally likely. The magnitude and frequency of all events are significantly affected by the change of the flow inside the scour hole. There is no effective event of the velocity fluctuations for altering the shear stress or moving the sediment out of the equilibrium scour hole. Although the existence of the bimodal distribution depends on the measuring location, it is significant that it disappears near the bed after scour and at the same distance above the bed as for the before-scour case.

As a further indication of the differences in the turbulence properties as the scour

hole develops, the integral time scale was computed for both the before-scour and after-scour time series associated with Figure 6.22 and Figure 6.23. The integral time scale is defined as a measure of the time over which a velocity component is dependent on its past values and a rough measure of the time interval over which a fluctuating velocity component is highly correlated with itself. It is obtained by integration of the measured autocorrelation distribution over time. It can be a measure of the memory of the process (Kundu 1990; Tennekes and Lumley 1972). As given in Table 6.1, it can be observed that the integral time scale in the vertical direction for the before-scour case is considerably higher than for the after-scour case, while in the streamwise direction the time scale is the same order of magnitude for both cases. The vertical fluctuation in the before-scour case may be a significant contributor to the processes of suspending and eroding sediment from the bed. Accordingly, a longer integral time scale of the velocity fluctuations gives more transport than a shorter integral time scale when the rate of sediment transport increases very rapidly at the initial stage of scour development.

Table 6.1 Comparison of integral time scales for before and after scour cases

	Before scour, sec	After scour, sec
Streamwise direction	1.8	1.3
Vertical direction	4.3	0.7

6.6 Flow Visualization For Motion of Sediment

The flow characteristics in the scour hole were just considered in terms of the temporal variation of velocities and turbulent intensities in the streamwise and vertical directions.

Also, the contribution of the velocity fluctuations to the scour depth was investigated with quadrant analysis of the experimental data. While the oscillation of the vortex system was explained based on the frequency analysis of the velocity data measured in front of the pier in the previous section, this section provides visualization of the sequence of sediment motions due to oscillations of the horseshoe vortex system. To investigate the motion of sediment near the pier, a video camera was used to take movies of the motion of sediment particles. The 1:40 scale model of the Chattahoochee River bridge pier was selected as shown in Figure 6.24 and Figure 6.26, respectively. Two different sizes of sediments, $d_{50} = 0.5\text{mm}$ and $d_{50} = 3.3\text{mm}$ were chosen to examine the features of the unsteady, large-scale coherent sediment motions in the horseshoe vortex system affected by two different values of b/d_{50} under approximately the same flow conditions.

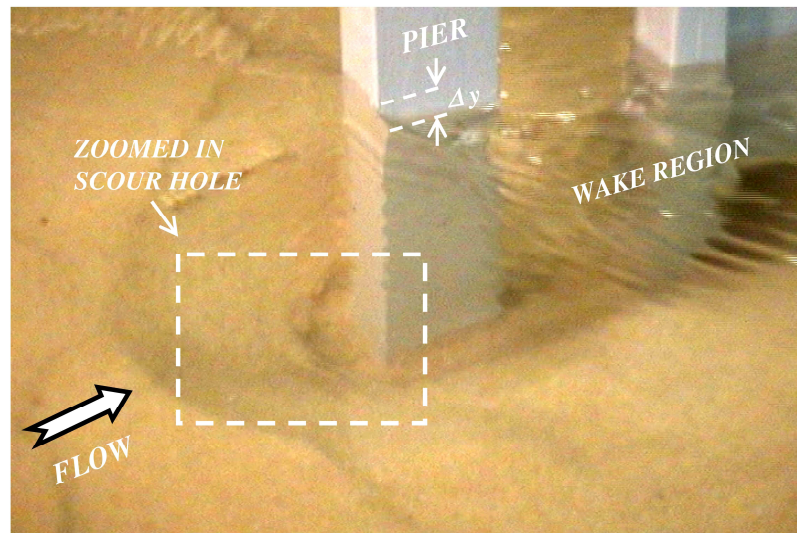


Figure 6.24 Profile of the 1:40 scale model of the Chattahoochee River bridge with $d_{50} = 0.5\text{mm}$ ($V_1/V_c = 0.70$, $y_1/b = 5.0$, $b/d_{50} = 50.9$)

The sequence of images for each case are captured focusing on the region in front of the pier as shown in Figure 6.25 and Figure 6.27, respectively. The flow direction and the height of surface roll-up (bow wave) are sketched on both figures.

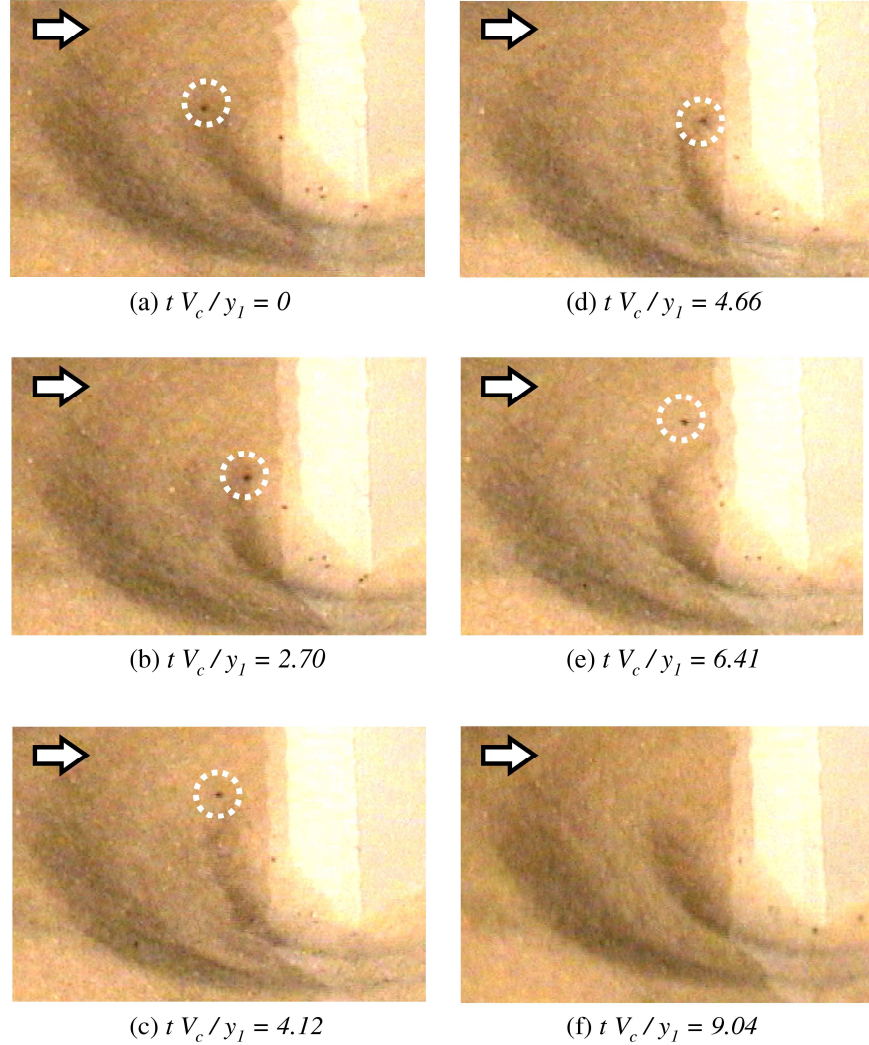


Figure 6.25 Sequence of the captured motions of sediments with dimensionless time scale, $t V_c / y_l$ ($V_l / V_c = 0.70$, $y_l / b = 5.0$, $b / d_{50} = 50.9$)

Figure 6.25 shows the temporal tracking of a tiny particle marked by the dashed circle on each sub-figure for $b / d_{50} = 50.9$. The size and weight of the marked particle is

approximately the same as the sediment and can be assumed to travel with the same tendency as the sediment in the horseshoe vortex system. It is observed that there are two different slopes of scour holes in front of the pier in Figure 6.25; the slope of the outer one is approximately equal to the angle of the repose of the sediment while the slope of the inner one underneath the primary horseshoe vortex is steeper than that of the outer one because this portion is affected by the combination of the downflow and horseshoe vortex. First, the particle slides into the inner scour hole as the outer one collapses as shown at (b) in Figure 6.25. The particle moves back to the upstream boundary of the inner scour hole due to the irregular oscillation of the horseshoe vortex while it remains suspended and at the same time, the particle drifts transversely along the pier due to the limbs of the horseshoe vortex in (c) and (d). It falls into the inner scour hole again due to the slope failure of the outer hole in (e), and finally, the particle is washed out when it is dislodged again by the horseshoe vortex to disappear in (f).

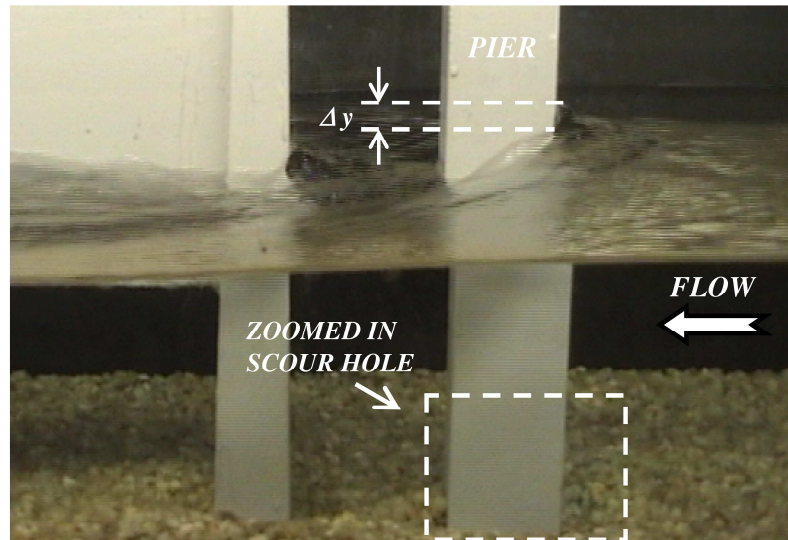


Figure 6.26 Profile of the 1:40 scale model of the Chattahoochee River bridge with $d_{50} = 3.3\text{mm}$ $V_1/V_c = 0.72$, $y_1/b = 5.0$, $b/d_{50} = 8.2$)

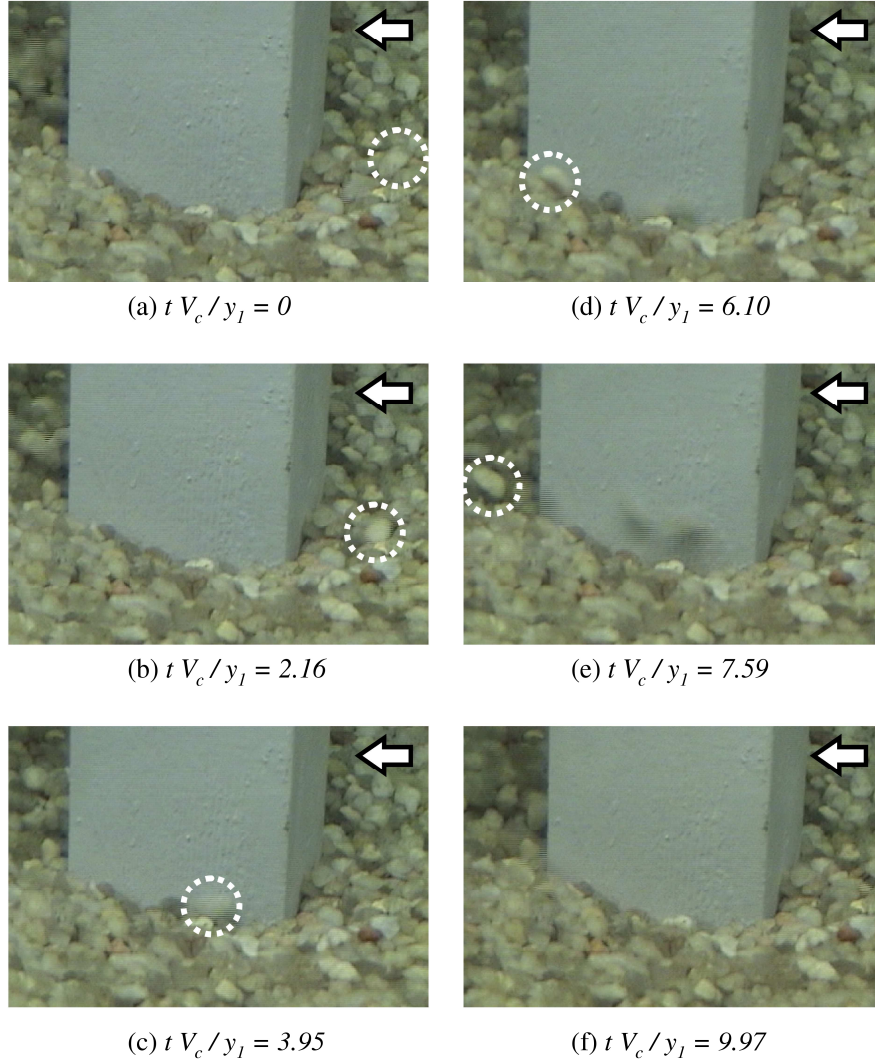


Figure 6.27 Sequence of the captured motions of sediments with dimensionless time scale, $t V_c / y_l$ ($V_l / V_c = 0.72$, $y_l / b = 5.0$, $b / d_{50} = 8.2$)

For the lower value of b/d_{50} of 8.2 (higher value of d_{50}), the process and pattern of the motion of the sediment particles is evidently different compared with the motion at the higher value of b/d_{50} as shown in Figure 6.27. In Figure 6.27, it is difficult to recognize the inner and outer slopes of the scour hole unlike the previous case. There is no evident reverse motion and suspension due to the horseshoe vortex at the lower value of b/d_{50} . The particle marked with the dashed circle vibrates and then moves in a short

sliding step only to come to rest again. The particle motion continues as a series of short steps until it is washed out along the pier by the limb of the horseshoe vortex.

It is similarly found in both cases that as the sediment particles are carried by the horseshoe vortex from upstream of the pier and into the wake region behind the pier, the particles jump higher and move more furiously due to the wake vortices in comparison to the motions in the horseshoe vortex upstream of the pier. The two different patterns of the sediment motion are observed for different values of b/d_{50} , which may affect the equilibrium scour depth in front of the pier.

6.7 Effect of the Ratio of Pier Width to Sediment Size

As discussed previously, the ratio of pier width to sediment size is a dimensionless parameter that is strongly implicated in the lack of agreement between field measurements of pier scour and predictions of pier scour based on formulas derived from laboratory data. There is no question in the literature that the local scour depth depends strongly on the effect of the ratio of pier width to sediment diameter. In general, larger sediment size relative to the pier width (smaller values of b/d_{50}) can impede the scour process effectively and confine the development of scour depth and width. This effect has been attributed to the dissipating effect of the pores of the larger sediment on the downflow of the horseshoe vortex (Melville and Coleman 2000). What is less clear is why pier scour depth should also decrease at very large values of b/d_{50} (Sheppard et al. 2004a). This section explores the development of a more comprehensive relationship between relative scour depths and b/d_{50} in a way that unifies both experimental and field

data. Then in the following section, reasons for this behavior are explored with respect to the general unsteady flow characteristics of the horseshoe vortex system as discussed in the previous two sections.

The experimental data from the flat bed and river model experiments in this study are plotted along with field measurements from the three field sites monitored in this study in Figure 6.28.

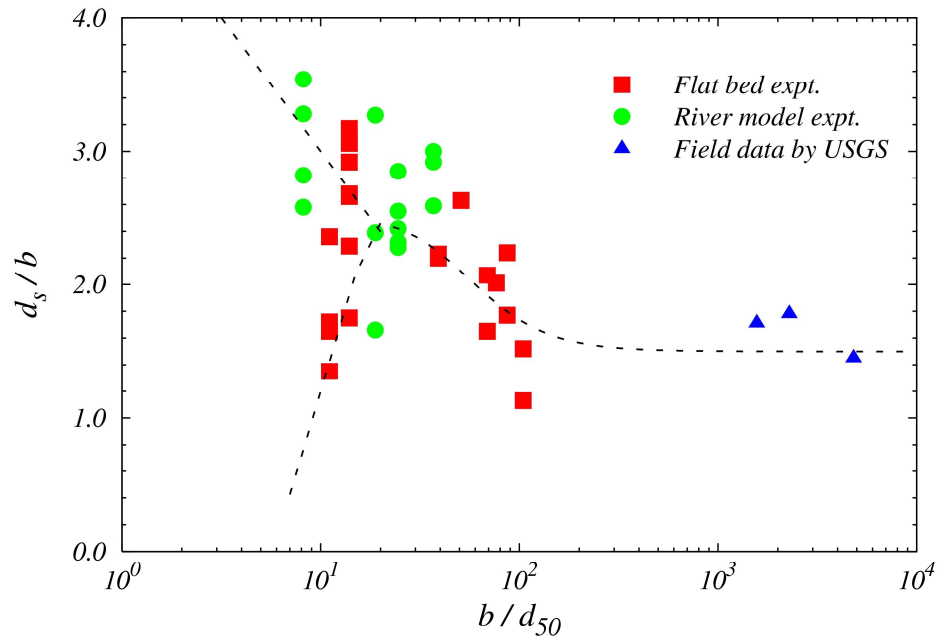


Figure 6.28 Variation of relative local scour depth with the values of pier and sediment sizes

All values of d_s/b were corrected with several factors related to the effects of flow intensity, pier shape, flow depth and skewness due to the angle of attack presented by Melville and Sutherland(1988) so as to isolate the effects of b/d_{50} on maximum pier scour depth. The equations and tables for all factors used for correction are presented in

Appendix A in detail. First, the value of d_s/b was divided by the value from the correction equation for V_1/V_c if $V_1/V_c < 1$ (clear-water scour condition), but if not, live-bed scour conditions occur and no correction for V_1/V_c was made based on the recommendations of the Melville and Sutherland formula. The factor of pier shape presented in Table A.1 is also applied as a correction, and the correction factor for flow depth was considered only if $y_1/b < 2.6$ with which d_s/b was also divided. For the skewness effect, the correction factor that was used is the same one suggested by HEC-18 (Richardson and Davis 2001).

There are two extensions of the relationship in Figure 6.28 for lower values of b/d_{50} which can be classified by the Froude number of the approach flow. When the Froude number is greater than 0.4, the relative scour depth decreases with increasing values of b/d_{50} . However, for the data with $Fr_1 < 0.4$, there is a peak in relative scour depth near the value of $b/d_{50} = 25$, which is in accord with the critical values presented in the literature (Breusers and Raudkivi 1991; Hoffmans and Verheij 1997; Melville 1997). However, these investigators suggested that no effect of b/d_{50} needs to be considered if b/d_{50} is greater than the threshold value of 25; in other words, they assume that no correction factor for b/d_{50} is necessary in this upper range (Melville and Coleman 2000).

6.7.1 Effect of b/d_{50} for $Fr_1 < 0.4$

As discussed previously, large values of the Froude number correspond to large values of the bow wave height at the front of the pier and a strong counter-rotating eddy that can interact with the horseshoe vortex at smaller values of depth. It was found that the data

segregate according to a value of the Froude number of about 0.4. Figure 6.29 shows the effect of the ratio of the pier width to the sediment size on relative scour depth for $Fr_1 < 0.4$. There is clearly a peak where the value of b/d_{50} is about equal to 25 when the values of relative scour depth, d_s/b , from the laboratory data are plotted with respect to b/d_{50} in Figure 6.29.

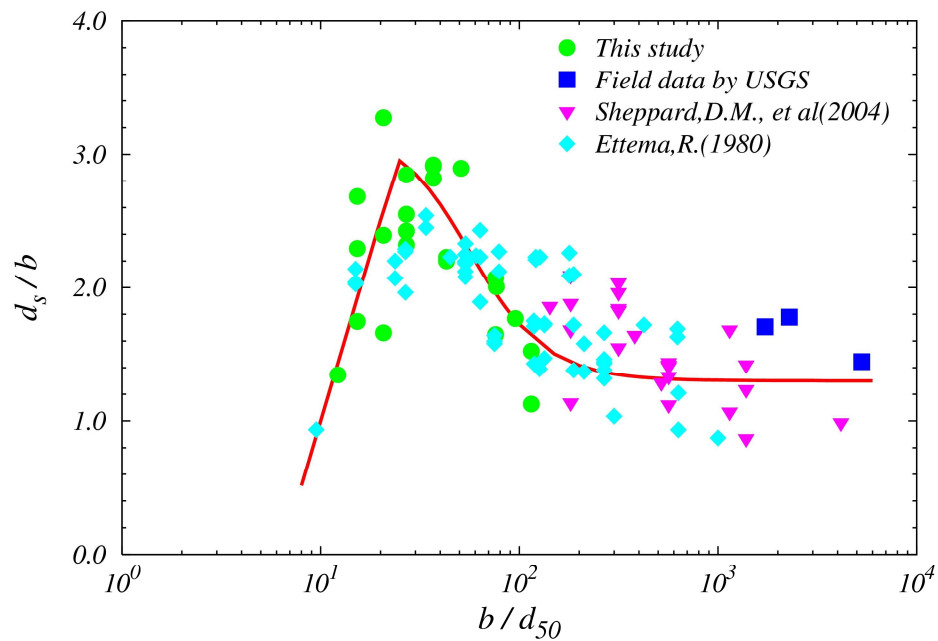


Figure 6.29 Effect of b/d_{50} on the corrected d_s/b for $Fr_1 < 0.4$

In addition, data from the literature have been added to Figure 6.29 in order to show more detailed trends and a wider range of applicability. Using a more extensive data set from the literature (Ettema 1980; Sheppard 2003; Sheppard et al. 2004a; Ting et al. 2001), the correction factors proposed by Melville and Sutherland (1988) were applied for their experimental data to maintain consistency in isolating the effect of b/d_{50} . Most

experimental data in the range of b/d_{50} from 140 to 4160 come from Sheppard's clear-water scour experiments (2004b) in a 6.1 m wide, 6.4 m deep, and 38.4 m long flume at the USGS Conte Research Center in Turners Falls, Massachusetts. Also, the field data measured by the USGS in this study for the Chattahoochee, Flint and Ocmulgee River have been included in Figure 6.29. These data clearly show a decrease in values of d_s/b as the value of b/d_{50} increases beyond 25.

A regression analysis using a fitting criterion of mean square error was utilized to find the optimized coefficients such that they minimized the mean square error between experimental data and computed values. In this analysis, the data were divided into two groups by the criteria of b/d_{50} being greater or less than 25. The resulting relationships between relative scour depth and the ratio of pier width to sediment size are presented in Equation 6.5 and Equation 6.6.

The best-fit equations from regression analysis of the laboratory data in Figure 6.29 are given by

For $1 \leq b/d_{50} \leq 25$:

$$\frac{d_s}{b} = 5.0 \log\left(\frac{b}{d_{50}}\right) - 4.0 \quad (6.5)$$

For $25 < b/d_{50} < 1 \times 10^4$:

$$\frac{d_s}{b} = \frac{1.8}{(0.02 b/d_{50} - 0.2)^2 + 1} + 1.3 \quad (6.6)$$

Based on Equation 6.5, the relative scour depth increases proportionally to the

logarithm of the ratio of pier width to sediment size for $b/d_{50} \leq 25$, while the relative scour depth decreases with increasing values of b/d_{50} for values greater than 25. For smaller values of b/d_{50} , a reduction of sediment size relative to pier width increases b/d_{50} and results in increasing relative scour depth since finer sediment is more vulnerable to motion due to the combined effects of the unsteady horseshoe vortex, lift force and shear stress up to $b/d_{50} = 25$. For $b/d_{50} > 25$, it appears from the flow visualizations shown previously that finer bed material is fluidized in high concentrations. Some of the highly concentrated suspended sediments are swept out of the scour hole while others settle back into the scour hole. The relative scour depth, therefore, starts to decrease even though the sediment size becomes smaller. This may be related to the large-scale unsteadiness of the horseshoe vortex which will be discussed in more detail in the next section.

When laboratory experiments need to be designed to reproduce the local scour depth for complex piers in the field, Figure 6.29 provides the first step in design guidance to select the sediment size in the laboratory for Froude number similarity and a distorted value of the flow intensity that will produce the same scour depth in model and prototype. Model design will be discussed in more detail at the end of this chapter.

Using the field measurements of Landers and Mueller (1996) and Mueller and Wagner (2005), the applicability of Equation 6.5 and Equation 6.6 to field data is examined in Figure 6.30. Before comparing the field data with the laboratory-derived equations, the field data were filtered from 493 local pier scour measurements presented by Mueller and Wagner (2005), many of which were reported earlier by Landers and Mueller (1996). However, in the latter report, no relationship was found between relative

scour depth and b/d_{50} when using the full data set. First, data were selected only for $Fr_1 < 0.4$, and secondly, data affected by debris accumulation on the pier were eliminated because there is no distinct relationship between debris accumulation and scour depth. Thirdly, if the sediment size was less than 0.1 mm, that data point was eliminated so as not to consider cohesive sediment effects. Fourthly, in the cases for which pier scour depth was measured both upstream and downstream of the bridge, only the maximum value was used. Finally, in cases where scour monitoring over time was conducted at the same bridge pier, only the maximum recorded scour depth was selected and presented in Figure 6.30. This left a total of 66 field data points, 26 of which were for clear-water scour conditions and 40 of which represented live-bed scour conditions. The filtered data are plotted in Figure 6.30 along with the laboratory-derived curve from Figure 6.29.

For clear water scour conditions, most of the field data in Figure 6.30 show reasonable agreement with the laboratory derived curve if it is considered as an upper envelope curve. For those clear-water scour data points plotting significantly below the curve, it can be argued that the scour depth did not reach the equilibrium or maximum state when they were measured because of the short duration of the flood relative to equilibrium time. Considerable uncertainty occurs for this method of scour measurement because it is never known whether the bed has reached an equilibrium state at the time of scour and discharge measurements. Similar discrepancies occurred for the live bed scour data but perhaps for different reasons. Even though the measured scour depth may represent equilibrium scour conditions for live-bed scour, it is possible that the measured scour depth was less than the equilibrium value due to the dynamic flow characteristics

and sediment transport conditions in the field such as the passage of dunes through the scour hole. However, the laboratory curve combined with filtering of the field data as shown in Figure 6.30 provides for the first time a clear confirmation of the decrease in relative scour depth at the large values of b/d_{50} often observed in the field.

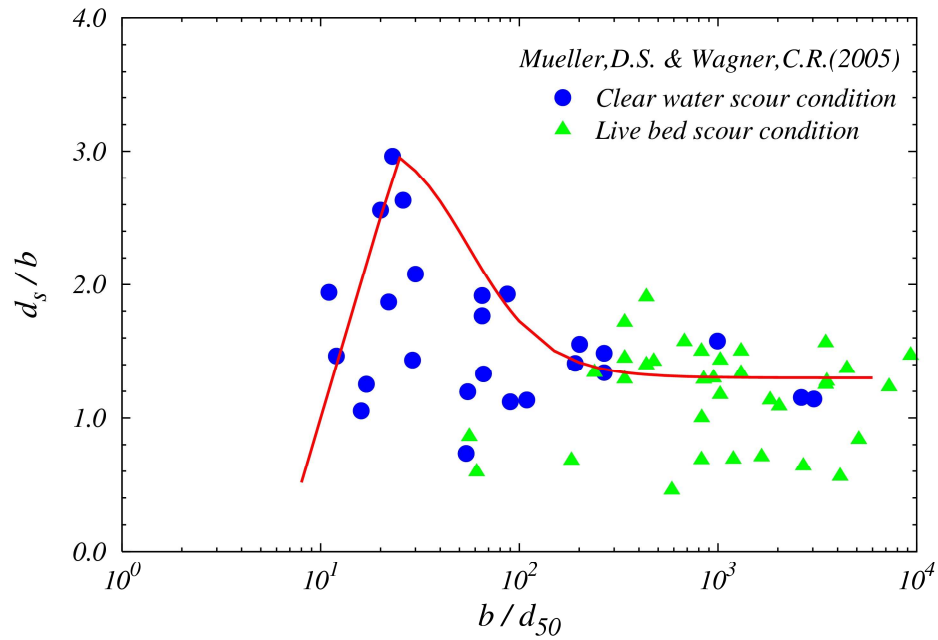


Figure 6.30 Plot of the ratio, b/d_{50} versus the corrected relative scour depth, d_s/b for selected field data with $Fr_1 < 0.4$ (Mueller and Wagner 2005)

6.7.2 Effect of b/d_{50} for $Fr_1 \geq 0.4$

For larger values of the Froude number, a significant discrepancy in the relative scour depth was found when comparing the experimental results from this study with Ettema's experimental results for $b/d_{50} < 20$ in Figure 6.31. If the approach velocity increases for the same flow depth to produce a higher Froude number, the horseshoe vortex strength

and shear stress increase with the approach velocity in clear-water scour resulting in an increase in relative scour depth for the same value of b/d_{50} as shown by the upper limb of the relationship shown in Figure 6.31. On the other hand, if the approach flow depth decreases to produce a higher Froude number with the same approach flow velocity, the scour depth may decrease due to the surface roller called the bow wave. The bow wave can reduce the scouring strength of the horseshoe vortex upstream of the bridge pier when the flow depth becomes so shallow that the surface roller affects the horseshoe vortex strength and size. Since the rotational direction of the bow wave is opposite to that of the horseshoe vortex, the strength of the horseshoe vortex tends to decrease due to the effect of the bow wave at the water surface. As a result, the scour depth values for $b/d_{50} < 20$ from Ettema's experimental results become smaller at the same value of b/d_{50} as illustrated by the lower limb of the curve in Figure 6.31. In other words, Ettema's experimental results in Figure 6.31 show smaller values of relative scour depth because they are for smaller values of y_1/b at the same value of b/d_{50} .

It can also be observed from Figure 6.31 that the relative scour depth for higher values of Froude number becomes relatively independent of the relative size of sediment for $b/d_{50} > 25$ based on Sheppard's data..

In order to present the relative scour depth as a function of a single parameter for higher Froude number values, the pier Froude number, $Fr_b = V_1/(gb)^{1/2}$, is introduced in Figure 6.32 to incorporate both Froude number and y_1/b effects. It is easily shown from an elementary application of the Bernoulli equation along the free surface from the approach flow to the stagnation point at the nose of the pier that the rise in depth of the

bow wave relative to the pier width is related approximately to the pier Froude number; that is, $\Delta y/b \approx Fr_b^2/2$.

Regression analysis was conducted to develop the envelope curve given by Equation (6.7) for $Fr_1 \geq 0.40$ and $b/d_{50} \leq 25$. The relationship is plotted in Figure 6.32 and it is given by

$$\frac{d_s}{b} = 1.5 + \frac{1.2}{Fr_b^2} \exp\left[-2 \left(\ln(Fr_b^2)\right)^2\right] \quad (6.7)$$

in which the pier Froude number is given by $Fr_b = V_1/\sqrt{g b}$.

The filtered field data for $Fr_1 \geq 0.4$ are also compared with Equation 6.7 as shown in Figure 6.33. All data from the field measurements are within the clear-water scour condition. It is observed in Figure 6.33 that the field data seem to follow the same trends as the curve based on laboratory data but are considerably below the presented curve.

In summary, the effect of the ratio of pier width to sediment size was quantitatively investigated in this section based on statistical methods. The Froude number was found to be the appropriate criterion to separate the relationships between relative scour and the ratio of the pier width to sediment size to produce predictive equations valid for both laboratory and field data. The equations presented in this section will be used to correct measured scour depths in terms of b/d_{50} to enable a comparison with selected predictive scour equations. First, however, we return to the discussion of why b/d_{50} should affect scour depths as it does in terms of the large-scale unsteady characteristics of the horseshoe vortex system.

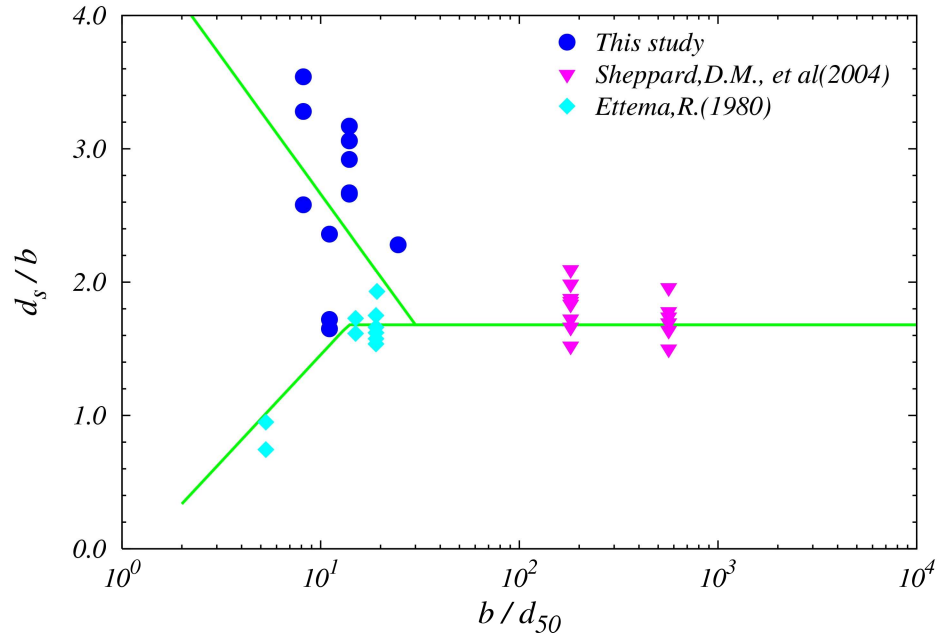


Figure 6.31 Effect of the pier and sediment size, b/d_{50} , on the corrected relative scour depth, d_s/b for $Fr_1 \geq 0.4$

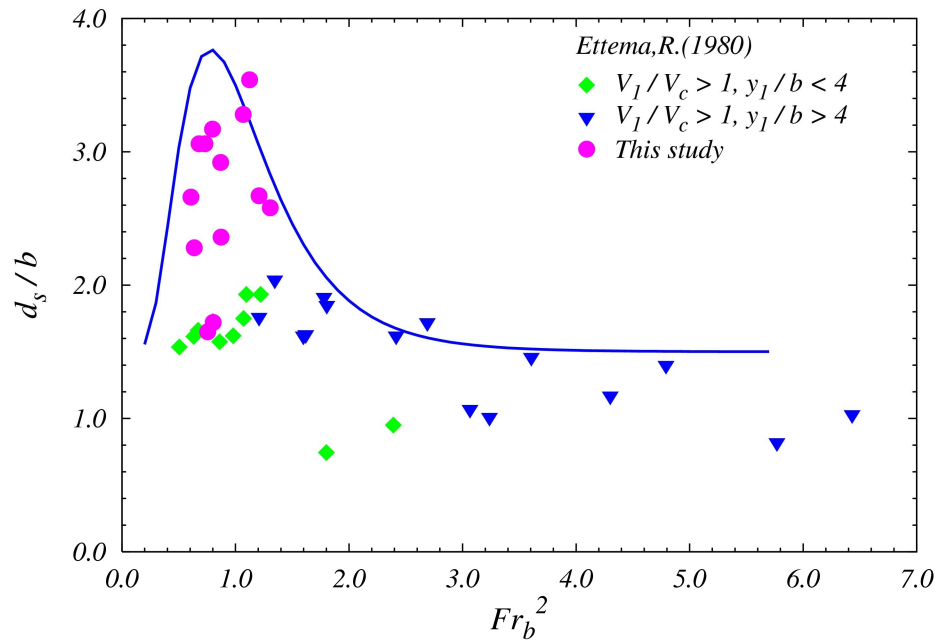


Figure 6.32 Effect of the pier Froude number on the pier scour depth, d_s/b , for $Fr_1 \geq 0.4$ and $b/d_{50} < 20$

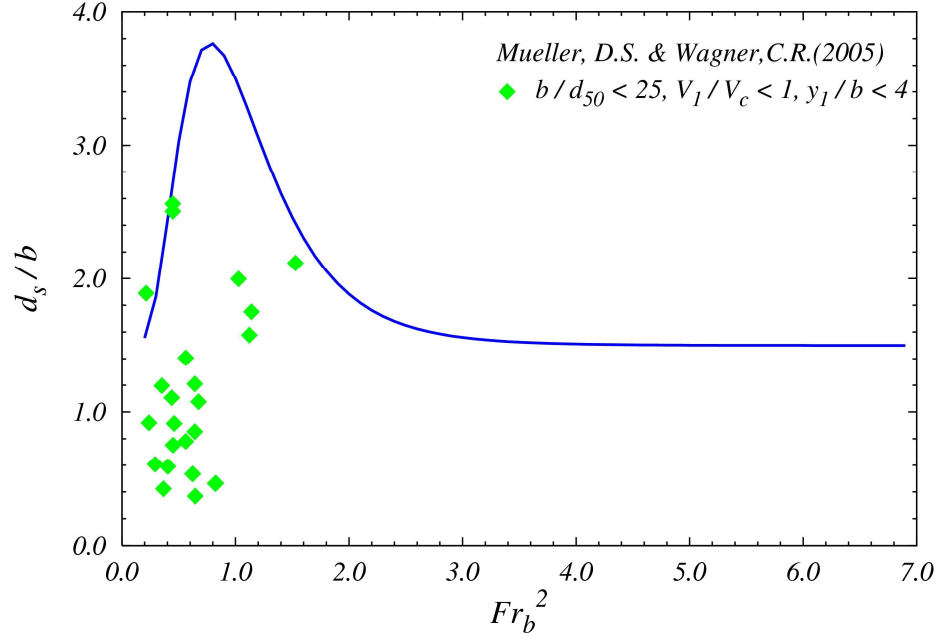


Figure 6.33 Plot of the ratio, b/d_{50} versus the corrected relative scour depth, d_s/b with the selected field data for $Fr_1 \geq 0.4$ (Mueller and Wagner 2005)

6.8 Effect of Large-Scale Unsteadiness on Scour Depth

As discussed above and as shown by flow visualization, the relative scour depth appears to be related to the large-scale unsteadiness of the horseshoe vortex upstream of the bridge pier when the effect of the ratio of the pier width to sediment size is considered for $Fr_1 < 0.4$. However, the time series of velocity measured with an ADV does not completely describe the unsteadiness at the nose of the pier if the time series is assumed to be stationary. The phase-averaging technique is introduced in this section to investigate the periodic time scale in the time series associated with the intermittency of the primary horseshoe vortex size as the separation point oscillates between two preferred

states in the streamwise direction. The time series was measured at a single point located at $x/b = 0.3$ upstream of the pier and at a relative elevation of $z/b = 0.17$ over a duration of 5 min. for the 1:23 scale Chattahoochee River model pier bent.

6.8.1 Phase-averaging Technique

The time series of three dimensional velocity and turbulence intensity were measured at the same location upstream of the bridge pier where the bimodal velocity distribution occurred for the fixed bed case under approximately the same hydraulic conditions except for b/d_{50} as given in Table 6.2. To investigate the effect of b/d_{50} on the relative scour depth in terms of the large-scale unsteadiness of the horseshoe vortex, it is hypothesized that the scour process occurs in two steps: first, sediment is detached from the bed and then entrained into the flow to be transported downstream as observed in the flow visualization videos described previously. The sediment grains slide, roll, and jump periodically from the bed due to the frequency of the vertical oscillations that act to lift the sediment off the bed, while all or a portion of the dislodged grains are entrained and transported downstream out of the scour hole at a streamwise frequency associated with sediment grain entrainment and transport.

Table 6.2 Summary of dimensionless experimental data for Chattahoochee River model pier bent

Run	Model	Scale	T_{eq} , hrs	Fr_1	V_1/V_c	y_1/b	b/d_{50}	d_s/b
7	FB	1/23	29.2	0.44	0.83	4.16	13.95	2.91
12	FB	1/23	22.3	0.19	0.82	4.16	86.84	2.02

FB¹=flat-bed model

What is required, therefore, is to extract the unsteady or frequency characteristics of the coherent structure of the horseshoe vortex from the velocity time series. Observation of the time series of the streamwise velocity components suggests that filtering is needed to distinguish the irregular periodic motion. Through Gaussian filtering of the high frequency fluctuations and electronic noise, it is found that the periodic velocity components of a certain frequency can be identified.

In the general unsteady-in-the-mean turbulent flow, the instantaneous velocity, $u(t)$, can be decomposed into three components shown in Figure 6.34 and given below:

$$u(t) = U + \hat{u}(t) + u''(t) = u_p(t) + u''(t) \quad (6.8)$$

$$U = \lim_{T \rightarrow \infty} \frac{1}{T} \int_0^T u(t) dt \quad (6.9)$$

$$u_p(t) = U + \hat{u}(t) = \lim_{N \rightarrow \infty} \frac{1}{N} \sum_{n=0}^{N-1} u(t + n\tau) \quad (6.10)$$

where, U is the global mean velocity over a long time period, $\hat{u}(t)$ is the statistical contribution of the organized periodic component, $u''(t)$ is the instantaneous value of velocity fluctuations, u_p is the phase-averaged velocity with coherent structure, and τ is the period of dominant frequency corresponding to the window size.

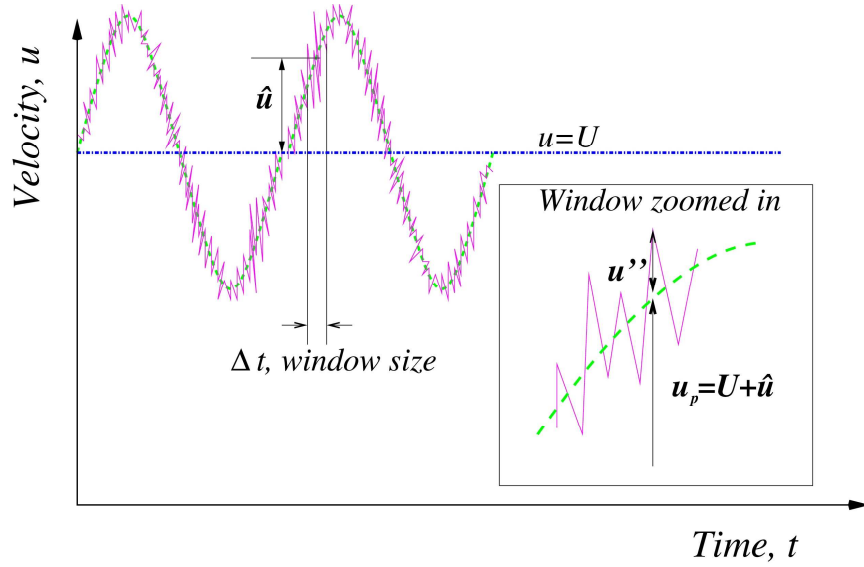


Figure 6.34 Schematic of velocity decomposition for phase averaging technique

In order to investigate the periodic components of the coherent structure, it is necessary to separate those components from the velocity time series, which can be accomplished with a phase-averaging technique. This method is implemented by averaging the instantaneous velocity over an appropriate measuring period or window size for a long time series. The size or magnitude of the window should be small enough to distinguish between the periodic variations and the residual turbulent fluctuations. (Zhang et al. 1997). The phase averaged quantities are given below:

$$U_p = \lim_{T \rightarrow \infty} \frac{1}{T} \int_0^T u_p(t) dt \quad (6.11)$$

$$u_p' = \sqrt{\frac{1}{N-1} \sum_{i=1}^N (u_{p_i} - U_p)^2} \quad (6.12)$$

where, U_p is the time average mean of u_p and u_p' is the root mean square value of

fluctuation of u_p after phase averaging. The time series of velocity measurements were filtered with the Gaussian low-pass filter having a cutoff frequency of 10% of Nyquist frequency corresponding to the approach flow velocity ($V_1 \approx 0.3 \sim 0.6 \text{ m/s}$) before applying the phase-averaging technique. Because the original data can include high-frequency unsteadiness or electronic noise which causes errors in determining the peak, it is difficult to detect the exact phase for the original data. The filtering, therefore, was employed for better detection of the phase. Once filtered, zero phase values were assigned at each maximum to reduce the effect of phase jitter and then phase-averaging was implemented with a selected averaging period or window size (Sung and Yoo 2001).

The mean component of longitudinal velocity, U_p , computed by the phase-averaging method nondimensionalized by the global mean velocity in the streamwise direction, U , is plotted with the ratio of the frequency corresponding to the window size for phase-averaging to the acoustic frequency of the ADV in Figure 6.35. The mean velocity, U_p for the smaller sediment (larger b/d_{50}) is more sensitive to the window size in phase-averaging.

Figure 6.36 shows the change in the ratio of the root mean square value of u'_p and w'_p , respectively, with the ratio of the window size in phase-averaging to the sampling frequency of the ADV. Based on these results, the relative window size for the phase-averaging is recommended to be less than 2 % of the sampling frequency of the ADV in order to retain the flow turbulence characteristics while simultaneously filtering the signal noise since the mean values and root mean square values are affected for larger sizes of window as shown in both Figure 6.35 and Figure 6.36.

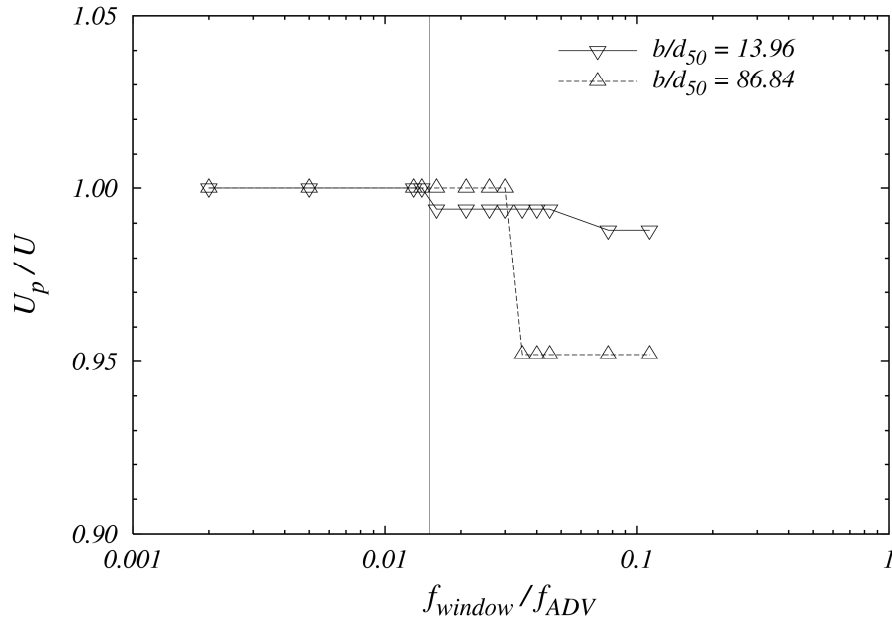


Figure 6.35 Comparison of the ratio of phase averaged mean velocity, U_p , to global mean velocity, U , with the relative window size

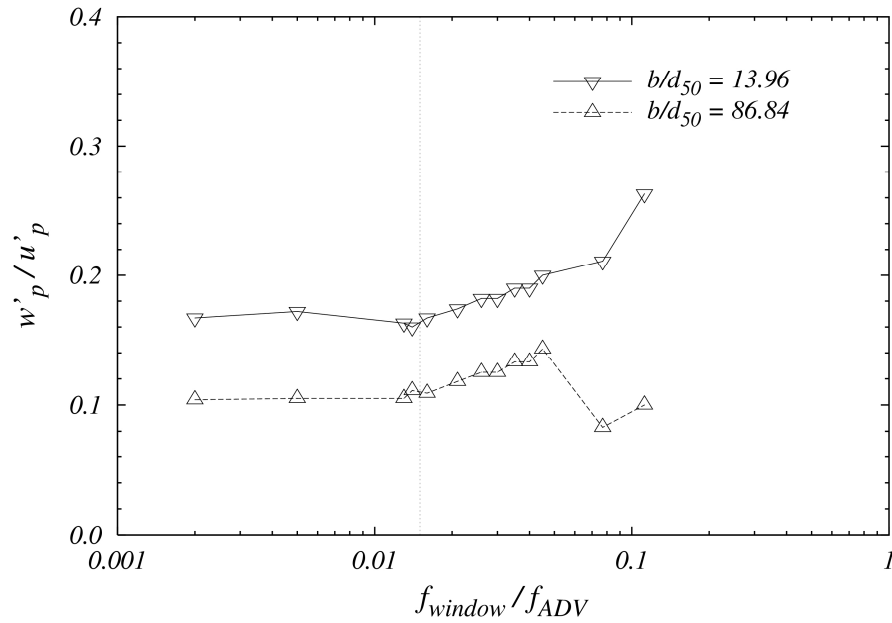


Figure 6.36 Comparison of the ratio of root mean square value of u_p in vertical direction to streamwise direction after phase averaging with the relative window size

In addition to phase averaging in the horseshoe vortex region just upstream of the bridge pier, phase averaging was also applied to the turbulence fields measured next to the pier bents over the depth as given previously in Chapter 5. The phase-averaged turbulent kinetic energy, based on the rms values of the fluctuation of phase averaged velocity components as shown in Equation 6.13, was calculated around the bridge pier:

$$k_p' = \frac{1}{2} \left(u_p'^2 + v_p'^2 + w_p'^2 \right) \quad (6.13)$$

The ratios of the phase-averaged turbulent kinetic energy to the total kinetic energy (TKE) were approximately 0.1 at locations 4, 5, 6, 7, and 8 around the bridge pier corresponding to Figure 5.10. Thus, the effect of unsteadiness due to the horseshoe vortex upstream of the pier may have little effect on the flow structure downstream of the pier at least for distances above the bed that are shown in Figure 5.13, for example. The profiles of TKE in that figure are more likely affected by the large-scale eddies successively shed from the upstream corner of the first pier and into the wake region. Devenport and Simpson (1990) were able to measure the footprint of the horseshoe vortex as it was swept around a wing but only by using an array of hot wires embedded in the bottom wall. They suggested that the frequency of the large-scale motions measured at the bed beside the wing are related to the large-scale turbulent structures in the outer portion of the approach boundary layer as they are swept downward in front of the wing and then pulsed away in the cross-stream direction around the base of the wing. This would agree with the observation of Dargahi (1989) who suggested that the horseshoe vortex is shed quasi-periodically and is practically independent of the wake vortices.

6.8.2 Effect of Large-Scale Unsteadiness on Scour Depth

The vertical motion of sediment is assumed to be related to the total fluctuation of the vertical velocity component with respect to the global time average while the frequency of the sweeping of dislodged sediment out of the scour hole is thought to be dependent on the phase-averaged streamwise periodic component of velocity measured at the nose of the pier. Based on the results in Figure 6.37, the ratio of turbulence intensity in the vertical direction to the root mean square value of the phase-averaged velocity, u_p' , in the streamwise direction can be assumed to be a constant of approximately 0.4 for a relative frequency ratio range less than 0.02 regardless of the value of b/d_{50} . It is for this reason that these two velocity scales are chosen to analyze the effect of flow unsteadiness on scour depth.

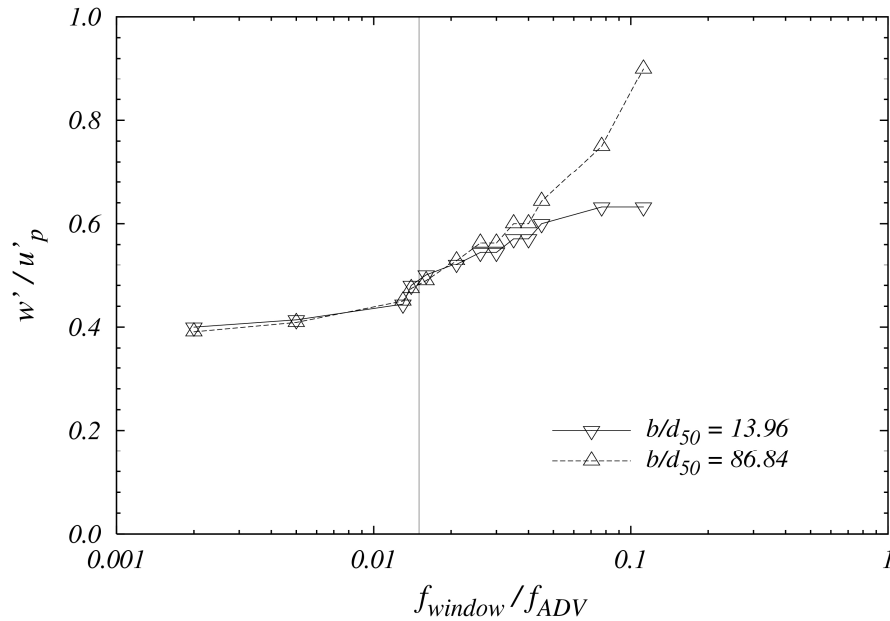


Figure 6.37 Ratio of the turbulence intensity to root mean square value of u_p in streamwise direction after phase averaged

Based on the constant value of the ratio of velocity scales in Figure 6.37, the bimodal characteristics of the horseshoe vortex, and the previous analysis of the flow visualization videos, it is proposed that there are two time scales governing the scour process which can be quantified. One is the time for lifting or dislodging sediment particles and the other is the time for entrainment of the sediment particles into the flow for transport out of the scour hole. Both time scales can be represented as a function of sediment size, pier width, and the velocity scales identified in Figure 6.37 as follows:

$$t_L \sim \frac{\alpha d_{50}}{w'} \quad (6.14)$$

$$t_E \sim \frac{b}{u_p'} \quad (6.15)$$

where t_L and t_E are time scales for lifting and entrainment of sediment, respectively, w' is the turbulence intensity in the vertical direction, u_p' is the root mean square value of the streamwise velocity fluctuations after phase-averaging, and α is a constant defining the grain lifting height in terms of the number of grain diameters. This is analogous to the grain movement step size in Einstein's sediment bedload formulation (Sturm 2001), or perhaps more appropriately the saltation (jumping or hopping) height in the bedload equation of van Rijn (1984).

The relationship between t_L and t_E can be defined in terms of b/d_{50} assuming the ratio, w'/u_p' , is a constant equal to 0.4 for the same hydraulic conditions as given below:

$$\frac{t_E}{t_L} = \frac{b}{\alpha d_{50}} \times \frac{w'}{u_p} = 0.04 \frac{b}{d_{50}} \quad (6.16)$$

in which it has been assumed for the sake of argument, that the average height of grain suspension is ten grain diameters, i.e. $\alpha = 10$. This value of α falls within the range of saltation heights measured by van Rijn (1984) but its actual value is immaterial to the overall argument. Nevertheless, for this value of α , the pier scour depth is maximum when $b/d_{50} = 25$ and therefore when $t_E/t_L = 1.0$.

Equation (6.16) contains the effects of both the turbulence characteristics and unsteadiness of the horseshoe vortex system and can help explain the effect of the ratio of the pier width to sediment size on the scour depth. Three categories in terms of t_L and t_E can be defined to explain the effect of b/d_{50} on scour depth. First, the maximum scour depth occurs when t_E becomes approximately equal to t_L at $b/d_{50} = 25$. When t_E becomes greater than t_L , the relative scour depth decreases with increasing values of b/d_{50} . The entire bed in front of the bridge pier periodically becomes fluidized and suspended but there is insufficient time in the suspension event for all of the available sediment to be carried out of the scour hole so that some of it is redeposited. The net effect is a reduction of the maximum scour depth at the nose of the bridge pier. For $t_E < t_L$, the relative scour depth also decreases but with decreasing values of b/d_{50} since the flow entrainment time becomes more and more limiting as it is insufficient to carry grains out of the scour hole during the time that they are suspended or saltating.

6.9 Evaluation of Scour Depth with Several Predictive Equations

In this section, relative scour depth is predicted using selected pier scour equations from the literature for both laboratory and field data from this study as well as from other investigations. The HEC-18 formula (Richardson and Davis 2001), Melville and Sutherland formula (1988), and Sheppard et al. formula (2004a) are used to compare with the measured data in the laboratory experiments and the field sites. The modified Melville and Sutherland (1988) formula using the correction function for relative sediment size (b/d_{50}) proposed in this study is also compared with the same data sets. The detailed descriptions of these formulas is given in Appendix A.

For quantitative comparisons between the scour formula predictions and scour depth observations, the root mean square error ($RMSE$) and the discrepancy ratio (r) are utilized. These statistical measures of the performance of scour prediction formulas are given by

$$RMSE = \sqrt{\frac{\sum_{i=1}^N (d_s/b_{predicted,i} - d_s/b_{measured,i})^2}{N-1}} \quad (6.17)$$

$$r = \frac{(d_s/b)_{predicted}}{(d_s/b)_{measured}} \quad (6.18)$$

$$\sigma_r = \sqrt{\frac{1}{N-1} \sum_{i=1}^N (r_i - \bar{r})^2} \quad (6.19)$$

in which, \bar{r} is the mean discrepancy ratio and σ_r is the standard deviation of the

discrepancy ratio. A value of unity for the discrepancy ratio indicates perfect agreement between the predicted and measured values of dimensionless scour depth. The standard deviation of the discrepancy ratio represents a measure of the scatter in the predictions relative to the mean value.

The laboratory data shown in Figure 6.38 are the combined points from the data measured for this study and the data sets collected from the literature (Ettema 1980; Sheppard 2003; Sheppard et al. 2004a; Ting et al. 2001) only for $Fr_1 < 0.4$. For Figure 6.39, the field measurements from Landers and Mueller (1996) and Mueller and Wagner (2005) are filtered in the same way as mentioned earlier. Also, the field data surveyed by the USGS for this study are included in Figure 6.39.

The summarized values of the statistical measures of performance for each selected formula are given in Table 6.3. For the laboratory data, the mean values of the discrepancy ratio for the three formulas in the literature overpredict the relative scour depth from 33% to 48%, while the formula suggested in this study results in a mean value of 6% overprediction. Of the first three formulas in Table 6.3, a discrepancy ratio of unity falls within the confidence limits of \pm one standard deviation from the mean only for the HEC-18 formula. The standard deviation of the discrepancy ratio for the laboratory data is smallest for the formula suggested in this study with a value of ± 0.24 as is the RMSE with a value of ± 0.17 . This is not unexpected since these were the data used to develop the formula.

Values of the discrepancy ratio and RMSE for comparisons between observations and predictions of the field data are also given in Table 6.3. All the formulas overestimate the relative scour depth for field conditions which is desirable since all the formulas are

utilized in bridge foundation design for which an acceptable factor of safety is often applied; however, the magnitude of overprediction is excessive, partly because of the reasons stated previously including non-equilibrium field scour conditions and discrete rather than continuous measurements with time in the field. The lack of agreement with the field data is not so much a shortcoming of the proposed scour prediction formula as it is of the difficulty in measuring field data using “flood-chasing” or discrete measurements in time without being able to take into account the unsteady development of the scour hole itself. It is encouraging to note that the method presented in this study produces the smallest RMSE value and discrepancy ratio by a relatively large amount for the field data as well as the laboratory data.

Table 6.3 Summary of the discrepancy ratio and root mean square error for each formula

	Laboratory data			Field data		
	\bar{r}^1	σ_r^2	RMSE ³	\bar{r}	σ_r	RMSE
HEC-18 (2001)	1.33	0.45	0.49	3.04	2.30	1.76
Melville and Sutherland (1988)	1.48	0.49	0.67	3.96	3.14	3.18
Sheppard, et al.(2004)	1.41	0.30	0.48	4.84	6.60	9.33
This study	1.06	0.24	0.17	2.36	1.90	0.86

\bar{r}^1 =mean discrepancy ratio, σ_r^2 =standard deviation of the discrepancy ratio,
RMSE³=root mean square error

Another method used to evaluate the scour formulas is the visual comparison between predicted and measured scour depths as shown in Figure 6.38 for the laboratory data and in Figure 6.39 for the field measurements. Both plots show how much the predicted values of relative scour depth deviate from the 1:1 curve. For all three accepted

scour prediction formulas, the predictions are generally located above the 1:1 curve for the laboratory data. For the field data in Figure 6.39, it is practically impossible to predict the scour depths based on field measurements alone without continuous time monitoring of scour. For reasons previously discussed, the result is a great deal of scatter in the data as shown in Figure 6.39 and as observed by other investigators.

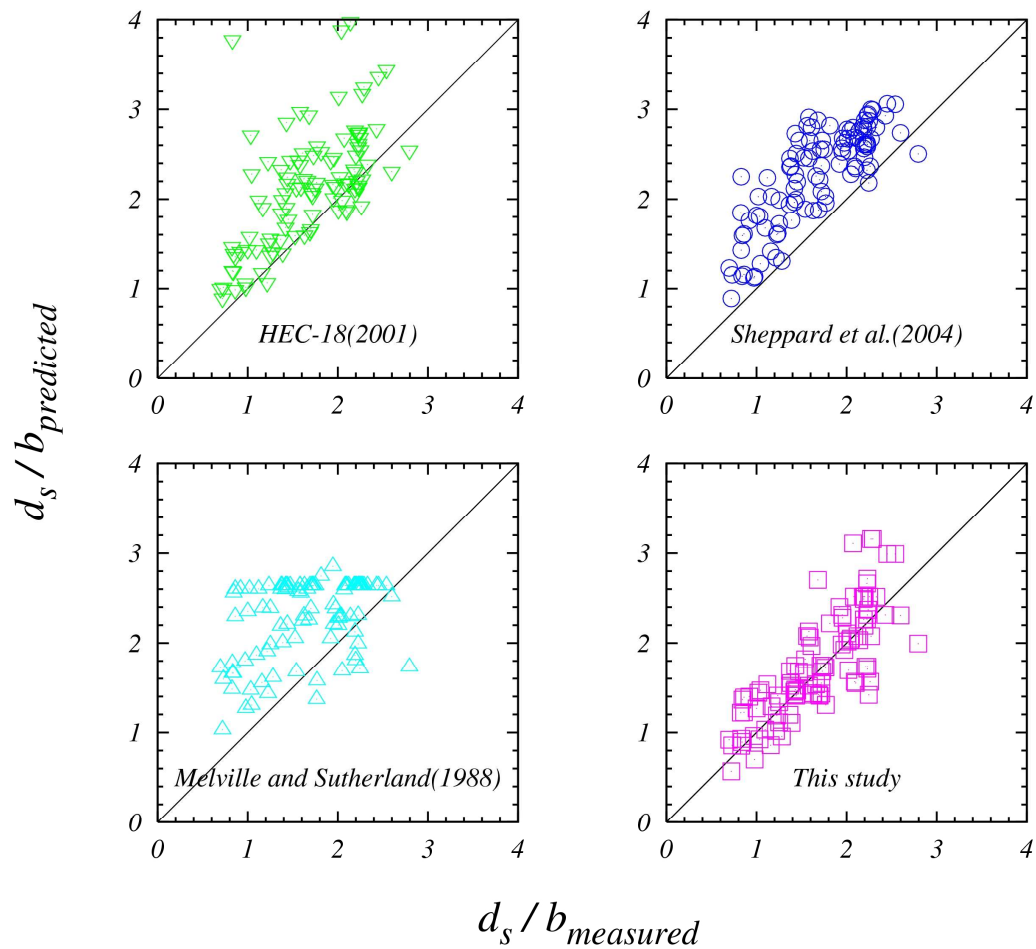


Figure 6.38 Comparison of measured relative scour depth from laboratory experiments including Ettema, R.(1980) and Sheppard, et al (2003; 2004) data with selected pier scour equations for $Fr < 0.4$ (∇ =HEC-18 (2001); Δ =Melville and Sutherland formula (1988); \circ =Sheppard et al. formula (2004); \square =This study)

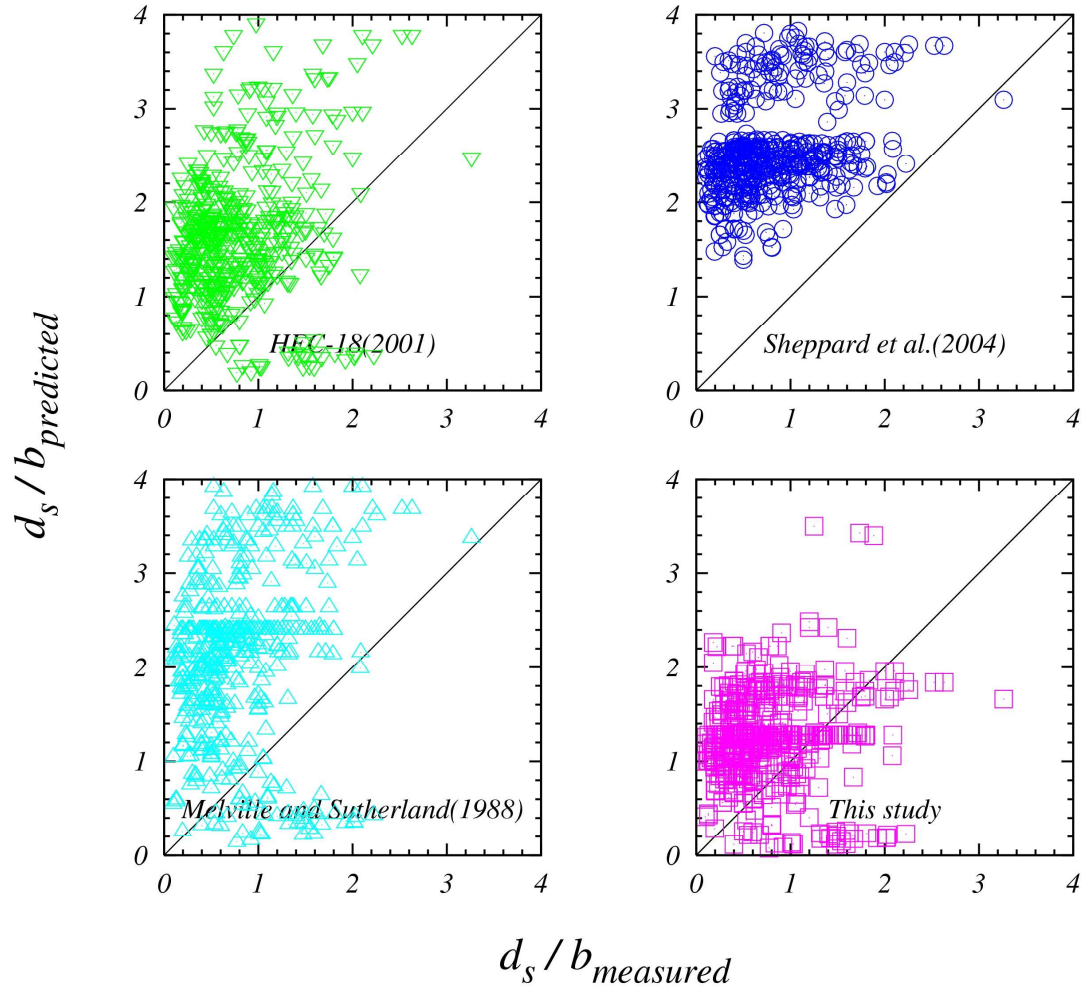


Figure 6.39 Comparison of measured relative scour depth in field (Mueller and Wagner 2005) with selected pier scour equations for $Fr < 0.4$ (∇ =HEC-18 (2001); Δ =Melville and Sutherland formula (1988); \circ =Sheppard et al. formula (2004); \square =This study)

The probability distribution of the discrepancy ratio is another measure to evaluate the selected formulas. Using the probability distribution, it is possible to observe the value of the discrepancy ratio at the peak probability for each formula and the band width as measured by the standard deviation in the probability distribution curve. The best formula performance is indicated by a narrow probability distribution with a single peak that is the highest and nearest a value of unity for the discrepancy ratio. In Figure

6.40 for the laboratory data, the equation presented in this study has only one peak but the others show two peaks near a value of unity for the discrepancy ratio. It is, however, hard to choose the minimum value of the band width from Figure 6.40. The minimum value of the standard deviation is 0.24 for the formula suggested in this study as shown in Table 6.3. It is also found that all formulas overestimate the relative scour depth for the field data in Figure 6.41. Only the equation developed in this study has a high probability of occurrence of a discrepancy ratio of 1.0, while all the formulas display a peak in probability near a discrepancy ratio of 2.2.

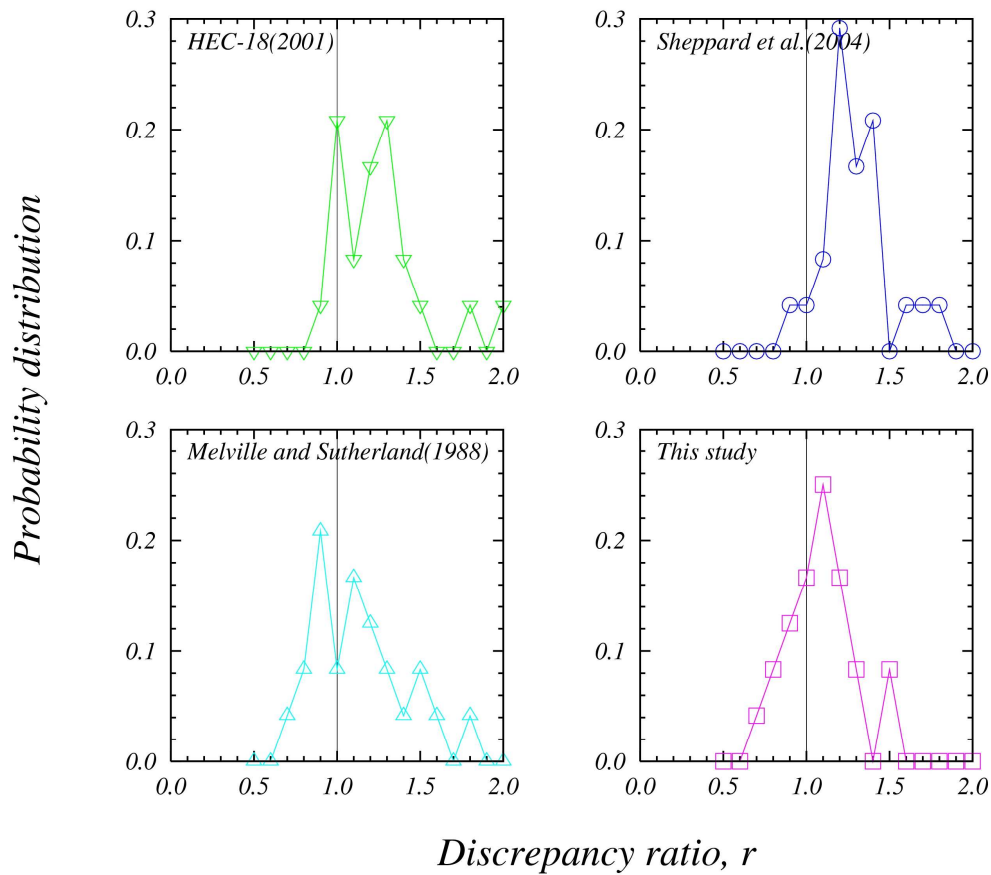


Figure 6.40 Probability distribution of the discrepancy ratio for the laboratory data (∇ =HEC-18 (2001); Δ =Melville and Sutherland formula (1988); \circ =Sheppard et al. formula (2004); \square =This study)

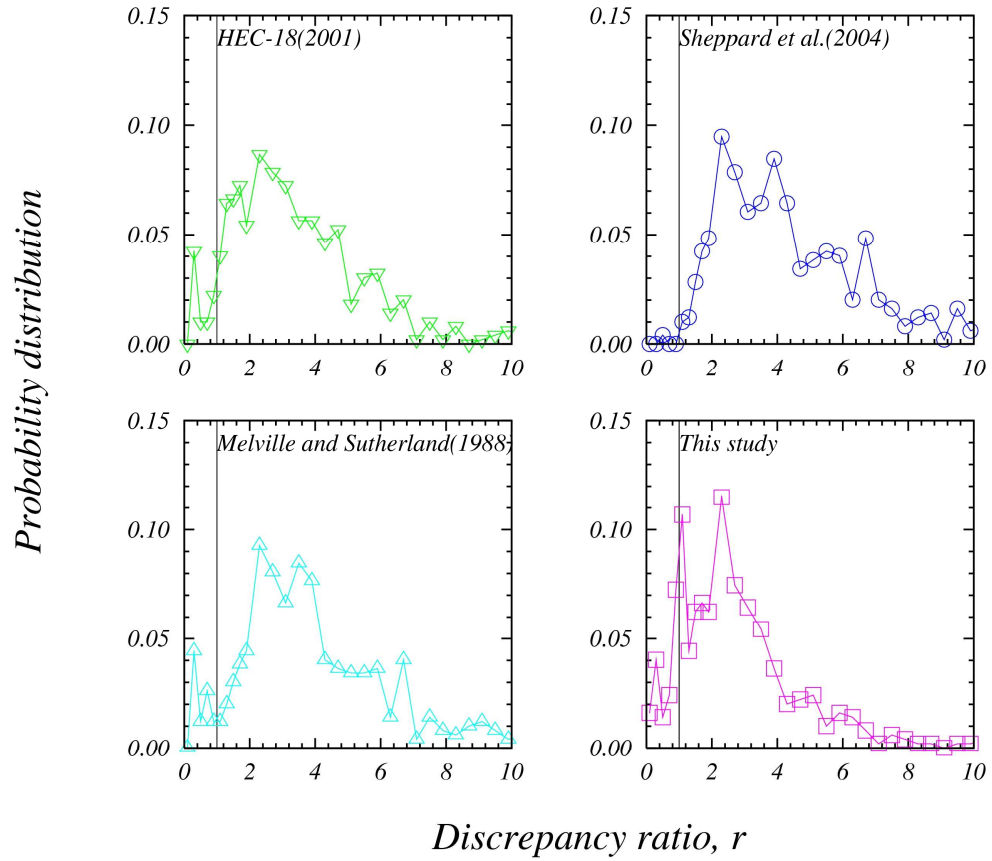


Figure 6.41 Probability distribution of the discrepancy ratio for the field data (∇ =HEC-18 (2001); Δ =Melville and Sutherland formula (1988); O =Sheppard et al. formula (2004); \square =This study)

Overall, the equation for estimation of scour depth presented in this study, with its dependence on b/d_{50} and connection with the large-scale unsteadiness of the horseshoe vortex, provides the highest accuracy in scour prediction for both laboratory and field data.. It is essential to estimate maximum scour depths more accurately during the bridge foundation design in order to prevent possible bridge failure. On the other hand, design of the bridge foundation based on overestimated scour depths may cause excessive construction cost. Thus, the more accurate estimation of scour depth will reduce cost while providing a quantifiable safety factor for risk-based design.

6.10 Hydraulic Model Design for Scour Depths around Complex Piers

Physical modeling with a single cylindrical pier has been conducted in the past to investigate scour depth and foundation design, which is inconsistent with reality because most bridge piers do have complicated structures instead of a single cylinder. In addition, the location of the maximum scour depth does not always occur in front of the first pier, as shown in a previous section. The selection of sediment size for physical models has to be done carefully because the effect of sediment size on the scour depth can be different in the laboratory when the value of b/d_{50} is smaller than in the field as shown in Figure 6.43. The general modeling approach illustrated in this section utilizes the relationship of Figure 6.43 developed in this study from scour depth measurements in front of the most upstream pier to select a sediment size in the model such that scour around complex piers, for which maximum scour depths and their locations are not easily predicted, can be determined reliably from a physical model study.

Local scour around complex piers is generally dependent on multiple factors and thus in the design of a physical model for local scour, it is difficult to satisfy all requisite similarity criteria. As a result, it is necessary to identify the primary factors affecting the scour process before designing a physical model. The governing characteristic spatial scales for local scour are the sediment size, the pier size (width), and the approach flow depth.

The model Reynolds number is kept large enough to reproduce the behavior of flow and sediment in fully rough turbulent flow (Ettema et al. 1998) with the pier Reynolds number greater than about 10^4 (see Figure 2.8). Therefore, Froude number

similarity can be utilized in dynamic similarity. Froude number similarity reproduces not only the wave run-up effects on the most upstream pier but also insures similarity of pressure gradients (water surface profiles) and energy losses through the bridge itself and thus macroscopic flow patterns around complex bridge pier bents. It is true that exact Froude number similarity may not be required to model an idealized single cylindrical pier as long as it is kept smaller than 0.4 in the laboratory, but for overall modeling of the entire bridge opening and the full complexity and interaction of the river bathymetry and bridge geometry, Froude number similarity is recommended. From the design flowrate, the corresponding approach flow depth, the width of pier and geometry, the flow intensity, V_1/V_c , the Froude number, the relative flow depth, y_1/b , and the relative sediment size, b/d_{50} can be obtained from field surveying and from a measured or calculated stage-discharge curve as shown in Figure 6.43 in which the subscripts, p and m of each variable are representing the prototype and model, respectively. When the length scale ratio is determined based on practical considerations of economics and constructability of a physical model, accordingly, the size of bridge piers, approach flow depth and flow velocity can be obtained for the model. From the literature, the clear-water scour condition typically occurs when $V_1/V_c = 0.5 \sim 1.0$; thus the range of the critical velocity of the sediment can be calculated as $V_{1m} \leq V_{cm} \leq 2 \times V_{1m}$ because the approach velocity, V_{1m} , for the physical model is already determined using the field measurement and Froude number similitude. From the range of the critical velocity, the allowable range of the sediment size for the physical model can be estimated. The sediment size for the laboratory model of local scour can be chosen by considering the actual available sediment size from the minimum to the maximum allowable value of the

sediment size calculated by the range of the critical velocity. After choosing the sediment size, d_{50m} for the physical model, the correction factors, K_{dm} , for b/d_{50} can be obtained from Figure 6.43 and Equation (6.20) or Equation (6.21) and K_{Im} , the correction factor for effect of the flow intensity is evaluated by the equation by Melville and Sutherland (1988) as presented in Appendix A. If other effects are assumed to be identical between the prototype and physical model, for instance, the angle of attack and the effect of pier shape, the scour ratio, SC_r , defined as the ratio of the predicted relative scour depth for the physical model to the one for the prototype as shown in Figure 6.43 can be evaluated. The scour ratio is used to estimate the scour depth in the prototype by conversion from the value of the scour depth obtained in the physical model to the expected value for the prototype since the relative scour depth in the physical model can be expected to be same as in the prototype considering the scale effect if other parameters are controlled under Froude number similitude.

The sediment size is iterated upon until the value of SC_r is approximately unity such that the effect of b/d_{50} and V_1/V_c are compensated to replicate the field scour depth in a satisfactory design of the physical model.

For $1 \leq b/d_{50} \leq 25$:

$$K_d = \frac{1}{2.44} \left[5.0 \log \left(\frac{b}{d_{50}} \right) - 4.0 \right] \quad (6.20)$$

For $25 < b/d_{50} < 1 \times 10^4$:

$$K_d = \frac{1}{2.44} \left[\frac{1.8}{(0.02 b/d_{50} - 0.2)^2 + 1} + 1.3 \right] \quad (6.21)$$

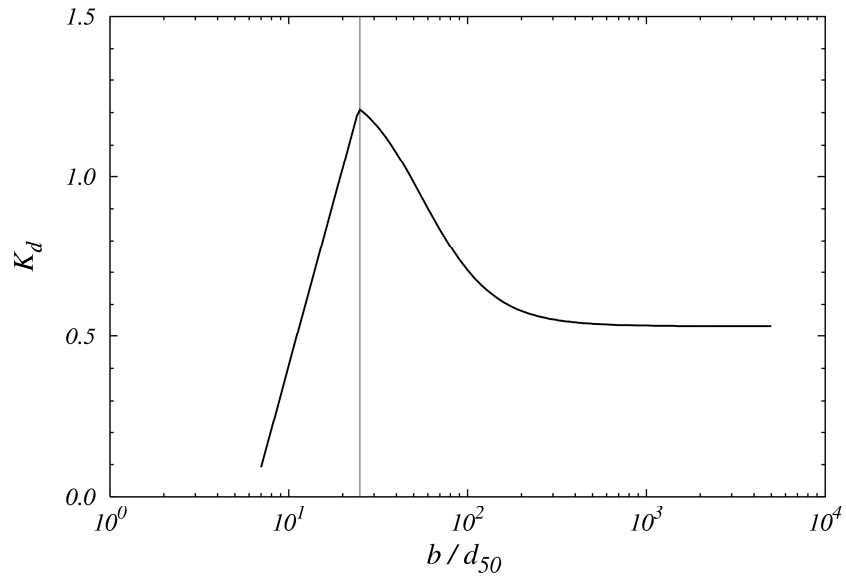


Figure 6.42 Correction factor for the effect of b/d_{50}

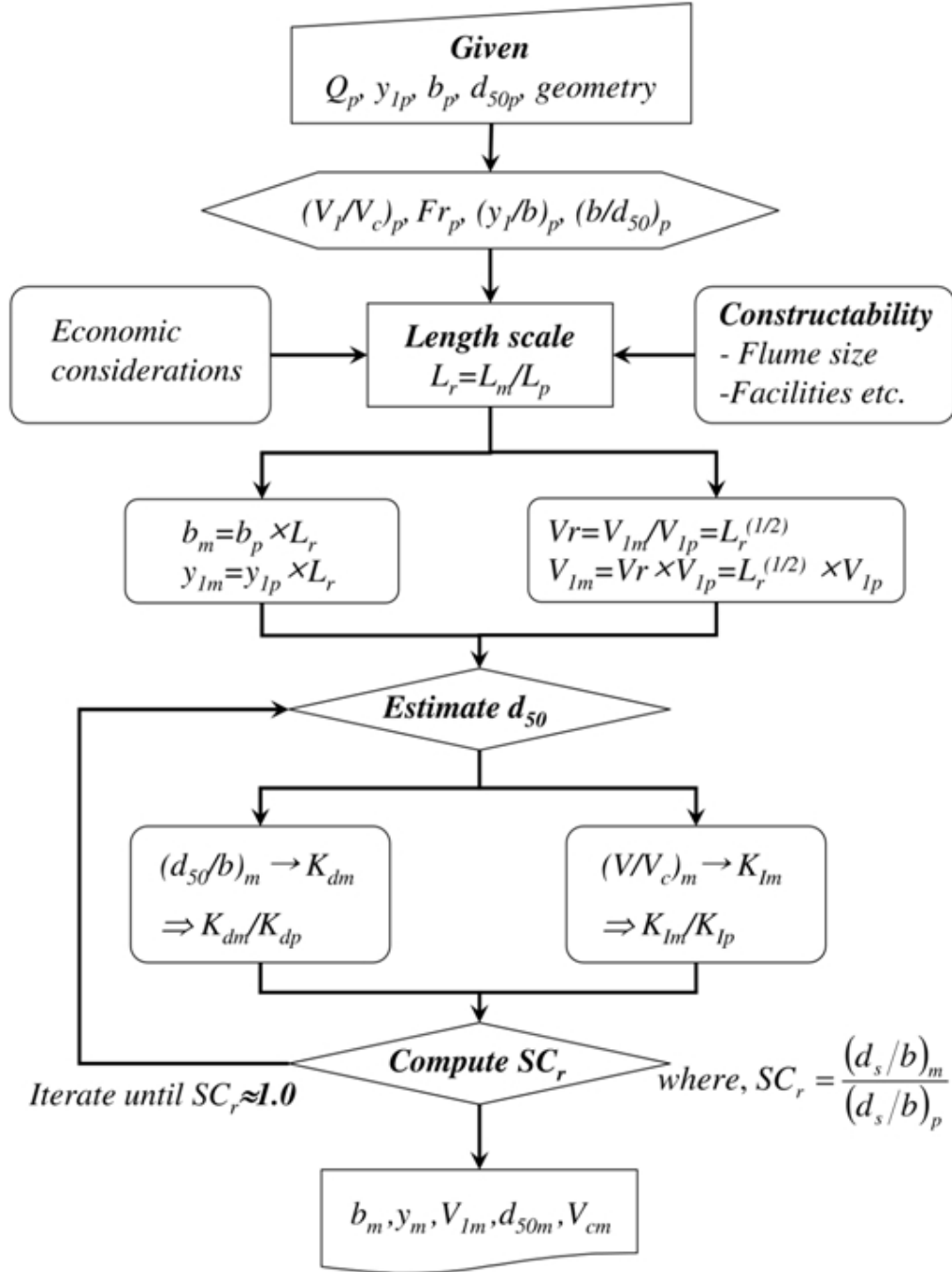


Figure 6.43 Schematic flowchart showing how to determine the experimental conditions for physical model

One numerical example is presented in Appendix B.

CHAPTER VII

SUMMARY AND CONCLUSIONS

7.1 Summary

Although local scour around bridge foundations is one of the main causes of bridge failures, there remain problems in scour prediction because of difficulties in understanding the complex flow structures and scour mechanisms around bridge foundations. In addition, most previous studies have focused on only one aspect of scour analysis: field measurements, laboratory experiments, or numerical simulations. In this study, the relationships among field, laboratory, and numerical studies were investigated for the purpose of improving scour prediction methods. The laboratory experiments are more realistic than most previous studies of local scour that consider only a single cylindrical pier on a flat bed in a rectangular flume. In this study, three prototype bridges in Georgia were modeled in the laboratory using different geometric scale ratios and different sediment sizes, but including the actual bridge and pier geometry as well as the river bathymetry. The laboratory results were compared both with results from a reliable 3D numerical model and with continuous field measurements to provide a more comprehensive collection of realistic local scour data than has been developed in the past.

Prototype bridges usually have complex pier configurations including shapes other than cylindrical, multiple columns with variable spacing in a single pier bent, and multiple pier bents at variable flow depths across the river that may be skewed relative to the main flow direction. In addition, the prediction and analysis of scour depth at

complex bridge piers in the field is further complicated by the difficulty and expense of obtaining field measurements. Under these circumstances, physical modeling is needed to reproduce the prototype flow characteristics and scour patterns including location of the maximum scour depths, which may not be in front of the pier as in idealized laboratory studies. In order to fabricate realistic physical models and interpret the results, modeling principles should be based on continuous and accurate field measurements including properties of the bed materials. In this study, scaled physical models were constructed including the river bathymetry based on field surveys. All experiments were conducted in the clear-water scour regime. The results are compared with field measurements, obtained by the USGS. An acoustic Doppler velocimeter was utilized to measure the velocity and the turbulence intensity as well as the bed elevations before and after scour. Comparisons of velocity distributions for all river models showed good agreement with the field measurements along each of the bridge decks during the flood events investigated. The shapes of the cross section and bed elevations along the bridge deck were well reproduced in laboratory experiments including the maximum pier scour depths in front of the pier, as shown in Chapter 5. How this good comparison was achieved is one of the important results of this research in that it provides a modeling methodology with scaling laws that can be used to design models of complex pier and bridge geometries, select the appropriate model sediment size, and then translate the results to the prototype as discussed below.

In Chapter 6, it is observed that the scouring rate in front of a pier is independent of the flow intensity, defined as the ratio of approach flow velocity to critical velocity of sediment, for $V_1/V_c > 0.7$ so that the relative scour depth, defined as the ratio of scour

depth to width of a pier, depends primarily on the dimensionless time, $V_c t / y_1$. While the relative sediment size, b/d_{50} , only weakly affects the rate of scouring, the equilibrium scour depth itself is highly influenced by the value of b/d_{50} . It is the effect of this independent variable about which the least is known or understood either for predicting scour depths or selecting the appropriate sediment size in physical models of scour. The location of the maximum scour depth around a complex pier is not consistent due to the variability of the horseshoe vortex system and the complexity of bridge geometry and river bathymetry, which gives another essential reason for the need to conduct a physical model study of local scour depth, especially for large, expensive bridges.

The laboratory and field data were compared with several existing pier scour formulas to judge their effectiveness. For higher Froude numbers, the HEC-18 formula showed better agreement with the laboratory data than the Melville and Sutherland formula or the Sheppard formula because these two formulas do not include the influence of Froude number. When the effect of b/d_{50} was considered by comparing the laboratory and field data with predicted scour depths, none of the accepted formulae provided a satisfactory estimate of scour depth with considerable overprediction occurring in many cases. These results emphasize the need for improvement in explaining and accounting for the effect of b/d_{50} in order to obtain more accurate scour predictions.

Measurements of the velocity and turbulence field around a pier bent showed good agreement with numerical predictions, but they were not as helpful as expected in predicting scour depths except to explain qualitative trends in scour patterns. There is no critical difference in the horizontal velocity vector plots for before-scour and after-scour

conditions measured at a relative height above the bed of $z/y_1 = 0.4$, for example. The measured mean velocity and turbulence kinetic energy (TKE) fields were compared with the computational results. The comparisons of mean velocity and TKE fields showed good agreement, but the location of the maximum mean shear stress did not correspond with the maximum scour depth in front of the piers since the values were all temporally averaged ones and so did not show the effects of the large-scale unsteadiness of the horseshoe vortex system upstream of a bridge pier.

More complete descriptions of flow characteristics of the horseshoe vortex system around a complex bridge pier are presented to better understand the scouring process and the relationship between scour depth and the horseshoe vortex. The relationship between the horseshoe vortex and the development of the scour hole was investigated using the probability distribution of instantaneous velocity components and quadrant analysis of velocity fluctuations in the horizontal and vertical directions. A velocity time series was collected near the bed at a location of $x/b \approx 0.33$ upstream of the pier near the bed for both the before-scour and after-scour conditions. At this location, the vertical and streamwise velocity components exhibited a bimodal probability distribution before scour as also observed by others for flow approaching the intersection of a wing and a solid boundary. The streamwise and vertical velocity fluctuations were observed to be dominated by sweeps and bursts, both of which contribute positively to the bed shear stress and exhibit a bimodal joint frequency distribution. The bursts and sweeps are likely the primary forcing function for creating the scour hole because they both represent positive shear stress. They are the result of irregular oscillation of the horseshoe vortex between two preferred states as the reverse flow near the bed in front of the pier either

extends upstream or retreats to a point closer to the pier. As a result, the sediment particles are lifted and entrained in an intermittent fashion. After scour is complete, the turbulent events no longer display a bimodal distribution near the bottom of the scour hole.

Through visualization of the sediment motion in front of the pier for different values of b/d_{50} , an important effect of b/d_{50} was found and connected to the large-scale unsteadiness of the horseshoe vortex. By incorporating the effect of b/d_{50} in the Melville scour prediction formula, improved estimates of scour depth were obtained and differences between laboratory and field effects were identified.

An enhanced relationship between b/d_{50} and d_s/b is presented considering the effect of the Froude number, which divides the scour depth data into two groups; one is for $Fr_1 < 0.4$ while the other is for $Fr_1 \geq 0.4$. When the effect of b/d_{50} is considered for $Fr_1 < 0.4$, the curve for relative scour depth with adjustments made for all other influences can be presented by two different equations according to the threshold value of $b/d_{50} = 25$, which approximately corresponds with the value for maximum relative scour depth in the literature. For b/d_{50} values both less than and greater than the value of 25, the relative scour depth decreases. Thus, scour depths measured in laboratory experiments for $b/d_{50} \approx 25$ overpredict field scour depths that occur at very large values of b/d_{50} . For $Fr_1 \geq 0.4$, the values of d_s/b are given as a function of the pier Froude number to incorporate both Froude number and y_1/b effects. An envelope curve is presented for $Fr_1 \geq 0.4$, showing that both laboratory and field data are below the presented curve.

The observed effect of b/d_{50} on relative scour depths is explained physically by further investigation of the time series data upstream of the pier in the region of the horseshoe vortex. Phase-averaging of the time series was utilized to show that the large-scale unsteadiness of the horseshoe vortex system upstream of the pier is related to the rate of scour and the maximum scour depth. It is shown that the relative balance between a time scale for lifting or mobilizing the sediment as a result of vertical turbulent fluctuations, and a time scale for entrainment and transport of sediment out of the scour hole due to oscillation of the horseshoe vortex is effectively captured by the b/d_{50} ratio. The result is an explanation of the effect of flow unsteadiness on scour depth as reflected by the value of b/d_{50} .

Predicted scour depths by several accepted formulas were compared with the extensive data measured in laboratory and field monitoring both in this and other studies. The formulae mostly overpredicted scour because they do not account properly for the effect of b/d_{50} on the maximum scour depth in front of the pier. However, the proposed modified formula with the enhanced correction factor for b/d_{50} developed from experimental results in this and other studies gave satisfactory results when compared with the large USGS field data sets that previously showed no real trends for scour depth..

During the design of physical models of local pier scour, one of the most important decisions is the selection of the model sediment size so that prototype scour depths can be reproduced in the laboratory. Through the improved scour prediction formula for scour depth in front of a pier developed in this study, a new procedure for modeling of scour around complex piers is presented so that measured scour depths can be properly scaled to prototype conditions. With this procedure, laboratory model results

for complex pier and bridge geometries, as affected by actual river bathymetry, can be reliably used to predict prototype scour at relatively low cost.

7.2 Conclusions

This contribution of this research to the problem of bridge pier scour prediction lies primarily in the development of an improved scour prediction formula that is based not only on extensive laboratory tests of actual bridges at different model scales with various model sediment sizes but also on detailed measurements of the turbulence characteristics of the horseshoe vortex and their connection to scour prediction. In addition, the proposed scour formula and suggested physical modeling technique developed in this research are strongly based on comparisons with field measurements. The research has an important application in designing physical models of complex piers that include river bathymetry and bridge geometry so that scour can be predicted in real-world cases rather than only in front of a single cylindrical pier on a flat bed. Specific results and conclusions from the study are given below.

- The experimental results from this study when combined with extensive experimental and field data from the literature have led to a modified scour prediction formula that more accurately describes the effect of the ratio of pier width to sediment size, b/d_{50} , on predicted pier scour depths.
- The Froude number is the relevant criterion to separate the relationships between b/d_{50} and relative scour depth, d_s/b , for the improved formula that is shown to be valid for both laboratory and field data.

- A quantitative physical connection is made between the effect of b/d_{50} on scour depth and the large-scale unsteadiness of the horseshoe vortex system in front of the pier by comparing time scales for lifting of the sediment particle and subsequent entrainment and transport of the particle out of the scour hole.
- Several scour prediction formulae were evaluated with extensive laboratory and field data, which showed that they mostly overpredicted scour depth due to the lack of consideration of the effect of b/d_{50} and that they did not perform as well as the proposed scour prediction formula.
- A more informed design method for physical models of local pier scour depth around complex piers, which is based on the relationship for the effect of b/d_{50} that is developed in this study, is presented in order to prevent bridge failures due to local scour.
- This study presents good agreement between field and laboratory measurements for velocity distribution and scour depth upstream of the bridge pier at three different field sites using the proposed new approach to physical modeling of scour.

7.3 Suggestions for Future Research

In general, the scour phenomena at a bridge site are found to consist of general bed degradation, contraction scour, and local scour (abutment and pier). Among these kinds of scour, local scour has been accounted for explicitly and individually through field

monitoring and by experimental and numerical methods. However, the interaction between local scour and contraction scour, which is mainly dependent on the geometry of the bridge site and river bathymetry, should be studied in more detail. Currently local scour and contraction scour are calculated independently and then summed to estimate total scour which does not account for their interaction. Using physical river modeling with river bathymetry constructed following the design method presented in this study, more accurate and practical predictions for total scour depth can be expected.

The unsteadiness of discharge during the passage of a flood event can affect the maximum scour depths around a bridge foundation. The maximum scour depth under the unsteady conditions of an actual flood (flood hydrograph) may be smaller than the predicted scour depth assumed to occur at a steady flowrate equal to the peak value of hydrograph. Thus, the predicted scour depth can be overestimated. A study of the effect of the flood hydrograph is needed for more accurate scour prediction and bridge foundation design.

In reality, bridge sites experience consecutive multiple flood events during the rainy season, and scouring often happens under live-bed scour conditions with infilling of the scour hole as the flood recedes and during smaller floods. A continuous series of scouring and infilling events is not well understood over a long time series because it is greatly affected by the conditions required to generally mobilize the entire bed and is further complicated by the movement of bed forms through the bridge section. Consecutive multiple floods occurring over a relatively long time period may show significant differences in terms of the maximum scour depth and scour contours around a bridge foundation. A well-designed physical model is needed to investigate these effects

including the modeling of bed forms such as dunes and ripples. Unless possible parameters mentioned in this study are carefully considered, realistic scour predictions cannot be realized.

APPENDIX A

EQUATIONS FOR BRIDGE PIER SCOUR

Ahmad (1953) proposed the local scour equation with English units

$$d_s = K V_1^{2/3} y_1^{2/3} - y_1 \quad (\text{A.1})$$

where K is a factor which is a function of the boundary geometry, pier width, pier shape, and angle of attack of approach flow. However the recommended range of K values is from 1.7 to 2.0.

Arunachalam (1965) converted the original relation suggested by Inglis (1949) in SI units:

$$\frac{d_s}{b} = \frac{d_r}{b} \left[1.95 \left(\frac{d_r}{b} \right)^{-1/6} - 1 \right] \quad (\text{A.2})$$

in which $d_r = 1.334 q^{2/3}$.

Baker (1980) proposed for clear-water scour condition:

$$\frac{d_s}{b} = (a_1 N - a_2) \tanh \left(a_3 \frac{y_1}{b} \right) \quad (\text{A.3})$$

where, a_1 , a_2 and a_3 are functions of d_*^2 and y_1/d_{50} , and N is the sediment number.

Baker (1981) improved the equation for scour depth in sand beds presented by Breusers, et al. (1977):

$$\frac{d_s}{b} = \left[g_1 \left(\frac{V_1}{V_c} \right) \right] \left[k_1 \tanh \left(k_2 \frac{y_1}{d_{50}} \right) \right] [g_2, g_3] \quad (\text{A.4})$$

where, k_1 and k_2 are functions of d_*^2 and y_1/d_{50} , g_1 is a function of V_1/V_c or N/N_c , g_2 and g_3 are functions of pier shape,

$$k_1 = \begin{cases} 1.625 \left[3.55 - \log \left(\frac{d_*^2}{10^3} \right) \right] \left[\frac{50}{y_1/d_{50}} + 0.35 \right] & \text{for } d_*^2 \leq 3.55 \times 10^5 \\ 1.625 \left[\frac{50}{y_1/d_{50}} + 0.35 \right] & \text{for } d_*^2 > 3.55 \times 10^5 \end{cases}$$

, and

$$k_2 = \begin{cases} 0.26 \log \left(\frac{d_*^2}{10^3} \right) + 0.32 & \text{for } d_*^2 \leq 3.55 \times 10^5 \\ 1.0 & \text{for } d_*^2 > 3.55 \times 10^5 \end{cases}$$

Basak et al. (1975) conducted local scour experiments with square piers in sand bed ($d_{50} = 0.65$ mm, $d_{90} = 1.0$ mm) for most live-bed scour conditions.

$$d_s = 0.558 b^{0.586} \quad (\text{A.5})$$

Blench-Inglis II equation is not dimensionless; as b, d_s and y_1 are in feet, V_1 is in feet per second and d_{50} is in mm (Blench 1962).

$$d_s = 1.53 b^{0.25} V_1^{0.5} y_1^{0.5} d_{50}^{-0.125} - y_1 \quad (\text{A.6})$$

Blench (1969) proposed the scour depth equation for live-scour conditions as following:

$$\frac{d_s}{b} = 1.8 \left(\frac{y_1}{b} \right)^{0.75} - \left(\frac{d_{50}}{y_1} \right) \quad (\text{A.7})$$

Breusers, et al. (1977)

$$\frac{d_s}{b} = \left[f_1 \left(\frac{V_1}{V_c} \right) \right] \left[2 \tanh \left(\frac{y_1}{b} \right) \right] [f_2, f_3] \quad (\text{A.8})$$

in which

$$f_1 = \begin{cases} 0 & \text{for } 0 \leq \frac{V_1}{V_c} \leq 0.5 \\ 2 \left(\frac{V_1}{V_c} \right) - 1 & \text{for } 0.5 \leq \frac{V_1}{V_c} \leq 1.0 \\ 1 & \text{for } 1.0 \leq \frac{V_1}{V_c} \end{cases}$$

and f_2 and f_3 are functions of the pier shape

Carstens (1966) formulated the similarity criteria for localized scour assuming that the velocity and velocity distribution in scour hole were a result of the disturbance element. He utilized the sediment number to present the terminal scour depth around a circular pier for live-bed scour

$$\frac{d_s}{b} = 0.546 \left(\frac{N_s^2 - 1.64}{N_s^2 - 5.02} \right)^{5/6} \quad (\text{A.9})$$

where, $N_s = V_1 / \sqrt{(SG - 1) g d_{50}}$ is referred to the sediment number.

Chitale (1962) found that the Froude number could characterize the relative scour depth as following:

$$\frac{d_s}{y_1} = -5.49 F_1^2 + 6.65 F_1 - 0.51 \quad (\text{A.10})$$

Coleman (1971) analyzed the data from Shen, et al. (1969)

$$\frac{d_s}{b} = 1.49 \left(\frac{V_1^2}{g y_1} \right)^{0.1} \quad (\text{A.11})$$

CSU equation presented by Richardson, et al. (1991)

$$\frac{d_s}{b} = 2.0 K_s K_\theta \left(\frac{y_1}{b} \right)^{0.35} F_1^{0.43} \quad (\text{A.12})$$

where K_s is the correction factor for pier shape shown in Table A.1:

Table A.1 Correction factor for pier nose shape, K_s (Richardson et al. 1991)

Shape	K_s
Sharp nosed	0.9
Circular and rounded nosed	1.0
Square nosed	1.1

and K_θ is the correction factor for angle of attack of the approach flow and the ratio of the pier length, l to the pier width, b as shown in Table A.2.

Table A.2 Correction factor for alignment, K_θ for square nosed pier (Richardson et al. 1991)

l/b	K_θ				
	$\theta = 0^\circ$	$\theta = 15^\circ$	$\theta = 30^\circ$	$\theta = 45^\circ$	$\theta = 90^\circ$
4	1.0	1.5	2.0	2.3	2.5
8	1.0	2.0	2.75	3.3	3.9
12	1.0	2.5	3.5	4.3	5.0

Froehlich (1988) proposed the scour equation for live-bed scour conditions

$$\frac{d_s}{b} = 0.32 K_1 K_2 \left(\frac{y_1}{b} \right)^{0.46} F_1^{0.2} \left(\frac{b}{d_{50}} \right)^{0.08} \quad (\text{A.13})$$

in which K_1 is the pier shape factor (1.3 for square nosed pier; 1.0 for round nosed pier; and 0.7 for sharp nosed pier) and $K_2 = (\cos \theta + l/b \sin \theta)^{0.62}$.

Hancu (1971) suggested the local pier scour equation only for $0.05 \leq V_c^2 / (g b) < 0.6$ and $0.5 < V_1 / V_c < 1.0$

$$\frac{d_s}{b} = 2.42 \left(2 \frac{V_1}{V_c} - 1 \right) F_{bc}^{2/3} = 3.3 \left(2 \frac{V_1}{V_c} - 1 \right) \left(\frac{b}{d_{50}} \right)^{-0.2} \left(\frac{y_1}{b} \right)^{0.13} \quad (\text{A.14})$$

where $F_{bc} = V_c / \sqrt{g b}$ and $V_c = 1.2 \sqrt{g d_{50} (SG - 1)} (y_1 / d_{50})^{0.2}$.

HEC-18 (Richardson and Davis 2001)

$$\frac{d_s}{b} = 2.0 K_s K_\theta K_b K_a \left(\frac{y_1}{b} \right)^{0.35} F^{0.43} \quad (\text{A.15})$$

where K_s is the correction factor for pier shape given at Table A.1; K_θ is the correction factor for angle of attack of approach flow shown in Table A.2 and calculated by $K_\theta = (\cos \theta + l/b \sin \theta)$; K_b is the correction factor for bed condition from Table A.3; K_a is the correction factor for armoring by bed material size ($= 1.0$ for $d_{50} < 2.0 \text{ mm}$ or $d_{90} < 20 \text{ mm}$, otherwise $= 0.4 (V_R)^{0.15}$ in which $V_R = (V_1 - V_{ic d_{50}}) / (V_{c d_{50}} - V_{ic d_{95}}) > 0$; $V_{ic d_{50}} = 0.645 (d_{50} / b)^{0.053} V_{c d_{50}}$; $V_{c d_{50}} = K_u y^{1/6} d_{50}^{1/3}$; $V_{ic d_{95}} = 0.645 (d_{95} / b)^{0.053} V_{c d_{95}}$; $V_{c d_{95}} = K_u y^{1/6} d_{95}^{1/3}$; K_u is 6.19 in SI units and 11.17 in English units. The minimum

value of K_a is 0.4 and it should only be used when $V_1 < V_{ic\ d_{50}}$.

Table A.3 Correction factor for bed condition, K_b (Richardson and Davis 2001)

Bed condition	Dune height, m	K_b
Clear-water scour	N/A	1.1
Plane bed and antidune	N/A	1.1
Small dune	$0.6 \leq H < 3.0$	1.1
Medium dune	$3.0 \leq H < 9.0$	1.2 to 1.1
Large dune	$9.0 \leq H$	1.3

Table A.4 Correction factor for armoring effect, K_a by d_{90}

	d_{50} , mm	$d_{90}/d_{50} \geq$	$V_1/V_c \leq$	K_a
Sand	< 20	-	-	1.0
Gravel	2 ~ 32	-	-	1.0
Gravel	32 ~ 64	4 ~ 3	0.50	0.95
Cobbles	64 ~ 250	3 ~ 2	0.50	0.90
	250 ~ 500	2 ~ 1	0.67	0.85
	500 >	1	0.67	0.80

Inglis-Lacey Equation was developed utilizing the data collected for scour around bridge piers at 17 bridges in Inda.

$$d_s = 0.946 \left(\frac{Q}{1.76 \sqrt{d_{50}}} \right)^{1/3} - y_1 \quad (\text{A.16})$$

where d_s and y_1 are in feet; Q is the cubic feet per second; and d_{50} is in millimeters.

Inglis-Poona I Equation was proposed based on local scour experiments around a single pier at the Central Water and Power Research Station in Poona, India in 1938 and 1939 (Inglis 1949).

$$\frac{d_s}{b} = 1.7 \left(\frac{q^{2/3}}{b} \right)^{0.78} - \frac{y_1}{b} \quad (\text{A.17})$$

in which d_s, b and y_1 are in feet, and q is the discharge intensity ($\text{ft}^3/\text{s}/\text{ft}$).

Inglis-Poona II Equation (1949) was developed in dimensionally homogeneous form as following:

$$\frac{d_s}{b} = 1.73 \left(\frac{y_1}{b} \right)^{0.78} - \frac{y_1}{b} \quad (\text{A.18})$$

Jain and Fischer (1980) suggested the pier scour equation at high flow velocities for $0.15 \leq (F_1 - F_c) \leq 1.2$ and $1 \leq y_1/b \leq 2$

$$\frac{d_s}{b} = 1.86 \left(\frac{y_1}{b} \right)^{0.5} (F_1 - F_c)^{0.25} \quad (\text{A.19})$$

where F_c is the critical Froude number at the initiation of bed material motion ($= V_c / \sqrt{g y_1}$ in which $V_c = 2.5 u_{*c} \ln(11 X y_1 / d_{50})$ and X is the Einstein's factor presented by Richardson et al. (1990)).

Kothyari et al. (1992a) conducted several live-bed scour experiments and proposed the model for prediction of temporal variation of scour depth and equilibrium scour depth during live bed scour

$$\frac{d_s}{b} = 0.99 \left(\frac{b}{d_{50}} \right)^{0.67} \left(\frac{y_1}{d_{50}} \right)^{0.4} \alpha^{-0.3} \quad (\text{A.20})$$

where, $\alpha = (B - b)/B$, B is the spacing between piers.

Larras (1963) analyzed the data presented by Chabert and Engeldinger (1956) and suggested the maximum scour equation near the critical velocity of the undisturbed sediments

$$d_s = 1.05 K_s b^{0.75} \quad (\text{A.21})$$

where K_s is the correction factor for pier shape(=1.0 for rounded pier; 1.1 to 1.4 for rectangular pier; and 0.85 for elliptical shape).

Laursen and Toch (1956) proposed pier scour equation for rectangular piers under zero angle of attack of approach flow

$$\frac{d_s}{b} = 1.5 \left(\frac{y_1}{b} \right)^{0.3} \quad (\text{A.22})$$

Laursen (1962) conducted numerous experiments with a rectangular pier aligned with the flow and found that the most important aspect of the geometry of the pier was the angle of attack of approach flow, coupled with the length-width ratio of the pier. The shape of pier is also significant if the pier is aligned with the flow.

$$\frac{b}{y_1} = 5.5 \left(\frac{d_s}{y_1} \right) \left[\left\{ \left(\frac{1}{11.5} \right) \left(\frac{d_s}{y_1} \right) + 1 \right\}^{1.7} - 1 \right] \quad (\text{A.23})$$

Melville and Sutherland (1988)

$$\frac{d_s}{b} = 2.4 K_I K_y K_d K_s K_\theta \quad (\text{A.24})$$

where K_I is the factor for flow intensity ($= [V_1 - (V_a - V_c)]/V_c$ for $[V_1 - (V_a - V_c)]/V_c < 1$

and otherwise 1.0); V_a is the armor velocity ($= 0.8 V_{ca}$ in which V_{ca} is the critical velocity of the coarsest possible armor size, $d_{50a} = d_{\max}/1.8$; d_{\max} can be determined by $d_{\max} = \sigma_g^m d_{50}$; and m values are shown in Table A.5 if a logarithmic distribution is assumed); K_y is the factor for flow depth ratio, y_1/b ($= 0.78 (y_1/b)^{0.255}$ if $y_1/b < 2.6$, otherwise 1.0); K_d is the factor for sediment size ratio, b/d_{50} ($= 0.57 \log(2.24 b/d_{50})$ for $b/d_{50} < 25$, otherwise 1.0); and K_s for pier shape and K_θ for angle of attack of approach flow are same as ones suggested by many researchers.

Table A.5 Exponent m -values of $d_{\max} = \sigma_g^m d_{50}$ for a logarithmic distribution

Assumed d_{\max}	m
d_{90}	1.28
d_{95}	1.65
d_{98}	2.06
d_{99}	2.34

Melville (1997) suggested the local scour depth at a bridge pier at equilibrium

$$\frac{d_s}{b} = K_I K_y K_d K_s K_\theta \quad (\text{A.25})$$

where K_y accounts for flow depth ratio, y_1/b ($= 4.5 y_1/b$ for $y_1/b < 0.2$; $2.0 \sqrt{y_1/b}$ for $0.2 \leq y_1/b < 1.4$; and 2.4 for $y_1/b > 1.4$).

Neil (1965)

$$\frac{d_s}{b} = 1.5 \left(\frac{y_1}{b} \right)^{0.3} \quad (\text{A.26})$$

Shen et al. (1969) found that the strength of the horseshoe vortex was a function of the pier Reynolds number and proposed local scour equation for clear-water scour condition

$$d_s = 0.00022 \left[\frac{V_1 b}{2 \nu} \right]^{0.619} \quad (\text{A.27})$$

which does not appropriately account for the pier shape and sediment size and is too conservative to be used for live-bed scour conditions.

Shen-Maza equation is associated with the pier Froude number (Shen et al. 1969)

$$\frac{d_s}{b} = \begin{cases} 11.0 F_p^2 & \text{for } F_p < 0.2 \\ 3.4 F_p^{0.67} & \text{for } F_p > 0.2 \end{cases} \quad (\text{A.28})$$

where F_p is the pier Froude number defined as $V_1 / \sqrt{g b}$.

Sheppard et al. (2004b) suggested pier scour equation for clear-water scour condition based on laboratory experiments

$$\frac{d_s}{b} = 2.5 f_1 \left(\frac{y_1}{b_*} \right) f_2 \left(\frac{V_1}{V_c} \right) f_3 \left(\frac{b_*}{d_{50}} \right) \quad (\text{A.29})$$

where

$$f_1 \left(\frac{y_1}{b_*} \right) = \tanh \left[\left(\frac{y_1}{b_*} \right)^{0.4} \right]$$

$$f_2 \left(\frac{V_1}{V_c} \right) = 1 - 1.75 \left[\ln \left(\frac{V_1}{V_c} \right) \right]^2$$

$$f_3\left(\frac{b}{d_{50}}\right) = \frac{b_*/d_{50}}{0.4 (b_*/d_{50})^{1.2} + 10.6 (b_*/d_{50})^{-0.13}}$$

and, b_* is the effective pier diameter(= $K_s b$, in which b is the width of the pier;

$K_s = 1.0$ for a circular pier and $K_s = 1.23$ for square pier).

Sheppard et al. (2003) conducted live bed local scour experiments

$$\frac{d_s}{b_*} = \begin{cases} f_1\left(\frac{y_1}{b_*}\right) \left[2.2 \frac{V_1 - V_c}{V_{lp} - V_c} + 2.5 f_3\left(\frac{b_*}{d_{50}}\right) \frac{V_{lp} - V_1}{V_{lp} - V_c} \right] & \text{for } 1.0 \leq \frac{V_1}{V_c} < \frac{V_{lp}}{V_c} \\ 2.2 \tanh\left[\left(\frac{y_1}{b_*}\right)^{0.4}\right] & \text{for } \frac{V_1}{V_c} \geq \frac{V_{lp}}{V_c} \end{cases} \quad (\text{A.30})$$

where V_{lp} is the velocity at which the live bed peak scour occurs and becomes the greater

between V_{lp1} and V_{lp2} given by:

$$V_{lp1} = \sqrt{26 \tau_{*c} (SG - 1) d_{50}} \left(18 \frac{m^{1/2}}{s} \right) \log_{10} \left(\frac{4 y_1}{d_{90}} \right) \text{ and } V_{lp2} = 0.8 \sqrt{g y_1}$$

Simplified Chinese scour equation was proposed (Gao et al. 1993).

$$d_s = \begin{cases} 0.78 K_{sc} B^{0.6} y_1^{0.15} d_{50}^{-0.07} \left(\frac{V_1 - V_c'}{V_c - V_c'} \right) & \text{for clear - water scour} \\ 0.46 K_{sc} B^{0.6} y_1^{0.15} d_{50}^{-0.07} \left(\frac{V_1 - V_c'}{V_c - V_c'} \right)^n & \text{for live - bed scour} \end{cases} \quad (\text{A.31})$$

where K_{sc} is a simplified pier shape coefficient defined as 1.0 for circular cylinders, 0.8

for round-nosed, 0.66 for shape-nosed piers; B is the ratio of depth with weighted pier to

footing width projected normal to flow (= $(B_p(y_1 - h) + B_F(h))/y_1$) for example,

$B_p = b \cos \alpha + l \sin \alpha$ for rectangular pier, $B_p = b - (l - b) \sin \alpha$ for round and sharp

nosed piers and $B_F = b_F \cos \alpha + l_F \sin \alpha$ for rectangular footing; $n = (V_c/V_1)^{9.35-2.23 \log d_{50}}$;

$V_c = (y_1/d_{50})^{0.14} \sqrt{17.6 (SG-1) d_{50} + 6.05 \times 10^{-7} (10 + y_1/d_{50}^{0.72})}$, and V_c' is the approach velocity associated with the critical velocity, V_c and incipient scour in the accelerated flow region at the bridge pier, which can be calculated by $V_c' = 0.645 (d_{50}/b)^{0.053} V_c$.

Torsethaugen (1975) suggested the temporal pier scour equations for $y_1/b < 1.0$ with a large diameter of pier (up to 0.75m) as following:

$$\frac{d_s}{d_{se}} = \exp \left[- \left(\frac{t_0}{t} \right)^{0.5} \right] \quad (\text{A.32})$$

in which d_{se} and t_0 are the equilibrium scour depth and time respectively.

$$\frac{d_{se}}{b} = 1.8 \left(\frac{V_1}{V_c} - 0.54 \right) \frac{y_1}{b} \quad (\text{A.33})$$

APPENDIX B

As the actual example, the USGS recorded a peak discharge of $3030 \text{ m}^3/\text{s}$ during the tropical storm Alberto at the bridge site, of which pier width is 1.83m, on the Flint River at Bainbridge, Georgia. The approach flow depth was 11.28m and the median sediment size was 0.38 mm. About 2.91m scour depth in front of the bridge pier occurred due to the flood event. Thus, the values of $(V_1/V_c)_p$, Fr_p , $(y_1/b)_p$, $(b/d_{50})_p$ can be naturally calculated. In order to design the physical model for this bridge site, first, the length ratio, L_r is determined as 1:90 and the values of pier width, approach flow depth, and approach flow velocity for physical model can be incessantly evaluated as presented in Figure 6.43. When the median sediment size for the physical model is chosen, $d_{50p} = 1.1\text{mm}$, the corresponding critical velocity becomes 0.43 m/s . The ratio of each correction factor for b/d_{50} can be obtained by Figure 6.40 and Equation (6.20) or Equation (6.21) while the ratio of each correction factor for V_1/V_c can be accounted for by the relationship from Melville and Sutherland's formula(1988). The results are 0.56 for the effect for b/d_{50} and 1.82 for the effect for V_1/V_c , respectively. Therefore, the scour ratio becomes 1.02, which means this design will be satisfactory and the scour depth from experiments with the physical model will be supposed to divided by the scour ratio to predict the maximum scour depth in field. All values calculated for this design are presented in Table B.1.

Table B.1 Sample calculations of the design for physical model for the tropical storm Alberto in Flint River at Bainbridge, Georgia

	V_1/V_c	b/d_{50}	y_1/b	Fr	K_I	K_d	K_{Im}/K_{Ip}	K_{dm}/K_{dp}	SC_r
Prototype	5.27	4812.6	6.17	0.22	1.0	0.53			
Model	0.56	18.8	6.17	0.22	0.56	0.97	0.56	1.82	1.02

In summary, the practical methodology is presented for the physical model in the study of the local pier scour if the appropriate data are given from field surveying. Also the scale effect due to the sediment size can be considered by SC_r when the values scale up from the physical model to prototype.

REFERENCES

- Ahmad, M. (1953). "Experiments on design and behavior of spur dikes." *Minnesota International Hydraulics Convention*, Minneapolis, Minnesota, 145-159.
- Ahmed, F., and Rajaratnam, N. (1997). "Three-dimensional turbulent boundary layer flow around bridge piers." *Journal of Hydraulic Research*, 35(2), 209.
- Ahmed, F., and Rajaratnam, N. (1998). "Flow around bridge piers." *Journal of Hydraulic Engineering*, 124(3), 288.
- Ali, K. H. M., and Karim, O. (2002). "Simulation d'écoulements autour de piles de ponts Simulation of flow around piers." *Journal of Hydraulic Research*, 40(2), 161.
- Ali, K. H. M., Karim, O. A., and O'Connor, B. A. (1997). "Flow patterns around bridge piers and offshore structures." *Proceedings, Congress of the International Association of Hydraulic Research, IAHR*, San Francisco, CA, USA, 225.
- Arunachalam, K. (1965). "Scour around bridge piers." *Journal of the Indian Roads Congress* (2), 189-210.
- Baker, C. J. (1978). "Vortex flow around the bases of obstacles," Ph.D Thesis, University of Cambridge, Cambridge, UK.
- Baker, C. J. (1980). "Theoretical approach to prediction of local scour around bridge piers." *Journal of Hydraulic Research*, 18(1), 1-12.
- Baker, C. J. (1981). "New design equations for scour around bridge piers." *Journal of the Hydraulics Division*, 107(4), 507-511.
- Basak, V., Basamisli, Y., and Ergun, O. (1975). "Maximum equilibrium scour depth around linear-axis square cross-section pier groups." 583, State Hydraulic Works, Ankara, Turkey.
- Bergstrom, D. J., Kotey, N. A., and Tachie, M. F. (2002). "The effects of surface roughness on the mean velocity profile in a turbulent boundary layer." *Journal of Fluids Engineering*, 124(3), 664-670.
- Blench, T. (1962). "Discussion of "scour at bridge crossing", by E. M. Laursen." *Transactions of the American Society of Civil Engineers*, 127, 180-183.
- Blench, T. (1969). *Mobile-bed fluviology; a regime theory treatment of rivers for engineers and hydrologists*, Alta., University of Alberta Press, Edmonton.

- Breusers, H. N. C. (1971). "Local scour near offshore structures." *Symposium in Offshore Hydrodynamics*, Wageningen.
- Breusers, H. N. C., Nicollet, G., and Shen, H. W. (1977). "Local Scour around Cylindrical Piers." *Journal of Hydraulic Research*, 15(3), 252.
- Breusers, H. N. C., and Raudkivi, A. J. (1991). *Scouring*, International Association for Hydraulic Research, Rotterdam, Netherland.
- Briaud, J.-L., Ting, C. K., Chen, H. C., Gudavalli, R., Perugu, S., and Wei, G. (1999). "SRICOS: prediction of scour rate in cohesive soils at bridge piers." *Journal of Geotechnical and Geoenvironmental Engineering*, 125(4), 237.
- Briaud, J. L., Ting, F. C. K., Chen, H. C., Gudavalli, S. R., and Kwak, K. (2002). "Maximum scour depth around a bridge pier in sand and in clay: Are they equal?" *Geotechnical Special Publication* (116), 385-395.
- Carstens, M. R. (1966). "Similarity laws for localized scour." *American Society of Civil Engineers Proceedings, Journal of the Hydraulics Division*, 92(HY3), 13.
- Chabert, J., and Engeldinger, P. (1956). *Etude des Affouilements autour des Piles des Ponts*, Laboratoire National d'Hydraulique, Chatou, France.
- Chang, W.-Y., Lai, J.-S., and Yen, C.-L. (2004). "Evolution of scour depth at circular bridge piers." *Journal of Hydraulic Engineering*, 130(9), 905-913.
- Chiew, Y.-M. (1984). "Local scour at bridge piers." 355, School of Engineering, University of Auckland, Auckland, New Zealand.
- Chitale, S. V. (1962). "Scour at bridge crossing." *Transactions of the American Society of Civil Engineers*, 127(1), 191-196.
- Coleman, N. L. (1971). "Analyzing laboratory measurements of scour at cylindrical piers in sand beds." *Proceedings 14th Congress, IAHR*, Paris, France, 307-313.
- Coleman, S. E. (2005). "Clearwater local scour at complex piers." *Journal of Hydraulic Engineering*, 131(4), 330-334.
- Cunha, L. V. (1975). "Time Evolution of Local Scour." *Proceedings 16th Congress, IAHR*, Sao Paulo, Braz, 285-299.
- Dargahi, B. (1989). "Turbulent flow field around a circular cylinder." *Experiments in Fluids*, 8(1-2), 1-12.
- De Falco, F., and Mele, R. (2002). "The monitoring of bridges for scour by sonar and sedimenti." *NDT and E International*, 35(2), 117-123.
- Devenport, W. J., and Simpson, R. L. (1990). "Time-dependent and time-averaged

- turbulence structure near the nose of a wing-body junction." *Journal of Fluid Mechanics*, 210, 23-55.
- Dey, S. (1996). "Sediment pick-up for evolving scour near circular cylinders." *Applied Mathematical Modelling*, 20(7), 534-539.
- Dey, S., and Bose, S. K. (1994). "Bed shear in equilibrium scour around a circular cylinder embedded in a loose bed." *Applied Mathematical Modelling*, 18(5), 265-273.
- Dou, G. (1974). "Similarity theory and its application to the design of total sediment transport model." Nanjing Hydraulic Research Institute, Nanjing, China.
- Dou, X., Jones, J. S., Young, G. K., and Stein, S. M. (1998). "Using a 3-D model to predict local scour." *International Water Resources Conference*, Memphis, 198-203.
- Dou, X. S., and Jones, J. S. (2000). "A new sediment transport formula for local scour prediction." *Joint Conference on Water Resources Engineering and Water Resources Planning & Management*, Minneapolis.
- Einstein, H. A. (1950). "Bed-load function for sediment transportation in open channel flows." United States Department of Agriculture (USDA), Washington, DC, United States, Bulletin 1027 71.
- Ettema, R. (1976). "Influence of bed material gradation on local scour," University of Auckland, Auckland, New Zealand.
- Ettema, R. (1980). "Scour at bridge piers." No. 216, Dept. of Civil Engineering, University of Auckland, Auckland, New Zealand.
- Ettema, R., Kirkil, G., and Muste, M. V. (2006). "Similitude of large-scale turbulence in experiments on local scour at cylinders." *Journal of Hydraulic Engineering*, 132(1), 33-40.
- Ettema, R., Melville, B. W., and Barkdoll, B. (1998). "Scale effect in pier-scour experiments." *Journal of Hydraulic Engineering*, 124(6), 639-642.
- Forde, M. C., McCann, D. M., Clark, M. R., Broughton, K. J., Fenning, P. J., and Brown, A. (1999). "Radar measurement of bridge scour." *NDT and E International*, 32(8), 481-492.
- Foxboro. (2004). "PSS-1-6f5." http://resource.invensys.com/instrumentation/specifications/pss/1/1_6f5a.pdf.
- Froehlich, D. C. (1988). "Analysis of onsite measurements of scour at piers." *Proceeding of the ASCE National Hydraulic Engineering Conference*, 534-539.

- Gao, D., Posada G, L., and Nordin, C. F. (1993). "Pier scour equations used in China." *Proceedings - National Conference on Hydraulic Engineering*, San Francisco, CA, USA, 1031-1036.
- Garde, R. J., Ranga Raju, K. G., and Kothiyari, U. C. (1989). "Research Report on Effect of Unsteadiness of Stratification on Local Scour." Civil Engineering Department, University of Roorkee, Roorkee, India.
- Ge, L., Lee, S. O., Sotiropoulos, F., and Sturm, T. (2005). "3D unsteady RANS modeling of complex hydraulic engineering flows. II: Model validation and flow physics." *Journal of Hydraulic Engineering*, 131(9), 809-820.
- Ge, L., and Sotiropoulos, F. (2005). "3D unsteady RANS modeling of complex hydraulic engineering flows. I: Numerical model." *Journal of Hydraulic Engineering*, 131(9), 800-808.
- Gosselin, M. S., and Sheppard, D. M. (1995). "Time rate of local scour." *International Water Resources Engineering Conference - Proceedings*, 775-779.
- Graf, W. H. (1995). "Local scour around piers." Annual Report, E. P. F. d. Lausanne, ed., Laboratoire de Recherches Hydrauliques, Lausanne, Switzerland, B.33.1-B.33.8.
- Graf, W. H., and Istiarto, I. (2002). "Flow pattern in the scour hole around a cylinder." *Journal of Hydraulic Research*, 40(1), 13-20.
- Hancu, S. (1971). "Sur le calcul des affouillements locaux dans la zone des piles de ponts." *Proceedings 14th Congress, IAHR*, Paris, France, 299-313.
- Hjorth, P. (1977). "A stochastic model of progressive scour." *proceedings, Second International IAHR Symposium on Stochastic Hydraulics*, University of Lund, Sweden, 365-383.
- Hoffmans, G. J. C. M., and Verheij, H. J. (1997). *Scour manual*, Brookfield, VT, Rotterdam, Netherlands.
- Hong, S. (2005). "Interaction of bridge contraction scour and pier scour in a laboratory river model," Georgia Institute of Technology, Atlanta, GA.
- Hosny, M. M. (1995). "Experimental study of local scour around circular bridge piers in cohesive soils," Colorado State University, Fort Collins.
- Inglis, C. C. (1949). "Behaviour and control of rivers and canals." Government of India Central Waterpower Irrigation and Navigation Research Station, Poona -- Research Publications, 487.
- Jain, S. C. (1981). "Maximum clear-water scour around circular piers." *Journal of Hydraulic Division*, 107(5), 611-626.

- Jain, S. C., and Fischer, E. E. (1980). "Scour around Bridge Piers at High Flow Velocities." *Journal of Hydraulic Division*, 106(11), 1827-1841.
- Johnson, P. A., and McCuen, R. H. (1991). "A temporal, spatial pier scour model." Transportation Research Board, National Research Council, Washington, D.C.
- Jones, J. S., Kilgore, R. T., and Mistichelli, M. P. (1992). "Effects of footing location on bridge pier scour." *Journal of Hydraulic Engineering*, 118(2), 280-290.
- Kan, M., and Kawamura, T. (2000). "Numerical study of flow structure around a flat plate standing on the sand." *Theoretical and Applied Mechanics*, 49, 197-203.
- Kandasamy, J. K. (1989). "Abutment scour: a report submitted to the Road Research Unit of the National Roads Board." no. 458, Dept. of Civil Engineering, University of Auckland, Auckland, New Zealand.
- Kawamura, T., Kan, M., and Hayashi, T. (1999). "Numerical study of the flow and the sand movement around a circular cylinder standing on the sand." *JSME International Journal, Series B*, 42(4), 605-611.
- Kirkil, G., Ettema, R., and Muste, M. V. (2004). "Similitude of coherent turbulence structures in flume studies of bridge scour." *2nd International conference on scour and erosion*, Singapore, 1-8.
- Kironoto, B. A., and Graf, W. H. (1994). "Turbulence characteristics in rough uniform open-channel flow." *Proceedings of the Institution of Civil Engineers, Water Maritime and Energy*, 106(4), 333-344.
- Kothyari, U. C., Garde, R. J., and Ranga Raju, K. G. (1992a). "Live-bed scour around cylindrical bridge piers." *Journal of Hydraulic Research*, 30(5), 701-715.
- Kothyari, U. C., Garde, R. J., and Ranga Raju, K. G. (1992b). "Temporal variation of scour around circular bridge piers." *Journal of Hydraulic Engineering*, 118(8), 1091-1106.
- Krogstad, P. A., and Antonia, R. A. (1999). "Surface roughness effects in turbulent boundary layers." *Experiments in Fluids*, 27(5), 450-460.
- Krogstad, P. A., Antonia, R. A., and Browne, L. W. B. (1992). "Comparison between rough- and smooth-wall turbulent boundary layers." *Journal of Fluid Mechanics*, 245, 599-617.
- Kundu, P. K. (1990). *Fluid mechanics*, Academic Press, San Diego.
- Landers, M. N., and Mueller, D. S. (1996). "Evaluation of selected pier-scour equations using field data." *Transportation Research Record* (1523), 186-195.
- Lane, S. N., Biron, P. M., Bradbrook, K. F., Butler, J. B., Chandler, J. H., Crowell, M. D.,

- McLelland, S. J., Richards, K. S., and Roy, A. G. (1998). "Three-dimensional measurement of river channel flow processes using acoustic Doppler velocimetry." *Earth Surface Processes and Landforms*, 23(13), 1247-1267.
- Larras, J. (1963). "Profondeurs maximales d'erosion des fonds mobiles autour des piles en riviere." *Annales des Ponts et Chaussees*, 133(4), 411-424.
- Laursen, E. M. (1962). "Scour at bridge crossings." *Transactions of the American Society of Civil Engineers*, 127(HY2, Part 1), 166-209.
- Laursen, E. M., and Toch, A. (1956). "Scour around bridge piers and abutments." Iowa Institute of Hydraulic Research.
- LeFeuvre, A. R., Altinbilek, H. D., and Carstens, M. R. (1970). "Sediment pickup function." *Journal of Hydraulic Division*, 96(10), 2051-2063.
- Marchioli, C., and Soldati, A. (2002). "Mechanisms for particle transfer and segregation in a turbulent boundary layer." *Journal of Fluid Mechanics*, 468, 283-315.
- Marsh-McBirney. (2002). "Instruction Mannul Model 523." Marsh-McBirney Inc.
- Melville, B. W. (1975). "Local scour at bridge sites." University of Auckland, School of Engineering, Auckland.
- Melville, B. W. (1997). "Pier and abutment scour: integrated approach." *Journal of Hydraulic Engineering*, 123(2), 125-136.
- Melville, B. W., and Chiew, Y. M. (1999). "Time scale for local scour at bridge piers." *Journal of Hydraulic Engineering*, 125(1), 59.
- Melville, B. W., and Coleman, S. E. (2000). *Bridge scour*, Water Resources Publications, Highlands Ranch, Colo.
- Melville, B. W., and Raudkivi, A. J. (1977). "Flow characteristics in Local Scour at Bridge Piers." *Journal of Hydraulic Research*, 15(4), 373-380.
- Melville, B. W., and Raudkivi, A. J. (1996). "Effects of foundation geometry on bridge pier scour." *Journal of Hydraulic Engineering*, 122(4), 203-209.
- Melville, B. W., and Sutherland, A. J. (1988). "Design method for local scour at bridge piers." *Journal of Hydraulic Engineering*, 114(10), 1210-1226.
- Mendoza-Cabral, C. (1993). "Computation of flow past a cylinder mounted on a flat plate." *Proceedings - National Conference on Hydraulic Engineering*, Venice, Italy, 899-904.
- Mia, F., and Nago, H. (2003). "Design method of time-dependent local scour at circular bridge pier." *Journal of Hydraulic Engineering*, 129(6), 420-427.

- Millard, S. G., Bungey, J. H., Thomas, C., Soutsos, M. N., Shaw, M. R., and Patterson, A. (1998). "Assessing bridge pier scour by radar." *NDT & E International*, 31(4), 251-258.
- Miller, W. (2003). "Model for the time rate of local sediment scour at a cylindrical structure," Book; Archival Material, University of Florida.
- Mueller, D. S., and Wagner, C. R. (2005). *Field observations and evaluations of streambed scour at bridges*, U.S. Department of Transportation, Federal Highway Administration, Research, Development, and Technology, Turner-Fairbank Highway Research Center, McLean, Va.
- Muzzamil, M., et al. (1989). "Vorticity Characteristics of Scouring Horseshoe Vortex." *Proceeding of 3rd International Workshop on Alluvial River Problems*, Roorkee, India, 19-26.
- Muzzammil, M., and Gangadhariah, T. (2003). "Caracteristiques moyennes d'un vortex en fer a cheval au droit d'une pile cylindrique(The mean characteristics of horseshoe vortex at a cylindrical pier)." *Journal of Hydraulic Research*, 41(3), 285-297.
- Nagata, N., Sosoda, T., Nakato, T., and Muramoto, Y. (2005). "Three-dimensional numerical model for flow and bed deformation around river hydraulic structures." *Journal of Hydraulic Engineering*, 131(12), 1074-1087.
- Nakagawa, H., and Suzuki, K. (1975). "Application of stochastic model of sediment motion to local scour around a bridge pier." *Proceedings 16th Congress, IAHR*, Sao Paulo, Braz, 285-299.
- Neill, C. R. (1965). "Measurments of bridge scour and bed changes in a flooding sand-bed river." Landon, England, 415-436.
- Nelson, J. M., Shreve, R. L., McLean, S. R., and Drake, T. G. (1995). "Role of near-bed turbulence structure in bed load transport and bed form mechanics." 31(8), 2071-2086.
- Nezu, I., and Nakagawa, H. (1993). *Turbulence in open-channel flows*, Brookfield, Rotterdam.
- Nezu, I., and Rodi, W. (1986). "Open-channel flow measurements with a laser Doppler anemometer." *Journal of Hydraulic Engineering*, 112(5), 335-355.
- Nikora, V., and Goring, D. (1998). "Spectral scaling for gravel-bed open channel flows." *NATO Advanced Research Workshop*, Moscow, 239-245.
- Nikora, V., and Goring, D. (2000). "Flow turbulence over fixed and weakly mobile gravel beds." *Journal of Hydraulic Engineering*, 126(9), 679-690.

- Okajima, A. (1982). "Strouhal numbers of rectangular cylinders." *Journal of Fluid Mechanics*, 123, 379-398.
- Oliveto, G., and Hagger, W. H. (2002). "Temporal evolution of clear-water pier and abutment scour." *Journal of Hydraulic Engineering*, 128(9), 811-820.
- Olsen, N. R. B., and Kjellesvig, H. M. (1998). "Three-dimensional numerical flow modeling for estimation of maximum local scour depth." *Journal of Hydraulic Research/De Recherches Hydrauliques*, 36(4), 579-590.
- Olsen, N. R. B., and Melaaen, M. C. (1993). "Three-dimensional calculation of scour around cylinders." *Journal of Hydraulic Engineering*, 119(9), 1048-1054.
- Qadar, A. (1981). "Vortex Scour Mechanism at Bridge Piers." *Proceedings of the Institution of Civil Engineers*, London, England, 739-757.
- Qadar, A., and Ansari, S. A. (1991). "Model studies on local scour." *Proceedings - National Conference on Hydraulic Engineering*, 1120-1126.
- Rahman, S., and Webster, D. R. (2005). "The effect of bed roughness on scalar fluctuations in turbulent boundary layers." *Experiments in Fluids*, 38(3), 372-384.
- Ram, S. (1998). "A theoretical model to predict local scour at bridge piers in non-cohesive soils." *The Seventh International Symposium on River Sedimentation*, Hong Kong, China, 173-178.
- Raudkivi, A. J. (1986). "Functional Trends of Scour at Bridge Piers." *Journal of Hydraulic Engineering*, 112(1-13), 1.
- Raudkivi, A. J., and Ettema, R. (1983). "Clear-water Scour at Cylindrical Piers." *Journal of Hydraulic Engineering*, 109(3), 338-350.
- Richardson, E. V. (1995). *Evaluating scour at bridges*, Federal Highway Administration, Washington, D.C.
- Richardson, E. V., and Davis, S. R. (2001). "Evaluating scour at bridges." R. C. E. Inc., ed., U.S. Federal Highway Administration.
- Richardson, E. V., Richardson, J. R., and Abed, L. (1991). "Estimating scour at bridges." *Third bridge engineering conference*, 2(1290), p. 245-253.
- Richardson, E. V., Simons, D. B., and Julien, P. Y. (1990). *Highways in the river environment: participant notebook*, Federal Highway Administration, McLean, VA.
- Roulund, A. (2000). "Three-dimensional numerical modelling of flow around a bottom-mounted pile and its application to scour," Dept. of Hydrodynamics and Water Resources, Technical University of Denmark, Lyngby, Denmark.

- Roulund, A., Sumer, B. M., Fredsoe, J., and Michelsen, J. (2005). "Numerical and experimental investigation of flow and scour around a circular pile." *Journal of Fluid Mechanics*, 534, 351-401.
- Sadiq, A. (1992). "Clear-water scour around bridge abutments in compound channels," Georgia Institute of Technology, Atlanta, GA.
- Salaheldin, T. M., Imran, J., and Chaudhry, M. H. (2004). "Numerical modeling of three-dimensional flow field around circular piers." *Journal of Hydraulic Engineering*, 130(2), 91-100.
- Shen, H. W., Schneider, V. R., and Karaki, S. S. (1969). "Local Scour Around Bridge Piers." *Journal of Hydraulic Division*, 95(HY6), 1919-1940.
- Sheppard, D. M. (2003). "Large scale and live bed local pier scour experiments. live bed experiments / Phase 2." Florida Dept. of Transportation.
- Sheppard, D. M., Odeh, M., and Glasser, T. (2004). "Large scale clear-water local pier scour experiments." *Journal of Hydraulic Engineering*, 130(10), 957-963.
- Sheppard, D. M., Sterling, J. J., and Mufeed, O. (2000). "Local sediment scour model tests for the woodrow wilson bridge piers." *2000 Joint Conference on Water Resource Engineering and Water Resources Planning & Management*, 132-141.
- Shirole, A. M. (1991). "Planning for a comprehensive bridge safety assurance program." *Transportation Research Board*, 1290, 137-142.
- Simpson, R. L. (2001). "Junction flows." *Annual Review of Fluid Mechanics*, 33, 415-443.
- Song, T., and Graf, W. H. (1996). "Velocity and turbulence distribution in unsteady open-channel flows." *Journal of Hydraulic Engineering*, 122(3), 141-154.
- SonTek. (2001). "ADV Principles of Operation." SonTek Inc., San Diego, CA.
- Stamey, T. C. (1996). "Summary of data-collection activities and effects of flooding from tropical storm Alberto in parts of Georgia, Alabama, and Florida, July 1994." 96-228, USGS.
- Sturm, T. W. (2001). *Open-channel hydraulics*, McGraw-Hill, Boston.
- Sturm, T. W. (2006). "Scour around Bankline and Setback Abutments in Compound Channels." *Journal of Hydraulic Engineering*, 132(1), 21-32.
- Sturm, T. W., Sotiropoulos, F., Landers, M. N., Gotvald, T., Lee, S., Ge, L., Navarro, R., and Escarriaza, C. (2004). "Laboratory and 3D numerical modeling with field monitoring of regional bridge scour in Georgia." 2002, Georgia Department of Transportation, Atlanta, GA.

- Sumer, B. M., Christiansen, N., and Fredsoe, J. (1992). "Time scale of scour around a vertical pile." *The Proceedings of the 2nd (1992) International Offshore and Polar Engineering Conference*, Golden, CO, 308-316.
- Sumer, B. M., and Fredsoe, J. (1997). *Hydrodynamics around cylindrical structures*, World Scientific, Singapore; River Edge, N.J.
- Sung, J., and Yoo, J. Y. (2001). "Three-dimensional phase averaging of time-resolved PIV measurement data." *Measurement Science and Technology*, 12(6), 655-662.
- Tennekes, H., and Lumley, J. L. (1972). *A first course in turbulence*, Mass., MIT Press, Cambridge.
- Ting, F. C. K., Briaud, J. L., Chen, H. C., Gudavalli, R., Perugu, S., and Wei, G. (2001). "Flume tests for scour in clay at circular piers." *Journal of Hydraulic Engineering*, 127(11), 969-978.
- Torsethaugen, K. (1975). "Lokal erosjon ved store konstruksjoner modellforsok." Vassdrags-og Havne-laboratoriet, Trondheim, Norway.
- Tseng, M.-H., Yen, C.-L., and Song, C. C. S. (2000). "Computation of three-dimensional flow around square and circular piers." *International Journal for Numerical Methods in Fluids*, 34(3), 257.
- van Rijn, L. C. (1984). "Sediment Transport, Part I; Bed Load Transport." *Journal of Hydraulic Engineering*, 110(10), 1431-1456.
- van Rijn, L. C. (1987). "Mathematical modeling of morphological processes in the case of suspended sediment transport." *PB89-109045*, Waterloopkundig Lab., Delft Hydraulics Comm-382, Delft, Netherlands.
- Varzeliotis, A. N. T. (1960). "Model studies of scour around bridge piers and stone aprons," University of Alberta, Alberta.
- Vincent, M. S., Ross, M. A., and Ross, B. E. (1993). "Tidal inlet bridge scour assessment model." *Transportation Research Record* (1420), 7-13.
- Voulgaris, G., and Trowbridge, J. H. (1998). "Evaluation of the Acoustic Doppler Velocimeter (ADV) for Turbulence Measurements." *Journal of Atmospheric and Oceanic Technology*, 15(1), 272-289.
- Wei, G. (1997). "Numerical simulation of scour process around bridge piers in cohesive soil," Texas A&M University, College Station, TX.
- Yalin, M. S. (1977). *Mechanics of sediment transport*, Pergamon Press, Oxford, England.
- Yanmaz, A. M., and Altinbilek, H. D. (1991). "Study of time-dependent local scour around bridge piers." *Journal of Hydraulic Engineering*, 117(10), 1247-1268.

Zhang, Z., Eisele, K., and Hirt, F. (1997). "The influence of phase-averaging window size on the determination of turbulence quantities in unsteady turbulent flows." *Experiments in Fluids*, 22(3), 265-267.